

ON THE ROAD TO IMAGING EXTRASOLAR PLANETS: NULL RESULTS,
OTHER DISCOVERIES ALONG THE WAY, AND SIGNPOSTS FOR THE
FUTURE

by
Eric Ludwig Nielsen

A Dissertation Submitted to the Faculty of the
DEPARTMENT OF ASTRONOMY
In Partial Fulfillment of the Requirements
For the Degree of
DOCTOR OF PHILOSOPHY
In the Graduate College
THE UNIVERSITY OF ARIZONA

2011

THE UNIVERSITY OF ARIZONA
GRADUATE COLLEGE

As members of the Dissertation Committee, we certify that we have read the dissertation prepared by Eric Ludwig Nielsen entitled "On the Road to Imaging Extrasolar Planets: Null Results, Other Discoveries Along the Way, and Signposts for the Future" and recommend that it be accepted as fulfilling the dissertation requirement for the Degree of Doctor of Philosophy.

Laird Close Date: 22 March 2011

Don McCarthy Date: 22 March 2011

Philip Hinz Date: 22 March 2011

Glenn Schneider Date: 22 March 2011

Final approval and acceptance of this dissertation is contingent upon the candidate's submission of the final copies of the dissertation to the Graduate College.

I hereby certify that I have read this dissertation prepared under my direction and recommend that it be accepted as fulfilling the dissertation requirement.

Dissertation Director: Laird Close Date: 22 March 2011

STATEMENT BY AUTHOR

This dissertation has been submitted in partial fulfillment of requirements for an advanced degree at The University of Arizona and is deposited in the University Library to be made available to borrowers under rules of the Library.

Brief quotations from this dissertation are allowable without special permission, provided that accurate acknowledgment of source is made. Requests for permission for extended quotation from or reproduction of this manuscript in whole or in part may be granted by the head of the major department or the Dean of the Graduate College when in his or her judgment the proposed use of the material is in the interests of scholarship. In all other instances, however, permission must be obtained from the author.

SIGNED: Eric Ludwig Nielsen

ACKNOWLEDGMENTS

I want to thank everyone who's helped me develop in my career as a scientist, allowing me to finish this work.

Thanks to those of you at Berkeley, who helped me gain a solid foothold in astronomy as an undergraduate: Debra Fischer, Geoff Marcy, Jason Wright, John Johnson, Bernie Walp, James Graham, Eugene Chiang, Alex Filippenko, Nate McCrady, Shane Bussmann, Brandon Swift, Lee Huss, Lindsey Pollack, and Amy Jordan.

Thanks to the great mentors I've had at the University of Arizona, including my great advisor, Laird Close, who gave me so many opportunities over the years. And thank you to Phil Hinz, Don McCarthy, Glenn Schneider, Erick Young, and Matt Kenworthy.

Thanks to my fellow graduate students over the years, Shane Bussmann and Brandon Swift again, as well as Jane Rigby, Andrea Leistra, Karen Knierman, Eric Mamajek, Jackie Monkiewicz, Patrick Young, Jeremy Bailin, Kris Eriksen, Wilson Liu, Suresh Sivanandam, Julia Greissl, Jenn Donley, Iva Momcheva, Krystal Tyler, Wayne Schlingman, Jonathan Trump, Vanessa Bailey, Dsika Narayanan, Amy Stutz, Brandon Kelly, and Beth Biller. And a special thank you to Kristian Finlator and Moire Prescott, who helped me get through both the best and most difficult times.

Thanks to those of you who keep Steward running, Michelle Cournoyer, Erin Carlson, Joy Facio, Catalina Diaz-Silva, Jeff Fookson, Cathi Duncan, Kim Chapman, Doris Tucker, Grisela Koeppen, and Paula Nielsen.

Another thank you to those beyond Steward who helped me move forward in my research: Michael Liu, Niranjana Thatte, Zahed Wahhaj, Fraser Clarke, Mathias Tecza, Wolfgang Brandner, Markus Janson, Markus Hartung, Jose Guirado, Trent Dupuy, Adam Kraus, and Justin Crepp.

Thank you to my family, to dad, Sven, Kristin, Ayumi, Gerri, and Joannie, for always being there to support me.

Thank you to those groups that have funded my research, directly or indirectly over the years, including NASA, the NSF, the LAPLACE Institute, and the Michelson Graduate Fellowship.

And finally, most of all, thank you to Sasha Kuchuk for being at my side. Without you, I'd never have been able to get to this point.

DEDICATION

This thesis is dedicated to my friends and family: to dad, Sven, and Kristin for always being there for me. To Kristian and Moire for getting me through the worst and the best of it. And to Sasha for being by my side whenever I needed her.

TABLE OF CONTENTS

LIST OF FIGURES	9
LIST OF TABLES	12
ABSTRACT	13
CHAPTER 1 INTRODUCTION TO DIRECT IMAGING SURVEYS FOR EXTRASOLAR PLANETS	14
1.1 Extrasolar Planets	14
1.2 How Direct Imaging Fits into Exoplanet Science	15
1.3 Spectroscopy of Giant Planets	18
1.4 Testing Models of Planetary Atmospheres and Formation Mecha- nisms	20
1.5 Direct Imaging Surveys as a Way to Set Constraints on Extrasolar Planet Populations	21
CHAPTER 2 AB DORADUS C: AGE, SPECTRAL TYPE, ORBIT, AND COMPARISON TO EVOLUTIONARY MODELS	24
2.1 Introduction	24
2.2 An Improved Spectral Reduction	26
2.3 Improved Orbit	32
2.4 Discussion	35
2.4.1 Spectral Type	35
2.4.2 The Age of AB Dor	38
2.4.3 HR Diagram and Evolutionary Models	41
2.5 New Spectra of AB Dor C from VLT SINFONI	43
2.5.1 Further Astrometric Confirmation	45
2.5.2 Spectral Fit and a New Spectral Type	48
2.5.3 Validation of the DUSTY models	52
2.6 Acknowledgements	55
CHAPTER 3 DESIGNING DIRECT IMAGING SURVEYS THROUGH SIM- ULATIONS OF EXTRASOLAR PLANET POPULATIONS	56
3.1 Introduction	57
3.2 Monte Carlo Simulations	58
3.3 Target Selection	63
3.4 Simulation Results	66
3.5 Conclusions	68
3.6 Acknowledgments	70

TABLE OF CONTENTS — *Continued*

CHAPTER 4 CONSTRAINTS ON EXTRASOLAR PLANET POPULATIONS FROM VLT NACO/SDI AND MMT SDI AND DIRECT ADAPTIVE OPTICS IMAGING SURVEYS: GIANT PLANETS ARE RARE AT LARGE SEPARATIONS		71
4.1	Introduction	72
4.2	Observations	76
4.2.1	Target Stars	77
4.3	Monte Carlo Simulations	83
4.3.1	Completeness Plots	83
4.3.2	Detection Probabilities Given an Assumed Distribution of Mass and Semi-major Axis of Extrasolar Planets	90
4.4	Analysis	96
4.4.1	Planet Fraction	96
4.4.2	Host Star Spectral Type Effects	99
4.4.3	Constraining the Semi-Major Axis Distribution	101
4.4.4	Testing Core Accretion Models	107
4.5	Discussion: Systematic Effects of Models on Results and Other Work	112
4.6	Conclusion	118
4.7	Acknowledgments	119
CHAPTER 5 A UNIFORM ANALYSIS OF 118 STARS WITH HIGH-CONTRAST IMAGING: LONG PERIOD EXTRASOLAR GIANT PLANETS ARE RARE AROUND SUN-LIKE STARS		120
5.1	Introduction	121
5.2	Observations	123
5.2.1	VLT NACO H and Ks Imaging	123
5.2.2	VLT NACO and MMT SDI	123
5.2.3	Gemini Deep Planet Survey	124
5.2.4	Target Stars	125
5.3	Monte Carlo Simulations	132
5.3.1	Theoretical Models of Giant Planet Fluxes	135
5.3.2	Narrowband to Broadband Colors	139
5.3.3	Completeness Plots	141
5.3.4	Testing Power Law Distributions for Extrasolar Planet Mass and Semi-Major Axis	147
5.3.5	The Dependence on Stellar Mass of the Frequency of Extrasolar Giant Planets	151
5.3.6	Ida & Lin (2004) Core Accretion Formation Models	164
5.4	Discussion	166
5.5	Conclusions	168

TABLE OF CONTENTS — <i>Continued</i>	
5.6	Online Figure Sets: Completeness Plots for Each Target Star 170
5.7	Acknowledgments 171
CHAPTER 6 CHOOSING THE TARGET LIST AND OBSERVING STRATEGY FOR THE GEMINI NICI PLANET-FINDING CAMPAIGN . . . 176	
6.1	The Near Infrared Coronagraphic Imager (NICI) 176
6.1.1	The Gemini NICI Planet-Finding Campaign 177
6.2	Defining the Input Target List 179
6.2.1	VLT Adaptive Optics H and Ks Band Imaging, SDI, GDPS Targets 179
6.2.2	A Stars 180
6.2.3	Hipparcos R'_{HK} Stars 180
6.2.4	Additional Moving Group Stars 181
6.2.5	Young Nearby M Stars 181
6.2.6	Debris Disk Host Stars 181
6.2.7	Additional Sources 182
6.3	Simulation Parameters 182
6.4	Constructing a Survey 185
6.4.1	Scaling the Upper Cut-Off with Spectral Type 188
6.4.2	Parameters of the Target Stars 193
6.4.3	The Curve of Growth 193
6.4.4	Implications for Spectral Type Composition of the Cam- paign Target List 198
6.4.5	Properties of the Detected Planets 202
6.5	Final Survey Design 211
6.6	Current NICI Planet-Finding Campaign Status 215
CHAPTER 7 CONCLUSIONS AND FUTURE DIRECTIONS 216	
7.1	A Unified Distribution of Extrasolar Planet Populations 216
7.2	Other Model Possibilities 218
7.2.1	Correlated Distributions 218
7.2.2	Alternatives to Single Power Law Fits 220
7.3	Upcoming Surveys with Dedicated High-Contrast Planet Finders . . 221
7.4	Direct Detection of Extrasolar Planets from Space 224
7.5	Final Thoughts 227
REFERENCES 230	

LIST OF FIGURES

1.1	The limits on planet populations set by direct imaging	16
1.2	The HR 8799 planetary system	19
2.1	Reflection and subtraction of AB Dor C spectra	28
2.2	Comparison of AB Dor C to USco 100	30
2.3	Comparison of AB Dor C to GSC 8047-0232	31
2.4	The orbit of AB Dor C	33
2.5	Improved orbital fit	34
2.6	AB Dor C compared to young, low-surface gravity objects	37
2.7	AB Dor C compared to high SNR template spectra of field objects	39
2.8	The age of the AB Dor moving group	40
2.9	AB Dor C on the color-magnitude diagram	42
2.10	AB Dor C with other young, low-mass calibrators	44
2.11	Orbit of AB Dor C including SINFONI data	46
2.12	Parameterized orbit of AB Dor C including SINFONI data	47
2.13	SINFONI spectra of AB Dor C compared to young templates	49
2.14	SINFONI spectra of AB Dor C compared to field templates, K band	50
2.15	SINFONI spectra of AB Dor C compared to field templates, H band	51
2.16	Comparison of our new AB Dor C parameters to DUSTY models	53
2.17	Placing AB Dor C in context with other young, low-mass objects with dynamical masses	54
3.1	Contrast curves for different planet-finding instruments	60
3.2	Mass and semi-major axis distributions	61
3.3	Simulations outputs for a single target star	64
3.4	Basic results from the simulation	67
3.5	Expected number of planets as a function of survey size	69
4.1	Target stars in the sample	78
4.2	Assumed eccentricity distribution	85
4.3	Simulation example at one grid point	89
4.4	Completeness plot for GJ 182	91
4.5	Assumed planet mass distribution	92
4.6	Assumed semi-major axis distribution	93
4.7	Detected and non-detected simulated planets around GJ 182	95
4.8	Upper limit on planet fraction for all stars, Burrows model	98
4.9	Upper limit on planet fraction for all stars, Baraffe model	100
4.10	Upper limit on planet fraction for AFGK stars, Burrows model	102
4.11	Upper limit on planet fraction for AFGK stars, Baraffe model	103
4.12	Upper limit on planet fraction for M stars, Burrows model	104

LIST OF FIGURES — *Continued*

4.13	Upper limit on planet fraction for M stars, Baraffe model	105
4.14	Constraints on models of semi-major axis distribution, Burrows model	109
4.15	Constraints on models of semi-major axis distribution, Baraffe model	110
4.16	Our ability to rule out different semi-major axis distributions	111
4.17	Constraints on Ida & Lin (2004) core accretion models	113
5.1	Target stars considered in this chapter	134
5.2	Comparing the Baraffe and Burrows models of planet luminosities	136
5.3	Comparing the Baraffe and Fortney models of planet luminosities .	138
5.4	Upper limit on planet fraction from all stars, using the Baraffe models	143
5.5	Upper limit on planet fraction from all stars, using the Burrows models	144
5.6	Upper limit on planet fraction from all stars, using the Fortney models	145
5.7	Constraints on the semi-major axis distribution of exoplanets	150
5.8	Limits on the power law index and upper cut-off of the semi-major axis distribution	152
5.9	Upper limit on planet fraction from M stars	154
5.10	Upper limit on planet fraction from FGK stars	155
5.11	The Johnson mass correction	156
5.12	Upper limit on planet fraction from all stars, mass-corrected to 1 Solar mass	159
5.13	Upper limit on planet fraction from all stars, mass-corrected to 0.5 Solar masses	160
5.14	Limits on the semi-major axis distribution, with the mass correc- tion applied	162
5.15	Limits on power law cut-off and index with the mass correction applied	163
5.16	Upper limit on the Ida and Lin (2004) core accretion models	165
5.17	Completeness to planets using Baraffe et al. (2003) models	173
5.18	Completeness to planets using Burrows et al. (2003) models	174
5.19	Completeness to planets using Fortney et al. (2008) models	175
6.1	SDI imaging with NICI	178
6.2	The assumed NICI contrast curve	184
6.3	Number of observable stars as a function of exposure time	186
6.4	60 AU fixed survey make-up	187
6.5	60 AU scaled survey make-up	189
6.6	30 AU scaled survey make-up	190
6.7	30 AU fixed survey make-up	192

LIST OF FIGURES — *Continued*

6.8	60 AU scaled stellar parameters, Burrows Models	194
6.9	60 AU scaled stellar parameters, Fortney models	195
6.10	30 AU fixed stellar parameters, Burrows models	196
6.11	30 AU fixed stellar parameters, Burrows models	197
6.12	60 AU scaled curve of growth	199
6.13	30 AU fixed curve of growth	200
6.14	Spectral type versus probability, 60 AU scaled	201
6.15	Spectral type versus probability, 30 AU fixed	203
6.16	Distance versus probability, 30 AU fixed	204
6.17	Age versus probability, 30 AU fixed	205
6.18	Histograms of detectable planets from the simulations, Burrows 60 AU scaled	207
6.19	Histograms of detectable planets from the simulations, Fortney 60 AU scaled	208
6.20	Histograms of detectable planets from the simulations, Burrows 30 AU fixed	209
6.21	Histograms of detectable planets from the simulations, Fortney 30 AU fixed	210
6.22	Detectable planets, Burrows 30 AU fixed	212
6.23	Detectable planets, Fortney 30 AU fixed	213
7.1	The GPI Contrast Curve	222
7.2	Simulated GMT sensitivity to planets for a young A star	225
7.3	Simulated GMT sensitivity to planets for an intermediate age G star	226

LIST OF TABLES

2.1	Astrometry of AB Dor C	35
2.2	Our Improved Parameters for the Reflex Motion of AB Dor A. . . .	36
2.3	Improved Astrometry of AB Dor C	45
4.1	Target Stars	80
4.2	Age Determination for Target Stars	82
4.3	Binaries	108
5.1	Target Stars	126
5.2	Age Determination for Target Stars	130
5.3	Summary of Results.	146
5.4	Binaries	148

ABSTRACT

I present my experiences designing, conducting, and analyzing the results from direct imaging surveys for extrasolar giant planets. Using the young, low-mass star AB Dor C, I show that models for low-mass stars and brown dwarfs at young ages are good representations of reality. I discuss the design of the Simultaneous Differential Imaging survey, and how Monte Carlo simulations of giant planet populations allow for the design of imaging surveys, including the choice of target list, that maximizes the expected yield of extrasolar planets. With the conclusion of the SDI survey, I examine how its null result for planets sets constraints on the allowable populations of long-period exoplanets, finding that fewer than 8% of sun-like stars can have planets more massive than $4M_{Jup}$ between 20 and 100 AU, at 68% confidence. When I include null results from other direct imaging surveys, these constraints are further strengthened: at 68% confidence, fewer than 20% of sun-like stars can have planets more massive than $4M_{Jup}$, at orbital semi-major axes between 8.1 and 911 AU. Even when applying the mass scaling of Johnson et al. (2007), and the “cold start” planet luminosity models of Fortney et al. (2008), the results remain consistent: giant planets are rare at large separations around sun-like stars. I explain how these constraints and planet simulations were used to design the Gemini South NICI Planet-Finding Campaign survey and target list, in order to maximize the chance of NICI detecting a planet, and so giving the campaign the greatest ability to strongly constrain populations of extrasolar giant planets, even in the case of a null result. Finally, I discuss future directions for direct imaging planet searches, and the steps needed to move from existing surveys to a truly unified distribution of extrasolar planet populations.

CHAPTER 1

INTRODUCTION TO DIRECT IMAGING SURVEYS FOR EXTRASOLAR PLANETS

Directly imaging giant extrasolar planets allows us to study a regime of planet populations that can't be accessed by any other method, and provides the opportunity for using spectroscopy to understand the composition and structure of these planets. With advances in adaptive optics at large telescopes, and improved observing and data reduction techniques, surveys to directly image giant planets have become increasingly sensitive. Despite this gain in sensitivity, discoveries of imaged giant planets have been quite sparse, especially given the large amount of telescope time dedicated to surveys. Nevertheless, the discoveries made to date have challenged existing theories of planet formation and structure, and further study of these and future planets will provide insight into the mechanisms by which planetary systems form and evolve.

1.1 Extrasolar Planets

The study of planets and planetary systems around other stars is of great interest not only to astronomers, but the public at large. By discovering and studying planets that orbit nearby stars, we can understand how our own solar system, and the Earth, fit into the context of planetary systems throughout the galaxy. The ultimate goal we are pushing toward is to find habitable planets, planets that can support life, and perhaps even detecting signs of life on those planets. Whether or not we are alone in the universe is a fundamental question, one that astronomers may finally be able to answer definitively in the coming decades.

While the technology required to determine if the atmospheres of extraso-

lar earth-like planets contain markers of life is still decades away, likely requiring a large-scale space telescope designed for the specific purpose of detecting and characterizing Earth-like planets, astronomers today have vastly superior knowledge of other planetary systems, compared to what was known just a few decades ago. In fact, the first extrasolar around a sun-like star was not discovered until 1995, and since then the field of studying extrasolar planets has rapidly expanded. We are now able to not only catalog extrasolar planets around nearby stars, but also to probe the mechanisms by which planetary systems form and evolve. We have a preliminary picture of how giant planets form and migrate over time, and we are moving toward understanding the conditions required for Earth-like planets to form and survive around other stars.

By studying and characterizing extrasolar planetary systems, we will be able to better understand how planets form, how the systems evolve over time, and what is the typical architecture of planetary systems around other stars. By understanding the mechanisms of planet formation and how systems evolve over time, we can better explain how these processes took place in our own Solar system, and so understand how our own planet fits into context with planets around other stars.

1.2 How Direct Imaging Fits into Exoplanet Science

The radial velocity (RV) technique has been key in driving exoplanet science over the last sixteen years. Since the discovery of a planet orbiting 51 Peg (Mayor & Queloz, 1995) in 1995, it has been RV detections of planets that have led the way in the number of known extrasolar planets. In the last few years, the discovery of planets by transit has become more efficient, and the Kepler spacecraft is finding dozens of potential planets, which are currently awaiting confirmation (Borucki

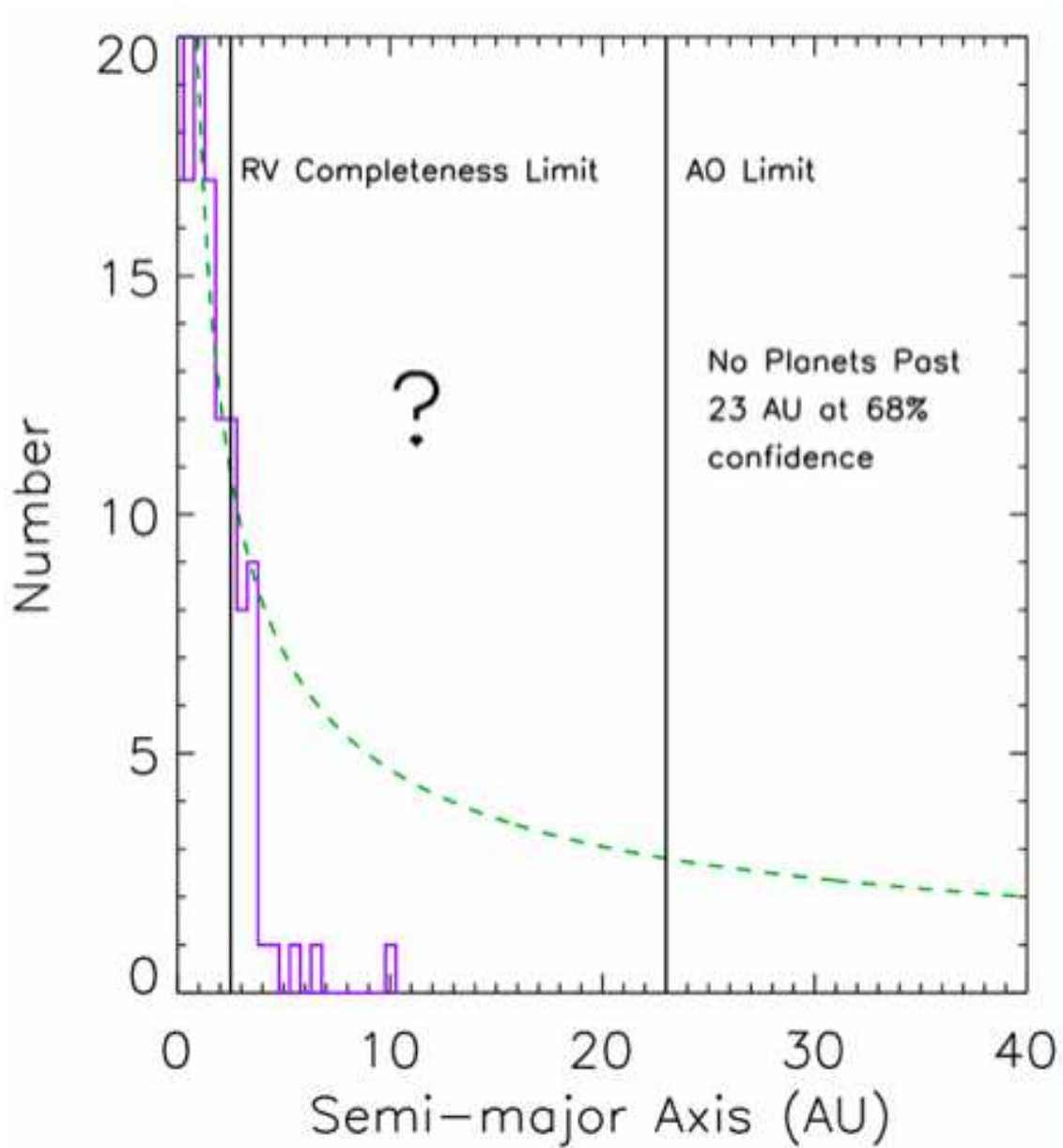


Figure 1.1 The distribution of radial velocity planets (purple histogram), compared to limits on planet populations from direct imaging of sun-like stars, assuming a power-law fit to the semi-major axis distribution of giant planets (see Chapter 5). The gap in between 2.5 and 23 AU remains to be probed, and direct imaging is well-suited to fill that gap.

et al., 2011). There has also been an increase in the detections coming from microlensing, with 10 planets confirmed to date (Gaudi, 2010). In terms of number of planets, direct imaging has historically lagged behind: as of the beginning of 2008, there was only one confirmed planetary-mass companion discovered by direct imaging, 2MASS 1207b (Chauvin et al., 2004). Since then, there has been a flurry of exciting discoveries of directly imaged planets around A stars, including four planets around HR 8799 (Marois et al., 2010), and single planets around Fomalhaut and Beta Pic (Kalas et al., 2008; Lagrange et al., 2009), and a very young planet around the solar-type star 1RXS J160929.1 - 210524 (Lafrenière et al., 2010).

Direct imaging represents a complementary detection mechanism to radial velocity, transits, and microlensing, probing a regime of planet properties that cannot be reached by other methods. While RV and transit methods become less sensitive to planets as orbital radius increases, and microlensing is most sensitive to planets in intermediate separations (a few AU), direct imaging can detect planets at very large separations. And while there has been increased success at obtaining transmission (very low resolution) spectra of transiting planets, direct imaging allows for the study of planets “in isolation,” where their structure has been allowed to evolve on its own, without being roasted in close proximity to the parent star. In Chapter 5, I will show how null results from current direct imaging surveys, when combined with a power-law fit to known distributions of radial velocity planets, suggest that planets should not be found beyond 23 AU (as imaged planets are found beyond this limit, clearly such a simple fit is not adequate to describe planets at all separations and around all masses of stellar hosts). Radial velocity surveys, meanwhile, are generally thought to be complete out to a few AU (the volume-limited sample of Fischer & Valenti (2005) was complete to 2.5 AU), so that the two techniques, pushing from opposite directions,

are coming close to together providing a unified picture of planet populations at all separations (see Fig. 1.1). Since moving outward with radial velocity requires a time baseline of at least one orbital period, it will be decades before RV alone can close this gap. Direct imaging, then, is the ideal solution to move these limits closer, until there is overlap and we truly have a complete picture of giant planet populations across all orbital periods.

1.3 Spectroscopy of Giant Planets

One of the great benefits of directly imaging extrasolar planets is the ability to obtain spectra of these objects and study their atmospheres. Fig. 1.2 shows an image of the four planets circling the A star HR 8799; just by making an image like this we can study the colors of these objects, and careful observations can provide spectra. The first spectra of these objects suggest much redder, dustier atmospheres than predicted by models of planetary mass objects of these ages (Marois et al., 2010; Patience et al., 2010).

Currie et al. (2011) have examined photometry of the HR 8799 planets from 1 to 5 μm and have found that in order to fit the observed properties of these planets, atmospheric models must include thicker cloud decks than have been used to fit brown dwarf spectra. Patience et al. (2010), studying high resolution IFU spectra of 2MASS 1207b, have similarly concluded that existing models cannot fully reproduce the observed features of this planet. Additionally, Skemer et al. (2011) have determined that dust external to 2MASS 1207b cannot be the culprit in explaining this mismatch, and instead this must be an intrinsic property of the planet itself.

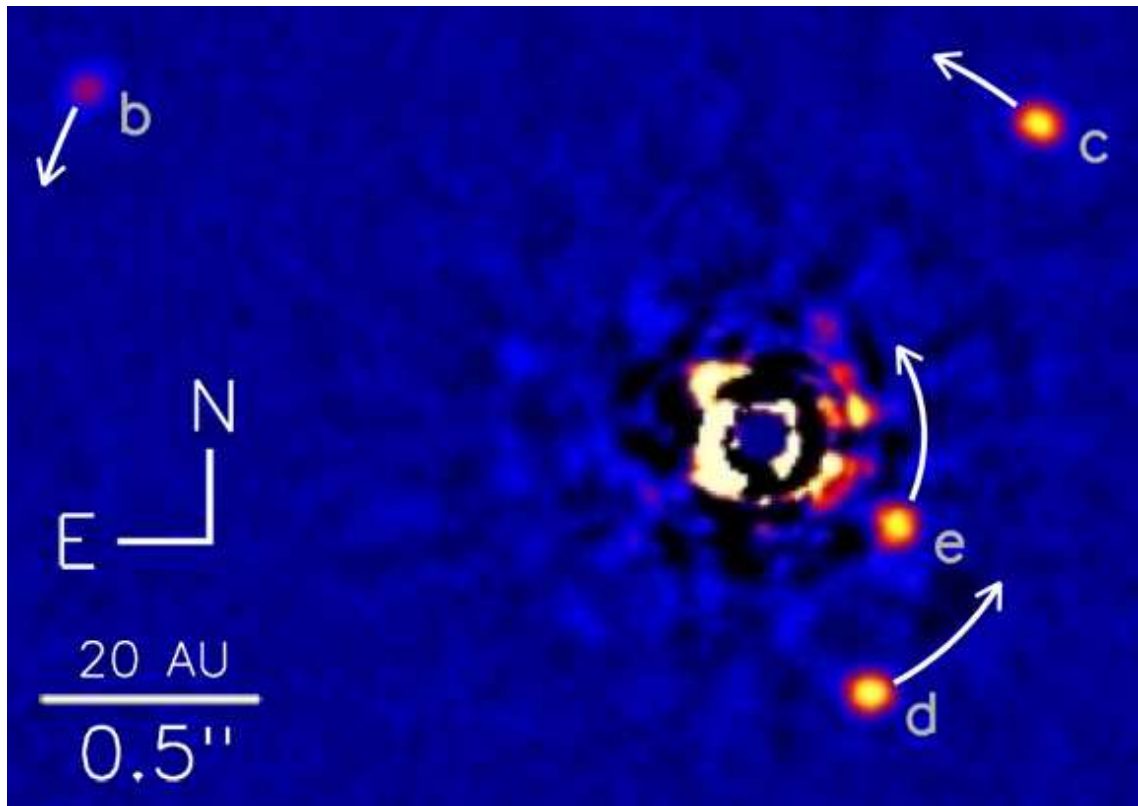


Figure 1.2 The HR 8799 planetary system, showing the orbits of the four planets detected to date. By being able to spatially separate the light of the host star from the light of the planet, it is possible to study in detail the atmospheres of these objects. Figure from Marois et al. (2010).

1.4 Testing Models of Planetary Atmospheres and Formation Mechanisms

Both the preparation and analysis of direct imaging surveys require the heavy use of theoretical models in order to convert between observed magnitudes and spectral features of planets and masses. As we have seen in the case of the HR 8799 planets, however, these models need substantial adjustment when compared to data from an actual imaged planet. This is the power of directly imaging planets: that these models of planet structure and atmospheres can be tested against actual planets. These newly refined models can then be used to inform future direct imaging surveys, and so theory and observation can move forward together. In Chapter 2, I describe my experience using the low-mass star AB Dor C to calibrate theoretical atmospheric models at young ages and low masses.

Since 2003, there have been two sets of atmospheric models of planets used in the direct imaging community, the models of Burrows et al. (2003) and Baraffe et al. (2003). These two models provide similar predictions for near IR magnitude of planets as a function of mass and age (e.g., Fig. 5.2). In 2008, a new set of models was produced by Fortney et al. (2008), which were directly tied to the core accretion scenario of planet formation. These new models predicted systematically fainter planets, especially at the youngest ages, as shown in Fig. 5.3. The main difference in the physics that goes into each model is the origin of the planets: the Burrows et al. (2003) and Baraffe et al. (2003) models represent the “hot start” assumption, where planets begin hot and bright at very young ages (~ 1 Myr). Fortney et al. (2008) represent the “cold start” scenario, with the post-accretion planets being relatively cool and faint, and then passively evolving forward from there.

In a way, determining which, if either, of these two model sets is correct will answer a key question about planet formation, solving the question of what is

the initial condition for young, giant planets. Another possibility is that there are two mechanisms for forming giant planets, core accretion (Ida & Lin, 2004) and gravitational instability (Boss, 2007), and that each is responsible for some fraction of the extrasolar planets that are observed. If this is the case, it would certainly be possible that the two formation scenarios would lead to separate relations between age, planet mass, and near infrared (NIR) flux. Analyses by Marois et al. (2010), Close (2010), and Currie et al. (2011) of the HR 8799 system show that neither camp of existing formation models adequately explains the observed properties of these planets. It will be through future discoveries that we will be able to learn if this is the norm for young, giant extrasolar planets, or if multiple sets of theoretical models, corresponding to different histories of formation and evolution, are required to fully reproduce the properties of different planets.

1.5 Direct Imaging Surveys as a Way to Set Constraints on Extrasolar Planet Populations

By conducting surveys to directly image extrasolar giant planets, we are probing areas of exoplanet parameter space that have been untouched by other techniques. Giant planets at large separations are best reached with direct imaging, and so the most sensitive direct imaging surveys will be able to set constraints on the behavior of planet populations at longer periods. Cumming et al. (2008) have fit power laws to the distributions of planet mass and orbital period based on RV detections for periods less than a few years. But direct imaging can determine if those distributions hold at larger separations, and if there is an upper cut-off to the semi-major axis distribution (see Chapters 5 and 4 for further details).

The semi-major axis distribution of giant planets will greatly inform models

of planet formation and evolution. The discovery of Hot Jupiters (planets the mass of Jupiter or larger, but in orbits with periods of a few weeks or less) by RV techniques was not predicted by any existing models; now modelers must account for the inward migration of planets in order to accurately describe observed planet populations. Similarly, if it is true that there are multiple mechanisms for planet formation (as we hypothesize in Section 1.4) that operate at different orbital radii, this should be detectable by examining the frequency of planets as a function of separations. In short, while there are known questions that can be answered with a complete distribution of exoplanets across all orbital separations, past experience has taught us to be on the lookout for new discoveries with new data, and the outer parts of extrasolar planetary systems are the next frontier to explore. One example of this is the discovery of a planet orbiting the star β Pic (Lagrange et al., 2009), a star that is well-known for hosting a large debris disk. The presence of a debris disk is associated with the process of planet formation, and so possibly a clue that a system contains giant planets. Indeed, the other two A stars with imaged planets, Fomalhaut and HR 8799, were also known to host debris disks before the discovery of their planets (Kalas et al., 2008; Marois et al., 2008). Whether the presence of a debris disk is a solid marker of giant planets will be borne out by further study, but it is an intriguing suggestion given current knowledge of wide-separation giant planets.

In Chapters 3 and 6, I discuss the construction of surveys to directly image extrasolar giant planets, using the metric of expected number of planets detected. This has the dual effect of maximizing the possibility of detecting a planet (given the best assumptions for populations of giant planets at the time the survey is being planned), and setting up the survey in such a way that even a null result is of great scientific interest, by placing strong constraints on the models of planet

populations that informed the survey design (Chapters 5 and 4 discuss how null results can be used to maximal advantage).

Maximizing the chances of detecting planets is paramount, as null results, while setting strong constraints on allowable models of planet populations, have limited ability to differentiate between different models of planet populations (and so theories of formation and evolution). For a given model (for example, the extension of radial velocity power law distributions to large separations, with no spectral type dependence on planet distributions or frequency), a null result can set limits on the parameters of that model (in this example, at 68% confidence, giant planets should not be found past 23 AU). And this can be done for any general type of model. But determining which model correctly describes planet populations at large separations requires actual detections. Additionally, the wealth of knowledge that can be gained by taking spectra of even a handful of directly imaged planets is strong motivation to construct surveys with the greatest likelihood of discovering planets, and in Chapter 7 I discuss future directions for direct imaging surveys. A unified distribution of planet populations is the ultimate goal, and direct imaging surveys are the tool we will use to reach it. At this point, it is just a matter of determining the optimal survey design for future surveys to maximize the science we get from this effort.

CHAPTER 2

AB DORADUS C: AGE, SPECTRAL TYPE, ORBIT, AND COMPARISON
TO EVOLUTIONARY MODELS

We expand upon the results of Close et al. (2005) regarding the young, low-mass object AB Dor C and its role as a calibration point for theoretical tracks. We present an improved spectral reduction of the VLT NACO spectrum of AB Dor C, and a new orbital solution with two additional epochs. Our improved reduction suggests a confirmation of our spectral type of M8 (± 1) and mass of $0.090 \pm 0.003 M_{\odot}$ for AB Dor C.

An analysis of a new spectrum, taken with the SINFONI instrument at the VLT, produces a better-quality spectrum that correctly preserves the continuum shape of AB Dor C. Analyzing this new spectrum leads us to significantly revise the spectral type of M8 suggested by the VLT NACO spectrum, and instead assign an earlier spectral type of $M5.5 \pm 1$. This places AB Dor C in good agreement with the DUSTY models. The significant change in spectral type from the new spectrum points to the superiority of IFU spectra over AO slit spectroscopy in determining an accurate spectral type of a high contrast close companion.

The material in this Chapter was first published in Nielsen et al. (2005), Close et al. (2007a), and Thatte et al. (2007).

2.1 Introduction

The study of young, low-mass objects has been yielding increasingly fruitful science, yet the field remains dependent on evolutionary models to properly interpret the data that are collected from these objects. In particular, mass, while a fundamental property, is very rarely measured directly, and instead must be in-

ferred from theoretical tracks (e.g., Burrows et al. (2003), Chabrier et al. (2000)). It is thus of great interest to find calibrating objects that can link a dynamically measured mass with observables such as NIR (1-2 μm) fluxes and spectral types.

In our previous work (Close et al., 2005), we reported the direct detection of the low-mass companion to the young star AB Dor A, along with measurements of the JHKs fluxes, spectral type, and dynamically determined mass of AB Dor C. Upon comparing these results with the predictions of Chabrier et al. (2000), we found the models to be systematically over-predicting the fluxes and temperature of AB Dor C, given an age of the system of 50 Myr. Put another way, the model masses seem to be underestimating the mass of a low-mass object given its age, NIR fluxes, and spectral type. Since the publication of these results, another calibrating object has been reported by Reiners et al. (2005): USco CTIO 5. While this equal-mass binary is younger (~ 8 Myr) and more massive (total mass $\geq 0.64 M_{\odot}$) than AB Dor C, Reiners et al. (2005) find the same trend of models under-predicting masses based simply on photometric and spectroscopic data applied to the HR diagram. A similar trend for such masses was previously noted by Hillenbrand & White (2004). Moreover, this trend has been theoretically predicted for higher masses by Mohanty et al. (2004), and by Marley et al. (2007) for planetary masses.

In this Chapter, we seek to expand on our earlier results from Close et al. (2005), using an improved spectral reduction and a more robust determination of the spectral type. We also present an improved orbital fit based on additional astrometric data, as well as address concerns raised by Luhman et al. (2005) regarding the age of the AB Dor system.

2.2 An Improved Spectral Reduction

As described in Close et al. (2005), in February 2004 we obtained 20 minutes of K-band spectra using the Very Large Telescope (VLT), following our initial detection of AB Dor C. We used the $R \approx 1200\text{-}1500$ ($2\text{-}2.5 \mu\text{m}$) grism and the $0.027''$ pixel camera of NACO (see Lenzen et al. (2004)), aligning the $0.086''$ slit along the centers of both AB Dor A and C. The observations themselves consisted of eight deep exposures, intentionally saturating the inner pixels of the spectral PSF (point-spread function), with the two objects (A and C) nodded along the slit between exposures. An additional eight exposures were obtained with a 180° rotation of the derotator, flipping the relative positions of A and C. The FWHM of the spectral PSF was approximately 3 pixels.

Given our measured separation of A and C of $0.156''$ (5.78 pixels), and a flux ratio at Ks of 80, the signal from AB Dor C lies beneath the wings of the PSF of A. Relying on the relative stability of the NACO PSF, we subtracted a 0° image from one at 180° , removing the signal from A while leaving a positive and negative spectrum of AB Dor C, which can then be extracted easily using the standard Image Reduction and Analysis Facility (IRAF) routines. This aligning of the PSFs is complicated by sub-pixel variations in the order position and orientation from image to image, as well as by variations in the total flux across different exposures.

To prepare for this subtraction, the first step is to align the 0° and 180° images. This pair of images is considered one dispersion pixel at a time (that is, we consider the 1024 spatial pixels along the chip corresponding to a single wavelength element), where one image undergoes a series of sub-pixel shifts before the two one-dimensional segments are subtracted. A series of reference pixels between 9 and 12 pixels ($0.24''$ and $0.32''$) from the center of the PSF is chosen so as to

avoid the saturated central pixels, and any signal from AB Dor C (which would be positive in the 0° images and negative in the 180° images, and so would not produce an accurate alignment). The minimum variance in these reference pixels after subtraction is taken to correspond to the best shift. This process is repeated for each of the 1024 dispersion pixels, a second-order polynomial (polynomial order chosen based on visually inspecting the 1024 individual shift offsets) is fit to these 1024 “best offsets”, and this fit is used to prepare the final subtraction.

We continue this procedure iteratively with various values of a global flux scaling of one of the two images, again minimizing the variance in the reference pixels to find the best fit. An example of this subtraction of a 0° and 180° image is shown in Figure 2.1. Each point represents a sum across all 1024 dispersion pixels corresponding to a given spatial pixel, with the dashed lines indicating the location of AB Dor C. The inner, saturated pixels show a large amount of noise as would be expected, but at the position of AB Dor C are obvious negative and positive peaks. We repeat these steps for each possible pairing of the eight 0° and eight 180° spectra, eliminating pairs where the routine did not converge, and choosing the best subtraction; this yields a total of 13 spectra (out of 16 possible), which are then combined.

We note that while there are many pairs where this process fails to converge, we never see a “false-positive” signal. That is, while for many of our spectra we see a positive peak to the right and a negative peak to the left, as seen in Figure 2.1, not even once (out of 64 trials) do we see a positive peak on the left or a negative peak on the right at the position of AB Dor A. This leaves us confident that we have extracted the signal from AB Dor C, rather than spurious light. Additionally, these 13 independent extractions of the spectra are all qualitatively similar; each appears as a late-M spectrum, clearly distinguishable from the spec-

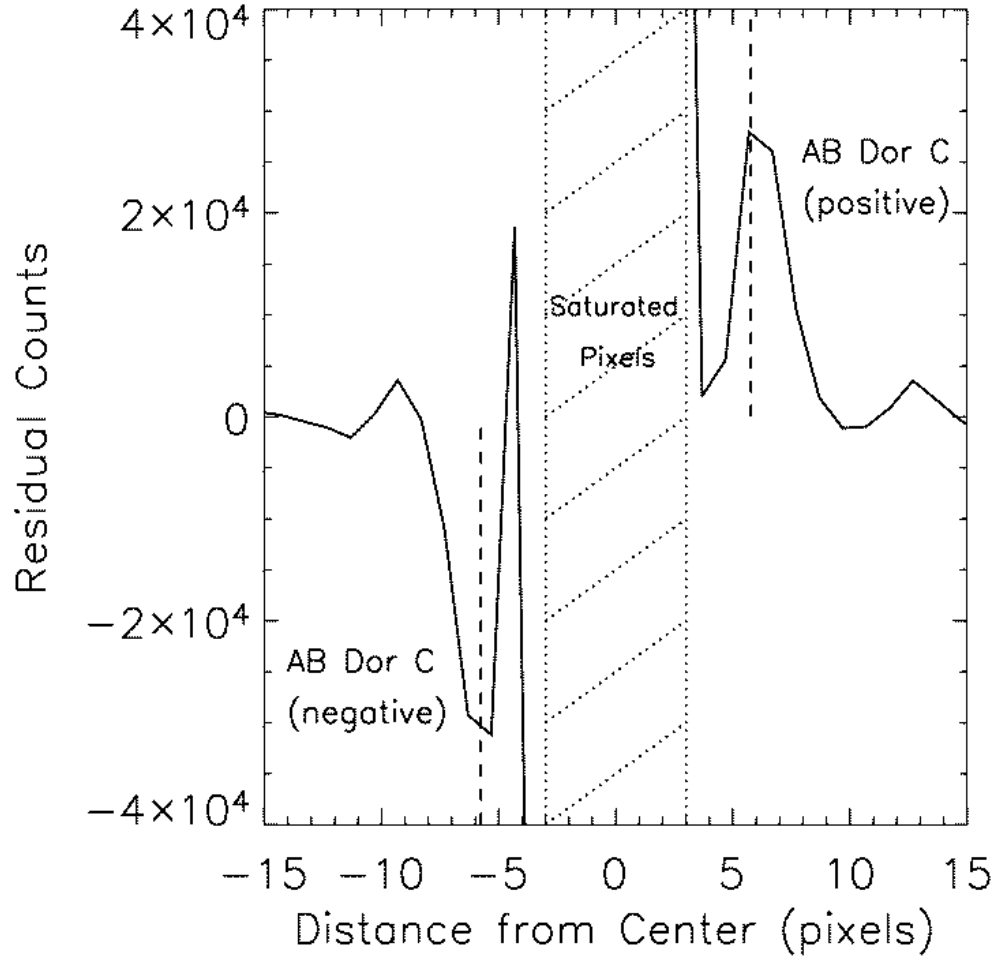


Figure 2.1 An example of a subtraction of a 0° image from a 180° , with each spatial pixel along the x-axis representing a sum along the dispersion direction. The expected positions of AB Dor C on either side are marked with dashed lines; the clear positive and negative signals at this location indicate a good subtraction of AB Dor A. We note there is still some random noise in this subtraction, as the positive and negative peaks of AB Dor C have different amplitudes (at the $\sim 12\%$ level), which we mitigate by median-combining spectra extracted from multiple images. The spectrum is extracted from both the positive peak on the right, as well as the negative peak on the left. The marked central region (where the data are not plotted) indicate the saturated pixels which were ignored during the reduction.

trum of AB Dor A.

Observations of a standard star (HIP 24153, G3V) taken within a half hour of the AB Dor images are used to remove telluric lines, and a modified solar spectrum compensates for stellar features from the standard (Maiolino et al., 1996).

The final spectrum is shown plotted against two young, late-M templates in Figures 2.2 and 2.3. Since we were unable to preserve the continuum of AB Dor C through our data reduction, we simply remove the continuum from our spectrum as well as that of the template (using polynomial fits of the same order). Judging by the depth of the CO breaks, and the strength of the Na I line at $2.21 \mu\text{m}$, these templates constrain the spectral type of AB Dor C between M7 and M9.5 at the 1σ level, as was previously reported in Close et al. (2005). Additionally, we found four features in the spectrum that do not seem consistent with any late-M. We compared our unsaturated spectrum of AB Dor A to other K1 spectra, and finding these features present in A as well, we determined these lines to be telluric features that were not fully removed, hence we have not plotted these small segments of the spectra.

We note in Figures 2.2 and 2.3 that while both AB Dor A and C show a Na I line at $2.21 \mu\text{m}$ and CO features between 2.3 and $2.4 \mu\text{m}$, AB Dor A shows a strong $2.26 \mu\text{m}$ Ca I triplet absorption feature while AB Dor C does not. Similarly, there is no correlation between the strength of the Mg I line ($2.28 \mu\text{m}$) or the Al I doublet ($2.11 \mu\text{m}$) between A and C, as would occur if our spectrum were dominated by spurious light from AB Dor A. Comparing the line strengths, we find the equivalent width of the Na I $2.21 \mu\text{m}$ doublet in C to be ~ 1.5 times that of A. Meanwhile, the Ca I $2.26 \mu\text{m}$ feature equivalent width for C is less than 5% of A. This leaves us confident that the amount of contamination from AB Dor A is $\leq 5\%$, with similar results obtained from analysis of the Al I doublet.

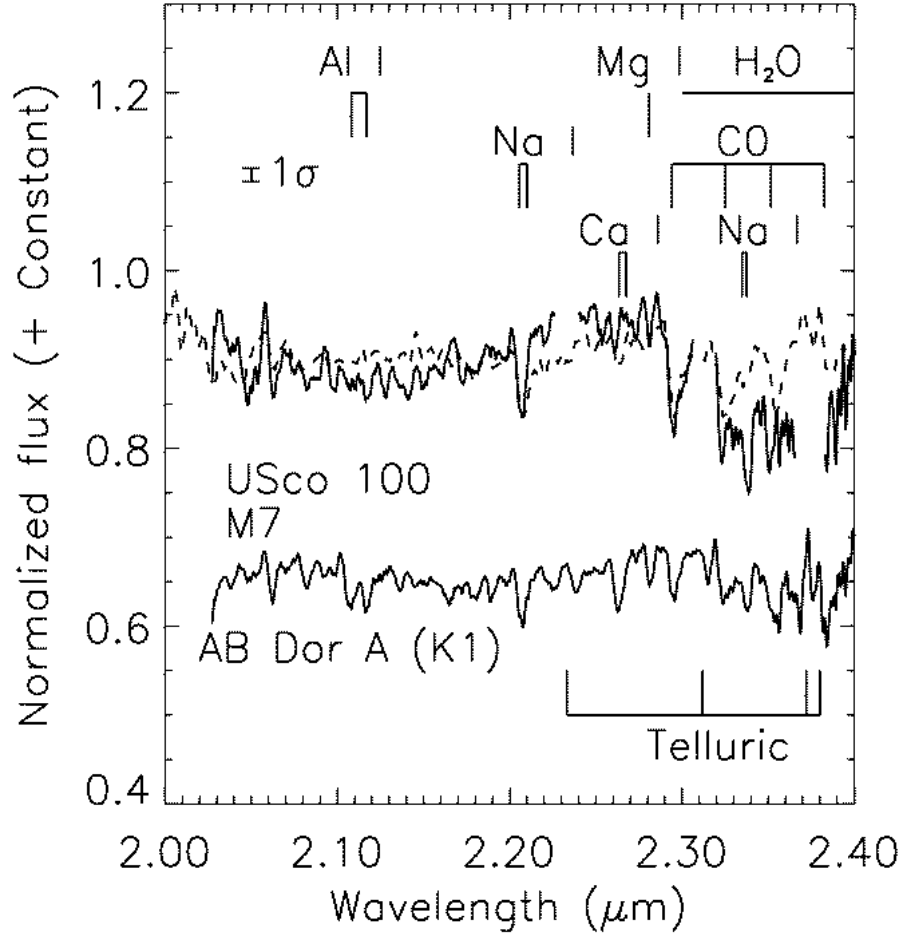


Figure 2.2 The spectrum of AB Dor C (upper solid line) shown against that of U Sco 100 (dashed line), a young (~ 8 Myr) M7 (Gorlova et al. 2003), with the continuum of both objects removed. Features arising from an incomplete removal of telluric lines are marked, and are not plotted in the AB Dor C spectrum. The strength of C's sodium line at $2.21 \mu\text{m}$ and the depth of the H_2O absorption and the first CO break at $2.3 \mu\text{m}$ suggest AB Dor C is cooler than an M7, at the 1σ level of the observational noise, as indicated in the figure (this noise, 0.015, was found by taking the standard deviation of the AB Dor C spectrum between 2.13 and $2.18 \mu\text{m}$, a featureless section of spectrum between the Al I and Na I doublets). The spectrum of AB Dor A (which was used as a reference for poorly-removed telluric features) is also shown at the bottom of the plot.

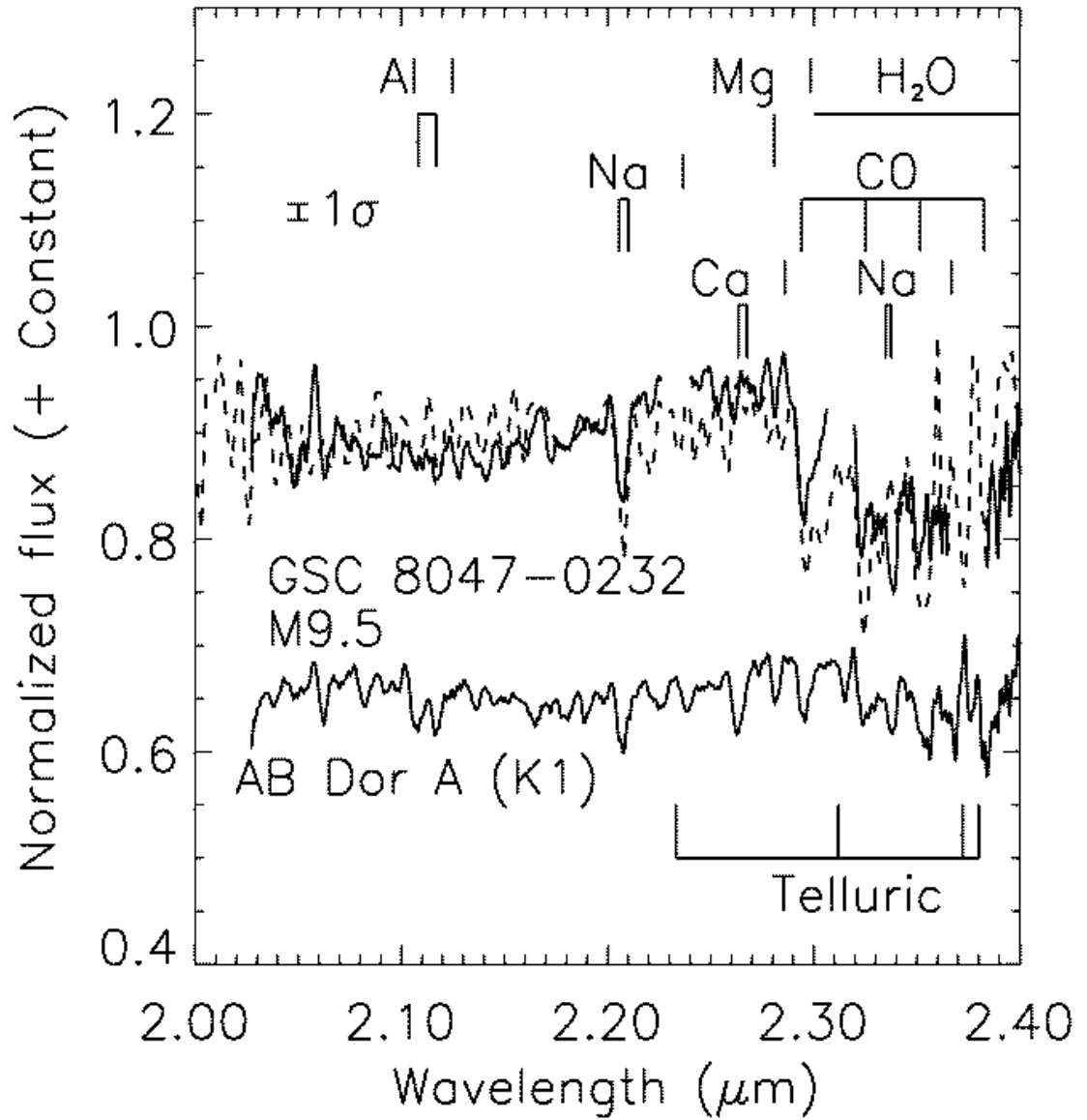


Figure 2.3 The spectrum of AB Dor C, this time plotted with GSC 8047-0232, a young (~ 30 Myr) M9.5 (Chauvin et al., 2005). The sodium and CO features of the template now appear cooler than those of AB Dor C, bounding the spectral type between M7 and M9.5, at the 1σ level.

2.3 Improved Orbit

Our earlier paper (Close et al., 2005) was based on observations conducted at the VLT in February of 2004. Since this work was published, we have reduced additional Simultaneous Differential Imaging (SDI, see Lenzen et al. (2004)) data from September and November of 2004. While data through the narrow-band SDI filters do not provide us with any improved photometric information (beyond confirmation that between AB Dor A and C, $\Delta H = 5.20$), these images do give us additional astrometric data points, allowing us to refine the orbit. To measure positions, we have replaced the saturated pixels of AB Dor A using unsaturated acquisition images. We then did standard PSF fitting to find the relative offsets between A and C in the pre-subtracted SDI images. As acquisition images from NACO SDI datasets are obtained within 10 minutes of the science data, using the same observing mode but a shorter exposure time, they provide an accurate measure of the shape of the peak of the PSF. We have used this method to measure the photometry of AB Dor Ba/Bb, finding agreement with the 2MASS flux ratio between AB Dor A and Ba/Bb at the 1% level, further validating this method. Since each SDI exposure gives us four images, we did astrometry on each of these four images of A and C (which gave us an estimate of the accuracy, $\sim 5\text{mas}$, though varying between the three observational epochs), then averaged the results. Lenzen et al. (2004) has used observations of binaries to measure the NACO SDI platescale to better than 0.1% accuracy (much smaller than the $5\text{ mas} / 218\text{ mas} = 2\%$ error we measure for AB Dor C's position), so we adopt our measurement precision as the accuracy of the position of AB Dor C. We present these measurements in Table 2.1. In Figure 2.4 we show the subtracted SDI images at each epoch where we measured the position of AB Dor C with respect to A.

We fit our three VLT SDI data points for the relative position between AB

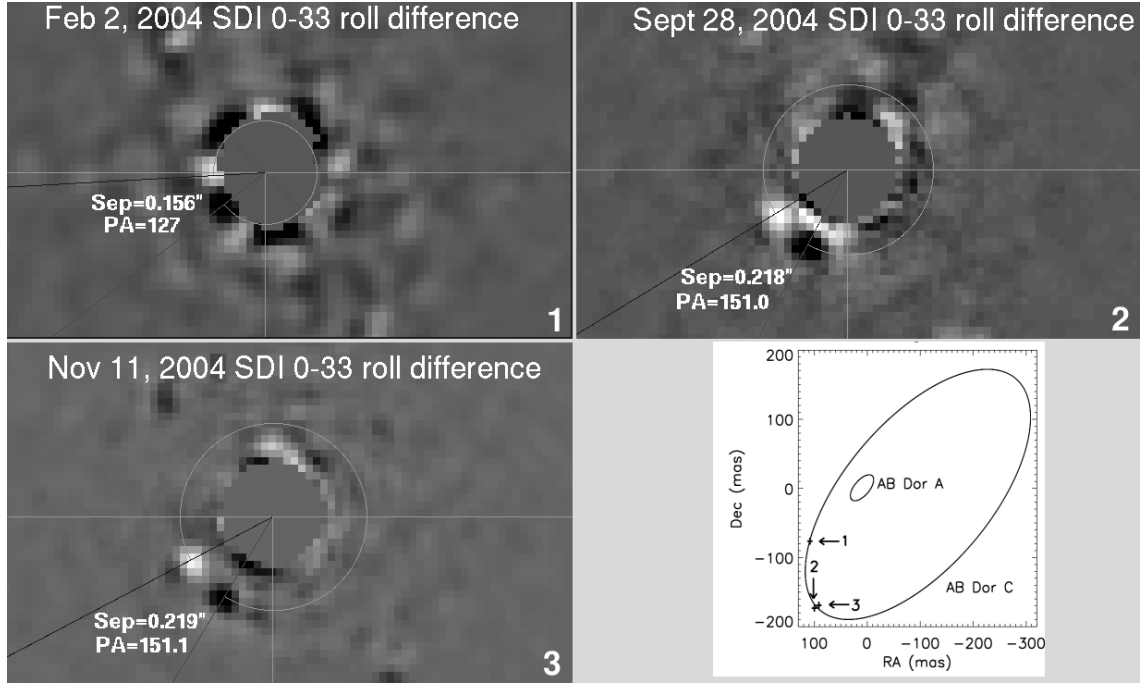


Figure 2.4 The different epochs of AB Dor C measured during 2004 with the VLT SDI device. Each of the numbered panels shows an individual epoch of SDI observations, with images at position angles of 0° and 33° subtracted from each other, showing a positive and negative signal from AB Dor C. The inner pixels of AB Dor A have been intentionally saturated, and have been removed from the image. The orbital motion of the companion can clearly be seen over this span of time. The bottom-right panel shows these locations against a plot of the full orbit of AB Dor C. The 11 additional VLBI/Hipparchos measurements of the reflex motion of AB Dor A (which went into finding the orbital solution) are not shown on this plot (Close et al., 2005).

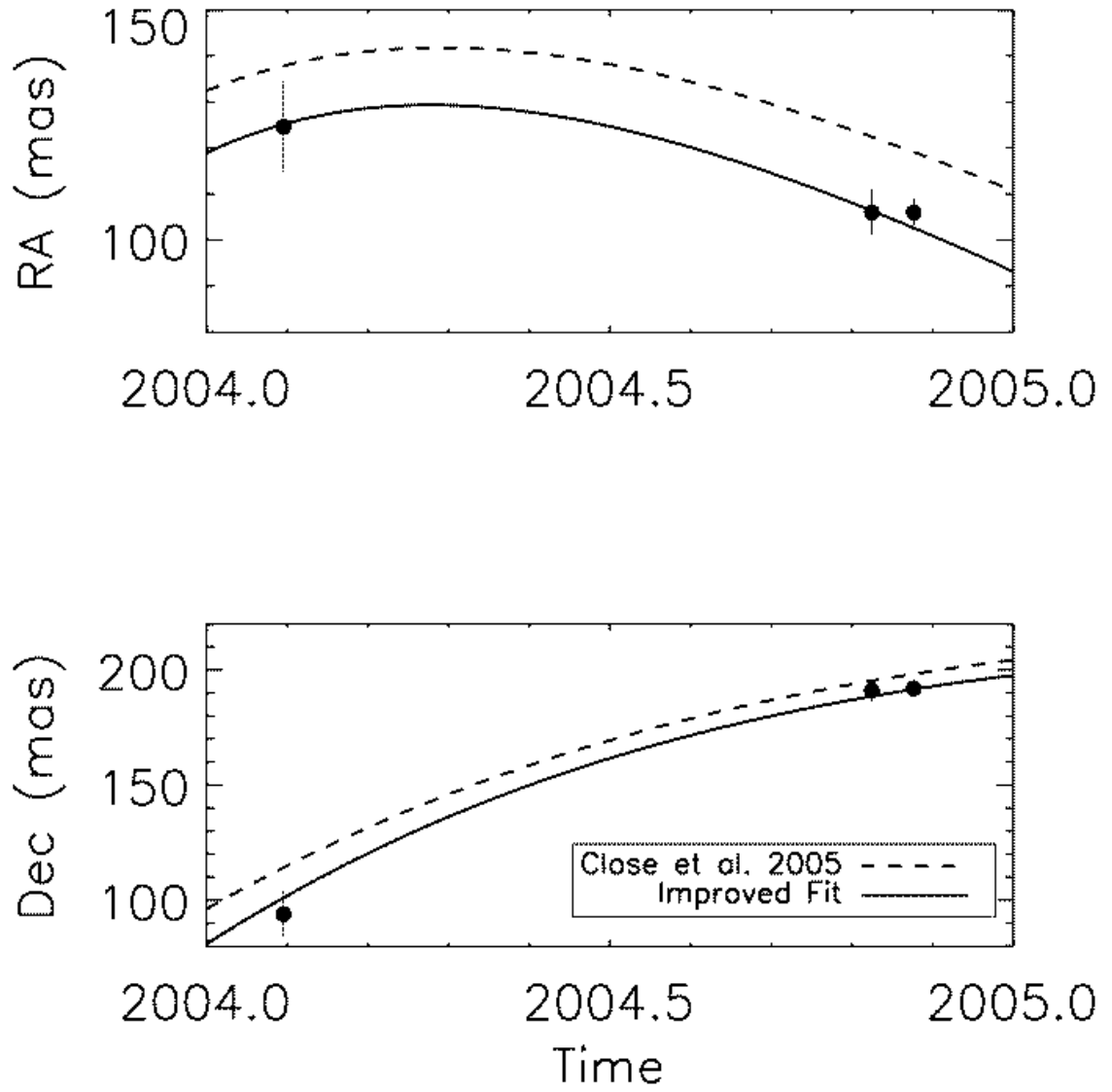


Figure 2.5 Detail of the reflex orbit of AB Dor A for the time period of our SDI observations. The previous orbit (Close et al., 2005) is also shown.

Table 2.1 Astrometry from our three epochs of SDI observations, with the offset of AB Dor C given with respect to AB Dor A. Errors in position are 10, 5, and 3 mas in the first, second, and third epochs, respectively. For astrometric measurements of AB Dor A at previous epochs, see Guirado et al. (1997).

Epoch	RA Offset (mas)	Dec offset (mas)	Position Angle
2004.096	125	-94	127
2004.825	106	-191	151
2004.877	106	-192	151.1

Dor A and C along with the existing VLBI/Hipparcos astrometry for AB Dor A (Guirado et al., 1997) to obtain an improved orbit of the reflex motion of AB Dor A. For this fit, we followed the procedure described in Guirado et al. (2006). The new orbital elements are shown in Table 2.2, and are mostly similar to those published in Close et al. 2005. The two orbits are compared with respect to the three 2004 epochs of SDI observations in Figure 2.5.

The most immediate consequence of our new orbital fit is that the mass of AB Dor C remains at $0.090 M_{\odot}$. As reported in Guirado et al. (2006), we notice that the error bars shrink from $0.005 M_{\odot}$ to $0.003 M_{\odot}$. This confidence with which we know the mass of AB Dor C makes it an ideal object for calibrating theoretical evolutionary tracks.

2.4 Discussion

2.4.1 Spectral Type

Using our new spectrum, we attempt to refine the determination of the spectral type of AB Dor C. Rather than use field objects as our standards (as we did in Close et al. (2005)), we choose young objects (with lower surface gravities) to

Table 2.2 Our Improved Parameters for the Reflex Motion of AB Dor A.

Parameter	Value	Error	Units
Period	11.74	0.07	years
Semi-Major Axis	0.0319	0.0008	“
Semi-Major Axis	0.476	0.012	AU
Eccentricity	0.61	0.03	
Inclination	66	2	deg.
Argument of Periastron	110	3	deg.
Position Angle of Node	133	2	deg.
Epoch of Periastron Passage	1991.92	0.03	years
Mass of AB Dor C	0.090	0.003	M_{\odot}

constrain the spectral type. Figure 2.6 shows our AB Dor C spectrum plotted against a variety of young, late-M spectra (WL 14, USco 67, USco 66, and USco 100 from Gorlova et al. (2003), GSC 8047-0232 from Chauvin et al. (2005)). Again, since AB Dor C lacks a continuum, we have removed the continuum of all the objects (using the same order of polynomial fit) for comparison purposes. Trends across the sequence are clearly visible: as we move to later spectral types, the strengths of the Na line, CO breaks, and H_2O absorption increases, while the Ca line weakens. For all these features, AB Dor C seems best bound between the M9.5 and M7 templates at 1σ , agreeing with the $J-Ks \sim 1.3 \pm 0.4$ magnitude color reported in Close et al. (2005).

All of the templates used in Figure 2.6 are significantly younger than AB Dor C. To properly bound the spectral type, we consider field objects, as we did in Close et al. (2005). Figure 2.7 again shows AB Dor C, now with templates of higher surface gravity (spectra from Cushing et al. (2005); since these spectra

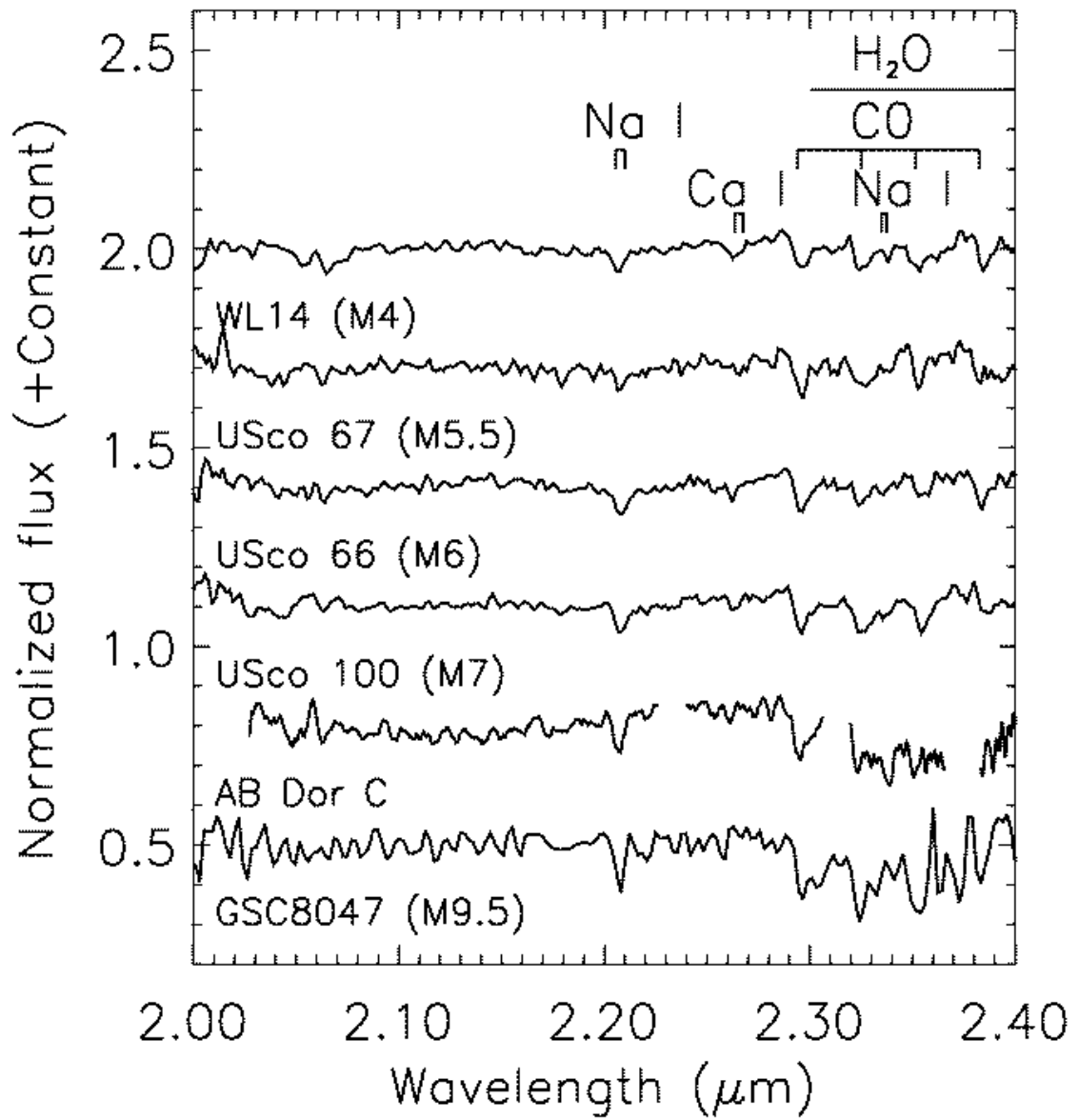


Figure 2.6 The spectrum of AB Dor C shown against a number of young (~ 10 Myr), low-surface gravity objects. The features seem to be bound between the M7 and M9.5 templates.

were taken at higher resolution, we have smoothed them to match the resolution of AB Dor C). The spectra no longer fit as nicely (especially the shapes of the CO features), but as before, the spectrum seems to fit best in the sequence between an M7 and an M9.

2.4.2 The Age of AB Dor

In Close et al. (2005) it was argued that due to the excess luminosity of AB Dor A and C compared to the Pleiades, and A's large Li equivalent width and very fast rotation, that the age of the system was 30-100 Myr. An age of 50 (-20, +50) Myr was adopted, which was consistent with the 50 Myr published age of the AB Dor moving group (Zuckerman et al., 2004). Recently Luhman et al. (2005) have suggested a slightly older age of 70-150 Myr. However, as Luhman et al. (2005) note, the AB Dor moving group is systematically over-luminous compared to the Pleiades (age 100-120 Myr) by ~ 0.1 magnitudes in M_{Ks} vs. V-Ks plots (see their Figure 1).

We have found similar results with a near-infrared color magnitude diagram, as seen in Figure 2.8. While the two groups of stars appear similar for the early-type members (where the isochrones overlap), beyond a color of J-Ks ~ 0.4 , the lower main sequence of the AB Dor Moving group appears to be above that of the Pleiades by about 0.15 magnitudes. We have run a series of simulations that suggest that only $\sim 10\%$ of the time would a group of Pleiades aged stars appear 0.15 magnitudes above the single-star locus as is observed for all the AB Dor group members.

We note that a 0.15 magnitude offset from the Pleiades single star locus suggests a group age of ~ 70 Myr from the Lyon group's models (Baraffe et al., 1998). We adopt an average age of 70 ± 30 Myr with 1σ error bars. Hence, there is a $\sim 10\%$ chance that the AB Dor moving group is as old as the Pleiades based on

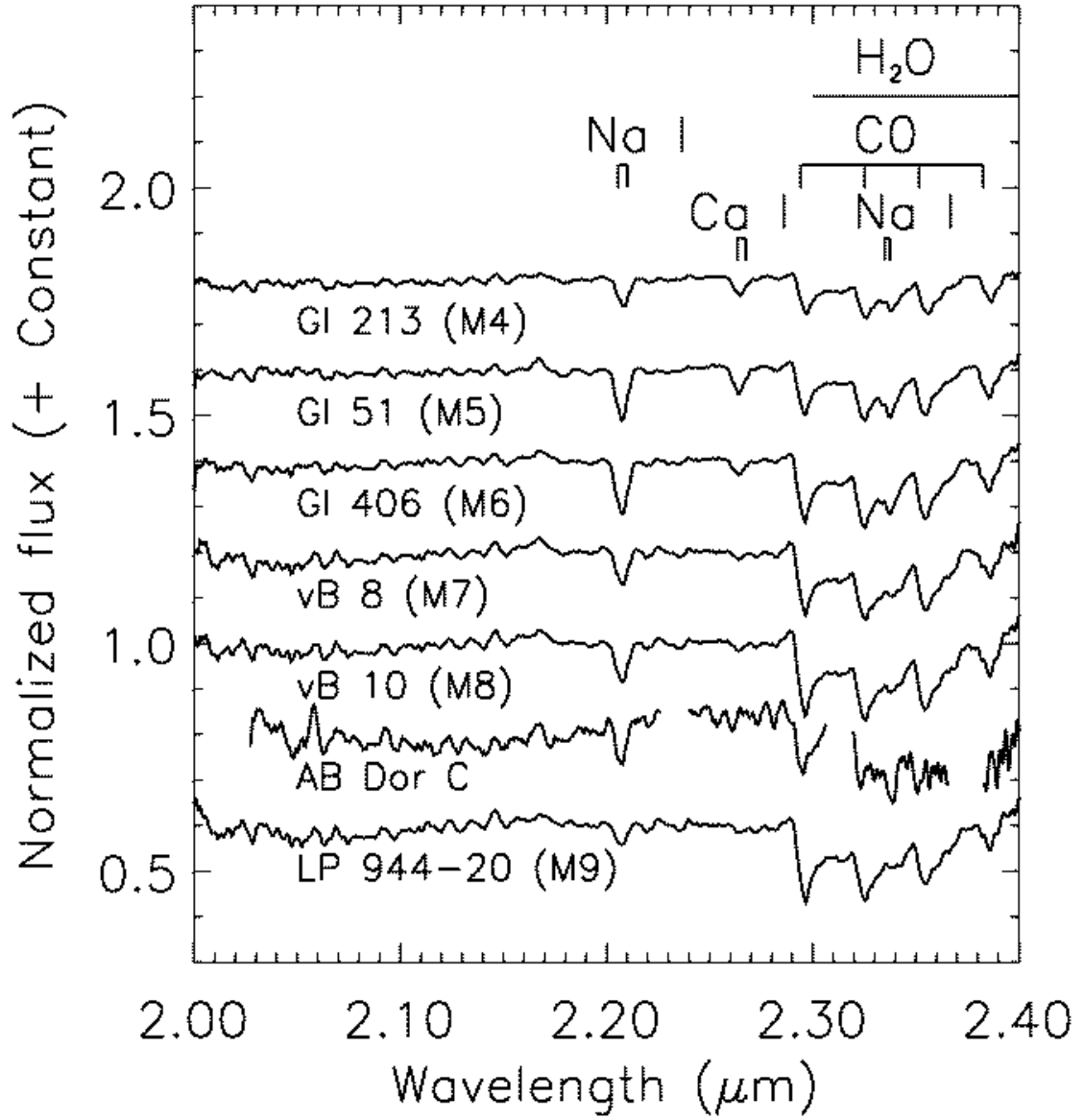


Figure 2.7 The spectrum of AB Dor C, this time plotted against field M dwarfs (~ 5 Gyr), with higher surface gravities. Again, a spectral type of $M8 \pm 1$ (1σ) seems most consistent with our spectrum (we find the 1 subclass error from visual inspection, noting that template spectra beyond this range are an increasingly poor fit to our AB Dor C spectrum).

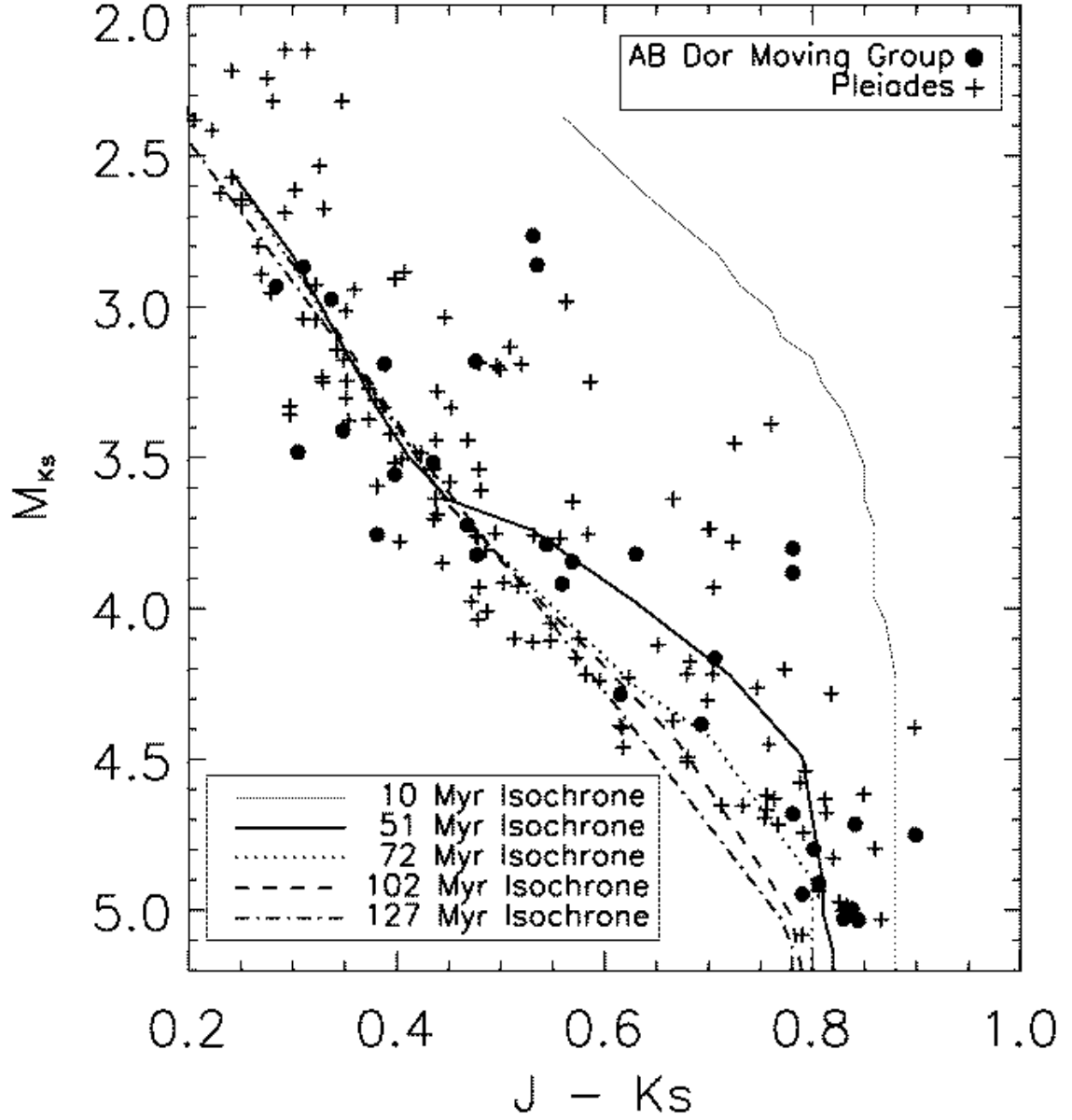


Figure 2.8 A NIR color-magnitude diagram of medium-mass members of the Pleiades (compiled from the literature) and the AB Dor moving group (Zuckerman et al., 2004), with the theoretical isochrones of Baraffe et al. (1998). The offset between the single star locus of the two groups redward of $J-Ks \sim 0.4$ suggests a younger age for the AB Dor moving group, closer to 70 Myr.

these color-magnitude diagrams.

Luhman et al. (2005) conclude that their increase in the age of the system (from 50 to 120 Myr) implies that the luminosity is correctly predicted by the models. But, as we will see in Section 2.4.3, even if the luminosity is close to the predicted value at an age of 100 Myr and $0.09 M_{\odot}$, there is still a very large error in the temperature. Hence, the models will overestimate the temperature (or underestimate the mass) of young, low-mass objects in the HR diagram regardless of the 70 or 120 Myr age of AB Dor.

2.4.3 HR Diagram and Evolutionary Models

In order to further compare our observations of AB Dor C with the theoretical models, we consider an HR diagram with our measured values and the DUSTY models. Using our spectral type of M8 and the absolute Ks from Close et al. (2005), we can derive an effective temperature and bolometric luminosity for AB Dor C. We plot AB Dor C in such an HR diagram in Figure 2.9, along with the DUSTY tracks, AB Dor Ba/Bb, and low-mass members of the Pleiades. We compile Pleiades members from Martín et al. (2000), as well as from other sources in the literature (Cluster identifications and spectral types from Briggs & Pye (2004), Pinfield et al. (2003), Terndrup et al. (1999), Festin (1998), Martin et al. (1996), and Ks-band fluxes from the 2MASS catalog) The bolometric luminosities and temperatures for all these objects (AB Dor Ba/Bb, C, and the Pleiades members) are derived using Allen et al. (2003) and Luhman (1999) (dwarf scale), respectively.

As is seen in Figure 2.9, AB Dor C is overluminous, above the Pleiades sequence (as expected from a younger object, ~ 70 Myr). We also show an arrow to its position in the HR diagram predicted by the DUSTY models appropriate to its age and mass.

It has been suggested that this overluminosity could be explained if AB Dor

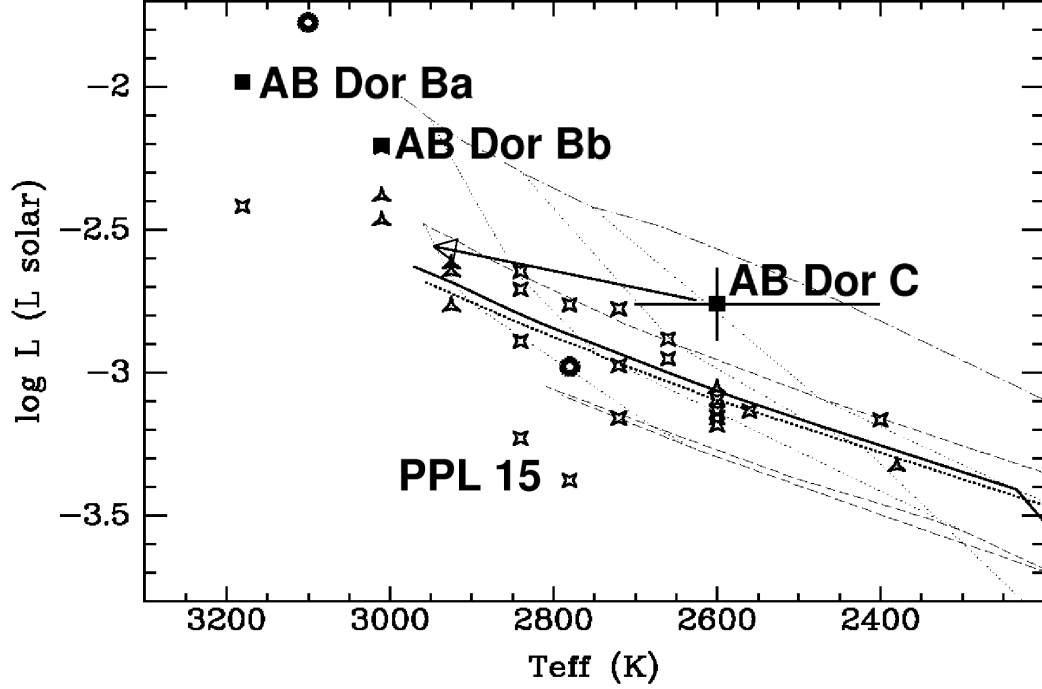


Figure 2.9 HR diagram showing low-mass Pleiades objects from Martin et al. 2000 (open stars), other low-mass members of the Pleiades taken from the literature (open triangles), and AB Dor Ba/Bb (filled boxes). Both AB Dor Ba/Bb and PPL 15 A/B are shown both as individual objects and as a single, blended source (rings). The dotted vertical lines are iso-mass contours for the DUSTY models (from left to right, 0.09, 0.07, 0.05, and 0.04 M_{\odot}), while the more horizontal, dashed lines are the DUSTY isochrones (top to bottom, 10, 50, 100, 120, 500, 1000 Myr). Note that the DUSTY models predict a 70-100 Myr object of 0.09 M_{\odot} should be ~ 400 K hotter than observed. *From the location of AB Dor C on the HR diagram, one would derive a mass of 0.04 M_{\odot} , a factor of 2 underestimate in mass.* As the temperatures and luminosities of the Pleiades objects in this plot were determined in the same manner used for AB Dor C, and these Pleiades points mostly fall along the appropriate 120 Myr DUSTY isochrone, we are assured that our temperature scale and bolometric correction are reasonable. With 1σ error bars, there is a $\sim 99\%$ chance that the DUSTY models underestimate the mass of AB Dor C from the HR diagram.

C were a close, unresolved binary (Martin private communication; Marois et al. (2005)). Were this the case, AB Dor C would split into two points in Figure 2.9, and move downward (as AB Dor Ba/Bb and PPL 15 do when deblended), appearing consistent with the Pleiades locus. While this interpretation cannot be currently ruled out, we will address this issue in more depth in Close et al. (2006). Briefly, however, we note that an AB Dor Ca/Cb system could only be stable with a maximum aphelion distance of 0.138 AU (Hoenig private communication 2005), else these proposed binary brown dwarfs would be disturbed by close passage to the K1 star AB Dor A. Based on the Reid et al. (2002) survey for spectroscopic binaries among low mass field dwarfs, we estimate the likelihood that AB Dor C is a binary system with such a separation to be $<5\%$.

Finally, we note an overall trend for young, low-mass objects where dynamic masses have been measured, as shown in Figure 2.10. There is a global offset to higher luminosities and temperatures for AB Dor C, USco CTIO 5, and Gl 569 Ba/Bb (in this last case, however, with an older object, the offset is within the measurement errors). These results suggest that further work must be done to bring theoretical evolutionary tracks in line with observations.

2.5 New Spectra of AB Dor C from VLT SINFONI

Since the publication of Nielsen et al. (2005), our group has obtained, reduced, and analyzed high resolution Integral Field Spectroscopy of AB Dor C using SINFONI at the VLT (Thatte et al., 2007; Close et al., 2007a). These observations benefit both from being conducted at a phase in the AB Dor C orbit when the A-C separation is larger (219 mas for the SINFONI data, compared to 155 mas for the discovery epoch, when the NACO slit spectra were obtained), and also from the superior capability of SINFONI to accurately measure spectra at high contrasts.

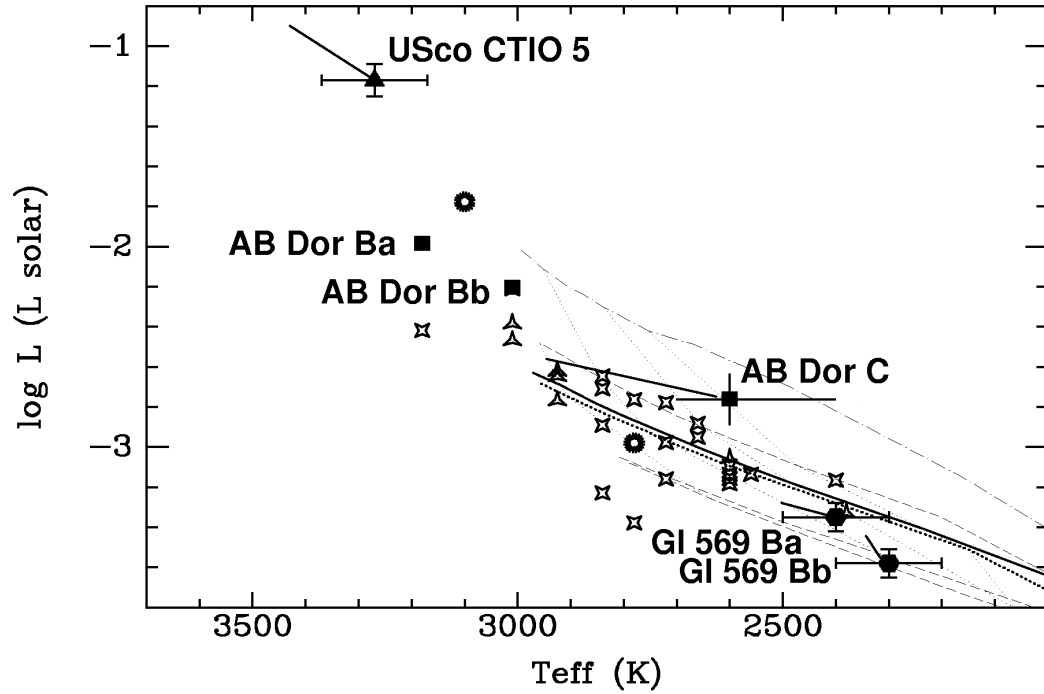


Figure 2.10 Again, an HR diagram with the Pleiades and certain other young, low-mass objects, spanning a range of dynamical masses. The points with error bars mark objects with dynamical masses, with the diagonal lines representing the displacement from the measured luminosity and temperature to the values predicted by the DUSTY and Next-Gen models. Upper Sco CTIO 5 (Reiners et al., 2005), AB Dor C, and Gl 569 Ba/Bb (Zapatero Osorio et al., 2004) all show a systematic trend where the measured HR diagram location is cooler and fainter than the models' predictions (though in the case of the older (300 Myr) Gl 569 B system, this is within the stated 1σ uncertainties. Seen another way, the masses predicted by the models are underestimates of the actual masses.

With this new spectra, we find a much earlier spectral type for AB Dor C (M5.5 ± 1), putting it in good agreement with the DUSTY models.

2.5.1 Further Astrometric Confirmation

In Nielsen et al. (2005), we published a new orbital fit to the AB Dor system, which led to a more precise measurement of the mass of AB Dor C. This fit was based on data taken through late 2004. Since then, we have obtained and reduced an additional AB Dor dataset, an AO Ks image, from 2005.017, and our SINFONI data of 2006.066 provides an even later measurement of the orbit. These new datapoints essentially double the length of the time baseline for following the orbit of AB Dor C. Table 2.3 shows the astrometric measurements from all five epochs. In Fig. 2.11 and 2.12, we see that the orbit of Nielsen et al. (2005) is an excellent fit to subsequent astrometric data, as each measurement is within 1σ of the predicted value. This analysis gives us even greater confidence in the validity of the astrometrically determined mass of AB Dor C, and strengthens the use of AB Dor C as a calibrator of theoretical evolution models for young, low-mass stellar objects.

Table 2.3 Astrometry of AB Dor C, expanded out to all five epochs of measurement at the VLT. Final two epochs from Close et al. (2007a).

Epoch	Separation offset (mas)	Position Angle
2004.096	156	127
2004.825	218	151
2004.877	219	151.1
2005.0170	219	156
2006.0660	202	181

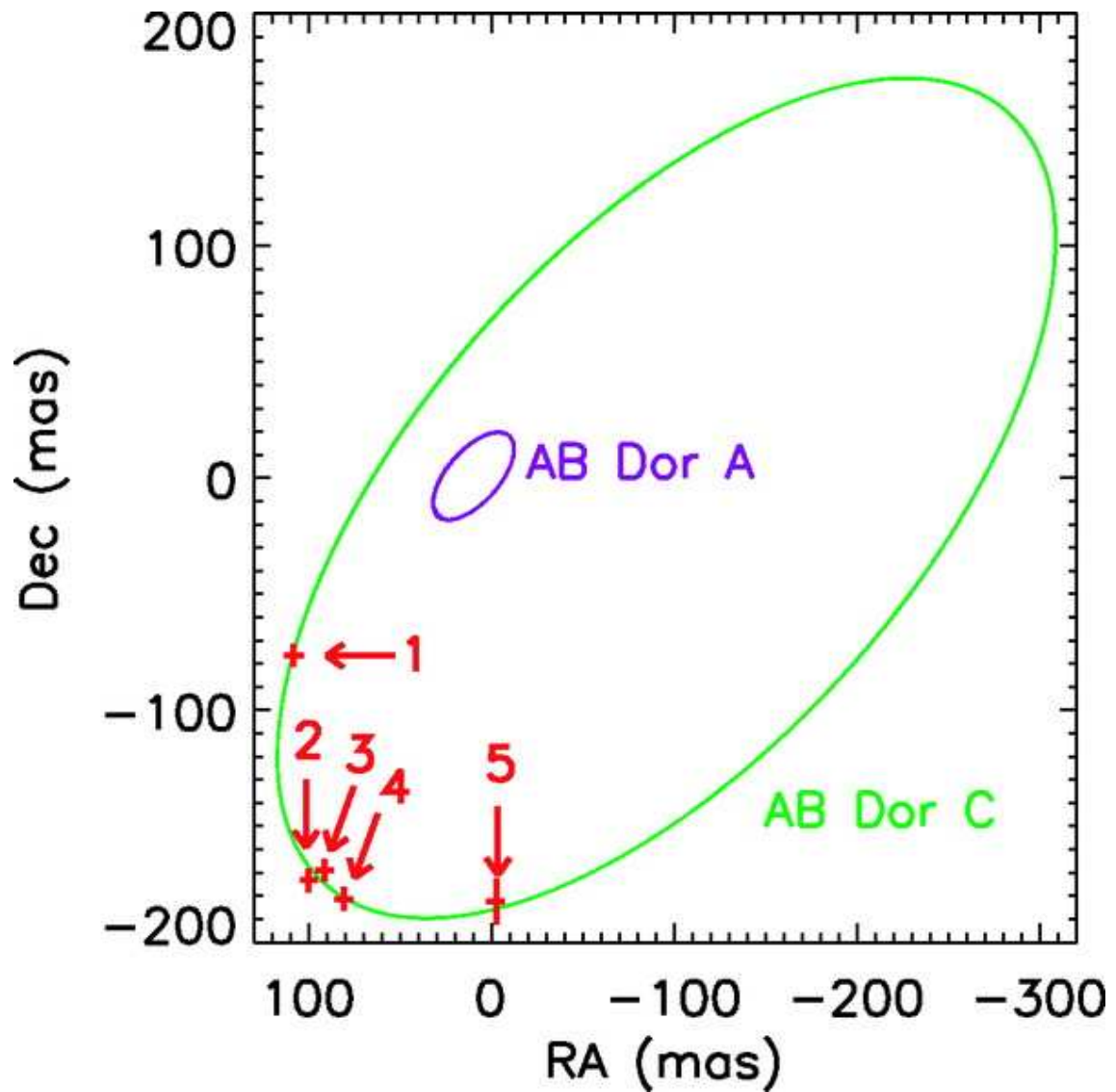


Figure 2.11 Orbit of AB Dor C, using the fit of Nielsen et al. (2005). The SINFONI astrometric measurement shows that AB Dor C is continuing to follow the predicted path, giving us greater confidence in the mass estimate of the system. Figure from Close et al. (2007a).

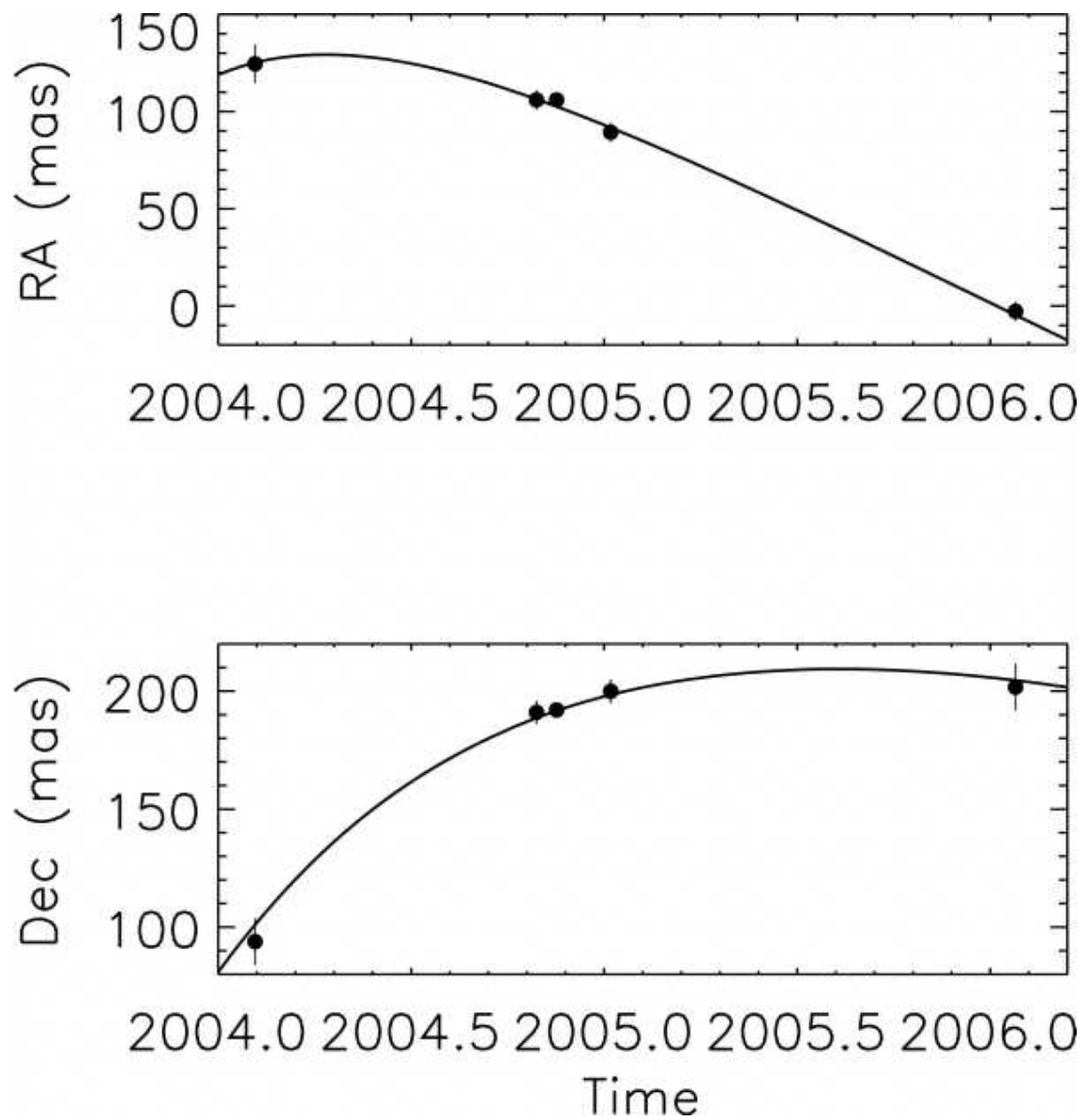


Figure 2.12 Orbit of AB Dor C, using the fit of Nielsen et al. (2005), now with RA and Dec plotted against time. AB Dor C is clearly following the expected orbital path. Figure from Close et al. (2007a).

2.5.2 Spectral Fit and a New Spectral Type

Taking the reduced spectra of AB Dor C (the observations and data reduction are described in depth in Thatte et al. (2007)), we proceed to analyze this spectra to determine the precise spectra type of this low-mass companion. With H and K spectra, including an accurate continuum shape, we are in a much stronger position to properly place AB Dor C in context among other low-mass templates.

In Fig. 2.13, we plot a smoothed version of the AB Dor C spectrum against three young late-M objects in Upper Sco (Gorlova et al., 2003). The templates are generally a good fit for AB Dor C, though we note that the low resolution (and uncertainty in the extinction correction to these Upper Sco objects) makes finding a precise spectral type difficult. In order to overcome this, we turn to the IRTF standard spectra of Cushing et al. (2005). While these spectra are at higher resolution, they represent field objects, which are a good deal older than AB Dor C (~ 5 Gyr, instead of 70 Myr). As a result, when comparing spectra we must be careful to note the disparate surface gravity between templates and AB Dor C.

Looking at the template spectra of field objects, we note that the continuum shape across H and K is best fit by the M5 and M6 templates, and the strength of the CO breaks are consistent with and M4 to M5 spectral types. The best fit to the H-band continuum seems to be the M5 template, while the Magnesium and Aluminum lines redward of $1.65 \mu\text{m}$ are best fit to the M6 template. Combining these data, we adopt a spectral type for AB Dor C of $M5.5 \pm 1$.

We note that this new spectral type is a significant departure from the spectral type of $M8 \pm 1$ presented in Close et al. (2005) and Nielsen et al. (2005), and is outside the 1σ error bars of the previous spectral type. We believe this mismatch came about as a result of our previous work underestimating the systematic effect of finding a best-fit template spectrum without a preserved continuum. By

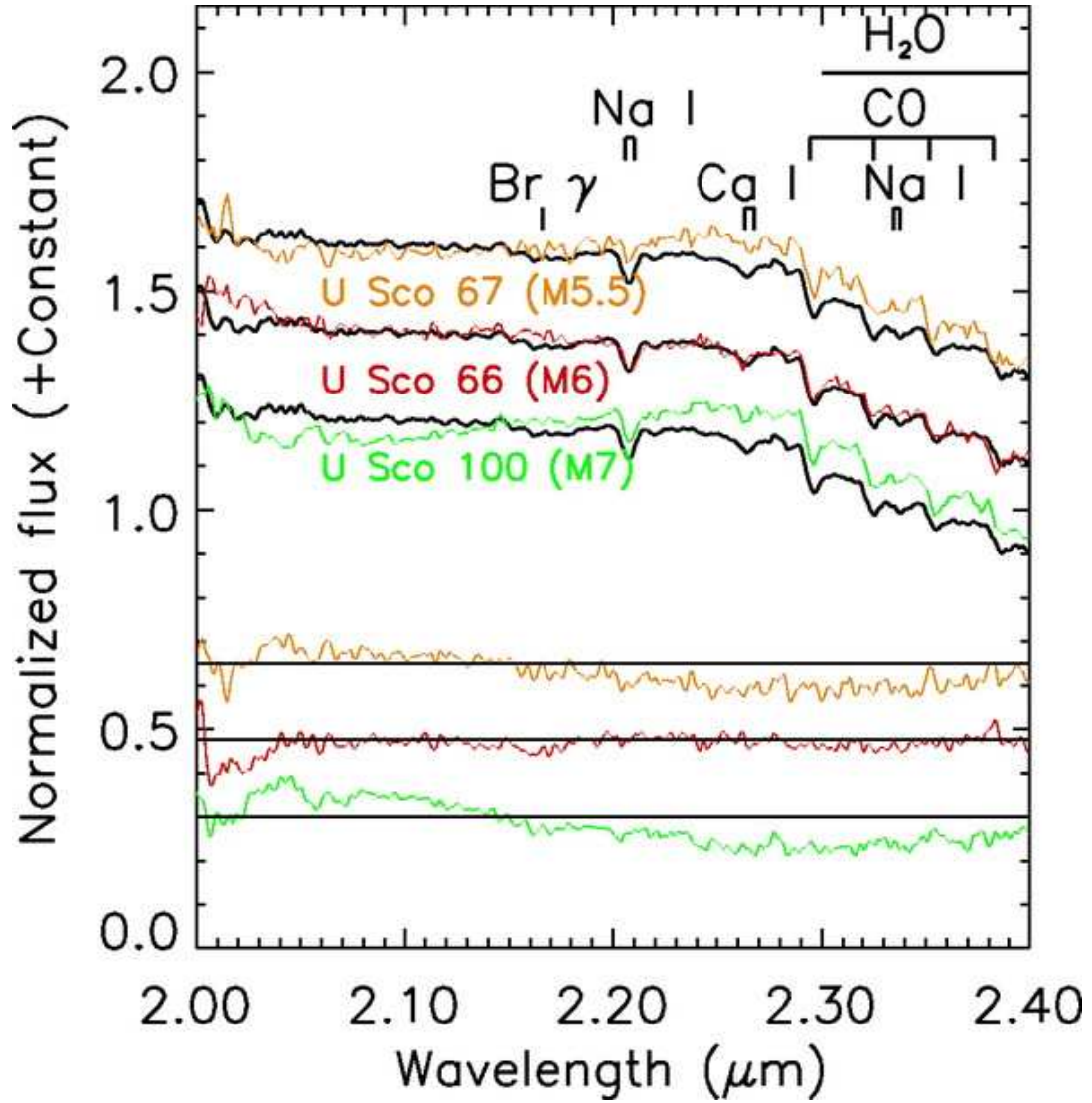


Figure 2.13 SINFONI spectra of AB Dor C plotted against young template spectra from Gorlova et al. (2003). The resolution of the Upper Sco objects is much lower than our SINFONI spectra, so the AB Dor C spectrum has been Gaussian smoothed to match the resolution of the templates. The shape of the continuum, and the sodium doublet and carbon monoxide bands, are well-fit with a M5.5 - M6 spectrum. Residuals are shown in the bottom of the plot, figure from Close et al. (2007a).

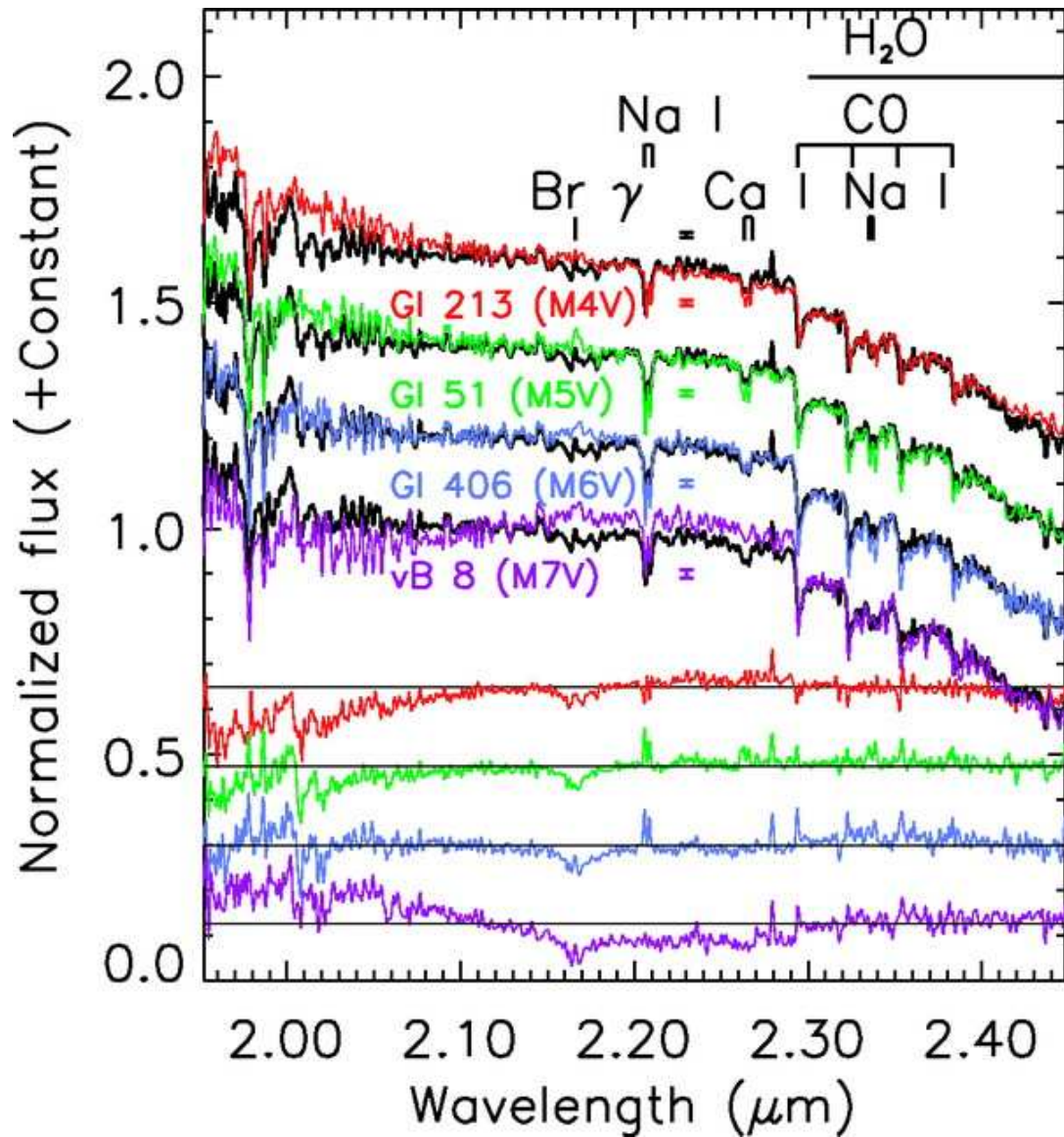


Figure 2.14 K band spectra of AB Dor C, plotted against higher surface gravity (older) late-M template spectra from the IRTF standard catalog (Cushing et al., 2005). The continuum shape is best fit by the M5 and M6 templates, and the shape of the CO breaks (which do not depend on surface gravity) are consistent with an M4-5 (the sodium doublet is gravity-dependent, and so we do not consider it here). Figure from Close et al. (2007a).

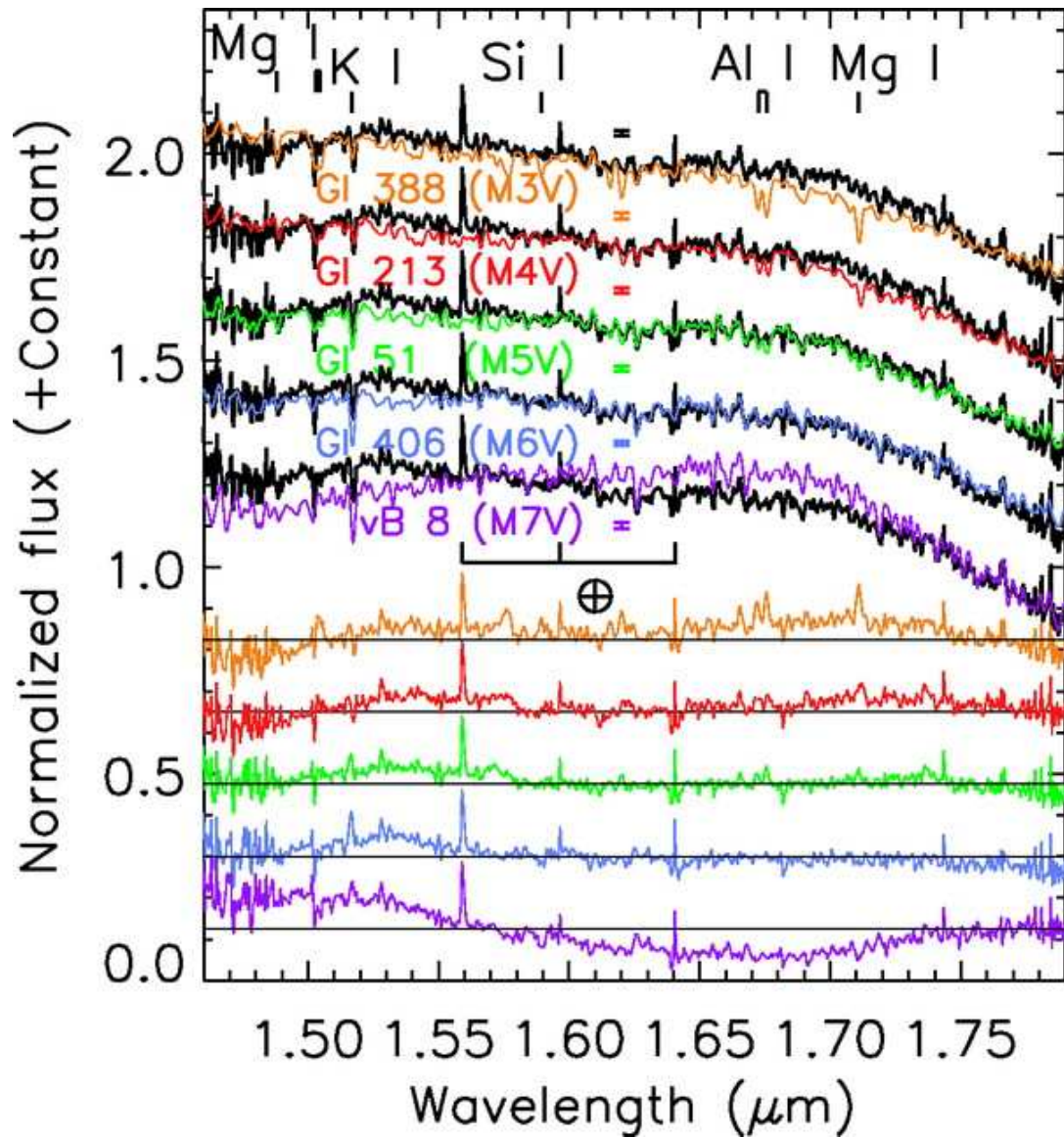


Figure 2.15 AB Dor C compared to the IRTF standards again, now with the H band shown. The continuum shows a poor fit to the M3 and M7 templates, and a better fit to the M5 and M6 spectra, as compared to the somewhat poorer quality fit to the M4 template. Combining this with the K-band plot, and the comparison to young standards, we converge on a spectral type of $M5.5 \pm 1$ for AB Dor C. Figure from Close et al. (2007a).

relying only on spectral features, and then comparing our spectrum to only to high-gravity templates, we not only arrived at an incorrect spectral type, but presented error bars on our measurement that were smaller than the actual uncertainty. With the SINFONI spectrum, and its preserved continuum, we considered template spectra at ages (and so surface gravities) that bracket AB Dor C, and so we believe this $M5.5 \pm 1$ spectral type and error region to be much more robust than our previous estimate.

2.5.3 Validation of the DUSTY models

A spectral type of AB Dor C of $M5.5 \pm 1$ is an unexpected departure from the later spectral type of $M8 \pm 1$ reported in Close et al. (2005) and Nielsen et al. (2005). The disagreement between the parameters of AB Dor C and the predictions of the DUSTY models hinged primarily on the age of the system (we adopted 50 Myr in Close et al. (2005), later revised upward to 70 Myr in Nielsen et al. (2005)) and the spectral type. With a revised spectral type of $M5.5$ and age of 70 Myr, AB Dor C is behaving very much in line with the theoretical DUSTY models. Using the spectral type conversion of Leggett et al. (1996), we find an effective temperature for AB Dor C of 2925^{+170}_{-140} K.

In Fig. 2.16, we compare our new parameters for AB Dor C to the theoretical DUSTY tracks of Baraffe et al. (1998). We also plot the analysis of the 2004 VLT NACO data (the dataset used by us in Close et al. (2005) and Nielsen et al. (2005)) by Luhman & Potter (2006). We suggest a younger age for the AB Dor system than Luhman & Potter (2006), but nevertheless both sets of analyses agree well with the relevant DUSTY iso-mass contours. The DUSTY models still predict brighter H and J luminosity than is observed, though we note that it is more difficult to accurately measure high contrast photometry at J band, where the Strehl is not as favorable as it is at longer wavelengths. In all, the NIR photometry

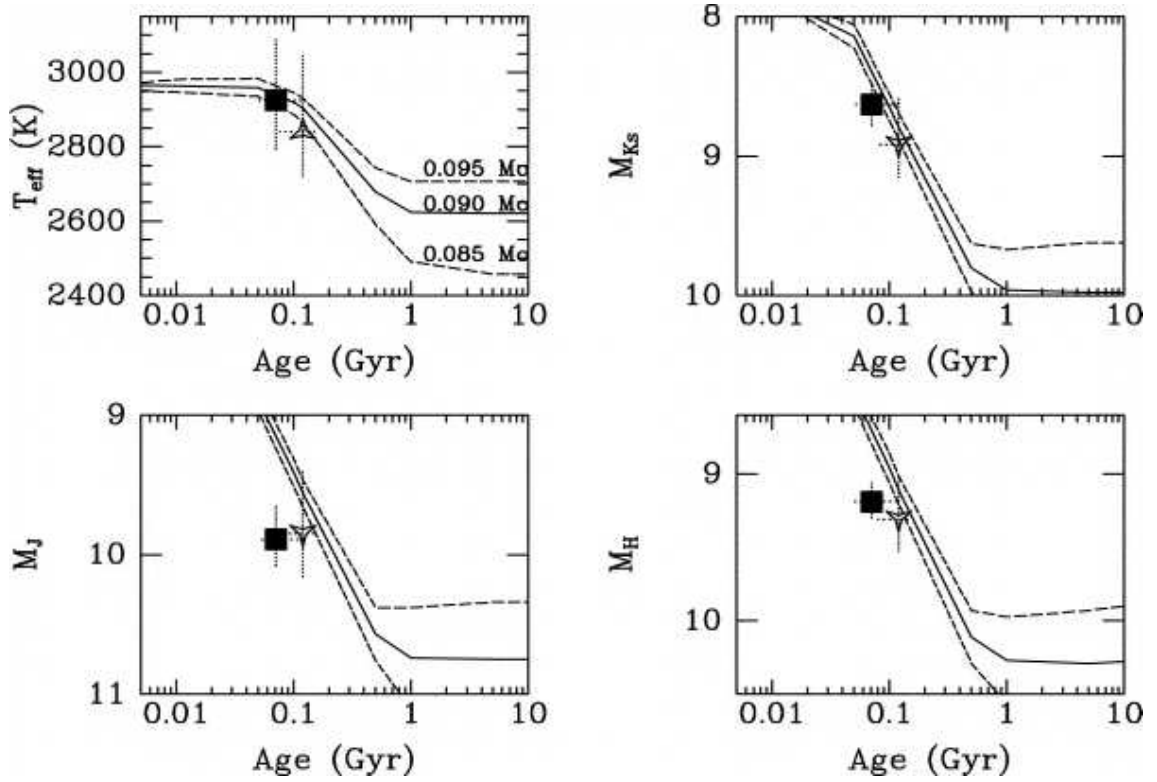


Figure 2.16 AB Dor C (solid square) compared to the theoretical DUSTY models of Baraffe et al. (1998), and analysis of Luhman & Potter (2006) (open triangles). The T_{eff} and Ks plots show much better agreement to the models than was found in Close et al. (2005), though the H and J plots still show an underluminous AB Dor C, compared to model predictions. Figure from Close et al. (2007a).

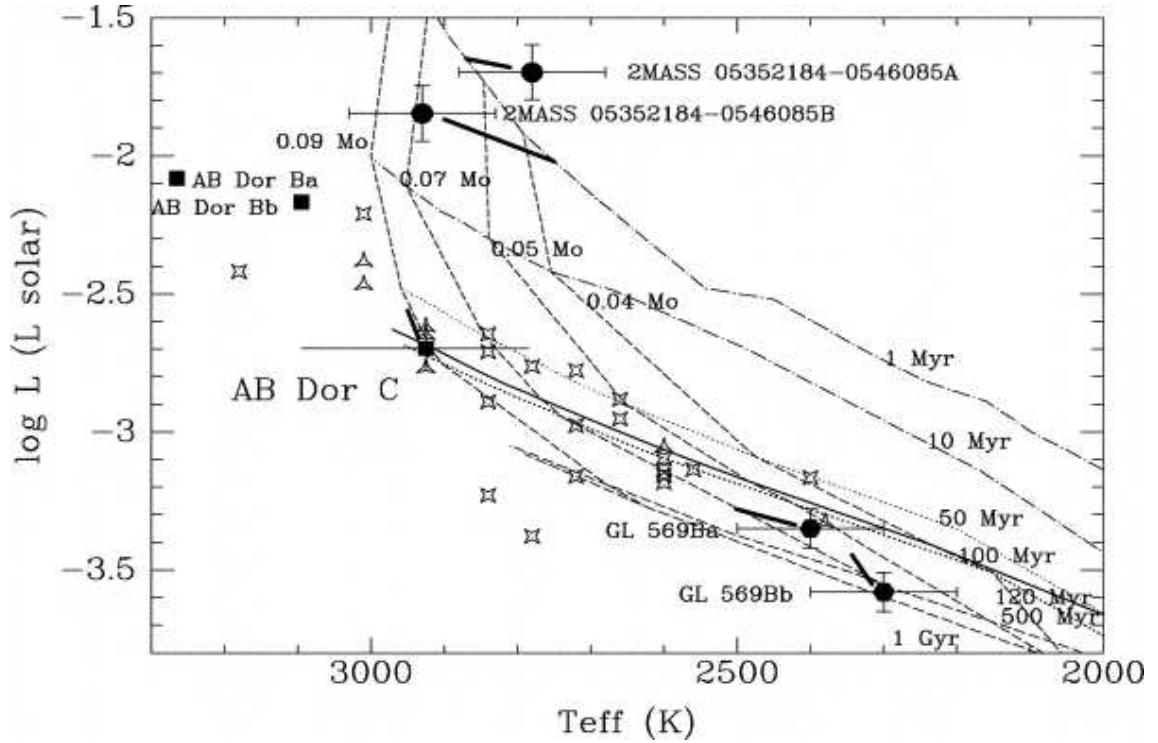


Figure 2.17 Comparison of AB Dor C to other low-mass objects with dynamical mass measurements, and the DUSTY models. There is general agreement between the mass measurements and the predictions of the DUSTY models. Figure from Close et al. (2007a).

and spectra of AB Dor C put it in good agreement with the predictions of the DUSTY models.

Fig. 2.17 shows that in general, there is good agreement between the DUSTY models and low mass objects with dynamical mass measurements. AB Dor C follows a trend of the DUSTY models accurately predicting masses given the position in the HR diagram, for brown dwarfs and low-mass stars. It is important to note, however, that such mass calibrators are much more rare at the lowest mass and age regime. In particular, there are no calibrators of the mass for self-luminous planetary-mass objects, so it is important to be careful when

using models in an area of parameter space where they have not been adequately calibrated.

2.6 Acknowledgements

We thank Gael Chauvin for providing an electronic copy of the spectrum of GSC 8047-0232, and Nadja Gorlova for providing spectra of many young, low-mass objects. We also thank the organizers of the ULMF conference for the chance to present this work.

This publication makes use of data products from the Two micron All Sky Survey, which is a joint project of the University of Massachusetts and the Infrared Processing and Analysis Center/California Institute of Technology, funded by the National Aeronautics and Space Administration and the National Science Foundation.

CHAPTER 3

DESIGNING DIRECT IMAGING SURVEYS THROUGH SIMULATIONS
OF EXTRASOLAR PLANET POPULATIONS

As direct imaging surveys are being designed and carried out to detect extrasolar planets around young, nearby stars it is important to carefully evaluate the criteria for selection of target stars, as well as the predicted success of a given system. We have developed a routine to simulate an ensemble of a large number of planets around each potential target star, and to determine what fraction can be reliably detected using a system's predicted or observed sensitivity curve (the maximum flux ratio between the parent star and a detectable planet as a function of projected radius). Each planet has a randomly assigned semi-major axis, mass, and eccentricity (following extrapolations of detected radial velocity planets), as well as viewing angles and orbital phase. The orbital parameters give a projected separation for each planet, while the mass is converted into a flux ratio in the appropriate bandpass of the detector using the models of Burrows et al. (2003); this allows the simulated planets to be directly evaluated against the system's sensitivity curve. Since this method requires basic parameters (age, distance, spectral type, apparent magnitude) for each target star, a target list can be constructed that maximizes the likelihood of detecting planets, or competing instrument designs can be evaluated with respect to their predicted success for a given survey. We are already employing this method to select targets for our Simultaneous Differential Imaging surveys (Biller et al., 2004), now underway at the VLT and MMT.

This Chapter is based on material originally published in Nielsen et al. (2006).

3.1 Introduction

With the number of detected extrasolar planets continuing to climb well over one hundred, astronomers are finally in a position to begin to characterize the process of planet formation, as well as give statistical descriptions of planet populations around nearby stars. A significant gap, however, exists in our knowledge for planets with orbits beyond that of Jupiter: the widest orbit known for a confirmed extrasolar planet is 6 AU, for 55 Cnc d (Marcy et al., 2002). Since this limit is set by the time baseline of radial velocity surveys, this threshold will march out slowly; it will take another 15 years to close an orbit equivalent to Saturn's (9.5 AU). Radial velocity detections of planets in this regime will be further hampered by the fact that the amplitude of the velocity declines with the inverse square root of the semi-major axis.

Direct imaging, then, serves as a completely complementary detection method to radial velocity surveys, as it is most sensitive to planets with large separations from their parent stars, with no real upper limit to detectable semi-major axes. If the two techniques could be brought together at intermediate separations, we will be able to start building up a complete picture of the distribution of planets. Again, since radial velocity surveys are slow to move outward, direct imaging is well-situated to close the gap.

SDI, or Simultaneous Differential Imaging, is a technique to achieve very high contrast images at small angular separations. By obtaining images simultaneously through narrow-band filters centered at the $1.6\ \mu\text{m}$ methane bandhead, we can greatly attenuate speckle noise from the star, and achieve very high contrasts for objects with a strong methane signature (most giant planets). We are currently conducting a survey for planets around young, nearby stars using SDI cameras installed at the VLT and MMT. For further information on SDI and the progress

of our survey, see Lenzen et al. (2004) and Biller et al. (2004).

3.2 Monte Carlo Simulations

The ability of a survey instrument to detect self-luminous, giant extrasolar planets is typically given in the form of a contrast curve: the minimum magnitude (expressed in relation to the magnitude of the parent star) at which a companion can be significantly detected, given as a function of the angular separation between the two objects. Here, we express contrast ratio in terms of ΔH , where $\Delta H = m_{H,planet} - m_{H,star}$, comparing the H-band flux from the planet to the H-band flux from the star. When computing this quantity from images, we calculate the 5σ contrast curve by measuring the residual noise in regions of varying angular separation from the star (see Section 3.3 of Biller et al. (2004) for a detailed explanation of this process). We have assembled a set of four sensitivity curves in order to illustrate the nature of our simulations, as shown in Fig. 3.1.

VLT NACO SDI represents a currently available system, on the 8.2m VLT telescope with a 200 element Shack-Hartmann wavefront sensor, using four-channel SDI optics to reduce speckle noise (Lenzen et al., 2004; Biller et al., 2004). This contrast curve was taken from observations of a star meant to represent median conditions for our survey, in terms of observing conditions, target star spectral type, and target brightness. We note that SDI contrast curves are actually measured in a narrowband filter within the H band, at $1.575 \mu\text{m}$; we convert to ΔH here (and through subsequent analysis) by assuming a constant conversion consistent with our NACO SDI observations of Gl 229 B (Biller et al., 2004).

Gemini NICI is expected to come on-line by 2006, utilizing the H85 AO systems, an 85 element curvature wavefront sensor, along with a coronagraph and two-channel SDI optics (NICI Request for Proposal , 2005). The contrast curve

used here is given by the NICI Request for Proposals (used as the baseline for teams competing for the NICI Planet-Finding Campaign). It represents the assumption of NICI’s performance (prior to being tested at the telescope) for median seeing, with a $V=13$ guide star (assumed strehl of 30%), of spectral type K or earlier. In this study, we scale the contrast curve by the assumed strehl for stars of later spectral type, as well as adjusting the minimum H-band flux level at which point sources can be detected. As with SDI, this contrast curve assumes a narrowband filter within the H band, at $1.6\ \mu\text{m}$ with a width of 1%, and we assume a constant conversion from narrowband to broadband.

We also include potential designs for Extreme Adaptive Optics Coronagraphs (ExAOC) at an 8m-class telescope, or at the proposed 24m Giant Magellan Telescope (Johns et al. , 2004). In either case, the instrument design consists of a spatially-filtered Shack-Hartmann wavefront sensor (750 element for the 8m telescope, 4000 for the GMT), a coronagraph, a focal-plane wavefront sensor for speckle suppression (Codona & Angel, 2004), and SDI optics for added contrasts (Codona et al. , 2005). We note that this represent a proposed system (“GemSDI”) for an ExAOC system at Gemini South, a proposal that was not ultimately accepted. Assumptions for the ExAOC curves are similar to that for the NICI curve, attempting to reproduce median conditions, in terms of seeing and target star properties. We again scale this curve according to expected strehl, given the V magnitude of each target star. For the 24m GMT case, we take a very conservative estimate of system performance, simply scaling up the 8m simulations to a larger telescope size. While this decreases the inner working angle, the outer working angle stays fixed, given our assumption about the number of actuators in the AO system producing the dark hole.

All contrast curves, for each instrument design, represent 5σ sensitivity to

planets.

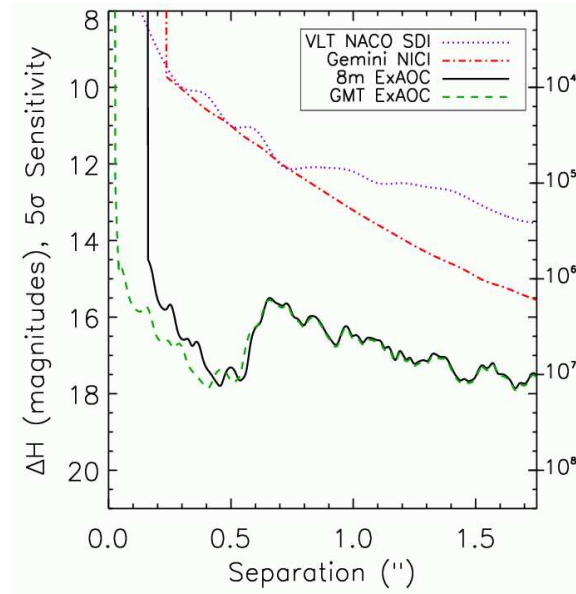


Figure 3.1 Sensitivity curves for the four planet-finding instruments we consider here. The curves represent the 5σ level of detection for a companion at a given angular distance from the parent star.

While the contrast curves of Fig. 3.1 describe the comparative abilities to image faint companions of the four systems, it is not immediately apparent how these curves translate into the figure of merit about which we're most concerned: the number of planets each system could detect from a survey. In order to evaluate this, we have constructed a Monte Carlo simulation to create an ensemble of planets, compute their projected separation and H-magnitude, then compare them to these contrast curves to determine what fraction can be detected with a given system.

For each target star, we simulate 100,000 planets, randomly generating six quantities for each planet: mass, semi-major axis, eccentricity, inclination angle, longitude of periastron, and orbital phase. Mass and semi-major axis are

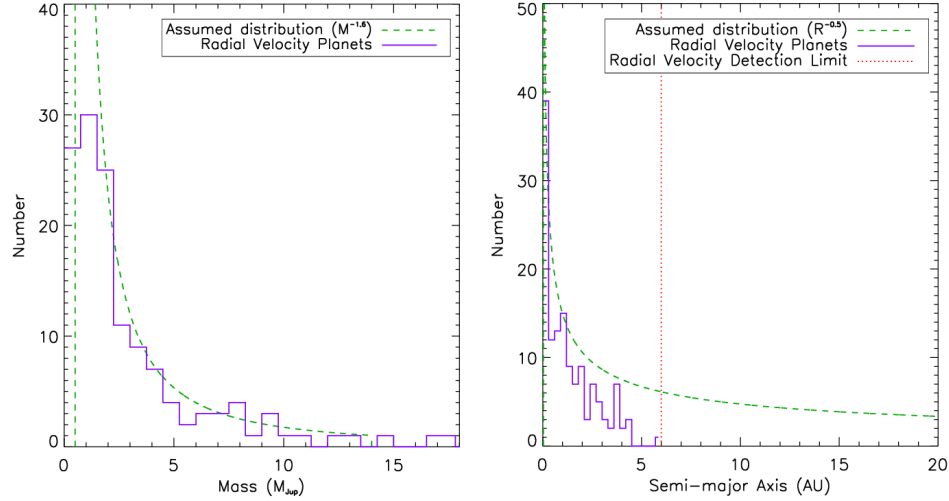


Figure 3.2 The assumed distributions of mass and semi-major axis of extrasolar giant planets, plotted against histograms of known planets from radial velocity surveys.

assumed to be governed by simple power-law distributions, with indices chosen to fit the population of known radial velocity planets, as shown in Fig. 3.2 (similar distributions were inferred by Lineweaver and Grether (2003) for mass and Graham et al. (2002) for semi-major axis). Distributions of extrasolar planets are taken from California & Carnegie Planet Search Almanac of Planets (2005). High and low mass cut-offs are imposed on the power law distribution at 0.5 and 14 M_{Jup} , and the semi-major axis distribution is truncated at 0.037 AU (orbital radius of the innermost known extrasolar planet, HD 73256) and 20 AU. This final value is uncertain, as the data from extrasolar planet surveys become incomplete beyond ~ 3 AU, and no data exist for extrasolar planets further out than 6 AU. We take 20 AU (the orbit of Uranus) as a conservative upper limit (Since the publication of Nielsen et al. (2006), the imaging of planets at much larger separations, including the HR 8799 planets (Marois et al., 2008), shows that this is likely too

stringent a constraint). The distribution for eccentricity is taken as a simple polynomial fit to the histogram of eccentricities of radial velocity planets.

It should be noted that we have assumed three independent distributions for mass, semi-major axis, and eccentricity for planets, which is almost certainly incorrect. With only 137 known planets, however, the statistics are not sufficient to suggest a more complex distribution. Additionally, our simulations allow for the possibility of multiple-planet systems, though we do not treat them explicitly. The Monte Carlo Simulations create a similar ensemble of simulated planets around each target star, with the assumption that a detected planet will represent a single simulated planet. Should there be a discovery of multiple planets, however, we would then assume that two of the simulated planets around the target star represent the actual discoveries. In fact, the RV planets used to build the power law distributions of planet populations include multiple planet systems, though as with our simulations, each planet is considered independent of any other planet orbiting the star. Again, this simplistic assumption is likely to be incorrect, as the presence of a single planet will strongly constrain the allowable masses and orbits of other planets. Nevertheless, we treat each simulated planet as independent, which should be a safe starting point for our analysis, to first order.

We also assign an inclination angle for the orbit (uniform in $\cos(i)$), longitude of periastron (uniform between 0 and 2π), and orbital phase (uniform random variable is time; between 0 and 1 orbital periods). From these six quantities we can solve for the instantaneous separation between planet and star, as viewed from the observer on earth. The distance to the target star can then be used to solve for angular separation. With the planet models of Burrows et al. (2003), the planet's mass (along with the age of the target star) are converted into an H-

magnitude, which we use to solve for ΔH , given the distance and 2MASS fluxes of the target star. Then, it is determined whether or not each planet can be detected, given the sensitivity curve of Fig. 3.1.

We show examples of these simulations for a single target star in Fig. 3.3. In addition to the sensitivity limit, we consider if the apparent magnitude of the planet is sufficient to be detected by photon noise arguments alone, and whether the planet is too massive to have a significant methane feature (SDI is most effective when there is a strong drop in the planet's spectrum at the methane band-head, $T_{eff} < 1200\text{K}$). We note that there are planets beyond 20 AU, since the 20 AU cut is in orbital semi-major axis, while the plot shows observed planet-star separation (given the assumed eccentricity distribution of exoplanets, for planets with 20 AU in semi-major axis, separations can be < 40 AU). We can now directly compare two systems by their ability to find planets: VLT NACO SDI should have a 6% chance of finding a planet around this star, while GMT ExAOC will be at 35%.

3.3 Target Selection

The ideal target star for a direct imaging survey for self-luminous extrasolar planets is characterized by three traits: the star should be young so the planet's luminosity is larger, the star should be nearby so the angular separation between primary and companion is greater, and the star should be of a late spectral type so that the inherent luminosity of the star does not overwhelm the planet's light. It is not trivial to find a balance between these factors to select an observing list for a survey. In particular, there is a lack of very young stars (< 30 Myr) very close (< 20 pc) to the sun, so compromises must be made. It is through the simulations described in this paper that we seek to disentangle these target star traits,

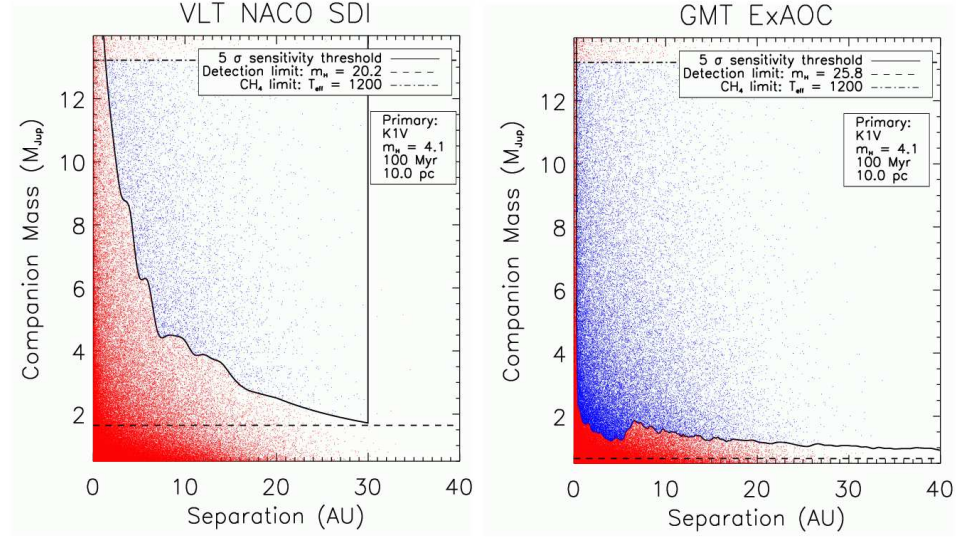


Figure 3.3 Example simulations for a particular target star with the VLT NACO SDI (left) and GMT ExAOC (right) systems. Each point represents a single simulated planet, out of a total of 100,000 in the simulation run. Detected planets lie above the sensitivity curve (solid line), the detection threshold (dashed line), and below the methane limit (dotted line). The detection threshold is the minimum detectable flux given the observation, regardless of the presence of a stellar halo. For VLT NACO SDI, 6% of these planets are detected; GMT ExAOC can detect 35%. The GMT ExAOC curve is generated assuming the use of simultaneous differential imaging, so it too has an upper methane cut-off.

so that every potential target gets a quantitative ranking. By constructing a survey that maximizes the expected number of planets detected, our results (even null results) become more meaningful.

We note that as we move to younger target stars, it is important to consider the effects of circumstellar dust upon the sensitivity of direct imaging observations to planets. For the planet-finding systems considered here, it is unlikely to be a major effect, as stars on the target list we use for this analysis are generally older than 10 Myr. Nevertheless, brighter disks can produce an additional noise source; we do not address this issue in the analysis presented here (of our target list, only AU Mic has a bright debris disk), however surveys focused on stars with disk will have to more properly account for this complication. A more accurate consideration of future very-high-contrast ground-based (and space based) planet-finding instruments will have to carefully weigh the effects of circumstellar dust, as these instruments become sensitive to fainter and fainter planets; however such higher order effects are beyond the scope of our considerations here.

Another important consideration (especially for higher-order AO systems such as ExAOC) is the limiting magnitude at which the adaptive optics can efficiently operate. More complex AO systems (more wavefront measurements, and more actuators to control) require more photons from the guide star (the target star in most cases), with declining Strehl ratios (and so contrasts) for fainter guide stars. Since our simulations indicate a preference for younger, further-out stars over older, nearby targets, a planet-finding system with a limiting magnitude that is too bright will exclude many of the best targets. For example, of the 40 best targets from our list of 153 (which we have compiled from the literature), the median *V* magnitude is 9.75; a next-generation AO system that can't lock onto targets fainter than 9th magnitude will simply not be an efficient planet

finder, as half the potential targets are eliminated before the survey begins. This effect can be mitigated by allowing the AO system's performance to be modulated depending on the target star (having the wavefront sensor integrate longer on fainter stars, for example), at the expense of contrasts. In any event, when designing future adaptive optics systems with the primary goal of detecting extrasolar planets, one must be keenly aware of the nature of the available science targets when evaluating potential instrument designs. The number of target stars for direct imaging surveys for self-luminous extrasolar planets is limited, and an instrument that cannot reach most of them would not be competitive.

3.4 Simulation Results

We now consider the implications of our simulation results for the selection of target stars. In Fig. 3.4 we examine the fraction of planets that can be detected around target stars of various ages and distances. As expected, younger, nearby targets are more likely to harbor detectable planets. The probability of detecting a planet around an older, or more distant, star drops quickly. We also look at results of the simulation for all 153 of our target stars, plotting the median separation of the detected planets (See Fig. 3.3) against the percentage of planets that are detectable. With the more sophisticated planet-finding systems, we see the most important aspect of the system design in the inner working radius, as we would expect most planets to lie at small angular separations from their parent stars.

We also consider the predicted results of a planet-search campaign, directed at our target list, using the four systems. Since the simulations return the probability of detecting a planet around a given star, the sum of these probabilities for many stars should give us the total number of planets we'd expect to detect at the end of a survey. In Fig. 3.5 we have grouped our targets by detection probability

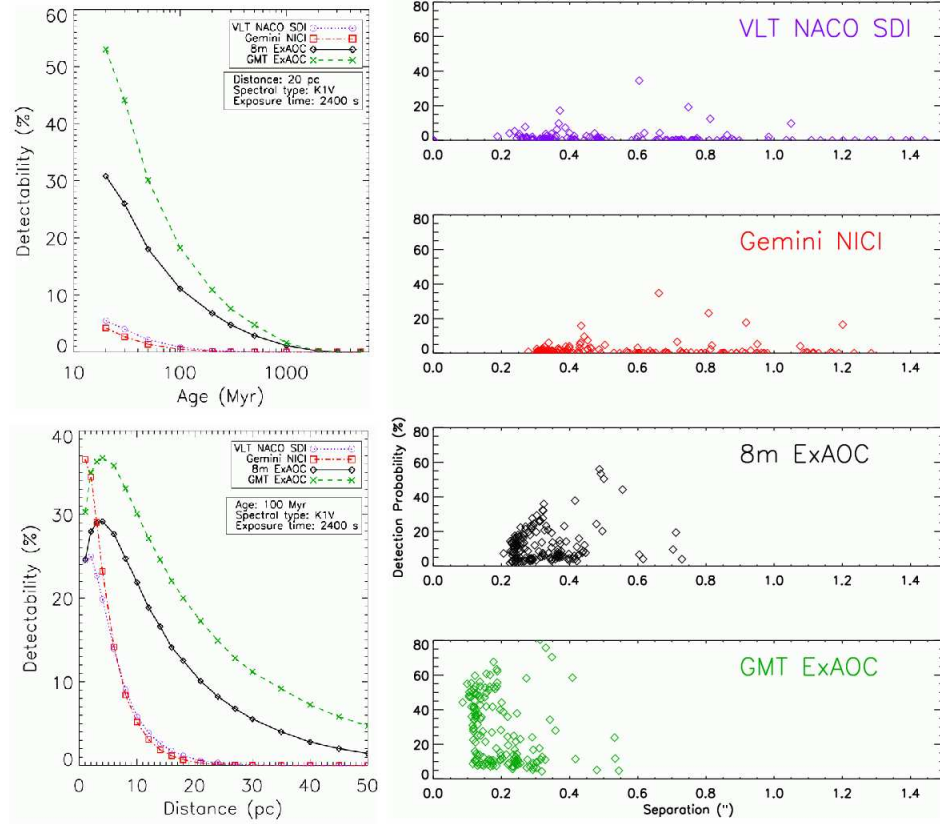


Figure 3.4 Basic results from the simulation. Top left shows the fraction of simulated planets detected (the detection probability) for target stars of different ages. As expected, younger stars are the preferred targets for finding self-luminous planets, and there is very little value in observing older target stars. Bottom left is a similar plot, only with distance being varied. In the right panel, we consider the properties of the simulated planets that can be detected with each system. For each of the 153 target stars, we plot the fraction of planets that can be detected (y-axis) against the median projected separation between primary and companion for those planets that can be detected. The pile-up at small separations underscores the importance of the inner working radius of any planet-finding system.

(so the highest-quality targets are observed first), and show the expected yield of planets from surveys of various sizes. Clearly, the best targets are observed first, and adding lesser-quality target stars to the observing campaign results in a slower gain in planets. The break in these curves, between rapid return of planets and a more gradual increase, depends on the nature of the instrument.

3.5 Conclusions

With these simple Monte Carlo simulations, extrapolating from populations of known extrasolar planets, we have a method to quantitatively rank stars in a target list for a planet search campaign, or to directly compare competing instrument designs for future planet finding systems. Our basic results suggest that there are a limited number of target stars suitable for direct imaging searches for self-luminous planets, a fact that must be considered when planning a survey or designing a new instrument.

Finally, we consider one of our basic assumptions: that each of our target stars has a planet described by the power laws of Fig. 3.2. While there is a lack of data for planet populations at large separations, we can make an estimate of total populations based on our initial assumptions and results from radial velocity surveys. Fischer & Valenti (2005) determine that in a volume-limited sample, about 6% of stars show the radial velocity signature of a massive planet with an orbital period shorter than 4 years (2.5 AU for a solar mass primary). Given this, we can then integrate our assumed semi-major axis distribution ($dN/da = a^{-0.5}$), to give the total number of planets between 0.03 and 20 AU (which we simulate), compared to the fraction found by Fischer & Valenti (2005) between 0.03 and 2.5 AU. From this argument, we'd expect 18% of all stars to have a giant planet, or 40% for stars of solar metallicity or greater. This simplistic argument

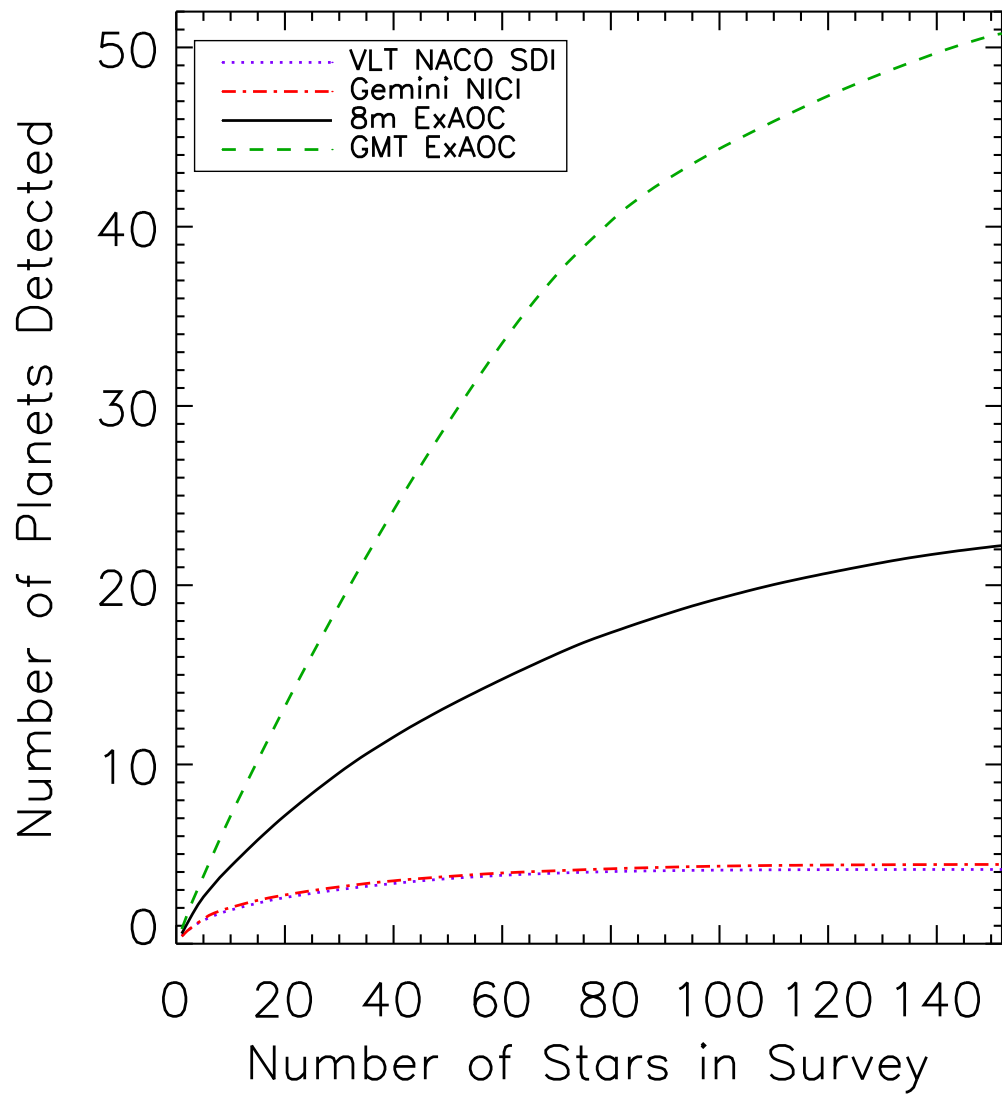


Figure 3.5 The number of planets expected to be detected, as a function of the number of stars in the survey. In each case, once the best targets are observed, there is a slow gain in planets detected as lower-quality targets are added to the survey. The location of this break, however, depends on the ability of the instrument.

does not take into account possible effects of changing planet populations (or overall frequency) with spectral type of the parent star, an issue that is still being studied. Nevertheless, as these simulations make real predictions about survey results, they place us in a strong position to interpret any results as they relate to the overall populations of extrasolar planets.

3.6 Acknowledgments

This work was performed in part under contract with the Jet Propulsion Laboratory (JPL) funded by NASA through the Michelson Fellowship Program. JPL is managed for NASA by the California Institute of Technology

CHAPTER 4

CONSTRAINTS ON EXTRASOLAR PLANET POPULATIONS FROM VLT
 NACO/SDI AND MMT SDI AND DIRECT ADAPTIVE OPTICS
 IMAGING SURVEYS: GIANT PLANETS ARE RARE AT LARGE
 SEPARATIONS

We examine the implications for the distribution of extrasolar planets based on the null results from two of the largest direct imaging surveys published to date. Combining the measured contrast curves from 22 of the stars observed with the VLT NACO adaptive optics system by Masciadri et al. (2005), and 48 of the stars observed with the VLT NACO SDI and MMT SDI devices by Biller et al. (2007) (for a total of 60 unique stars: the median star for our survey is a 30 Myr K2 star at 25 pc), we consider what distributions of planet masses and semi-major axes can be ruled out by these data, based on Monte Carlo simulations of planet populations. We can set the following upper limit with 95% confidence: the fraction of stars with planets with semi-major axis between 20 and 100 AU, and mass above $4 M_{Jup}$, is 20% or less. Also, with a distribution of planet mass of $\frac{dN}{dM} \propto M^{-1.16}$ in the range of $0.5\text{--}13 M_{Jup}$, we can rule out a power-law distribution for semi-major axis ($\frac{dN}{da} \propto a^\alpha$) with index 0 and upper cut-off of 18 AU, and index -0.5 with an upper cut-off of 48 AU. For the distribution suggested by Cumming et al. (2008), a power-law of index -0.61, we can place an upper limit of 75 AU on the semi-major axis distribution. At the 68% confidence level, these upper limits state that fewer than 8% of stars have a planet of mass $>4 M_{Jup}$ between 20 and 100 AU, and a power-law distribution for semi-major axis with index 0, -0.5, and -0.61 cannot have giant planets beyond 12, 23, and 29 AU, respectively. In general, we find that even null results from direct imaging surveys are very powerful in con-

straining the distributions of giant planets ($0.5\text{--}13 M_{Jup}$) at large separations, but more work needs to be done to close the gap between planets that can be detected by direct imaging, and those to which the radial velocity method is sensitive.

This Chapter is based on material originally published in Nielsen et al. (2008).

4.1 Introduction

There are currently well over 200 known extrasolar planets, the bulk of which were discovered by radial velocity surveys (e.g. Butler et al. (2006)). While this field has initially been dominated by the study of the relatively easy-to-find Hot Jupiters (planets with orbital periods of order days), over the past several years there has been an increasing amount of data describing planets in larger orbits. In particular, Fischer & Valenti (2005) compared radial velocity target stars with known planets to stars that had been monitored but did not show signs of planets; they concluded that about 5% of stars had planets of mass greater than $1.6 M_{Jup}$, in orbits shorter than 4 years (within 2.5 AU). Additionally, they determined that planet fraction increased with the host star's metal abundance. Butler et al. (2006) have also considered the distributions of semi-major axis and planet mass of known radial velocity planets, and found that both distributions are well-fit by power laws. Cumming et al. (2008) have examined the biases of the radial velocity technique, and found that the semi-major axis distribution found by Butler et al. (2006), $\frac{dN}{dP} \propto P^{-1}$, should be modified in light of the decreasing sensitivity of the radial velocity method with orbital distance, and suggest a power law index of -0.74 for period, instead (for solar-like stars, this corresponds to a power law distribution for semi-major axis where $\frac{dN}{da} \propto a^{-0.61}$).

A careful consideration of sensitivity of microlensing observations to planets by Gould et al. (2006) suggests that for certain lensing geometries, at projected

separations of $\sim 1\text{--}4$ AU, the lower limit for the frequency of Neptune-mass planets is 16%, making low-mass planets more common than giant planets in the inner solar system (though we note that the range of separations probed by Gould et al. (2006) and Fischer & Valenti (2005) do not precisely overlap, and the target star samples are not uniform between the two surveys). Additionally, Gaudi et al. (2002) found that from existing microlensing data, a third or less of M dwarfs in the galactic bulge have $1 M_{Jup}$ planets in orbits between 1.5 and 4 AU, and $\leq 45\%$ of M dwarfs have planets between 1 and 7 AU of mass $3 M_{Jup}$.

One outstanding question is how the abundance of planets varies as one considers planets in longer orbits. Raymond (2006) has studied the dynamics of terrestrial planet formation in systems with giant planets, and found from numerical simulations that giant planets impede the formation of earth-like planets when the giant planet orbits within 2.5 AU, and that water delivery to a terrestrial planet is only possible in significant amounts when the giant planet is beyond 3.5 AU. The full extent to which giant planets impede (or encourage) water-rich terrestrial planet formation is still unknown. A greater understanding of the distribution of giant planets is a precursor to investigating the conditions under which habitable terrestrial planets form and evolve.

The global distribution of giant planets has also been considered from the theoretical direction. Ida & Lin (2004) have produced distributions of planets forming in disks by core accretion, showing a continuation of a power law from the radial velocity regime (within 2.5 AU) for giant planets, out to about 10 AU, then trailing off at larger radii. It is possible that the lack of outer planets in these simulations may be due (at least in part) to the fact that these models do not consider the effects of planet-planet scattering after planets are formed, or it may simply be a function of the initial conditions of the simulation. In order to

constrain such models it is necessary to measure the distribution of giant planets in longer orbits, so as to fully sample parameter space.

With the advent of adaptive optics (AO) systems on large ($\sim 8\text{m}$) telescopes, the ability to detect and characterize planets by directly imaging the companion is becoming increasingly viable. Already planetary mass companions (in most cases $\sim 13 M_{Jup}$ at 40-300 AU, or even lower mass objects with brown dwarf hosts) have been detected in certain favorable circumstances (e.g. companions to 2MASS1207: Chauvin et al. (2004), AB Pic: Chauvin et al. (2005), Oph 1622: Brandeker et al. (2006), Luhman et al. (2007), Close et al. (2007), CHXR 73: Luhman et al. (2006), and DH Tau: Itoh et al. (2005)), and numerous surveys are underway for planets around nearby, young stars (since a self-luminous planet is brightest at young ages). While the paucity of traditional planets (that is, planets $< 13 M_{Jup}$ and < 40 AU orbiting a star) detected by this method has been disappointing, in this Chapter we consider how even a null result from these direct imaging surveys can be used to set constraints on the population of giant planets. As the sensitivity of radial velocity surveys to planets at larger separations decreases (due both to the smaller radial velocity signal, and the much longer orbital period requiring a longer time baseline of observations to adequately constrain the orbital parameters), at orbits wider than 10 AU only direct imaging is efficient at characterizing the extrasolar planet population.

Janson et al. (2007) used VLT SDI data (part of the data considered in this work) for the known planet host star ϵ Eridani, to search for the radial velocity planet, given its predicted position from the astrometric orbit of Benedict et al. (2006). Though upper limits were found for the planet of $M_H \sim 19$, the predicted flux of the planet could be up to 10 magnitudes fainter, given the likely age of the system of 800 Myr. While this is young compared to the rest of the radial velocity

planet host stars, it is quite old by the standards of direct imaging planet searches, so the inability to detect this planet's flux is unsurprising. Previous work has been done by Kasper et al. (2007) to study the region of parameter space unprobed by the radial velocity method, large orbital separations, by observing 22 young, nearby stars in the L-band from the VLT. The null result from this survey was used to set constraints on combinations of power-law index and upper cut-off for the distribution of the observed separation (not semi-major axis) of extrasolar planets.

Masciadri et al. (2005) conducted a survey of 28 young, nearby stars, with a null result for planets. They found that their observations were sufficient to detect a $5 M_{Jup}$ planet at projected separations greater than 14 AU around 14 of their target stars, and above 65 AU for all 28 stars. Similarly, their observations would have been sensitive to a $10 M_{Jup}$ planet with a projected separation of 8.5 AU or beyond for half their sample, and greater than 36 AU for the full sample. These results (obtained by adopting published ages for the target stars, and using the appropriate planet models of Baraffe et al. (2003)) point to a rarity of giant planets at large separations from their parent stars.

Lowrance et al. (2005) conducted a survey of similar scope to this VLT survey, looking at 45 stars with HST NICMOS, though they considered a range of spectral types, while Masciadri et al. (2005) considered only target stars of spectral types K and M. Since direct imaging surveys are more sensitive to planets around fainter target stars, the NICMOS survey could detect an object more massive than $30 M_{Jup}$ between 15 and 200 AU around the median target star, and $5 M_{Jup}$ beyond 30 AU for 36 (Lowrance et al., 2005). The results, then, from both surveys are similar, that there is a rarity of giant planets at large separations.

In this Chapter we enlarge the sample beyond that considered by Masciadri

et al. (2005), and consider the implications of our null result with respect to the full orbital parameters of potential planets. We aim to set quantitative limits on the distribution of planets in semi-major axis space, and statistically rule out models of planet populations.

4.2 Observations

We begin with contrast plots (sensitivity to faint companions as a function of angular separation from the target star) from two surveys for extrasolar planets, using large telescopes and adaptive optics. Masciadri et al. (2005) carried out a survey of 28 young, nearby, late-type stars with the NACO adaptive optics system at the 8.2 meter Very Large Telescope (VLT). These observations have exposure times of order 30 minutes, with stars being observed in the H or Ks bands. Subsequent to these observations, a survey of 54 young, nearby stars of a variety of spectral types (between A and M) was conducted between 2003 and 2005, with the results reported in Biller et al. (2007). This second survey used the Simultaneous Differential Imager (SDI) at the 6.5 meter MMT and the 8 meter VLT, an adaptive optics observational mode that allows higher contrasts by imaging simultaneously in narrow wavelength regions surrounding the $1.6\ \mu\text{m}$ methane feature seen in cool brown dwarfs and expected in extrasolar planets (Lenzen et al., 2004; Close et al., 2005). This allows the light from a hypothetical companion planet to be more easily distinguishable from the speckle noise floor (uncorrected starlight), as the two will have very different spectral signatures in this region. This translates to higher sensitivity at smaller separations than the observations of Masciadri et al. (2005), which were conducted before the VLT SDI device was commissioned (see Fig. 14 of Biller et al. (2007) for a more detailed comparison of the two surveys). For most of these SDI targets, the star was ob-

served for a total of 40 minutes of integration time, which includes a 33 degree roll in the telescope’s rotation angle, in order to separate super speckles—which are created within the instrument, and so will not rotate—from a physical companion, which will rotate on the sky (Biller et al., 2006).

For both sets of target stars, contrast curves have been produced which give the 5σ ¹ noise in the final images as a function of radius from the target stars, and thus an upper limit on the flux of an unseen planet in the given filter of the observations. As no planets were detected in either survey at the 5σ level, we use these contrast curves to set upper limits on the population of extrasolar planets around young, nearby stars.

4.2.1 Target Stars

We construct a target list using 22 stars from the Masciadri et al. (2005) survey, and 48 stars from the survey of Biller et al. (2007), for a total of 60 targets (10 stars were observed by both surveys). This first cut was made by considering stars from the two surveys that had contrast curves, and stars whose age could be determined by at least one of: group membership, lithium abundance, and the activity indicator R'_{HK} (in three cases, ages from the literature were used, though these are stars that are generally older than our sample as a whole, and so uncertainties in the assumed ages will not adversely affect our results). Ages are determined by taking the age of the moving group to which the target star belongs; if the star does not belong to a group, the lithium or R'_{HK} age is used, or the two are averaged if both are available. Lithium ages are found by comparing to lithium abundances of members of clusters of known ages, and similarly for R'_{HK} (Mamajek, 2007). We give the full target list in Table 4.1, and details on the

¹We note that for the SDI observations this threshold corresponds to independent 5σ measurements in both the 0° and 33° images, see Biller et al. (2007) for details.

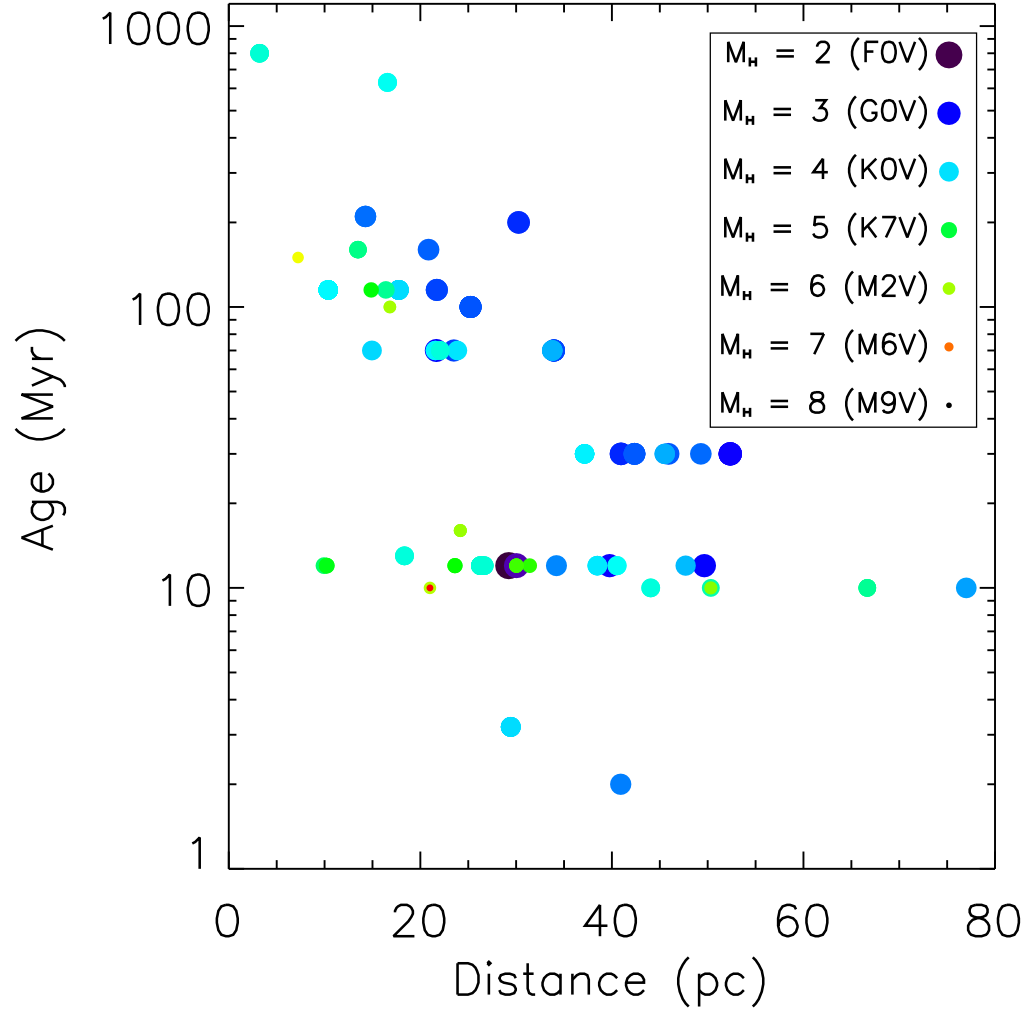


Figure 4.1 The 60 target stars from our two surveys (though five stars are too old to appear on this plot). These stars are some of the youngest, nearest stars known, spanning a range of spectral type. The size of the plotting symbol and the color is proportional to the absolute H magnitude of the star: a bigger, bluer symbol corresponds to a brighter and hotter star. The legend gives approximate spectral type conversions for main sequence stars, but we note that these stars have been plotted by their 2MASS H-band fluxes, and as a result their actual spectral type can vary from that shown in the legend. See Table 4.1 for more complete properties of these stars. The median target star is a 30 Myr K2 star at 25 pc.

age determination in Table 4.2. We also plot our target stars in Fig. 4.1. Overall, our median survey object is a 30 Myr K2 star at 25 pc.

Table 4.1. Target Stars

Target	RA ¹	Dec ¹	Distance (pc) ²	Sp. Type	Age (Myr)	V ¹	H ³	Ks ³	Obs. Mode ⁴
Biller et al. (2007)									
HIP 1481	00 18 26.1	-63 28 39.0	40.95	F8/G0V	30	7.46	6.25	6.15	VLT SDI
HD 8558	01 23 21.2	-57 28 50.7	49.29	G6V	30	8.54	6.95	6.85	VLT SDI
HD 9054	01 28 08.7	-52 38 19.2	37.15	K1V	30	9.35	6.94	6.83	VLT SDI
HIP 9141	01 57 48.9	-21 54 05.0	42.35	G3/G5V	30	8.11	6.55	6.47	VLT SDI
BD+05 378	02 41 25.9	+05 59 18.4	40.54	M0	12	10.20	7.23	7.07	VLT SDI
HD 17925	02 52 32.1	-12 46 11.0	10.38	K1V	115	6.05	4.23	4.17	VLT SDI
Eps Eri	03 32 55.8	-09 27 29.7	3.22	K2V	800	3.73	1.88	1.78	VLT SDI
V577 Per A	03 33 13.5	+46 15 26.5	33.77	G5IV/V	70	8.35	6.46	6.37	MMT SDI
GJ 174	04 41 18.9	+20 54 05.4	13.49	K3V	160	7.98	5.31	5.15	VLT SDI
GJ 182	04 59 34.8	+01 47 00.7	26.67	M1Ve	12	10.10	6.45	6.26	VLT SDI/Ks
HIP 23309	05 00 47.1	-57 15 25.5	26.26	M0/1	12	10.09	6.43	6.24	VLT SDI/Ks
AB Dor	05 28 44.8	-65 26 54.9	14.94	K1III	70	6.93	4.84	4.69	VLT SDI
GJ 207.1	05 33 44.8	+01 56 43.4	16.82	M2.5e	100	9.50	7.15	6.86	VLT SDI
UY Pic	05 36 56.8	-47 57 52.9	23.87	K0V	70	7.95	5.93	5.81	VLT SDI
AO Men	06 18 28.2	-72 02 41.4	38.48	K6/7	12	10.99	6.98	6.81	VLT SDI/Ks
HIP 30030	06 19 08.1	-03 26 20.0	52.36	G0V	30	8.00	6.59	6.55	MMT SDI
HIP 30034	06 19 12.9	-58 03 16.0	45.52	K2V	30	9.10	7.09	6.98	VLT SDI
HD 45270	06 22 30.9	-60 13 07.1	23.50	G1V	70	6.50	5.16	5.05	VLT SDI
HD 48189 A	06 38 00.4	-61 32 00.2	21.67	G1/G2V	70	6.15	4.75	4.54	VLT SDI
pi01 UMa	08 39 11.7	+65 01 15.3	14.27	G1.5V	210	5.63	4.28	4.17	MMT SDI
HD 81040	09 23 47.1	+20 21 52.0	32.56	G0V	2500	7.74	6.27	6.16	MMT SDI
LQ Hya	09 32 25.6	-11 11 04.7	18.34	K0V	13	7.82	5.60	5.45	MMT/VLT SDI/Ks
DX Leo	09 32 43.7	+26 59 18.7	17.75	K0V	115	7.01	5.24	5.12	MMT/VLT SDI
HD 92945	10 43 28.3	-29 03 51.4	21.57	K1V	70	7.76	5.77	5.66	VLT SDI
GJ 417	11 12 32.4	+35 48 50.7	21.72	G0V	115	6.41	5.02	4.96	MMT SDI
TWA 14	11 13 26.5	-45 23 43.0	46.00 ⁵	M0	10	13.00	8.73	8.49	VLT SDI
TWA 25	12 15 30.8	-39 48 42.0	44.00 ⁵	M0	10	11.40	7.50	7.31	VLT SDI
RXJ1224.8-7503	12 24 47.3	-75 03 09.4	24.17	K2	16	10.51	7.84	7.71	VLT SDI
HD 114613	13 12 03.2	-37 48 10.9	20.48	G3V	4200	4.85	3.35	3.30	VLT SDI
HD 128311	14 36 00.6	+09 44 47.5	16.57	K0	630	7.51	5.30	5.14	MMT SDI
EK Dra	14 39 00.2	+64 17 30.0	33.94	G0	70	7.60	6.01	5.91	MMT SDI
HD 135363	15 07 56.3	+76 12 02.7	29.44	G5V	3	8.72	6.33	6.19	MMT SDI
KW Lup	15 45 47.6	-30 20 55.7	40.92	K2V	2	9.37	6.64	6.46	VLT SDI
HD 155555 AB	17 17 25.5	-66 57 04.0	30.03	G5IV	12	7.20	4.91	4.70	VLT SDI/Ks
HD 155555 C	17 17 27.7	-66 57 00.0	30.03	M4.5	12	12.70	7.92	7.63	VLT SDI/Ks
HD 166435	18 09 21.4	+29 57 06.2	25.24	G0	100	6.85	5.39	5.32	MMT SDI
HD 172555 A	18 45 26.9	-64 52 16.5	29.23	A5IV/V	12	4.80	4.25	4.30	VLT SDI
CD -64 1208	18 45 37.0	-64 51 44.6	34.21	K7	12	10.12	6.32	6.10	VLT SDI/Ks
HD 181321	19 21 29.8	-34 59 00.5	20.86	G1/G2V	160	6.48	5.05	4.93	VLT SDI
HD 186704	19 45 57.3	+04 14 54.6	30.26	G0	200	7.03	5.62	5.52	MMT SDI
GJ 799B	20 41 51.1	-32 26 09.0	10.22	M4.5e	12	11.00	0.00	-99.00	VLT SDI/Ks
GJ 799A	20 41 51.2	-32 26 06.6	10.22	M4.5e	12	10.25	5.20	4.94	VLT SDI/Ks
GJ 803	20 45 09.5	-31 20 27.1	9.94	M0Ve	12	8.81	4.83	4.53	VLT SDI/Ks
HD 201091	21 06 53.9	+38 44 57.9	3.48	K5Ve	2000	5.21	2.54	2.25	MMT SDI

Table 4.1—Continued

Target	RA ¹	Dec ¹	Distance (pc) ²	Sp. Type	Age (Myr)	V ¹	H ³	Ks ³	Obs. Mode ⁴
Eps Indi A	22 03 21.7	-56 47 09.5	3.63	K5Ve	1300	4.69	2.35	2.24	VLT SDI
GJ 862	22 29 15.2	-30 01 06.4	15.45	K5V	6300	7.65	5.28	5.11	VLT SDI
HIP 112312 A	22 44 57.8	-33 15 01.0	23.61	M4e	12	12.20	7.15	6.93	VLT SDI
HD 224228	23 56 10.7	-39 03 08.4	22.08	K3V	70	8.20	6.01	5.91	VLT SDI
Masciadri et al. (2005)									
HIP 2729	00 34 51.2	-61 54 58	45.91	K5V	30	9.56	6.72	6.53	VLT Ks
BD +2 1729	06 18 28.2	-72 02 42	14.87	K7	30	9.82	6.09	5.87	VLT H
TWA 6	07 39 23.0	02 01 01	77.00 ⁵	K7	30	11.62	8.18	8.04	VLT Ks
BD +1 2447	10 18 28.8	-31 50 02	7.23	M2	12	9.63	5.61	5.31	VLT H
TWA 8A	10 28 55.5	00 50 28	21.00 ⁵	M2	115	12.10	7.66	7.43	VLT Ks
TWA 8B	11 32 41.5	-26 51 55	21.00 ⁵	M5	100	15.20	9.28	9.01	VLT Ks
TWA 9A	11 32 41.5	-26 51 55	50.33	K5	800	11.26	8.03	7.85	VLT Ks
TWA 9B	11 48 24.2	-37 28 49	50.33	M1	70	14.10	9.38	9.15	VLT Ks
SAO 252852	11 48 24.2	-37 28 49	16.40 ⁶	K5V	160	8.47	5.69	5.51	VLT H
V343 Nor	14 42 28.1	-64 58 43	39.76	K0V	12	8.14	5.99	5.85	VLT Ks
PZ Tel	15 38 57.6	-57 42 27	49.65	K0Vp	12	8.42	6.49	6.37	VLT Ks
BD-17 6128	18 53 05.9	-50 10 50	47.70	K7	70	10.60	7.25	7.04	VLT Ks

¹ from the CDS Simbad service² derived from the Hipparcos survey Perryman et al. (1997)³ from the 2MASS Survey Cutri et al. (2003)⁴ In cases where target stars were observed by both Masciadri et al. (2005) and Biller et al. (2007), the star is listed in the Biller et al. (2007) section, with Obs. Mode given as “VLT SDI/Ks,” for example.⁵ Distance from Song et al. (2003)⁶ Distance from Zuckerman et al. (2001a)

Table 4.2. Age Determination for Target Stars

Target	Sp. Type*	Li EW (mÅ)*	Li Age (Myr)	R' _{HK} *	R' _{HK} Age	Group Membership ¹	Group Age ¹	Adopted Age
Biller et al. (2007)								
HIP 1481	F8/G0V ²	129 ³	100	-4.360 ⁴	200	Tuc/Hor	30	30
HD 8558	G6V ²	205 ⁵	13			Tuc/Hor	30	30
HD 9054	K1V ²	170 ⁵	160	-4.236 ⁶	<100	Tuc/Hor	30	30
HIP 9141	G3/G5V ⁷	181 ⁸	13			Tuc/Hor	30	30
BD+05 378	M0 ⁹	15 ¹⁰				β Pic	12	12
HD 17925	K1V ⁷	194 ⁸	50	-4.357 ⁶	200	Her/Lyr	115	115
Eps Eri	K2V ¹¹			-4.598 ⁶	1300			800 ¹²
V577 Per A	G5IV/V ¹³	219 ¹³	3			AB Dor	70	70
GJ 174	K3V ¹⁴	118 ⁸	160	-4.066 ⁶	<100			160
GJ 182	M1Ve ¹⁰	280 ¹⁵	12					12
AB Dor	K1III ²	267 ⁸	10	-3.880 ⁶	<100	AB Dor	70	70
GJ 207.1	M2.5e ¹⁶							100 ¹⁷
HIP 23309	M0/1 ¹⁸	294 ¹⁸	12	-3.893 ⁶		β Pic	12	12
UY Pic	K0V ¹⁹	263 ⁸	10	-4.234 ⁶	<100	AB Dor	70	70
AO Men	K6/7 ¹⁸	357 ¹⁸	6	-3.755 ⁶		β Pic	12	12
HD 45270	G1V ²	149 ⁵				AB Dor	70	70
HD 48189 A	G1/G2V ²	145 ⁸	25	-4.268 ⁶	100	AB Dor	70	70
HIP 30030	G0V ²⁰	219 ⁸	2			Tuc/Hor	30	30
HIP 30034	K2V ²					Tuc/Hor	30	30
π 101 UMa	G1.5V ²¹	135 ⁸	100	-4.400 ²²	320			210
DX Leo	K0V ²¹	180 ⁸	100	-4.234 ⁶	<100	Her/Lyr	115	115
HD 81040	G0V ²¹	24 ²³	2500					2500
LQ Hya	K0V ²¹	247 ⁸	13					13
HD 92945	K1V ²¹	138 ⁸	160	-4.393 ⁶	320	AB Dor	70	70
GJ 417	G0V ²⁴	76 ²⁵	250	-4.368 ²⁶	250	Her/Lyr	115	115
TWA 14	M0 ²⁷	600 ²⁷	8			TW Hya	10	10
RXJ1224.8-7503	K2 ²⁸	250 ²⁸	16					16
TWA 25	M0 ⁹	494 ²⁹	10			TW Hya	10	10
HD 114613	G3V ³⁰	100 ³¹	400	-5.118 ⁶	7900			4200
EK Dra	G0 ³²	212 ⁸	2	-4.180 ²²	<100	AB Dor	70	70
HD 128311	K0 ²¹			-4.489 ²⁶	630			630
HD 135363	G5V ²¹	220 ⁸	3					3
KW Lup	K2V ³⁰	430 ³³	2					2
HD 155555 AB	G5IV ¹⁸	205 ⁸	6	-3.965 ⁶	<100	β Pic	12	12
HD 155555 C	M4.5 ¹⁸					β Pic	12	12
CD -64 1208	K7 ¹⁸	580 ¹⁸	5			β Pic	12	12
HD 166435	G0 ³⁴			-4.270 ²²	100			100
HD 172555 A	A5IV/V ²					β Pic	12	12
HD 181321	G1/G2V ³⁰	131 ⁸	79	-4.372 ⁶	250			160
HD 186704	G0 ³⁵			-4.350 ²²	200			200
GJ 799A	M4.5e ¹⁶					β Pic	12	12
GJ 799B	M4.5e ¹⁶					β Pic	12	12
GJ 803	M0Ve ¹⁶	51 ⁸	30			β Pic	12	12
HD 201091	K5Ve ¹⁶			-4.704 ⁶	2000 ⁺			2000

4.3 Monte Carlo Simulations

In order to place constraints on the properties of planets from our null results, we run a series of Monte Carlo simulations of an ensemble of extrasolar planets around each target star. Each simulated planet is given full orbital parameters, an instantaneous orbital phase, and a mass, then the planet’s magnitude in the observational band is determined from these properties (using the target star’s age and distance, and theoretical mass-luminosity relations) as is its projected separation from the star. Finally, this magnitude is compared to the measured contrast curve to see if such a planet could be detected. Determining which simulated planets were detected, and which were not, allows us to interpret the null result in terms of what models of extrasolar planet populations are excluded by our survey’s results.

4.3.1 Completeness Plots

As in Biller et al. (2007), we use completeness plots to illustrate the sensitivity to planets as a function of planet mass and semi-major axis. To do this, for each target star, we create a grid of semi-major axis and planet mass. At each grid location we simulate 10^4 planets, and then compute what fraction could be detected with the contrast curve for that star.

In general, most orbital parameters are given by well-known distributions. Inclination angle has a constant distribution in $\sin(i)$, while the longitude of the ascending node and the mean anomaly are given by uniform distributions between 0 and 2π . Since contrast plots are given in terms of radius alone, it is not necessary to consider the argument of periastron in the simulations.

To simulate the eccentricities of the planet orbits, we examine the orbital parameters of known extrasolar planets from radial velocity surveys. We consider

Table 4.2—Continued

Target	Sp. Type*	Li EW (mÅ)*	Li Age (Myr)	R'_{HK} *	R'_{HK} Age	Group Membership ¹	Group Age ¹	Adopted Age
Eps Indi A	K5Ve ¹⁶			-4.851 ⁶	4000			1300 ³⁶
GJ 862	K5V ¹⁶	5 ¹⁵		-4.983 ⁶	6300 ⁺			6300
HIP 112312 A	M4e ⁹					β Pic	12	12
HD 224228	K3V ³⁰	53 ⁸	630	-4.468 ⁶	500	AB Dor	70	70
Masciadri et al. (2005)								
HIP 2729	K5V ²					Tuc/Hor	30	30
BD +2 1729	K7 ²¹					Her/Lyr	115	115
TWA 6	K7 ³⁷	560 ³⁷	3			TW Hya	10	10
BD +1 2447	M2 ³⁸					TW Hya	150	150
TWA 8A	M2 ³⁷	530 ³⁷	3			TW Hya	10	10
TWA 8B	M5 ³⁷	560 ³⁷	3			TW Hya	10	10
TWA 9A	K5 ³⁷	460 ³⁷	3			TW Hya	10	10
TWA 9B	M1 ³⁷	480 ³⁷	3			TW Hya	10	10
SAO 252852	K5V ³⁹					Her/Lyr	115	115
V343 Nor	K0V ²	300 ³¹	5			β Pic	12	12
PZ Tel	K0Vp ¹⁹	267 ⁴⁰	20			β Pic	12	12
BD-17 6128	K7 ⁴¹	400 ⁴²	3			β Pic	12	12

¹Group Membership for TWA, β Pic, Tuc/Hor, and AB Dor from Zuckerman & Song (2004), Her/Lyr from López-Santiago et al. (2006). Group Ages from Zuckerman & Song (2004) (TWA, β Pic, and Tuc/Hor), Nielsen et al. (2005) (AB Dor), and López-Santiago et al. (2006) (Her/Lyr)

* Measurement References: 2: Houk & Cowley (1975), 3: Waite et al. (2005), 4: Henry et al. (1996), 5: Torres et al. (2000), 6: Gray et al. (2006b), 7: Houk & Smith-Moore (1988), 8: Wichmann et al. (2003), 9: Zuckerman & Song (2004), 10: Favata et al. (1995), 11: Cowley et al. (1967), 12: Benedict et al. (2006), 13: Christian & Mathioudakis (2002), 14: Leaton & Pagel (1960), 15: Favata et al. (1997), 16: Gliese & Jahreiss (1991), 17: Lowrance et al. (2005), 18: Zuckerman et al. (2001a), 19: Houk (1978), 20: Cutispoto et al. (1995), 21: Montes et al. (2001), 22: Wright et al. (2004), 23: Sozzetti et al. (2006), 24: Bidelman (1951), 25: Gaidos et al. (2000), 26: Gray et al. (2003b), 27: Zuckerman et al. (2001b), 28: Alcalá et al. (1995), 29: Song et al. (2003), 30: Houk (1982), 31: Randich et al. (1993), 32: Gliese & Jahreiß (1979), 33: Neuhauser & Brandner (1998), 34: Eggen (1996), 35: Abt (1985), 36: Lachaume et al. (1999), 37: Webb et al. (1999), 38: Vyssotsky et al. (1946), 39: Evans (1961), 40: Soderblom et al. (1998), 41: Nesterov et al. (1995), 42: Mathioudakis et al. (1995)

⁺In general, we have only determined Ca R'_{HK} ages for stars with spectral types K1 or earlier, but in the case of these two K5 stars, we have only the R'_{HK} measurement on which to rely for age determination. The calibration of Mt. Wilson S-index to R'_{HK} for K5 stars (B-V \sim 1.1 mag) has not been well-defined (Noyes et al. (1984); specifically the photospheric subtraction), and hence applying a R'_{HK} vs. age relation for K5 stars is unlikely to yield useful ages. Although we adopt specific values for the ages of these stars, it would be more accurate to state simply that these stars have ages >1 Gyr. As a result, almost all simulated planets are too faint to detect around these stars, so the precise error in the age does not significantly affect our final results.

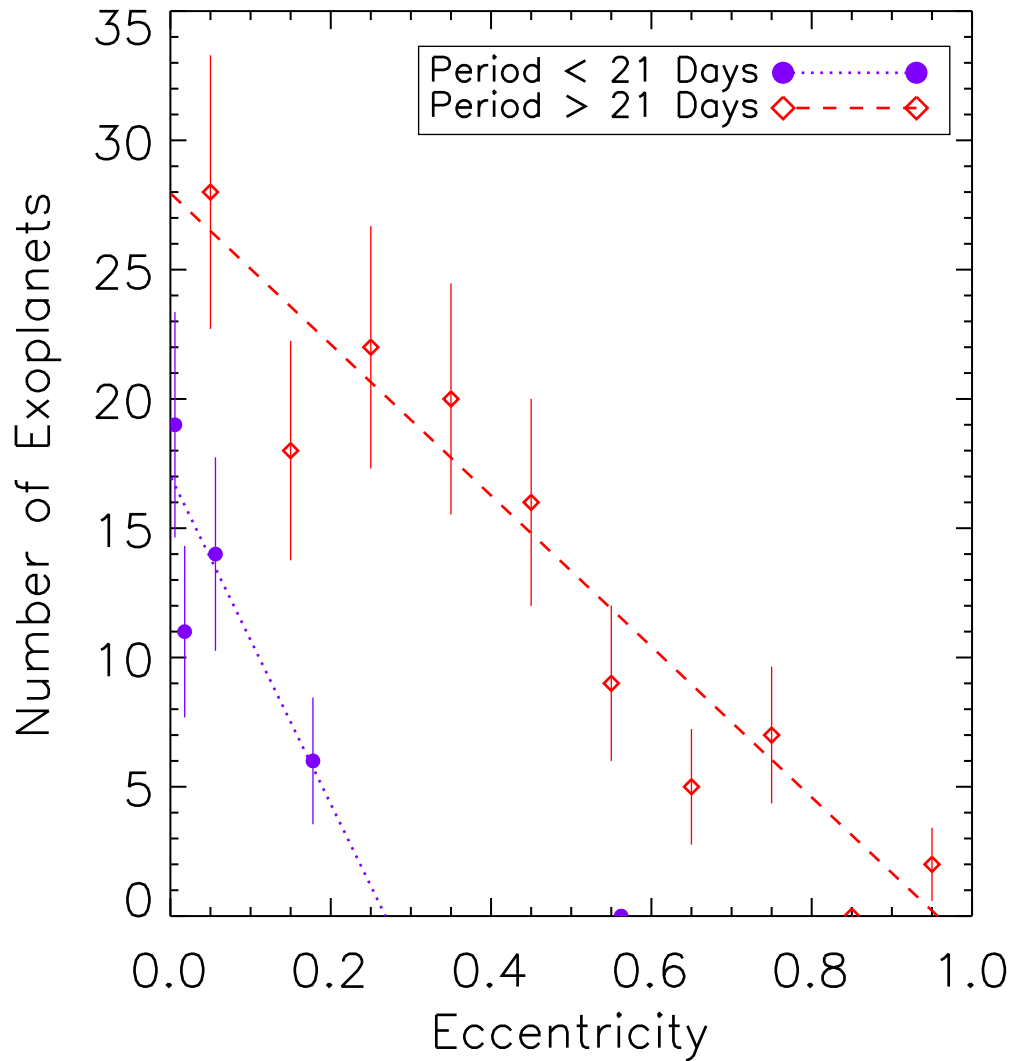


Figure 4.2 The assumed distribution for the orbital eccentricities of extrasolar planets. The datapoints represent the histograms for planets found to date with the radial velocity method (Butler et al., 2006), with error bars as 1-sigma Poisson noise based on the number of planets per bin. Planets are divided to separate “Hot Jupiters,” based on a period cut at 21 days; long period planets are divided into linear bins, short-period ones into logarithmic bins. In both cases, a simple linear fit is a good representation of the data.

the orbits of planets given by Butler et al. (2006), and show their distribution of eccentricities in Fig. 4.2. By dividing the sample into two populations, based on a cut at an orbital period of 21 days, we can separate out the population of Hot Jupiters, which we expect to have experienced orbital circularization as a result of their proximity to their host stars. For both sets of populations, we fit a simple straight line to the distributions (the logarithmic bins for the Hot Jupiter population means this line translates to a quadratic fit). We note that the Hot Jupiter fit is plagued by small number statistics, and so the fit is likely to be less reliable than that for long period planets. Additionally, the choice of 21 days as the cut-off is a result of the RV sample being comprised almost entirely of solar-type (FGK) stars, and were we to consider planets around target stars of a wide range of masses, this cut-off would likely prove to be a function of stellar mass, as the circularization radius will ultimately depend on the gravitational force felt by the planet. However, even for our closest target stars, such an orbital period gives star-planet separations less than $0.1''$, a regime where our contrast curves show we are not sensitive to planets. As a result, the manner in which the orbits of Hot Jupiters are simulated has effectively no impact on our final results.

For each simulated planet, the on-sky separation is determined at the given orbital phase, and mass is converted into absolute H or Ks magnitude, following the mass-luminosity relations of both Burrows et al. (2003) and Baraffe et al. (2003); both of these sets of models have shown success at predicting the properties of young brown dwarfs (e.g. Stassun et al. (2007) and Close et al. (2007a)). In the case of the models of Burrows et al. (2003), we use a Vega spectrum to convert the various model spectra into absolute H and Ks magnitudes. We also note that the Burrows et al. (2003) models only cover a range of planet masses greater than $1 M_{Jup}$, and ages above 100 Myr. Since the range of ages of our tar-

get stars extends down to 2 Myr, and we wish to consider planets down to masses of $0.5 M_{Jup}$, we perform a simple extrapolation of the magnitudes to these lower ages and masses. While this solution is clearly not ideal, and will not reflect the complicated physical changes in these objects as a function of mass and age, we feel that this method provides a good estimation of how the Burrows et al. (2003) models apply to our survey.

At this point, we use the distance to the target star, as well as its 2MASS flux density in either H or Ks, to find the delta-magnitude of each simulated planet. With this, and the projected separation in the plane of the sky, we can compare each simulated planet to the 5σ contrast curve, and determine which planets can be detected, and which cannot. We also apply a minimum flux limit, based on the exposure time of the observation, as to what apparent magnitude for a planet is required for it to be detected, regardless of its distance from the parent star. For the SDI observations, which make use of optimized (compared to basic H-band observing) methane filters, we add an additional factor of $\Delta H=0.6$ magnitudes (appropriate for a T6 spectral type, a conservative estimate for young planets; see Biller et al. (2007) for details on this factor). Also, for these SDI observations, we place an upper cut-off on masses where, for the age of the system, the planet reaches an effective temperature of 1400 K. Above this temperature, methane in the atmosphere of the planet is destroyed, and the methane feature disappears, so that the SDI subtraction now attenuates any planets, as well as stellar speckles. While non-methane objects further out than $0.2''$ are not totally removed in the image (e.g. Fig. 4 of Nielsen et al. (2005)), for consistency we ignore this possibility when considering upper limits.

In many cases in our survey, a single target star was observed at several epochs, in some cases with different observational parameters (such as VLT NACO

SDI and VLT NACO Ks broadband) or even different telescopes (MMT and VLT). As a result, to be considered a null detection, a simulated planet must lie below the 5σ detection threshold at each observational epoch, and this threshold must reflect the appropriate contrast curve for the given observation. To account for this, for target stars with multiple observations, an ensemble of simulated planets is created for the earliest observational epoch, as described above, and compared to the contrast curve for that observation. The simulated planets then retain all the same orbital parameters, except for orbital phase which is advanced forward by the elapsed time to the next observational epoch, and the simulated planets are now compared to the contrast curve from the later epoch (and so on for every available contrast curve). A planet that lies above the contrast curve at any epoch is considered detectable. Typically this elapsed time is about a year, and so is a minor effect for planets with long-period orbits; we nevertheless include this complexity for completeness. The major benefit of this method is that for stars observed both with SDI (Biller et al., 2007) and at H or Ks (Masciadri et al., 2005), it is possible to leverage both the higher contrasts at smaller separations with SDI and the insensitivity to the methane feature of broadband imaging, which allows planets of higher masses to be accessed. The epochs used when considering each observation are those given in Table 3 of Masciadri et al. (2005) and Tables 2 and 3 of Biller et al. (2007).

We plot an example of this simulation at a single grid point in mass and semi-major axis in Fig. 4.3, for the target star GJ 182, the 18th best target star in our survey, using the planet models of Burrows et al. (2003). 10^4 simulated planets (only 100 are plotted in this figure, for clarity) are given a single value of mass ($6.5 M_{Jup}$) and semi-major axis (10 AU). Since each planet has unique orbital parameters (eccentricity, viewing angle, and orbital phase), the projected separation

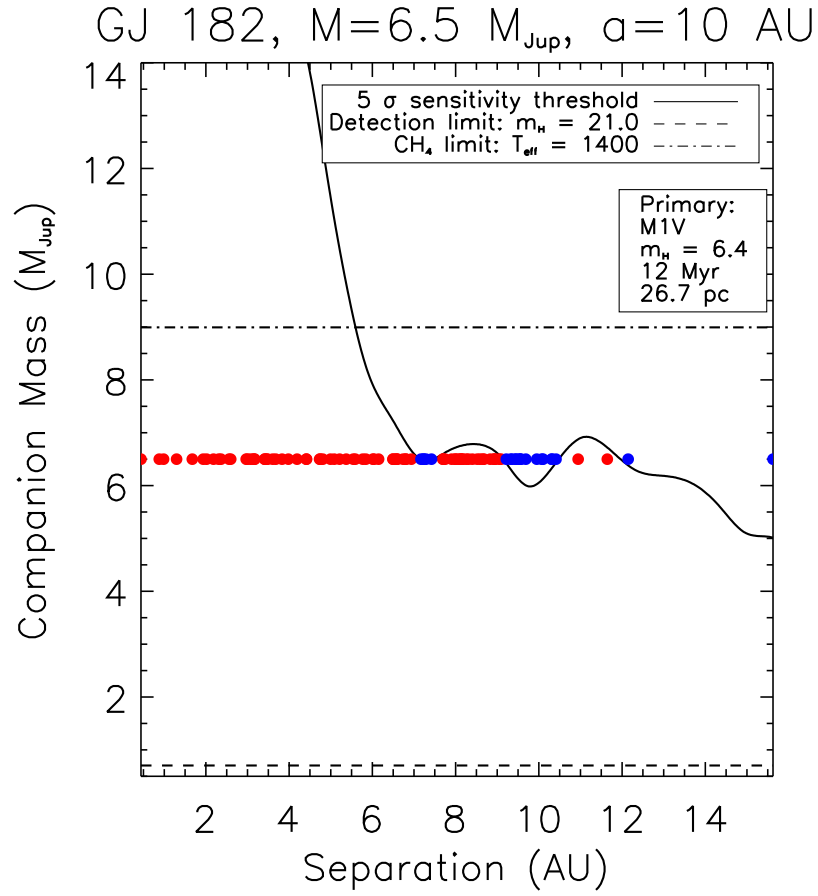


Figure 4.3 The results of a single simulation of 10^4 planets around the SDI target star GJ 182 (for clarity, only 100 points are plotted here) (Biller et al., 2007). Each planet has a mass of $6.5 M_{\text{Jup}}$, and a semi-major axis of 10 AU. Due to various values of eccentricity, viewing angle, and orbital phase, the projected separation of each simulated planet departs from the semi-major axis, and the points smear across the horizontal direction, with projected separation running between 0 and 14 AU. Planets that are above the contrast curve are detected (blue dots), while those below are not (red dots). In this case, 20% of these simulated planets were detected. By running this simulation over multiple grid points of mass and semi-major axis, we produce a full completeness plot, such as Fig. 4.4.

varies from planet to planet, so some are above the 5σ detection threshold of the contrast curve (the blue dots in the figure), while others are not (the red dots). For this particular target star and simulated planets of mass $6.5 M_{Jup}$ and semi-major axis 10 AU, 20% of these planets can be detected.

To produce a complete contour plot, we consider a full grid of mass (100 points, between 0.5 and $17 M_{Jup}$) and semi-major axis (200 points, between 1 and 4000 AU), running a simulation as in Fig. 4.3 at each of the 20,000 grid points. We then plot contours showing what fraction of planets we can detect that have a given mass and semi-major axis, in Fig. 4.4, again for the target star GJ 182. The hard upper limit is set by the methane cut-off, where the planet mass becomes high enough (for the age of the given target star) for the effective temperature to exceed 1400 K, at which point the methane feature is much less prominent in the planet's spectrum. Although there exists a Ks dataset for the star GJ 182, and additional observational epochs with SDI, for clarity we only use a single SDI contrast curve to produce this figure; the full dataset is used for subsequent analysis. If GJ 182 had a planet with mass and semi-major axis such that it would fall within the innermost contour of Fig. 4.4, we would have an 80% chance of detecting it. Obviously, these plots make no statements about whether these stars have planets of the given parameters, but instead simply express our chances of detecting such a planet if it did exist.

4.3.2 Detection Probabilities Given an Assumed Distribution of Mass and Semi-major Axis of Extrasolar Planets

With the large number of currently-known extrasolar planets, it is possible to assume simple power-law representations of the distributions of mass and semi-major axis of giant planets, which allows for a more quantitative interpretation of our null result. Butler et al. (2006) suggest a power law of the form $\frac{dN}{dM} \propto M^{-1.16}$

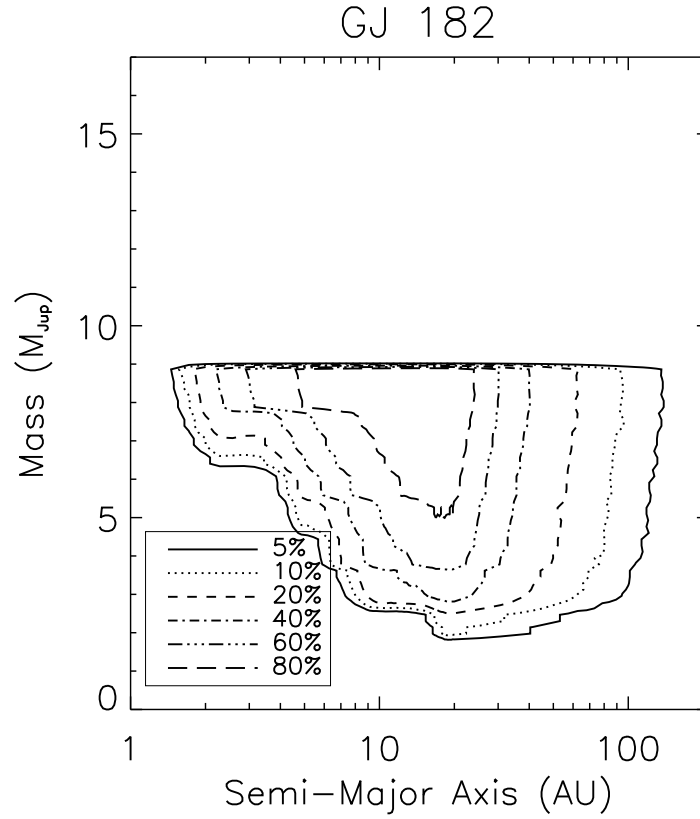


Figure 4.4 A full completeness plot for the target star GJ 182. As a function of planet mass and semi-major axis (with grid points between 0.5 and 17 M_{Jup} for mass, and semi-major axis between 1 and 4000 AU, though only the inner 210 AU are plotted here), the contours give the probability of detecting a planet with those parameters given the available contrast curve. At each grid point, 10^4 planets are simulated, as shown in Fig. 4.3, and the fraction that can be detected is returned. The left edge is strongly influenced by the shape of the contrast curve, while the right edge depends mainly on the projected field of view of the observation. The hard upper limit at 9 M_{Jup} is set by the methane cut-off imposed by the SDI method, when the simulated planets exceed 1400 K and cease to have a strong methane signature in the spectrum. The fact that the contours do not precisely line up at this limit is simply a result of the interpolation used to plot the contours. Completeness plots for all 60 survey stars are available online at <http://exoplanet.as.arizona.edu/%7Elclose/exoplanet.html>

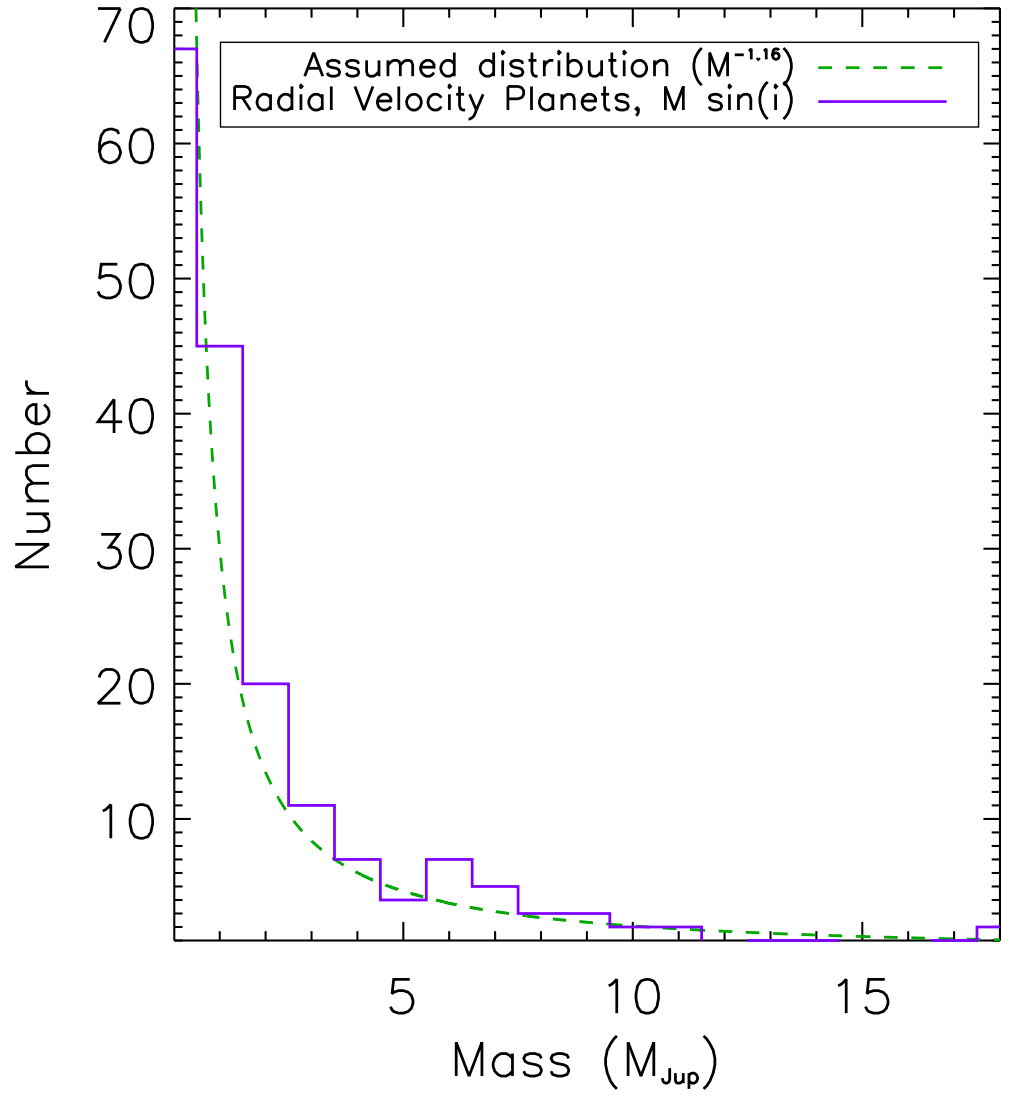


Figure 4.5 The assumed mass distribution of extrasolar planets, plotted against the histogram of known planets detected by the radial velocity method (as of May 2007). Throughout this Chapter we adopt a power law of the form $\frac{dN}{dM} \propto M^{-1.16}$, as suggested by Butler et al. (2006), and the data shown here are well-represented by this power-law fit.

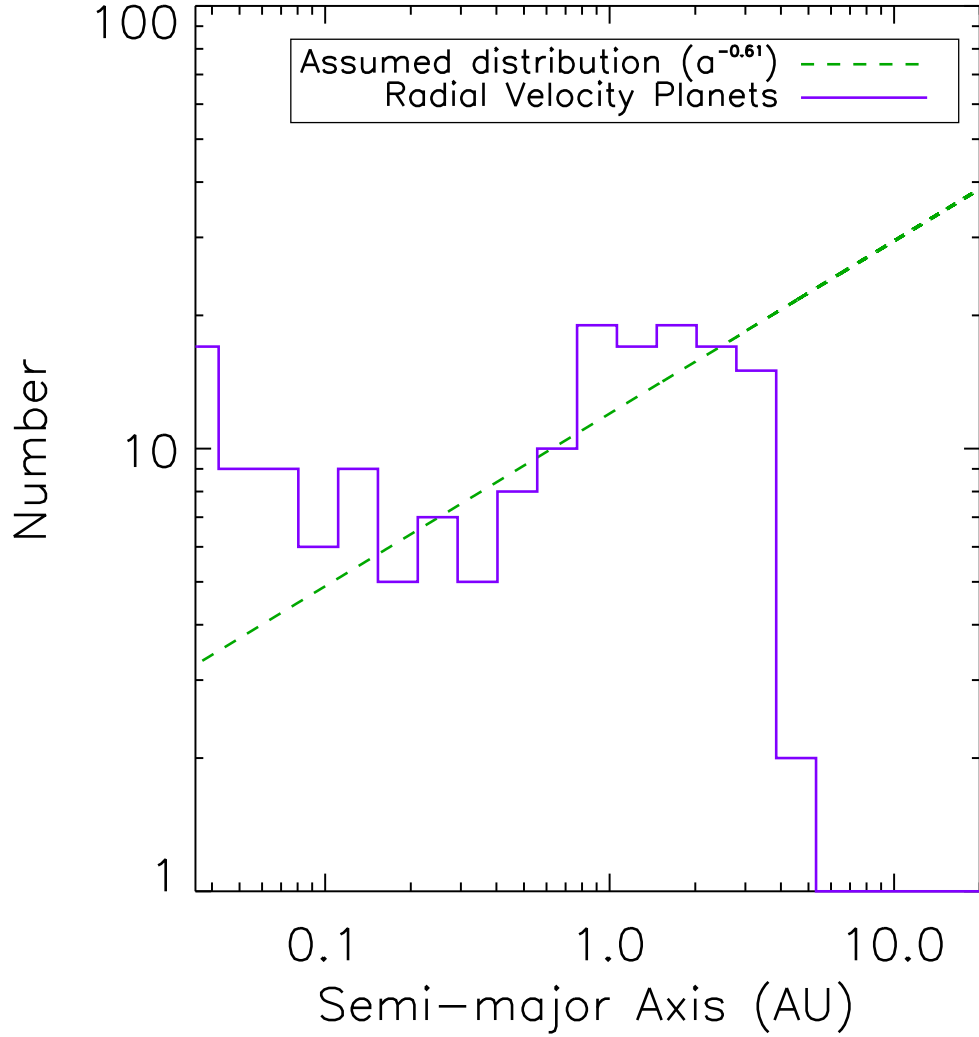


Figure 4.6 The distributions that we consider for semi-major axis of extrasolar planets, again with the histogram of known radial velocity planets, detected as of May 2007. We adopt the observed distribution of Cumming et al. (2008), with $\frac{dN}{da} \propto a^{-0.61}$, which is suggestive of the existence of wider planets, given that radial velocity surveys should be especially sensitive to hot Jupiters (producing an over-abundance at small separations) and less sensitive to long-period orbits (resulting in a decline in detected planets at larger separations).

for mass, while Cumming et al. (2008) use the power law $\frac{dN}{da} \propto a^{-0.61}$ for semi-major axis, in order to describe the distributions of known extrasolar planets. We make histograms for mass (Fig. 4.5) and semi-major axis (Fig. 4.6) from the parameters of all currently-known extrasolar planets (parameters taken from the Catalog of Nearby Exoplanets, <http://exoplanets.org>, in May 2007). In both cases, the power laws do a reasonable job of fitting the data, above $1.6 M_{Jup}$ and within 3.5 AU. For smaller planets, or longer periods, we would expect the observational biases of the radial velocity method to make the sample incomplete, thus accounting for the drop-off of planets from what would be predicted by the power law. We echo the caution of Butler et al. (2006) that these planets are drawn from many inhomogeneous samples, but we believe with the relatively large numbers the derived distributions are not far off from the actual distributions.

In general, then, if one assumes that these power laws are universal to all stars, and that the semi-major axis power law continues to larger separations with the same index, the only outstanding question is to what outer limit (or “cut-off”) this distribution continues before it is truncated. This cut-off is a term that can be uniquely well constrained by the null results from our survey. We return to this issue, after considering the results from our survey, in Section 4.4.3.

For the Monte Carlo simulations using these assumptions, in addition to the other orbital parameters, we obtain mass and semi-major axis through random variables that follow the given power law distributions, and again find what fraction of planets can be detected given the contrast curve for that particular target star. An example of this simulation, again for GJ 182, is given in Fig. 4.7, showing that with an assumed upper limit for semi-major axis of 70 AU, and a power law with index -0.61, and mass power law index of -1.16 between 0.5 and $13 M_{Jup}$, we

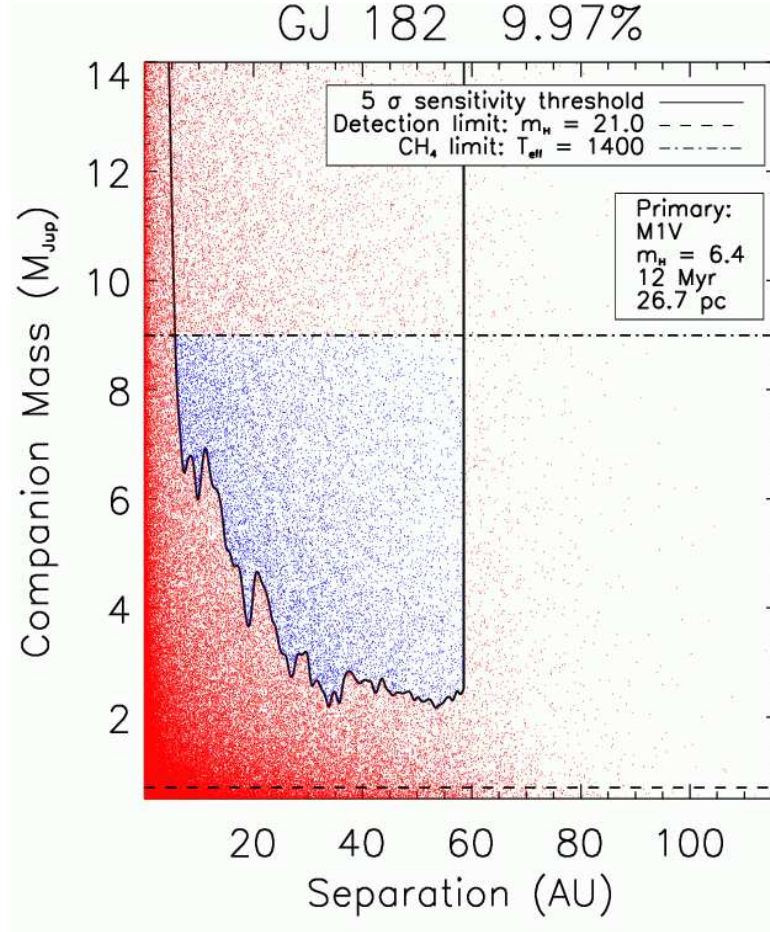


Figure 4.7 10^5 simulated planets around the SDI target star GJ 182, following the distributions for mass ($\frac{dN}{dM} \propto M^{-1.16}$) of Butler et al. (2006) and semi-major axis ($\frac{dN}{da} \propto a^{-0.61}$) of Cumming et al. (2008), with mass running from 0.5 to $13 M_{Jup}$, and semi-major axis cut off at 70 AU (since there is a range of eccentricities for the simulated planets, instantaneous projected separation can exceed the semi-major axis cut-off of 70 AU, and so some planets are seen at observed separations beyond 70 AU). Detected planets (blue dots) are those that lie above the contrast curve, above the minimum flux level, and below the methane cut-off. In this case, 10% of the simulated planets could be detected with this observation. Using the metric of completeness to planets with this mass and semi-major axis distribution, GJ 182 is the 18th best target star in our sample.

would be able to detect 10% of the simulated planets. Again, for this figure, we simply show the results using the models of Burrows et al. (2003).

4.4 Analysis

Having developed the tools to produce completeness plots, as well as compute the fraction of detected planets for various assumed models of semi-major axis, we proceed to combine the results over all our target stars in order to place constraints on the populations of extrasolar planets from these two surveys.

4.4.1 Planet Fraction

A simplistic description of the number of planets expected to be detected is given by the expression

$$N(a, M) = \sum_{i=1}^{N_{obs}} f_p(a, M) P_i(a, M) \quad (4.1)$$

That is, the number of planets one expects to detect at a certain semi-major axis and mass is given by the product of the detection probability (P_i) for a planet of that mass (M) and semi-major axis (a), and the fraction of stars (f_p) that contain such a planet (or “planet fraction”), summed over all target stars (in this case, $N_{obs} = 60$). In this treatment, we ignore two major effects: we assume that there is no change in the mass or separation distribution of planets, or their overall frequency, as a function of spectral type of the primary; we also do not consider any metallicity dependence on the planet fraction. While these assumptions are clearly incorrect (e.g. Johnson et al. (2007), Fischer & Valenti (2005)), it is a good starting point for considering what constraints can be placed on the population of extrasolar planets. Also, we note that our sample includes 24 binaries, which may inhibit planet formation, though most of these binaries have separations greater than 200 AU. This leaves only ten binaries with separations in the range of likely

planet orbits that might potentially contaminate our results. For simplicity, we leave these binaries in our sample, and we will return to this issue in Section 4.4.3.

Using the contrast curves from each of our 60 target stars (as in Fig. 4.4), we simply sum the fraction of detectable planets at each grid points for all of our stars. This gives the predicted number of detectable planets at each combination of mass and semi-major axis, assuming each target star has one planet of that mass and semi-major axis ($f_p(a, M)=1$).

More instructively, if we assume a uniform value of the planet fraction for all target stars, we can solve for f_p . Then by assuming a particular value for the predicted number of planets (ΣP_i), our null result allows us to place an upper limit on the planet fraction at a corresponding confidence level, since our survey measured a value of $N(a, M)=0$. In a Poisson distribution, the probability of obtaining a certain value is given by $P = e^{-\mu} \frac{\mu^\nu}{\nu!}$, which for the case of a null result, $\nu = 0$, becomes $P = e^{-\mu}$, so a 95% confidence level requires an expectation value, μ , of 3 planets. We can thus rewrite Eq. 4.1, using $\Sigma P_i = 3$, as

$$f_p(a, M) \leq \frac{3}{\sum_{i=0}^{N_{obs}} P_i(a, M)} \quad (4.2)$$

Put another way, if we expected, from our 5σ contrast curves, to detect 12 planets ($\Sigma P=12$, for $f_p = 1$), in order to have actually detected 0 planets from our entire survey ($N=0$), the planet fraction must be less than $\frac{3}{12} = 25\%$ ($f_p < 0.25$), at the 95% confidence level. Doing this at each point in the grid of our completeness plots allows for an upper limit on the planet fraction as a function of mass and semi-major axis.

We plot the contours of this upper limit in Fig. 4.8, using the planet models of Burrows et al. (2003). A general result from these data is that, again at the 95% confidence level, we would expect fewer than 20% of stars to have planets of mass greater than $4M_{Jup}$ with semi-major axis between 20 and 100 AU. There

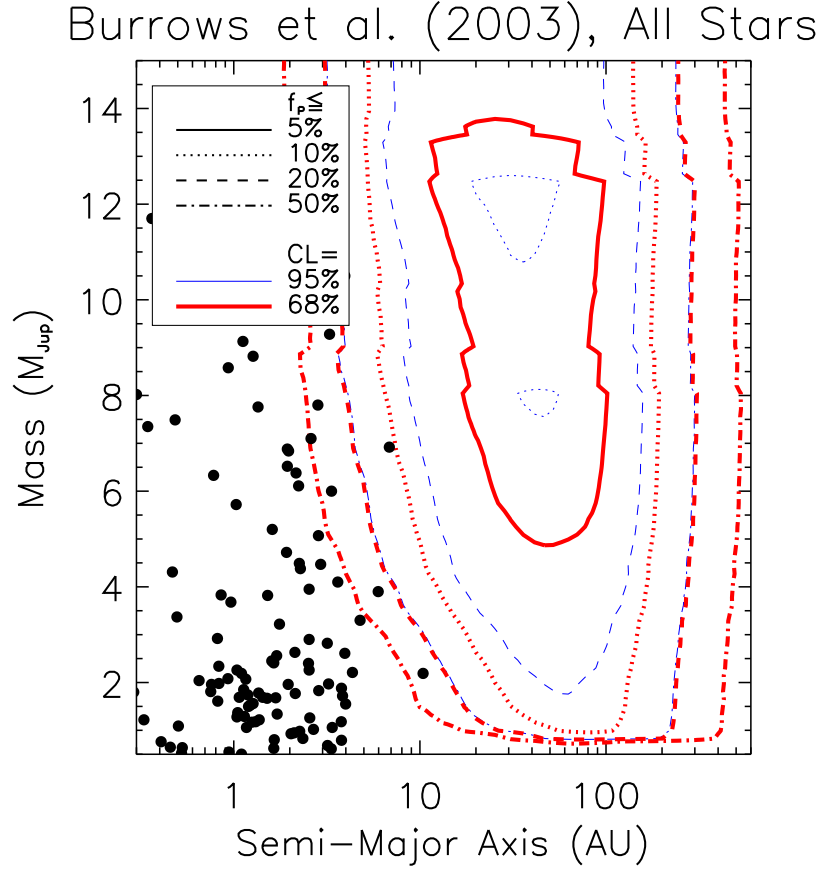


Figure 4.8 The upper limit on the fraction of stars with planets (f_p), as a function of mass and semi-major axis (see Eq. 4.2), using the planet models of Burrows et al. (2003), with the 95% confidence level plotted as thin blue lines. We also plot in thicker red lines the 68% confidence level contours. Given the results of our survey, we would expect, for example, less than 20% (as indicated by the thin dashed blue line) of stars to have a planet of mass greater than $4 M_{Jup}$ in an orbit $20 < a < 100$ AU, and less than 50% of stars (the dot-dashed thin blue line, which falls almost on top of the thick red dashed line) to have planets more massive than $4 M_{Jup}$ with semi-major axes between 8 and 250 AU, at the 95% confidence level. Also plotted in the solid circles are known extrasolar planets. There is still a gap between planets probed by direct imaging surveys (such as the ones described in this work), and those using the radial velocity method.

appears to be no “oasis” of giant planets (more massive than Jupiter) in long-period orbits: at the 85% confidence level, this upper limit on the fraction of stars with giant planets drops to less than 10%.

We present the same plot, this time using the COND models of Baraffe et al. (2003), in Fig. 4.9. As the two sets of models predict quite similar planet NIR magnitudes, the plots are virtually the same. The main difference between these models is that, given the age distribution of our target stars, higher mass planets appear slightly brighter in the Baraffe et al. (2003) models, with the trend reversing and lower mass planets becoming fainter, as compared to the models of Burrows et al. (2003). Marley et al. (2007) have recently produced a third set of models, which globally predict lower luminosities for giant planets. Since synthetic spectra for these models are not currently available, we do not examine the consequences of these models here, though we discuss possible effects in Section 4.5. But we note that while at 30 Myr and at $4 M_{Jup}$ there is only a $\sim 3X$ decrease in the luminosity predicted by Marley et al. (2007) compared to Burrows et al. (2003), the temperature of these objects is lower, therefore increasing the number of planets with methane that can be detected using SDI. As a result, even with the future use of the Marley et al. (2007) models, our results will not change dramatically, with respect to the total number of planets to which we are sensitive.

4.4.2 Host Star Spectral Type Effects

From the perspective of direct imaging searches for extrasolar planets, M-stars are especially appealing: their lower intrinsic luminosity means a given achievable contrast ratio allows fainter companions to be detected, and so makes the detection of planet-mass companions seem more likely. Nevertheless, there appears to be mounting evidence that even if the fraction of stars with planets does

Baraffe et al. (2003), All Stars

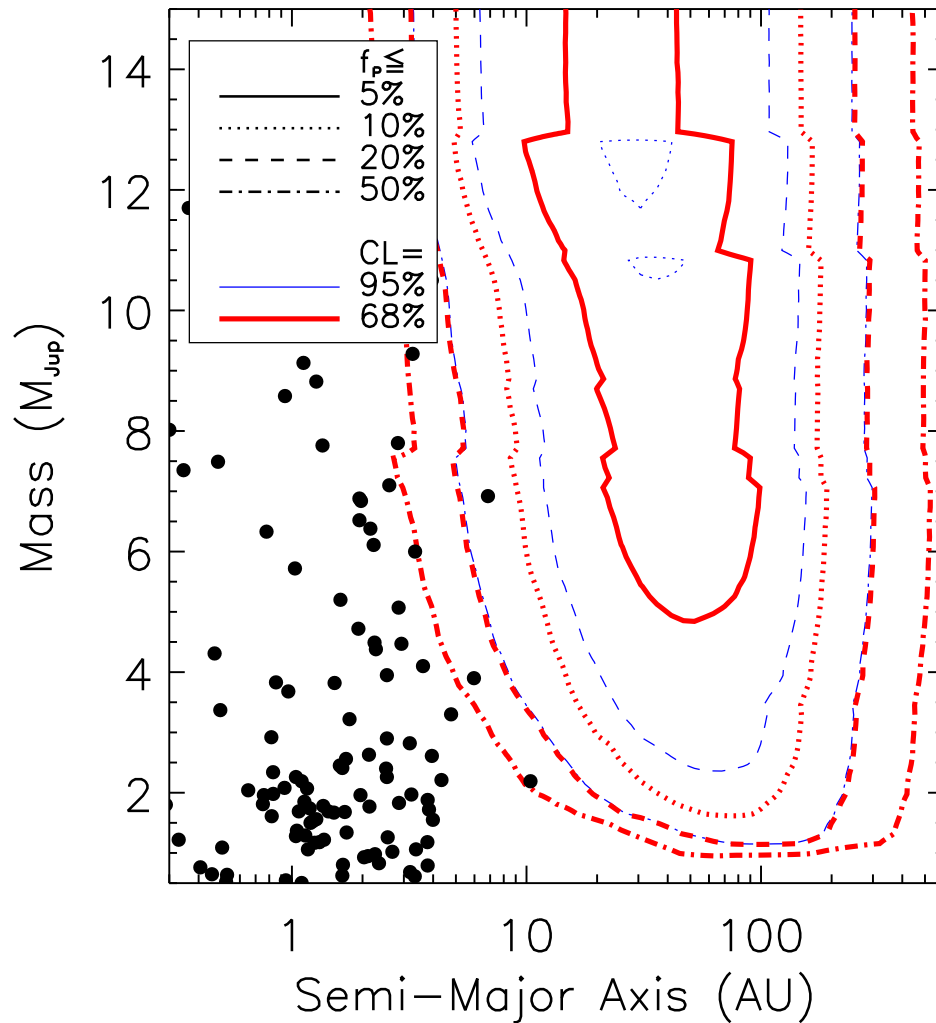


Figure 4.9 The same as Fig. 4.8, but instead using the models of Baraffe et al. (2003) to convert between planet mass and NIR magnitudes. The COND models generally predict brighter planets for higher masses, but fainter planets at lower masses, compared to the Burrows et al. (2003) models. Nevertheless, the two sets of models predict similar overall results.

not decline when moving to later spectral types (and the work of Johnson et al. (2007) suggests this fraction does decrease for M stars), the mean planet mass is likely to decrease (e.g. Butler et al. (2004), Bonfils et al. (2005)). While it seems natural that the initial mass of the circumstantial disk (and so the mass of formed planets) should scale with the mass of the parent star, such a relation is not easily quantified for planets at all orbital separations. Additionally, it is problematic for us to model planet distributions for M star hosts on radial velocity planets, when these planets are almost entirely in systems observationally biased with a host star of spectral type F, G, or K.

In order to investigate this effect, we divide our stars by spectral type, then recompute what limits we can set on the planet fraction. In Fig. 4.10 and 4.11 we plot the upper limit on the planet fraction for only the solar-like stars (K or earlier) in our survey (45 of our 60 target stars, this includes the one A star in our survey, HD 172555 A). As we would expect, the statistics in the inner contour remain largely the same, but the contours move upward and to the right, as less massive and closer-in planets become harder to detect against the glare of earlier-type stars.

We also consider the fifteen M stars in our sample, in Fig. 4.12 and 4.13. The effect of the smaller number of stars is apparent, though the shape of the contours is again roughly the same. If, as is suggested by Johnson et al. (2007), giant planets are less common around low mass stars, or less massive stars harbor less massive planets, it becomes difficult to probe the population of M star planets with surveys such as these.

4.4.3 Constraining the Semi-Major Axis Distribution

We now consider what constraints can be placed on planet populations if we assume a basic form to the distributions. In particular, if we take the mass power-

Burrows et al. (2003), AFGK Stars

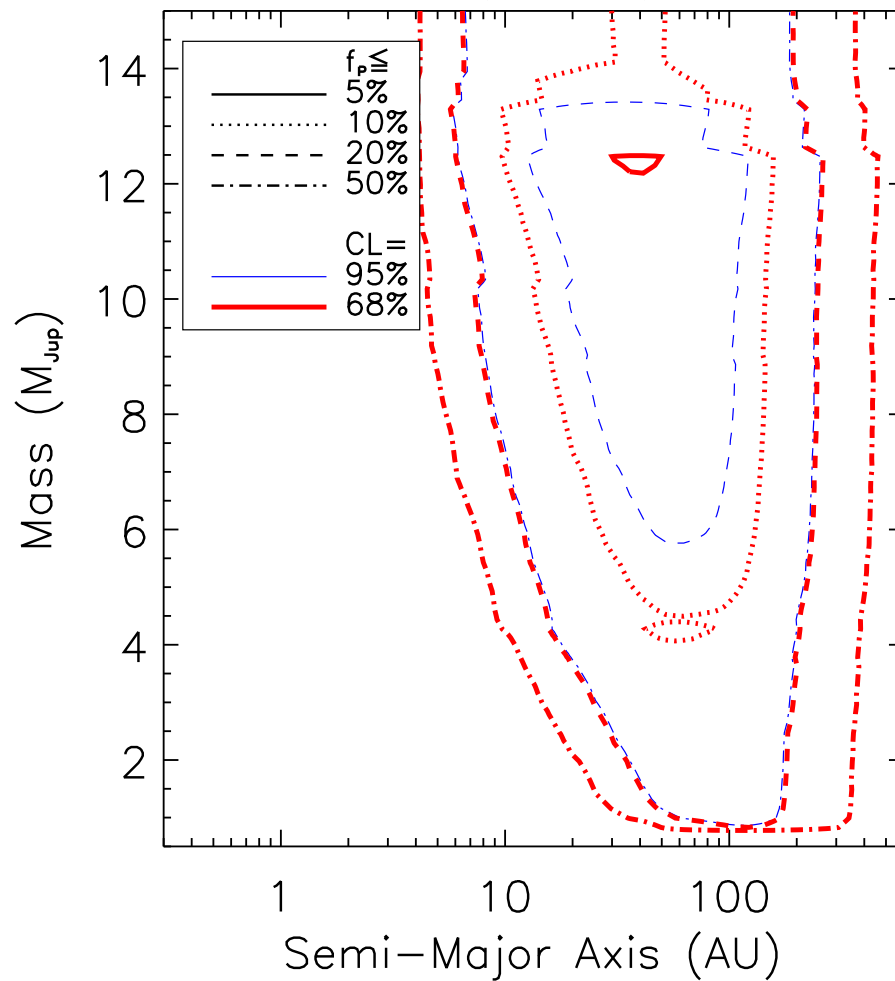


Figure 4.10 The 95% and 68% confidence upper limit on planet fraction, limited only to stars of spectral type A through K, using the Burrows et al. (2003) models. Since with earlier spectral types the parent star is intrinsically brighter, it becomes more difficult to access planets of smaller masses or smaller separations. For AFGK stars we can only say, at the 95% confidence level, that less than 20% of stars have $M > 7M_{Jup}$ planets at 30-70 AU, or a limit of 50% for planets with masses above $6 M_{Jup}$ at 10-200 AU.

Baraffe et al. (2003), AFGK Stars

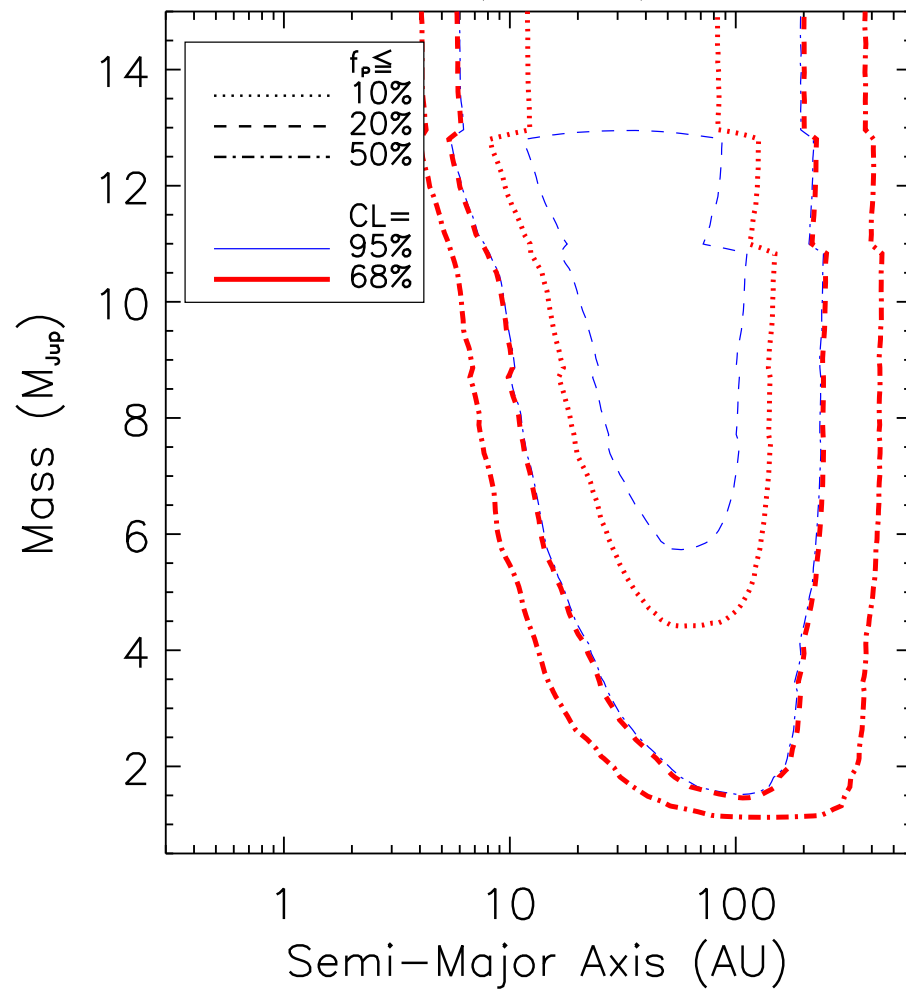


Figure 4.11 The same as Fig. 4.10, but with the Baraffe et al. (2003) models used to find planet masses.

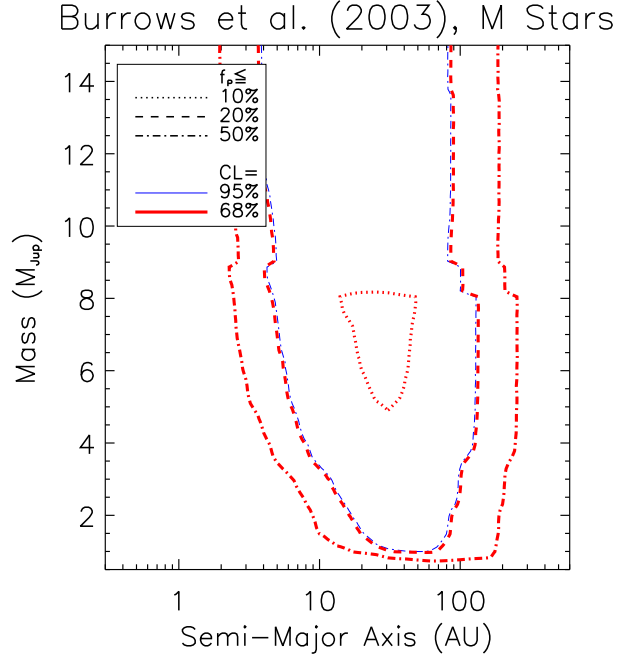


Figure 4.12 Now using only our 15 M stars, we again plot the 95% and 68% confidence level upper limit on planet fraction, using the Burrows et al. (2003) models. While the plot follows the shape of Fig. 4.8, the removal of about three-quarters of the target stars reduces the upper limit that can be set on the planet fraction. Hence less than 50% of M stars should have planets with $M > 4M_{Jup}$ from 10 to 80 AU, at 95% confidence. The analysis of microlensing results by Gaudi et al. (2002) sets upper limits on the planet fraction of M dwarfs in the galactic bulge of 45% for 3 M_{Jup} planets between 1 and 7 AU, and 33% for 1 M_{Jup} planets between 1.5 and 4 AU. While even our 50% contour (at the 68% confidence level) does not probe the area of parameter space considered by Gaudi et al. (2002), which places upper limits on 1 M_{Jup} planets between 1.5 and 4 AU around M dwarfs of $\leq 33\%$, and $\leq 45\%$ for 3 M_{Jup} planets between 1 and 7 AU, the microlensing upper limits are unsurprising given our limits at somewhat larger separations for planets of the same mass. Though we note that the composition (especially in terms of stellar metallicity) is likely to differ greatly between the two samples. Also, we again draw attention to the fact that Johnson et al. (2007) have shown that for M stars, giant planets at small radii are less common than around more massive stars.

Baraffe et al. (2003), M Stars

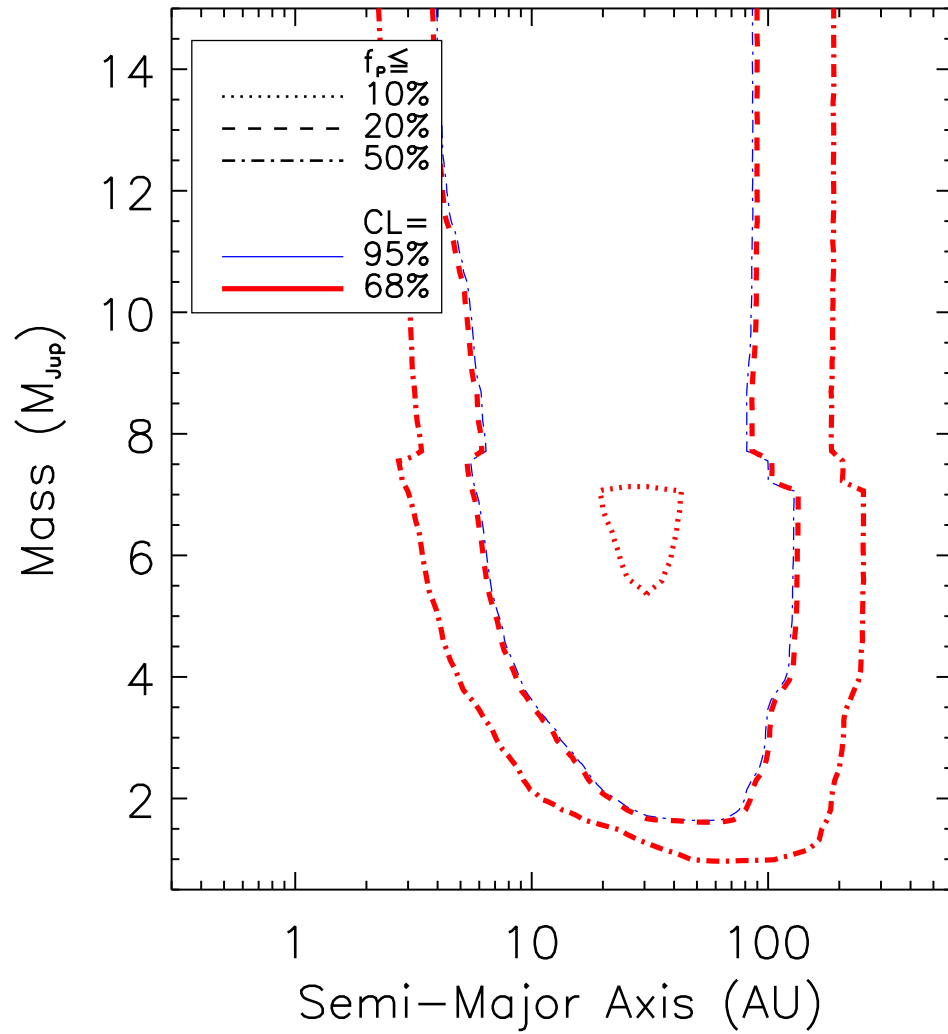


Figure 4.13 As with Fig. 4.12, only now with the Baraffe et al. (2003) models used to find planet masses.

law from currently-known extrasolar planets, $\frac{dN}{dM} \propto M^{-1.16}$ (Butler et al., 2006), we can constrain what types of power laws for semi-major axis are allowed by our survey null result. To accomplish this, we simulate planets using a grid of power law indices and upper cut-offs for semi-major axis for each of our target stars. Then, the sum of the detection fractions over the entire survey gives the expected number of detected planets, assuming each star has one planet (for example, if for 10 stars, we had a 50% chance of detecting a planet around each star, we'd expect to detect 5 planets after observing all 10 stars). Since we've set the distribution of planets, we can determine the actual planet fraction: radial velocity surveys tell us this value is 5.5% for planets more massive than $1.6 M_{Jup}$ and with periods shorter than 4 years (closer-in than 2.5 AU) (Fischer & Valenti, 2005). We can then use the mass and semi-major axis power laws to find the planet fraction for planets down to 0.5 Jupiter masses and out to the given semi-major axis cut-off, while always preserving the value of 5.5% for the planet fraction for planets $>1.6 M_{Jup}$ and <2.5 AU. Then, by multiplying this planet fraction by the sum of detection probabilities, we find the expected number of planets we'd detect given each distribution. At this point, we can again use the Poisson distribution to convert this to a confidence level (CL) for rejecting the model, given our null result: $CL = 1 - e^{-\mu}$, where μ is the expected number of planets for that model.

Since stellar multiplicity can disrupt planet formation, especially for small binary separations, we exclude all known stellar binaries from our target list with projected separations less than 200 AU. Since our results deal mainly with the inner 100 AU around our target stars, binaries that are any closer would greatly influence the formation of planets at these radii, creating an entirely different population. Bonavita & Desidera (2007) have shown that while the overall planet fraction (for radial velocity planets, as taken from the volume limited sample of

Fischer & Valenti (2005)) is similar between single stars and wide binaries, it decreases for stars in tight binary systems. Our inner cut-off on binary separation is at a larger separation than that noted in Bonavita & Desidera (2007), but we consider planets in much wider orbits than those detectable with the radial velocity method. Additionally, it has been shown by Quintana et al. (2002) and Holman & Wiegert (1999) that terrestrial planets could form and survive in the α Cen AB system, despite the relatively tight (23 AU), high eccentricity (0.5) orbit. Holman & Wiegert (1999) also found that for most cases, a planet is stable in a binary system if its orbital radius is less than $\sim 10\text{-}20\%$ of the binary separation. Applying this additional condition to our sample, we remove 1 star from the Masciadri et al. (2005) survey, and 9 from the Biller et al. (2007) sample, leaving 50 stars in our sample. We give further details on the binaries in our sample in Table 4.3.

In Fig. 4.14 and 4.15, we plot the confidence with which we can reject the model for various combinations of power law index and upper cut-off for the semi-major axis distribution. For the favored model of a power law distribution given by $\frac{dN}{da} \propto a^{-0.61}$, we can place, at the 95% confidence level, an upper-limit on the semi-major axis cut-off of 75 AU (94 AU using the models of Baraffe et al. (2003) instead of those of Burrows et al. (2003)). In other words, if the power law index has a value of -0.61, there can be no planets in orbits beyond $a=75$ AU at the 95% confidence level (29 AU at the 68% confidence level). In Fig. 4.16, we show how these assumptions of power law index compare with the distributions of known radial velocity planets, as well as to what confidence we can exclude various models.

4.4.4 Testing Core Accretion Models

We also consider more sophisticated models of planet populations, namely the core accretion models of Ida & Lin (2004). Using their Fig. 12, we extract all the

Table 4.3. Binaries

Target	Sep (")	Sep. (AU)	Reference	Companion Type
Biller et al. (2007)				
HIP 9141	0.15	6.38	Biller et al. (2007)	
V577 Per A	7	230	Pounds et al. (1993)	M0
AB Dor	9 (Ba/Bb)	134 (Ba/Bb)	Close et al. (2005)	Binary M stars
AB Dor	0.15 (C)	2.24 (C)	Close et al. (2005)	Very low-mass M Star
HIP 30034	5.5	250	Chauvin et al. (2005)	Planet/Brown Dwarf
HD 48189 A	0.76 (B)	16.5	Fabricius & Makarov (2000)	K star
HD 48189 A	0.14	3.03	Biller et al. (2007)	
DX Leo	65	1200	Lowrance et al. (2005)	M5.5
EK Dra	SB	SB	Metchev & Hillenbrand (2004)	M2
HD 135363	0.26	7.65	Biller et al. (2007)	
HD 155555 AB	SB (AB)	SB (AB)	Bennett et al. (1967)	G5 and K0 SB
HD 155555 AB	18 (C)	1060 (C)	Zuckerman et al. (2001a)	Target Star 155555 C, M4.5
HD 172555 A	71	2100	Simon & Drake (1993)	Target Star CD -64 1208, K7
HD 186704	13	380	Aitken & Doolittle (1932)	
GJ 799A	3.6	36	Wilson (1954)	Target Star GJ 799B, M4.5
HD 201091	16	55	Baize (1950)	K5
Eps Indi A	400	1500	McCaughrean et al. (2004)	Binary Brown Dwarf
HIP 112312	100	2400	Song et al. (2002)	M4.5
Masciadri et al. (2005)				
TWA 8A	13	270	Jayawardhana et al. (1999)	Target Star TWA 8B, M5
TWA 9A	9	576	Jayawardhana et al. (1999)	Target Star TWA 9B, M1
SAO 252852	15.7	260	Poveda et al. (1994)	HD 128898, Ap
V343 Nor	10	432	Song et al. (2003)	M4.5
BD-17 6128	2	100	Neuhäuser et al. (2002)	M2

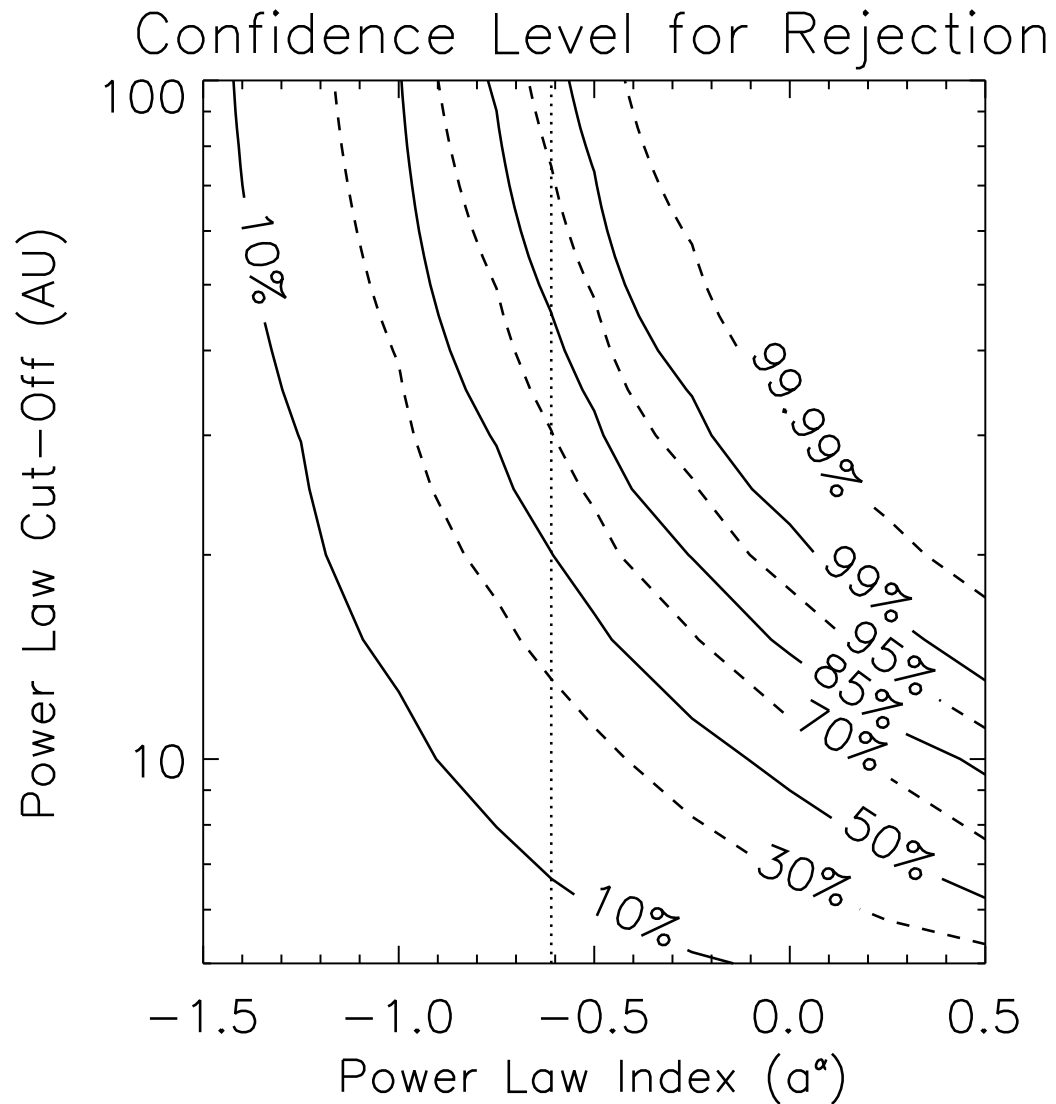


Figure 4.14 The confidence level with which we can reject models of planet populations, assuming a power-law distribution for semi-major axes ($\frac{dN}{da} \propto a^\alpha$), as a function of the power law index and upper cut-off ($N(a)=0$ for $a \geq a_{Cut-off}$). The expected power-law index from the radial velocity distribution (see Fig 4.6) is -0.61 (Cumming et al., 2008), and given these data we can place a 95% confidence limit on the upper cut-off of 75 AU. At 68% confidence, there cannot be giant planets in orbits beyond 29 AU, for this choice of power law index. For this figure, we use the models of Burrows et al. (2003)

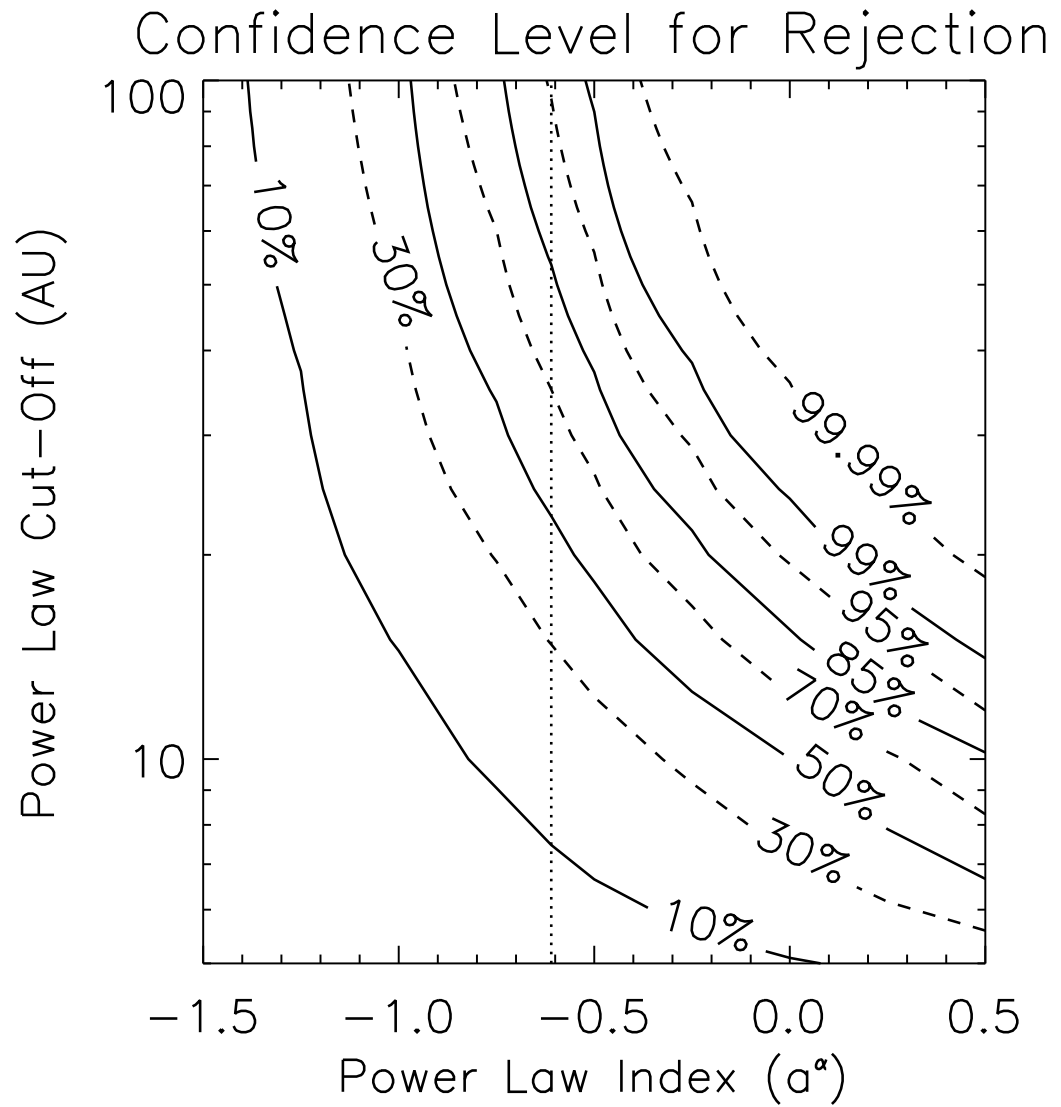


Figure 4.15 The same as Fig. 4.14, but using the models of Baraffe et al. (2003). The 95% confidence upper cut-off for semi-major axis for the $\frac{dN}{da} \propto a^\alpha$ model now moves to 94 AU.

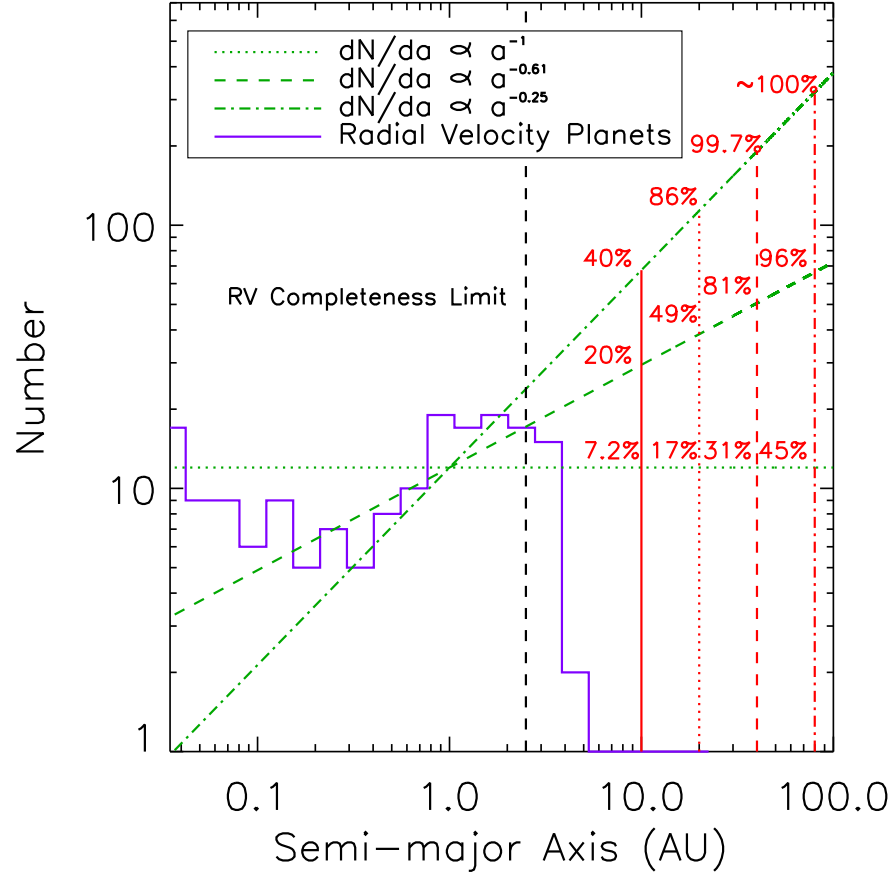


Figure 4.16 The histogram (in blue) of the distribution of known extrasolar giant planets found with the radial velocity method, plotted against a series of power laws considered in Fig. 4.14 and 4.15. Since radial velocity observations are only complete to about 2.5 AU, a less steep drop-off of planets with semi-major axis is possible. We give the confidence with which we can rule out various combinations of power law index and upper cut-off (the percentages in red), for indices of -1, -0.61, -0.25, and upper cut-offs of 10 AU, 20 AU, 40 AU, and 80 AU. While we have insufficient statistics to place strong constraints on the power law of index -1, we can rule out the other two with increasing confidence as larger values of the upper limit are considered. For example, a power law of the form $\frac{dN}{da} \propto a^{-0.25}$ must cut-off at 26 AU (95% confidence), while the most likely power law of index -0.61 must have its cut-off at 75 AU (also at the 95% confidence level).

non-Hot-Jupiter giant planets, and of the 200-300 resulting planets, we run our Monte Carlo simulation by, for each simulated planet, randomly selecting one planet from this figure, adopting its values of mass and semi-major axis, then assigning it the other orbital elements as usual. We consider each of the three cases modeled by Ida & Lin (2004).

In Fig. 4.17 we plot the predicted number of planets detected from these three distributions. Again, the planet fraction for each curve is set to match the planet fraction of Fischer & Valenti (2005) for planets above $1.6 M_{Jup}$ and within 2.5 AU. Since the predicted total number of planets detected range between about 0.6 and 0.7 at the end of our survey, we cannot place any strong constraints on these models from our null result. For the three cases of Ida & Lin (2004), A, B, and C, we can only “rule them out” at the confidence levels of 45%, 49%, and 50% respectively, and again only after leaving all binaries in the sample. Additionally, since we are considering target stars of all spectral type, we are not staying faithful to the original simulations of Ida & Lin (2004), which consider only solar mass host stars. In summary, the core-accretion simulations of Ida & Lin (2004) are quite consistent with our results.

4.5 Discussion: Systematic Effects of Models on Results and Other Work

We underscore the dependence of these results upon the accuracy of the mass-luminosity relations of Burrows et al. (2003) and Baraffe et al. (2003). In particular, these models utilize the “Hot Start” method for giant planet formation, at odds with the core accretion mechanism suggested by the planet-metallicity relation of Fischer & Valenti (2005). The giant planet models of Marley et al. (2007) incorporate formation by core accretion, and predict systematically fainter fluxes for these young planets (typically ~ 3 times fainter for a 30 Myr, $4 M_{Jup}$ planet,

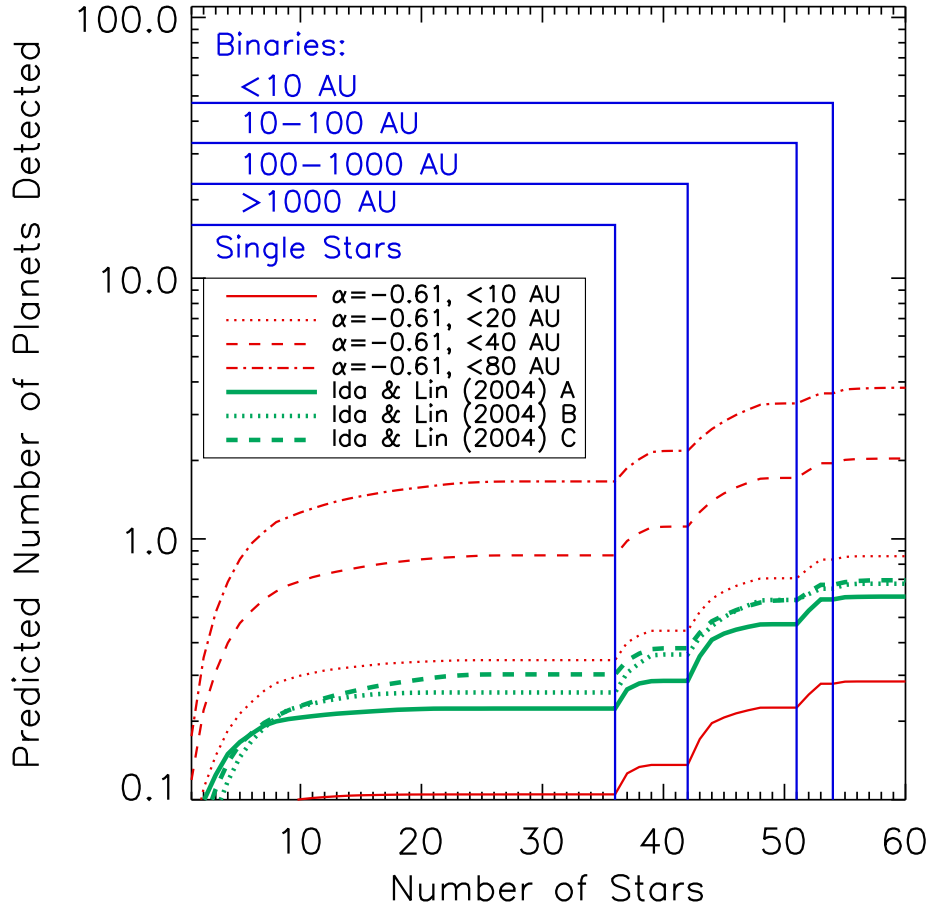


Figure 4.17 The number of planets we would expect to detect at the end of the survey, as a function of the number of target stars observed, out of our total sample of 60. Stars are divided into bins based on binarity, and within each bin the stars are arranged so that the best targets are observed first. The first four models use power laws with $\frac{dN}{da} \propto a^{-0.61}$, with the upper cut-off given. These models can be ruled out with increasing confidence with cut-offs beyond 40 AU as increasingly close binaries are added to the sample. Since the three Ida & Lin (2004) models predict less than one planet from our survey, we can only place very limited constraints on these models at this time, namely that cases A, B, and C are inconsistent with our null result at the 45%, 49%, and 50% confidence levels, respectively, if all binaries are included in our sample.

yet the overall effect is difficult to predict without detailed models and spectra). Another result of moving to these models, however, would be that these planets are also cooler, so that the SDI method (limited to objects with effective temperatures lower than 1400 K) will likely reach planets of higher masses than would be predicted by the models of Burrows et al. (2003) and Baraffe et al. (2003).

It is possible to envision a scenario with extrasolar planets being built by both disk instability (e.g. Boss (2007)) and core accretion, with the two types of planets segregated in orbital distance: inner planets being more common in orbit around metal-rich stars, consistent with core accretion, while outer planets (the type to which the surveys discussed here are sensitive) form by disk instability. In that case, the use of the Hot Start models would be entirely reasonable, as these models have been shown to be mostly consistent with young, low-mass objects that likely form in this way (e.g. Stassun et al. (2007), Close et al. (2007a)). This possibility (which we again note is pure speculation) endangers any conclusions drawn from Fig. 4.14 and 4.15, which assume a single, consistent population of planets, not allowing for the possibility of two overlapping populations (such as one described by broken power laws). Our results for the upper limit on planet fraction would remain valid, however, since these make no assumptions on extrasolar planet populations beyond the eccentricity distribution (a minor factor) and the mass-luminosity relation.

Clearly, these constraints would be stronger with a larger sample size to improve our statistics. Such an increase in sample size is hampered by the limited number of young, nearby stars: observing older targets tends to require an order of magnitude increase in number of targets so as to assure a similar number of detected planets. The greatest improvement in these results is likely to come with more advanced planet-finding instruments, which increase the contrast and

inner working angle to which one can detect planets close to their parent stars. Two such Extreme AO systems, slated to come online in the next several years, are VLT-SPHERE and the Gemini Planet Imager (GPI). Surveys of a sample of young, nearby stars (likely very similar to the target list of this work) with these planet-finders should be able to greatly close the gap between the sensitivities to planets of direct imaging and radial velocity surveys.

Additionally, new observing techniques, such as Angular Differential Imaging (Marois et al., 2008), or better data reduction techniques like LOCI (Lafrenière et al., 2007), will further improve achievable contrasts. Indeed, the power of LOCI to improve contrasts from high contrast imaging data suggests the possibility of re-reducing existing direct imaging datasets. The improved contrasts could potentially lead to discoveries of previously undetectable companions or, failing that, provide increased constraints on planet populations.

While radial velocity surveys continue to have great success in finding planets, the limiting factor is orbital time: a planet at 10 AU takes over 30 years to complete a single orbit, and radial velocity planets are generally not confirmable until at least one orbit has elapsed. As a result, the onus on determining the characteristics of giant planets beyond ~ 10 AU is largely upon direct imaging surveys.

A survey planned for the immediate future uses the NICI (Near Infrared Coronagraphic Imager) instrument currently being commissioned on the Gemini South Telescope, with plans for a 50-night survey for extrasolar giant planets. It is hoped, of course, that these future surveys will produce actual detections, not just more null results, which when considered alongside the targets that were not found to harbor planets, should continue to constrain parameter space on the distribution of outer extrasolar giant planets.

Another direct imaging survey for giant planets has recently been completed, searching for companions to 79 young, nearby stars: the Gemini Deep Planet Survey (Lafrenière et al., 2007). For completeness, we run an extra set of simulations to compare our results to theirs. Lafrenière et al. (2007) consider the case of planets with masses between 0.5 and $13 M_{Jup}$, governed by a power law of index -1.2 (quite similar to our value of -1.16), and with a power law of index -1 for semi-major axis. They then set an upper limit on the planet fraction in three ranges of semi-major axis: 28% for 10-25 AU, 13% for 25-50 AU, and 9.3% for 50-200 AU, all at the 95% confidence level, using the models of Baraffe et al. (2003). Adopting these same simulation parameters, we find upper limits on planet fractions of 37%, 24%, and 28%, respectively. We attribute our somewhat lower sensitivity to the increased number of stars in the Lafrenière et al. (2007) survey, as well as their increased field of view (9'' compared to the 2.2'' for SDI), which makes their method better-suited to detecting planets at the very large orbital radii of the last two bins. Also, the Lafrenière et al. (2007) survey was more consciously focused on closer stars: all 85 of their target stars are within 35 parsecs, 18 of our 60 stars are beyond 35 pc. The overall results of both our work and that of Lafrenière et al. (2007), however, are in good agreement for the case of planets in shorter orbits: for example, we reach the same upper limits as Lafrenière et al. (2007) reached at the 95% confidence level, if we degrade our confidence level to 89% for 10-25 AU, 80% for 25-50 AU, and 63% for 50-200 AU. Hence the conclusions from both works are the same: giant planets are rare at large separations.

We also note that the value of the planet fraction in these intervals can be estimated from the uniform detectability sample of Fischer & Valenti (2005), which gives 5.5% of stars having planets within 2.5 AU, and more massive than $1.6 M_{Jup}$. When using a model of planet mass with index -1.2, and semi-major axis

power law index -1, as above, the planet fractions for the semi-major axis bins 10-25 AU, 25-50 AU, and 50-200 AU become 2.1%, 1.6%, and 3.2%, respectively. It should be noted that the samples of Fischer & Valenti (2005) and Lafrenière et al. (2007) (as well as the one discussed in this Chapter, for that matter) are not directly comparable, as the Fischer & Valenti (2005) sample is made up primarily of older stars (>1 Gyr), and exclusively FGK spectral types, whereas the sample of Lafrenière et al. (2007) is made up of younger stars, and contains stars of M spectral type. These two effects push the planet fractions in opposite directions: younger stars are more likely to be metal-rich², and so have a higher planet fraction (Fischer & Valenti, 2005), whereas M stars are less likely to harbor giant planets (Johnson et al., 2007). Overall, then, the upper limits from both works are consistent with the predictions from radial velocity detections, with respect to this particular model of planet populations.

Finally, we note that although four of our target stars do, in fact, harbor extra-solar planets (HIP 30034 (AB Pic) has a wide (5.5'') companion at the planet/brown dwarf boundary, while Eps Eri, HD 81040, and HD 128311 all have radial velocity planets), our survey can be regarded as a null result. Even though these planets were orbiting our target stars, we were unable to detect them, as they were either outside our field of view (as with AB Pic B), or too faint (due to their host star's age) to be detected from our images, as was the case with the radial velocity planets. The motivation behind our simulations is to find what population of hidden (undetected) planets are consistent with a lack of planet detections, and the knowledge of existing planets around some target stars does not change this.

²Although Table 1 of Lafrenière et al. (2007) gives the metallicity for most of their target stars, which give a median value of $[\text{Fe}/\text{H}] = 0$, more metal poor than the overall sample of Fischer & Valenti (2005) by ~ 0.1 dex, it is notoriously difficult to make accurate metallicity measurements of young stars. As a result, it is likely that these reported metallicities are systematically lower than their actual values.

4.6 Conclusion

Even without detecting extrasolar planets from our surveys, the null results provide a basis for setting limits on the allowable distribution of giant planets. From our data, using the planet models of Burrows et al. (2003), we can exclude any model for planet distributions where more than 20% of stars of all spectral types have planets more massive than $4M_{Jup}$ between 20 and 100 AU, at 95% confidence (this upper limit becomes 8% of stars with such planets at the 68% confidence level). If we create simple models of planet populations with the semi-major axis distribution governed by the power law $\frac{dN}{da} \propto a^\alpha$, and mass by $\frac{dN}{dM} \propto M^{-1.16}$, we can exclude giant planets in the case of $\alpha = 0$ beyond 18 AU, and with $\alpha = -0.5$ beyond 48 AU. Using the distribution of Cumming et al. (2008), based on radial velocity observations, with $\alpha = -0.61$, there can be no giant planets beyond 75 AU. All these statements are at the 95% confidence level; for the 68% confidence level, these upper limits for the outer cut-offs of giant planets become 12 AU, 23 AU, and 29 AU, for power law indices of 0, -0.5, and -0.61, respectively. With our data, the most we can say of the models of Ida & Lin (2004) is that they are consistent with our observations at the $\sim 50\%$ confidence level. We again note that these conclusions are highly dependent on the models of planet luminosity as a function of the planet's age and mass. Additionally, we caution that since our sample differs from the volume-limited sample of Fischer & Valenti (2005), known correlations of planet fraction with stellar mass and metallicity will likely shift our results from the values reported here. Nevertheless, the analysis presented here is an important first step in constraining the populations of extrasolar giant planets.

4.7 Acknowledgments

We thank the anonymous referee for many helpful comments that have improved the quality of this work. We thank Eric Mamajek for a great deal of assistance both in selecting targets for the SDI survey, and determining the ages of our target stars. We thank Remi Soummer for the idea of presenting sensitivity to planets as a grid of mass and semi-major axis points, and we thank Daniel Apai for presenting the idea of constructing a grid of semi-major axis power law indices and cut-offs. We also thank Thomas Henning and Wolfgang Brandner for their important work in the original data gathering, and helpful comments over the course of the project. This work makes use of data from the European Southern Observatory, under Program 70.C - 0777D, 70.C - 0777E, 71.C-0029A, 74.C-0548, 74.C-0549, and 76.C-0094. Observations reported here were obtained at the MMT Observatory, a joint facility of the University of Arizona and the Smithsonian Institution. This publication makes use of data products from the Two Micron All-Sky Survey, which is a joint project of the University of Massachusetts and the Infrared Processing and Analysis Center/California Institute of Technology, funded by the National Aeronautics and Space Administration and the National Science Foundation. This research has made use of the SIMBAD database, operated at CDS, Strasburg, France. ELN is supported by a Michelson Fellowship. LMC is supported by an NSF CAREER award and the NASA Origins of the Solar System program. BAB is supported by the NASA GSRP grant NNG04GN95H and NASA Origins grant NNG05GL71G.

CHAPTER 5

A UNIFORM ANALYSIS OF 118 STARS WITH HIGH-CONTRAST
IMAGING: LONG PERIOD EXTRASOLAR GIANT PLANETS ARE RARE
AROUND SUN-LIKE STARS

We expand on the results of Nielsen et al. (2008), using the null result for giant extrasolar planets around the 118 target stars from the VLT NACO H and Ks band planet search (Masciadri et al., 2005), the VLT and MMT Simultaneous Differential Imaging (SDI) survey (Biller et al., 2007), and the Gemini Deep Planet Survey (Lafrenière et al., 2007) to set constraints on the population of giant extrasolar planets. Our analysis is extended to include the planet luminosity models of Fortney et al. (2008), as well as the correlation between stellar mass and frequency of giant planets found by Johnson et al. (2007). Doubling the sample size of FGKM stars strengthens our conclusions: a model for extrasolar giant planets with power-laws for mass and semi-major axis as given by Cumming et al. (2008) cannot, with 95% confidence, have planets beyond 65 AU, compared to the value of 94 AU reported in Nielsen et al. (2008), using the models of Baraffe et al. (2003). When the Johnson et al. (2007) correction for stellar mass (which gives fewer Jupiter-mass companions to M stars with respect to solar-type stars) is applied, however, this limit moves out to 82 AU. For the relatively new Fortney et al. (2008) models, which predict fainter planets across most of parameter space, these upper limits, with and without a correction for stellar mass, are 180 and 230 AU, respectively.

This Chapter is based on material originally published in Nielsen & Close (2010).

5.1 Introduction

There are currently close to 300 extrasolar planets known, most detected by the radial velocity method (Mayor & Udry, 2008; Marcy et al., 2008). These planets have provided a great deal of information on the distribution of giant planets in short period orbits. The likelihood of a star harboring a close-in giant planet increases with the metal abundance of the parent star (Fischer & Valenti, 2005; Santos et al., 2004), and power laws were found to accurately represent the distributions of mass and semi-major axis of exoplanets (Cumming et al., 2008). While radial velocity surveys have moved on to discovering and building up statistics on smaller Neptune-mass planets, direct imaging surveys continue to struggle to reach even the highest mass planets.

Many observing campaigns have been conducted in the last decade to detect and characterize planets through direct imaging, especially aimed at young target stars, when the self-luminosity of hosted planets is large enough to overcome the glare of the parent star. Improvements in adaptive optics and instrumentation designed solely to detect planets, as well as specialized observing techniques, have improved the contrasts achievable close to the target star. This has allowed a large increase in sensitivity to planets, and resulted in the discovery of several planetary-mass ($<13 M_{Jup}$) objects, including companions to 2MASS 1207-3932 (Chauvin et al., 2004), HIP 30034 (AB Pic) (Chauvin et al., 2005), Oph 1622 (Close et al., 2007; Brandeker et al., 2006; Luhman et al., 2007), and DH Tau (Itoh et al., 2005). These objects were discovered with projected separations of 42, 260, 243, and 330 AU, respectively. Few, if any, of these wide companions (>200 AU for objects found around stars) are likely to have formed in the primordial circumstellar disk of the primary.

Recently there have been exciting discoveries of planetary-mass objects around

the higher-mass A stars: HR 8799, Fomalhaut, and β Pic (Marois et al., 2008; Kalas et al., 2008; Lagrange et al., 2009). In the case of the triple planet system HR 8799, we know that the largest separation planet (HR 8799 b, with a projected separation of 68 AU) has the same parallax as the primary (Close & Males, 2009) and so it (and very likely HR 8799 c and d) formed together around the A5 star HR 8799. While this is an amazing system, in this study we concentrate on lower mass stars, more similar to the Sun.

Nielsen et al. (2008) presented null results from the direct imaging surveys for extrasolar giant planets of Masciadri et al. (2005) and Biller et al. (2007), using the contrast curves for each of 60 unique target stars to set constraints on the populations of extrasolar planets. We concluded that extrasolar giant planets are rare at large separations (>60 AU). Just prior to the publication of our work, Lafrenière et al. (2007) published the null results from the Gemini Deep Planet Survey (GDPS) for 85 stars, reaching conclusions very similar to ours. In this Chapter, we combine the samples from these three surveys, to improve the statistical constraints we can place on extrasolar giant planet populations.

Also since these past publications, two papers directly relevant to this analysis have been published, Johnson et al. (2007) compared radial velocity target stars of different masses, and found that less massive stars have a lower likelihood of hosting a giant planet ($>0.8 M_{Jup}$). Since direct imaging surveys lean heavily on the M stars in their samples (as these are intrinsically fainter, making the detection of close-in planets easier), we attempt here to estimate the corresponding decrease in the strength of earlier null results. Also, a new set of planet luminosity models has been published by Fortney et al. (2008), which differs from the popular “hot start” models of Burrows et al. (2003) and Baraffe et al. (2003) which had been previously utilized in such work. These new models are based heavily

on the “core accretion” model of planet formation, and tend to predict consistently fainter fluxes for giant planets, especially at the youngest ages and largest planet masses. In addition to significantly enlarging the sample, this Chapter takes into account the stellar mass dependence of planet frequency, and the new core accretion models of Fortney et al. (2008), to present more realistic constraints on the distribution of extrasolar giant planets around Sun-like stars.

5.2 Observations

5.2.1 VLT NACO H and Ks Imaging

Masciadri et al. (2005) carried out a survey of 28 young, nearby, late-type stars with the NACO adaptive optics system at the 8.2 meter Very Large Telescope (VLT). These observations have exposure times of order 30 minutes, with stars being observed in the H or Ks bands. For the 22 stars used (see Section 5.2.4) from the VLT NACO survey of Masciadri et al. (2005), the median target star is a 12 Myr old K7 star at 30 pc.

5.2.2 VLT NACO and MMT SDI

A survey of 54 young, nearby stars of a variety of spectral types (between A and M) was conducted between 2003 and 2005, with the results reported in Biller et al. (2007). This second survey used the Simultaneous Differential Imager (SDI) at the 6.5 meter MMT and the 8 meter VLT, an adaptive optics observational mode that allows higher contrasts by imaging simultaneously in narrow wavelength regions surrounding the $1.6\ \mu\text{m}$ methane feature seen in cool brown dwarfs and expected in extrasolar planets (Lenzen et al., 2004; Close et al., 2005) (Swain et al. (2008) have recently detected methane in the atmosphere of the transiting extrasolar planet HD 189733b). This allows the light from a hypothetical companion planet to be more easily distinguishable from the speckle noise floor (uncorrected

starlight), as the two will have very different spectral signatures in this region. This translates to higher sensitivity at smaller separations than the observations of Masciadri et al. (2005), which were conducted before the VLT SDI device was commissioned (see Fig. 14 of Biller et al. (2007) for a more detailed comparison of the two surveys). For most of these SDI targets, the star was observed for a total of 40 minutes of integration time, which includes a 33 degree roll in the telescope’s rotation angle, in order to separate super speckles—which are created within the instrument, and so will not rotate—from a physical companion, which will rotate on the sky (Biller et al., 2006) (this technique has been previously used frequently with HST observations, e.g. Schneider & Silverstone (2003)). The 50 stars used from the Biller et al. (2007) SDI survey have a median age, distance, and spectral type of 70 Myr, 24 pc, and K1, respectively.

5.2.3 Gemini Deep Planet Survey

At about the same time as the Biller et al. (2007) SDI survey, a direct imaging campaign was underway from the Gemini North telescope using the Altair AO system and NIRI camera, imaging in a narrow-band H filter with transmission between 1.54-1.65 μm . The observations were done using the Angular Differential Imaging (ADI) technique, which leaves the Cassegrain instrument rotator off during a sequence of exposures on the star, so that instrumental effects like super speckles will stay fixed, while physical companions (like planets) will rotate throughout the observation (Liu, 2004; Marois et al., 2006; Lafrenière et al., 2007). This technique is most effective at producing high contrasts at larger star-planet angular separations, with the contrasts achieved exceeding those with SDI (Biller et al., 2007) beyond $\sim 0.7''$. For the 71 of the 85 stars from the GDPS survey of Lafrenière et al. (2007) which we consider here, the median target star is a K0 star at a distance of 22 pc, with an age of 250 Myr. Hence, the target stars of this sur-

vey are somewhat closer and older, whereas the southern VLT SDI survey was focused on more distant, though younger, stars.

5.2.4 Target Stars

Between the three surveys listed above, our analysis considers 118 distinct target stars, with some overlap between surveys. General properties of the target stars, including name, position, distance, spectral type, age, fluxes, and observation method are given in Table 5.1. We attempt to derive ages in a uniform manner for all target stars, using the same method as in Nielsen et al. (2008). If the star is a member of a known moving group, the age of that group is adopted as the age of the star. We limit moving group identifications to the well-studied and established groups AB Dor, Her/Lyr, Tuc/Hor, β Pic, and TW Hya. Membership in more controversial associations, such as the Local Association and IC 2391 (e.g. Fernández et al. (2008)), are not adopted here. If the star is not a member of a group, but has a measured value of the calcium emission indicator R'_{HK} and a measurement of the equivalent width of the lithium absorption at 6708 Å, the average of the ages from the two methods is used. If only one of these two spectral age indicators is available, the age from that measurement is used. If a star from any of the three surveys has none of these three sources for an age estimate, it is simply not used in this work. As a result, 6 stars from the Masciadri et al. (2005) survey, 1 star from the Biller et al. (2007) survey, and 14 stars from the Lafrenière et al. (2007) survey were dropped.

Table 5.1. Target Stars

Target	RA ¹	Dec ¹	Distance (pc) ²	Sp. Type	Age (Myr)	V ¹	H ³	Ks ³	Obs. Mode ⁴
Biller et al. (2007)									
HIP 1481	00 18 26.1	-63 28 39.0	40.95	F8/G0V	30	7.46	6.25	6.15	VLT SDI
HD 8558	01 23 21.2	-57 28 50.7	49.29	G6V	30	8.54	6.95	6.85	VLT SDI
HD 9054	01 28 08.7	-52 38 19.2	37.15	K1V	30	9.35	6.94	6.83	VLT SDI
HIP 9141	01 57 48.9	-21 54 05.0	42.35	G3/G5V	30	8.11	6.55	6.47	VLT SDI
BD+05 378	02 41 25.9	+05 59 18.4	40.54	M0	12	10.20	7.23	7.07	VLT SDI
HD 17925	02 52 32.1	-12 46 11.0	10.38	K1V	200	6.05	4.23	4.17	VLT SDI/GDPS
Eps Eri	03 32 55.8	-09 27 29.7	3.22	K2V	1100	3.73	1.88	1.78	VLT SDI/GDPS
V577 Per A	03 33 13.5	+46 15 26.5	33.77	G5IV/V	70	8.35	6.46	6.37	MMT SDI
GJ 174	04 41 18.9	+20 54 05.4	13.49	K3V	280	7.98	5.31	5.15	VLT SDI
GJ 182	04 59 34.8	+01 47 00.7	26.67	M1Ve	12	10.10	6.45	6.26	VLT SDI/Ks/GDPS
HIP 23309	05 00 47.1	-57 15 25.5	26.26	M0/1	12	10.09	6.43	6.24	VLT SDI/Ks
AB Dor	05 28 44.8	-65 26 54.9	14.94	K2Vk	70	6.93	4.84	4.69	VLT SDI
UY Pic	05 36 56.8	-47 57 52.9	23.87	K0V	70	7.95	5.93	5.81	VLT SDI
AO Men	06 18 28.2	-72 02 41.4	38.48	K6/7	12	10.99	6.98	6.81	VLT SDI/Ks
HIP 30030	06 19 08.1	-03 26 20.0	52.36	G0V	30	8.00	6.59	6.55	MMT SDI
HIP 30034	06 19 12.9	-58 03 16.0	45.52	K2V	30	9.10	7.09	6.98	VLT SDI
HD 45270	06 22 30.9	-60 13 07.1	23.50	G1V	70	6.50	5.16	5.05	VLT SDI
HD 48189 A	06 38 00.4	-61 32 00.2	21.67	G1/G2V	70	6.15	4.75	4.54	VLT SDI
pi01 UMa	08 39 11.7	+65 01 15.3	14.27	G1.5V	200	5.63	4.28	4.17	MMT SDI/GDPS
HD 81040	09 23 47.1	+20 21 52.0	32.56	G0V	2500	7.74	6.27	6.16	MMT SDI
LQ Hya	09 32 25.6	-11 11 04.7	18.34	K0V	13	7.82	5.60	5.45	MMT/VLT SDI/Ks/GDPS
DX Leo	09 32 43.7	+26 59 18.7	17.75	K0V	200	7.01	5.24	5.12	MMT/VLT SDI/GDPS
HD 92945	10 43 28.3	-29 03 51.4	21.57	K1V	70	7.76	5.77	5.66	VLT SDI/GDPS
GJ 417	11 12 32.4	+35 48 50.7	21.72	G0V	200	6.41	5.02	4.96	MMT SDI/GDPS
TWA 14	11 13 26.5	-45 23 43.0	46.00 ⁵	M0	10	13.00	8.73	8.49	VLT SDI
TWA 25	12 15 30.8	-39 48 42.0	44.00 ⁵	M0	10	11.40	7.50	7.31	VLT SDI
RXJ1224.8-7503	12 24 47.3	-75 03 09.4	24.17	K2	16	10.51	7.84	7.71	VLT SDI
HD 114613	13 12 03.2	-37 48 10.9	20.48	G3V	8800	4.85	3.35	3.30	VLT SDI
HD 128311	14 36 00.6	+09 44 47.5	16.57	K0	630	7.51	5.30	5.14	MMT SDI
EK Dra	14 39 00.2	+64 17 30.0	33.94	G0	70	7.60	6.01	5.91	MMT SDI/GDPS
HD 135363	15 07 56.3	+76 12 02.7	29.44	G5V	3	8.72	6.33	6.19	MMT SDI/GDPS
KW Lup	15 45 47.6	-30 20 55.7	40.92	K2V	2	9.37	6.64	6.46	VLT SDI
HD 155555 AB	17 17 25.5	-66 57 04.0	30.03	G5IV	12	7.20	4.91	4.70	VLT SDI/Ks
HD 155555 C	17 17 27.7	-66 57 00.0	30.03	M4.5	12	12.70	7.92	7.63	VLT SDI/Ks
HD 166435	18 09 21.4	+29 57 06.2	25.24	G0	110	6.85	5.39	5.32	MMT SDI
HD 172555 A ⁶	18 45 26.9	-64 52 16.5	29.23	A5IV/V	12	4.80	4.25	4.30	VLT SDI
CD -64 1208	18 45 37.0	-64 51 44.6	34.21	K7	12	10.12	6.32	6.10	VLT SDI/Ks
HD 181321	19 21 29.8	-34 59 00.5	20.86	G1/G2V	160	6.48	5.05	4.93	VLT SDI
HD 186704	19 45 57.3	+04 14 54.6	30.26	G0	210	7.03	5.62	5.52	MMT SDI
GJ 799B	20 41 51.1	-32 26 09.0	10.22	M4.5e	12	11.00	5.20	-99.00	VLT SDI/Ks
GJ 799A	20 41 51.2	-32 26 06.6	10.22	M4.5e	12	10.25	5.20	4.94	VLT SDI/Ks
GJ 803	20 45 09.5	-31 20 27.1	9.94	M0Ve	12	8.81	4.83	4.53	VLT SDI/Ks/GDPS
HD 201091	21 06 53.9	+38 44 57.9	3.48	K5Ve	2000	5.21	2.54	2.25	MMT SDI
Eps Indi A	22 03 21.7	-56 47 09.5	3.63	K5Ve	4000	4.69	2.35	2.24	VLT SDI

Table 5.1—Continued

Target	RA ¹	Dec ¹	Distance (pc) ²	Sp. Type	Age (Myr)	V ¹	H ³	Ks ³	Obs. Mode ⁴
GJ 862	22 29 15.2	-30 01 06.4	15.45	K5V	6300	7.65	5.28	5.11	VLT SDI
HIP 112312 A	22 44 57.8	-33 15 01.0	23.61	M4e	12	12.20	7.15	6.93	VLT SDI
HD 224228	23 56 10.7	-39 03 08.4	22.08	K3V	70	8.20	6.01	5.91	VLT SDI
Masciadri et al. (2005)									
HIP 2729	00 34 51.2	-61 54 58	45.91	K5V	30	9.56	6.72	6.53	VLT Ks
BD +2 1729	07 39 23.0	02 11 01	14.87	K7	200	9.82	6.09	5.87	VLT H/GDPS
TWA 6	10 18 28.8	-31 50 02	77.00 ⁵	K7	10	11.62	8.18	8.04	VLT Ks
BD +1 2447	10 28 55.5	00 50 28	7.23	M2	70	9.63	5.61	5.31	VLT H/GDPS
TWA 8A	11 32 41.5	-26 51 55	21.00 ⁵	M2	10	12.10	7.66	7.43	VLT Ks
TWA 8B	11 32 41.5	-26 51 55	21.00 ⁵	M5	10	15.20	9.28	9.01	VLT Ks
TWA 9A	11 48 24.2	-37 28 49	50.33	K5	10	11.26	8.03	7.85	VLT Ks
TWA 9B	11 48 24.2	-37 28 49	50.33	M1	10	14.10	9.38	9.15	VLT Ks
SAO 252852	14 42 28.1	-64 58 43	16.40 ⁷	K5V	200	8.47	5.69	5.51	VLT H
V343 Nor	15 38 57.6	-57 42 27	39.76	K0V	12	8.14	5.99	5.85	VLT Ks
PZ Tel	18 53 05.9	-50 10 50	49.65	K0Vp	12	8.42	6.49	6.37	VLT Ks
BD-17 6128	20 56 02.7	-17 10 54	47.70	K7	12	10.60	7.25	7.04	VLT Ks
Lafrenière et al. (2007)									
HD 166	00 06 36.7839	+29 01 17.406	13.70	K0V	200	6.13	4.63	4.31	GDPS
HD 691	00 11 22.4380	+30 26 58.470	34.10	K0V	260	7.96	6.26	6.18	GDPS
HD 1405	00 18 20.890	+30 57 22.23	30.60	K2V	70	8.60	6.51	6.39	GDPS
HD 5996	01 02 57.2224	+69 13 37.415	25.80	G5V	440	7.67	5.98	5.90	GDPS
HD 9540	01 33 15.8087	-24 10 40.662	19.50	K0V	2900	6.96	5.27	5.16	GDPS
HD 10008	01 37 35.4661	-06 45 37.525	23.60	G5V	200	7.66	5.90	5.75	GDPS
HD 14802	02 22 32.5468	-23 48 58.774	21.90	G0V	5200	5.19	3.71	3.74	GDPS
HD 16765	02 41 13.9985	-00 41 44.351	21.60	F7IV	290	5.71	4.64	4.51	GDPS
HD 17190	02 46 15.2071	+25 38 59.636	25.70	K1IV	4300	7.81	6.00	5.87	GDPS
HD 17382	02 48 09.1429	+27 04 07.075	22.40	K1V	430	7.62	5.69	5.61	GDPS
HD 18803	03 02 26.0271	+26 36 33.263	21.20	G8V	4400	6.72	5.02	4.95	GDPS
HD 19994	03 12 46.4365	-01 11 45.964	22.40	F8V	6200	5.06	3.77	3.75	GDPS
HD 20367	03 17 40.0461	+31 07 37.372	27.10	G0V	380	6.41	5.12	5.04	GDPS
2E 759	03 20 49.50	-19 16 10.0	27.00	K7V	200	10.26	7.66	7.53	GDPS
HIP 17695	03 47 23.3451	-01 58 19.927	16.30	M3e	70	11.59	7.17	6.93	GDPS
HD 25457	04 02 36.7449	-00 16 08.123	19.20	F5V	70	5.38	4.34	4.18	GDPS
HD 283750	04 36 48.2425	+27 07 55.897	17.90	K2	300	8.42	5.40	5.24	GDPS
HD 30652	04 49 50.4106	+06 57 40.592	8.00	F6V	4500	3.19	1.76	1.60	GDPS
HD 75332	08 50 32.2234	+33 17 06.189	28.70	F7V	270	6.22	5.03	4.96	GDPS
HD 77407	09 03 27.0820	+37 50 27.520	30.10	G0	120	7.10	5.53	5.44	GDPS
HD 78141	09 07 18.0765	+22 52 21.566	21.40	K0	270	7.99	5.92	5.78	GDPS
HD 90905	10 29 42.2296	+01 29 28.025	31.60	G0V	230	6.90	5.60	5.52	GDPS
HD 91901	10 36 30.7915	-13 50 35.817	31.60	K2V	1000	8.75	6.64	6.57	GDPS
HD 93528	10 47 31.1553	-22 20 52.927	34.90	K1V	310	8.36	6.56	6.51	GDPS
HIP 53020	10 50 52.0645	+06 48 29.336	5.60	M4	200	11.66	6.71	6.37	GDPS
HD 96064	11 04 41.4733	-04 13 15.924	24.60	G8V	250	8.41	5.90	5.80	GDPS
HD 102392	11 47 03.8343	-11 49 26.573	24.60	K4.5V	3400	9.05	6.36	6.19	GDPS
HD 105631	12 09 37.2563	+40 15 07.399	24.30	K0V	1500	8.26	5.70	5.60	GDPS

In order to determine ages from the R'_{HK} value, we utilize the polynomial fit derived by Mamajek & Hillenbrand (2008). The authors derive their relation from R'_{HK} values of young clusters, and find a precision of 0.2 dex for ages derived from this relation.

For lithium values, we compare the equivalent width of the 6707 Å lithium line and effective temperature of the star to a set of young stellar clusters. For each cluster (NGC 2264 - 3 Myr (Soderblom et al., 1999), IC 2602 - 50 Myr (Randich et al., 2001), Pleiades - 125 Myr (Soderblom et al., 1993a), M34 - 250 Myr (Jones et al., 1997), Ursa Majoris - 300 Myr (Soderblom et al., 1993b), M67 - 5200 Myr (Jones et al., 1999)), the mean lithium equivalent width is fit as a function of effective temperature. Then, for our target stars, we interpolate between the fits to each cluster for that star's effective temperature, and the lithium value gives us the age (E. Mamajek private communication).

For target stars with both a lithium and an R'_{HK} age measurement, the median scatter between the two is a factor of 3. When we consider stars in our target list that belong to a single moving group (e.g. AB Dor or β Pic), and compute their ages using only the lithium or R'_{HK} method (that is, we temporarily ignore their membership in a group), we find the scatter in the computed age, between members of the same moving group, to also be about a factor of 3. This suggests that the noise in our age measurements is primarily astrophysical in nature. While finding a precise age for any single target star is notoriously difficult, our hope is that by using a large sample of stars the individual errors will average out of our final results.

Table 5.1—Continued

Target	RA ¹	Dec ¹	Distance (pc) ²	Sp. Type	Age (Myr)	V ¹	H ³	Ks ³	Obs. Mode ⁴
HD 107146	12 19 06.5015	+16 32 53.869	28.50	G2V	190	7.07	5.61	5.54	GDPS
HD 108767 B	12 29 50.908	-16 31 14.99	26.90	K2V	140	8.51	6.37	6.24	GDPS
HD 109085	12 32 04.2270	-16 11 45.627	18.20	F2V	100	4.31	3.37	3.37	GDPS
BD +60 1417	12 43 33.2724	+60 00 52.656	17.70	K0	270	9.40	7.36	7.29	GDPS
HD 111395	12 48 47.0484	+24 50 24.813	17.20	G5V	1000	6.31	4.70	4.64	GDPS
HD 113449	13 03 49.6555	-05 09 42.524	22.10	K1V	70	7.69	5.67	5.51	GDPS
HD 116956	13 25 45.5321	+56 58 13.776	21.90	G9V	710	7.29	5.48	5.41	GDPS
HD 118100	13 34 43.2057	-08 20 31.333	19.80	K4.5V	280	9.31	6.31	6.12	GDPS
HD 124106	14 11 46.1709	-12 36 42.358	23.10	K1V	1700	7.92	5.95	5.86	GDPS
HD 130004	14 45 24.1821	+13 50 46.734	19.50	K2.5V	5100	7.60	5.67	5.61	GDPS
HD 130322	14 47 32.7269	-00 16 53.314	29.80	K0III	2900	8.05	6.32	6.23	GDPS
HD 130948	14 50 15.8112	+23 54 42.639	17.90	G2V	420	5.88	4.69	4.46	GDPS
HD 139813	15 29 23.5924	+80 27 00.961	21.70	G5	270	7.31	5.56	5.45	GDPS
HD 141272	15 48 09.4630	+01 34 18.262	21.30	G9V	280	7.44	5.61	5.50	GDPS
HIP 81084	16 33 41.6081	-09 33 11.954	31.93	K9Vkee	70	11.29	7.78	7.55	GDPS
HD 160934	17 38 39.6261	+61 14 16.125	24.54	K7	70	10.18	7.00	6.81	GDPS
HD 166181	18 08 16.030	+29 41 28.12	32.58	G5V	60	7.70	5.61	5.61	GDPS
HD 167605	18 09 55.5001	+69 40 49.788	30.96	K2V	500	8.60	6.45	6.33	GDPS
HD 187748	19 48 15.4478	+59 25 22.446	28.37	G0	140	6.66	5.32	5.26	GDPS
HD 201651	21 06 56.3893	+69 40 28.548	32.84	K0	6800	8.20	6.41	6.34	GDPS
HD 202575	21 16 32.4674	+09 23 37.772	16.17	K3V	700	7.91	5.53	5.39	GDPS
HIP 106231	21 31 01.7137	+23 20 07.374	25.06	K3Vke	70	9.24	6.52	6.38	GDPS
HD 206860	21 44 31.3299	+14 46 18.981	18.39	G0VCH-0.5	200	6.00	4.60	4.56	GDPS
HD 208313	21 54 45.0401	+32 19 42.851	20.32	K2V	6400	7.78	5.68	5.59	GDPS
V383 Lac	22 20 07.0258	+49 30 11.763	10.68	K0	40	8.57	6.58	6.51	GDPS
HD 213845	22 34 41.6369	-20 42 29.577	22.74	F5V	200	5.20	4.27	4.33	GDPS
HIP 114066	23 06 04.8428	+63 55 34.359	24.94	M0	70	10.87	7.17	6.98	GDPS
HD 220140	23 19 26.6320	+79 00 12.666	19.74	K2V _k	85	7.73	5.51	5.40	GDPS
HD 221503	23 32 49.3999	-16 50 44.307	13.95	K6V _k	550	8.60	5.61	5.47	GDPS
HIP 117410	23 48 25.6931	-12 59 14.849	27.06	K5V _{ke}	55	9.57	6.49	6.29	GDPS

¹ from the CDS Simbad service² derived from the Hipparcos survey Perryman et al. (1997)³ from the 2MASS Survey Cutri et al. (2003)⁴ In cases where target stars were observed by multiple surveys, the star is listed only in the first section of this table where it appears, either in the Biller et al. (2007) or Masciadri et al. (2005) section, with Observing Mode given as “VLT SDI/Ks” or “VLT H/GDPS,” for example.⁵ Distance from Song et al. (2003)⁶ As this is the only star in our sample earlier than F2, we consider this work to be a survey of FGKM stars.⁷ Distance from Zuckerman et al. (2001a)

Table 5.2. Age Determination for Target Stars

Target	Sp. Type*	Li EW (mÅ)*	Li Age (Myr)	R'_{HK} *	R'_{HK} Age ⁺⁺	Group Membership ¹	Group Age ¹	Adopted Age ⁺⁺⁺
Biller et al. (2007)								
HIP 1481	F8/G0V ²	129 ³	100	-4.360 ⁴	221	Tuc/Hor	30	30
HD 8558	G6V ²	205 ⁵	13			Tuc/Hor	30	30
HD 9054	K1V ²	170 ⁵	160	-4.236 ⁶	100	Tuc/Hor	30	30
HIP 9141	G3/G5V ⁷	181 ⁸	13			Tuc/Hor	30	30
BD+05 378	M0 ⁹					β Pic	12	12
HD 17925	K1V ⁷	194 ⁸	50	-4.357 ⁶	216	Her/Lyr	200	200
Eps Eri	K2V ¹⁰			-4.598 ⁶	1129 ⁺			1100
V577 Per A	G5IV/V ¹¹	219 ¹¹	3			AB Dor	70	70
GJ 174	K3V ¹²	45 ⁸	280	-4.066 ¹³				280
GJ 182	M1Ve ¹⁴	280 ¹⁵	12					12
HIP 23309	M0/1 ¹⁶	294 ¹⁶	12	-3.893 ⁶		β Pic	12	12
AB Dor	K2Vk ¹⁷	267 ⁸	10	-3.880 ⁶	<50	AB Dor	70	70
UY Pic	K0V ¹⁸	263 ⁸	10	-4.234 ⁶	78	AB Dor	70	70
AO Men	K6/7 ¹⁶	357 ¹⁶	6	-3.755 ⁶		β Pic	12	12
HIP 30030	G0V ¹⁹	219 ⁸	2			Tuc/Hor	30	30
HIP 30034	K2V ²					Tuc/Hor	30	30
HD 45270	G1V ²	149 ⁵	90	-4.378 ⁶	254	AB Dor	70	70
HD 48189 A	G1/G2V ²	145 ⁸	25	-4.268 ⁶	105	AB Dor	70	70
π101 UMa	G1.5V ²⁰	135 ⁸	100	-4.400 ²¹	300			200
HD 81040	G0V ²⁰	24 ²²	2500					2500
LQ Hya	K0V ²⁰	247 ⁸	13					13
DX Leo	K0V ²⁰	180 ⁸	100	-4.234 ⁶	78	Her/Lyr	200	200
HD 92945	K1V ²⁰	138 ⁸	160	-4.393 ⁶	285	AB Dor	70	70
GJ 417	G0V ²³	76 ²⁴	250	-4.368 ¹³	235	Her/Lyr	200	200
TWA 14	M0 ²⁵	600 ²⁵	8			TW Hya	10	10
TWA 25	M0 ⁹	494 ²⁶	10			TW Hya	10	10
RXJ1224.8-7503	K2 ²⁷	250 ²⁷	16					16
HD 114613	G3V ²⁸	100 ²⁹	400	-5.118 ⁶	7900			8800
HD 128311	K0 ²⁰			-4.489 ¹³	565			630
EK Dra	G0 ³⁰	212 ⁸	2	-4.106 ¹³	<50	AB Dor	70	70
HD 135363	G5V ²⁰	220 ⁸	3					3
KW Lup	K2V ²⁸	430 ³¹	2					2
HD 155555 AB	G5IV ¹⁶	205 ⁸	6	-3.965 ⁶	<50	β Pic	12	12
HD 155555 C	M4.5 ¹⁶					β Pic	12	12
HD 166435	G0 ³²			-4.270 ²¹	107			110
HD 172555 A	A5IV/V ²					β Pic	12	12
CD -64 1208	K7 ¹⁶	580 ¹⁶	5			β Pic	12	12
HD 181321	G1/G2V ²⁸	131 ⁸	79	-4.372 ⁶	243			160
HD 186704	G0 ³³			-4.350 ²¹	205			210
GJ 799B	M4.5e ³⁴					β Pic	12	12
GJ 799A	M4.5e ³⁴					β Pic	12	12
GJ 803	M0Ve ³⁴	51 ⁸	30			β Pic	12	12
HD 201091	K5Ve ³⁴			-4.704 ¹³	2029 ⁺			2000
Eps Indi A	K5Ve ³⁴			-4.851 ⁶	3964 ⁺			4000

Table 5.2—Continued

Target	Sp. Type*	Li EW (mÅ)*	Li Age (Myr)	R' _{HK} *	R' _{HK} Age ⁺⁺	Group Membership ¹	Group Age ¹	Adopted Age ⁺⁺⁺
GJ 862	K5V ³⁴			-4.983 ⁶	6280 ⁺			6300
HIP 112312 A	M4e ⁹					β Pic	12	12
HD 224228	K3V ²⁸	53 ⁸	630	-4.468 ⁶		AB Dor	70	70
Masciadri et al. (2005)								
HIP 2729	K5V ²					Tuc/Hor	30	30
BD +2 1729	K7 ²⁰					Her/Lyr	200	200
TWA 6	K7 ³⁵	560 ³⁵	3			TW Hya	10	10
BD +1 2447	M2 ³⁶					AB Dor	70	70
TWA 8A	M2 ³⁵	530 ³⁵	3			TW Hya	10	10
TWA 8B	M5 ³⁵	560 ³⁵	3			TW Hya	10	10
TWA 9A	K5 ³⁵	460 ³⁵	3			TW Hya	10	10
TWA 9B	M1 ³⁵	480 ³⁵	3			TW Hya	10	10
SAO 252852	K5V ³⁷					Her/Lyr	200	200
V343 Nor	K0V ²	300 ²⁹	5	-4.159 ⁶	40	β Pic	12	12
PZ Tel	K0Vp ¹⁸	267 ³⁸	20	-3.780 ⁴	<50	β Pic	12	12
BD-17 6128	K7 ³⁹	400 ⁴⁰	3			β Pic	12	12
Lafrenière et al. (2007)								
HD 166	K0V ⁴¹	74 ⁴²	290	-4.458 ¹³	460	Her/Lyr	200	200
HD 691	K0V ⁴³	110 ⁸	260	-4.380 ²¹	260			260
HD 1405	K2V ⁴⁴	271 ⁴⁵				AB Dor	70	70
HD 5996	G5V ⁴⁶			-4.454 ¹³	440			440
HD 9540	K0V ⁷			-4.774 ⁶	2900			2900
HD 10008	G5V ⁴⁷	103 ⁴⁸	280	-4.530 ¹³	740	Her/Lyr	200	200
HD 14802	G0V ¹⁷	51 ⁴⁹	4000	-4.985 ⁶	6300			5200
HD 16765	F7IV ⁵⁰	73 ¹⁴	270	-4.400 ¹³	300			290
HD 17190	K1IV ⁵¹			-4.870 ²¹	4300			4300
HD 17382	K1V ⁵¹			-4.450 ²¹	430			430
HD 18803	G8V ⁵²			-4.880 ²¹	4400			4400
HD 19994	F8V ⁵³	12 ⁵⁴	8000	-4.880 ²¹	4400			6200
HD 20367	G0V ⁵⁵	113 ⁸	150	-4.500 ²¹	610			380
2E 759	K7V ⁵⁶	63 ⁵⁷	260			Her/Lyr	200	200
HIP 17695	M3e ⁵⁸					AB Dor	70	70
HD 25457	F5V ⁵⁹	91 ⁶⁰	80	-4.390 ²¹	280	AB Dor	70	70
HD 283750	K2 ⁶¹	33 ⁸	300	-4.057 ¹³				300
HD 30652	F6V ⁶²	15 ¹⁴	7500	-4.650 ²¹	1500			4500
HD 75332	F7V ⁵⁰	125 ⁸	50	-4.470 ²¹	500			270
HD 77407	G0 ⁶³	162 ⁴⁵	50	-4.340 ²¹	190			120
HD 78141	K0 ⁶⁴	107 ⁸	270					270
HD 90905	G0V ⁶⁵	136 ⁸	80	-4.430 ²¹	370			230
HD 91901	K2V ⁷	7 ⁶⁶	1000					1000
HD 93528	K1V ¹⁷	100 ⁸	260	-4.424 ⁶	360			310
HIP 53020	M4 ⁶⁷					Her/Lyr	200	200
HD 96064	G8V ⁶⁸	114 ⁸	250	-4.373 ¹³	250			250
HD 102392	K4.5V ¹⁷			-4.811 ⁶	3400 ⁺			3400
HD 105631	K0V ⁶⁹			-4.650 ²¹	1500			1500

Table 5.2 gives details on measurements (if available) for each of the three age determination methods used here, as well as the final adopted age, for each target star. We also plot our targets in Fig. 5.1, giving the age, distance, and spectral type (using absolute H magnitude as a proxy) for each star. Overall, for all 118 of the stars considered in this Chapter, the median target star is a K1 star at a distance of 24 pc with an age of 160 Myr.

5.3 Monte Carlo Simulations

As in Nielsen et al. (2008) we use Monte Carlo simulations of “fake” planets around each of the target stars in the three direct imaging surveys considered here. A large number (10^4 - 10^5 , depending on the application) of simulated planets are given random values of eccentricity, viewing angles, and orbital phase based on the appropriate distributions. Planet mass and semi-major axis are assigned either from a grid (see Section 5.3.3), or from power-law distributions (as in Section 5.3.4). For graphical representations of the distributions of extrasolar planet orbital parameters, see Fig. 2, 5, and 6 of Nielsen et al. (2008), and the discussion therein. For each observation of a given target star, the flux of each simulated planet is computed based on the planet’s mass and the target star’s age, using one of three planet models (see Section 5.3.1). The angular separation between parent star and simulated planet, as well as the flux ratio between planet and star, are then computed given the distance to the star. These are compared to the contrast curve for the observation, which give the faintest detectable companion (at the 5σ level) to the star, in the observation band, as a function of angular separation from the star.

In cases where the same target star is observed in multiple epochs, and sometimes among different surveys (a common occurrence, the 22, 50, and 71 stars we

Table 5.2—Continued

Target	Sp. Type*	Li EW (mÅ)*	Li Age (Myr)	R' _{HK} *	R' _{HK} Age ⁺⁺	Group Membership ¹	Group Age ¹	Adopted Age ⁺⁺⁺
HD 107146	G2V ⁷⁰	125 ⁸	180	-4.340 ²¹	190			190
HD 108767 B	K2V ⁷¹	175 ⁷²	140					140
HD 109085	F2V ¹⁷	37 ⁷³	100					100
BD +60 1417	K0 ⁷⁴	96 ⁸	270					270
HD 111395	G5V ⁵²			-4.580 ²¹	1000			1000
HD 113449	K1V ¹⁷	142 ⁸	200	-4.340 ¹³	190	AB Dor	70	70
HD 116956	G9V ⁶⁸	31 ²⁴	1000	-4.447 ¹³	420			710
HD 118100	K4.5V ⁶⁸	25 ¹⁵	280	-4.090 ¹³				280
HD 124106	K1V ¹⁷			-4.675 ⁶	1700			1700
HD 130004	K2.5V ⁶⁸			-4.919 ¹³	5100 ⁺			5100
HD 130322	K0III ⁷⁵			-4.780 ²¹	2900			2900
HD 130948	G2V ⁵²	116 ⁸	230	-4.500 ²¹	610			420
HD 139813	G5 ⁷⁶	119 ⁸	230	-4.400 ²¹	300			270
HD 141272	G9V ⁶⁸			-4.390 ²¹	280			280
HIP 81084	K9V ^{kee77}			-4.210 ⁶		AB Dor	70	70
HD 160934	K7 ⁷⁸	40 ⁷⁹	280			AB Dor	70	70
HD 166181	G5V ⁸⁰	186 ⁸	60					60
HD 167605	K2V ⁸¹	14 ⁵⁷	500					500
HD 187748	G0 ⁶³	114 ⁸	140					140
HD 201651	K0 ⁴⁷			-5.010 ²¹	6800			6800
HD 202575	K3V ⁶⁸			-4.522 ¹³	700 ⁺			700
HIP 106231	K3V ^{ke68}	140 ⁸	180	-3.906 ¹³		AB Dor	70	70
HD 206860	G0VCH-0.5 ¹⁷	110 ⁸²	190	-4.400 ⁶	300	Her/Lyr	200	200
HD 208313	K2V ⁶⁸			-4.987 ¹³	6400 ⁺			6400
V383 Lac	K0 ⁸³	259 ⁸	40					40
HD 213845	F5V ¹⁷			-4.547 ⁶	830	Her/Lyr	200	200
HIP 114066	M0 ⁷⁸					AB Dor	70	70
HD 220140	K2V ^{ke68}	218 ⁸	85	-4.074 ¹³				85
HD 221503	K6V ^{ke17}			-4.486 ⁶	550 ⁺			550
HIP 117410	K5V ^{ke17}			-4.194 ⁶	55 ⁺			55

¹ Group Membership for TWA, β Pic, Tuc/Hor, and AB Dor from Zuckerman & Song (2004), Her/Lyr from López-Santiago et al. (2006). Group Ages from Zuckerman & Song (2004) (TWA, β Pic, and Tuc/Hor), Nielsen et al. (2005) (AB Dor), and López-Santiago et al. (2006) (Her/Lyr)

* Measurement References: 2: Houk & Cowley (1975), 3: Waite et al. (2005), 4: Henry et al. (1996), 5: Torres et al. (2000), 6: Gray et al. (2006b), 7: Houk & Smith-Moore (1988), 8: Wichmann et al. (2003), 9: Zuckerman & Song (2004), 10: Cowley et al. (1967), 11: Christian & Mathioudakis (2002), 12: Leaton & Pagel (1960), 13: Gray et al. (2003b), 14: Favata et al. (1995), 15: Favata et al. (1997), 16: Zuckerman et al. (2001a), 17: Gray et al. (2006b), 18: Houk (1978), 19: Cutispoto et al. (1995), 20: Montes et al. (2001), 21: Wright et al. (2004), 22: Sozzetti et al. (2006), 23: Bidelman (1951), 24: Gaidos et al. (2000), 25: Zuckerman et al. (2001b), 26: Song et al. (2003), 27: Alcalá et al. (1995), 28: Houk (1982), 29: Randich et al. (1993), 30: Gliese & Jahreiß (1979), 31: Neuhauser & Brandner (1998), 32: Eggen (1996), 33: Abt (1985), 34: Gliese & Jahreiss (1991), 35: Webb et al. (1999), 36: Vyssotsky et al. (1946), 37: Evans (1961), 38: Soderblom et al. (1998), 39: Nesterov et al. (1995), 40: Mathioudakis et al. (1995), 41: Rufener & Bartholdi (1982), 42: Zboril et al. (1997), 43: Eggen (1962), 44: Ambruster et al. (1998), 45: Montes et al. (2001a), 46: Helmer et al. (1983), 47: Perryman et al. (1997), 48: López-Santiago et al. (2006), 49: Pasquini et al. (1994), 50: Cowley (1976), 51: Heard (1956), 52: Harlan & Taylor (1970b), 53: Herbig & Spalding (1955), 54: Israelian et al. (2004), 55: Sato & Kuji (1990), 56: Fleming et al. (1989), 57: Favata et al. (1993), 58: Appenzeller et al. (1998), 59: Malaroda (1975), 60: Lambert & Reddy (2004), 61: Oswalt et al. (1988), 62: Morgan & Keenan (1973), 63: Perry (1969), 64: Schwöpe et al. (2000), 65: Harlan (1974), 66: Strassmeier et al. (2000), 67: Bidelman (1985), 68: Gray et al. (2003b), 69: Schild (1973), 70: Harlan & Taylor (1970a), 71: Mora et al. (2001), 72: Pallavicini et al. (1992), 73: Mallik et al. (2003), 74: Roeser & Bastian (1988), 75: Upgren & Staron (1970), 76: Pye et al. (1995), 77: Fan et al. (2006), 78: Reid et al. (1995), 79: Zuckerman et al. (2004), 80: Eggen (1964), 81: Stocke et al. (1991), 82: Chen et al. (2001), 83: Bowyer et al. (1996)

⁺ In general, we have only determined Ca R'_{HK} ages for stars with spectral types K1 or earlier, but in the case of these K2-K6 stars, we have only the R'_{HK} measurement on which to rely for age determination. The calibration of Mt. Wilson S-index to R'_{HK} for K5 stars (B-V \sim 1.1 mag) has not been well-defined (Noyes et al. (1984); specifically the photospheric subtraction), and hence applying a R'_{HK} vs. age relation for K5 stars is unlikely to yield accurate ages.

⁺⁺ Using Eq. 3 of Mamajek & Hillenbrand (2008) to convert R'_{HK} into age

⁺⁺⁺ In general, ages derived from lithium and/or calcium alone are likely accurate to within a factor of \sim 2

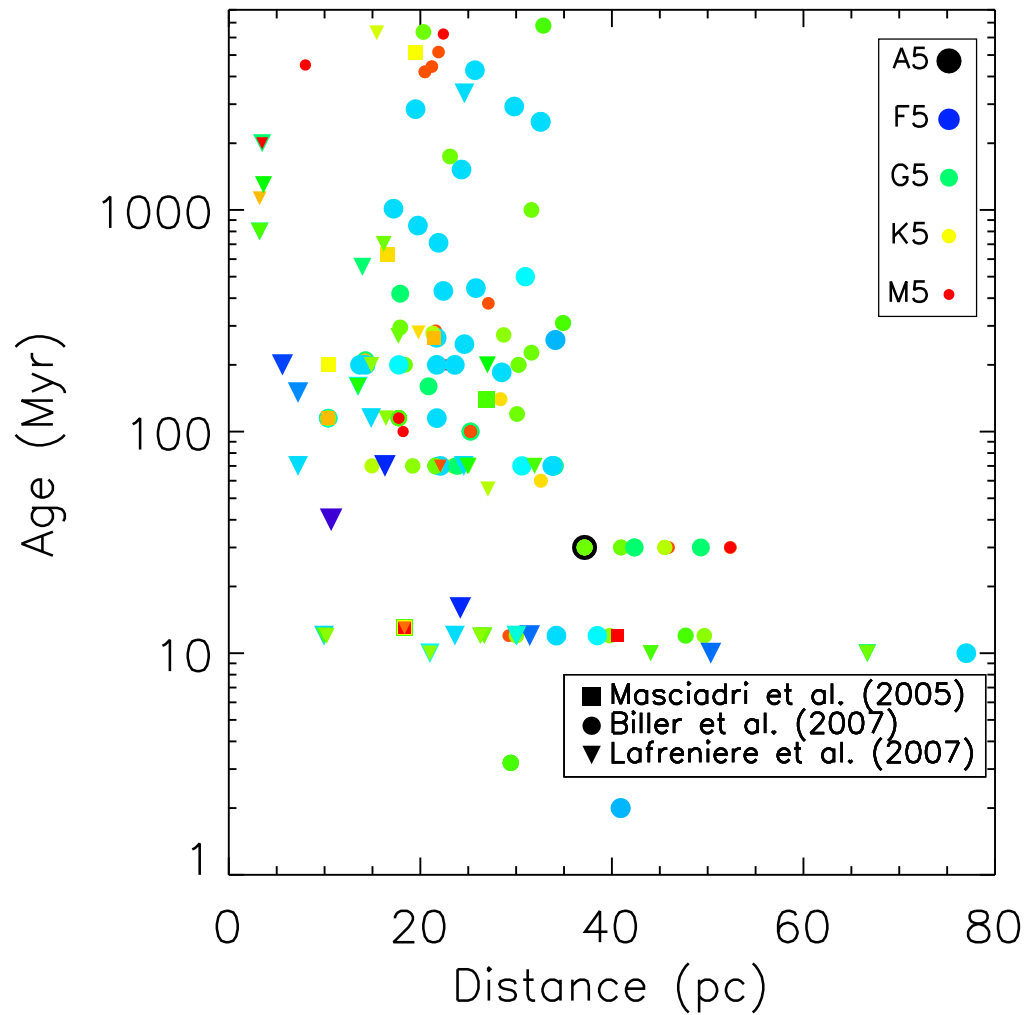


Figure 5.1 The 118 unique stars used in this Chapter, collected from the direct imaging planet surveys of Masciadri et al. (2005) (squares), Biller et al. (2007) (circles), and Lafrenière et al. (2007) (Triangles). Table 5.1 gives other properties of these stars, and Table 5.2 provides details on how the individual ages were determined. The median target star is a 160 Myr K1 star at 24 pc. The size and color of the plotting symbols indicates the spectral type of each target star. The top legend gives the conversion between size and color of the plotting symbol and spectral type: the color scheme follows the visible spectrum, with early-type stars represented by large dark purple symbols, while late-type stars are small red symbols.

use in this work would suggest a sample size of 143 target stars, but there are only 118 unique target stars between these three surveys with reliable age estimates), the additional elapsed time is taken into account. Simulated planets are generated at the earliest epoch as usual, and compared to that contrast curve. Their parameters are then used again, with orbital phase advanced forward by the time between observations (often a small effect for the planets to which these surveys are sensitive, a 30 AU orbit around a solar-type star has a 160 year period, and the typical time span between observations is at most about 3 years), the fluxes of the simulated planets are now computed in the new observation band, and compared to the new contrast curve. The process is repeated for each observational epoch for the given target star, and a simulated planet that is detectable in any of the observational epochs is considered detectable. Again, Nielsen et al. (2008) provides more details on these simulations, in particular their Fig. 3, 4, and 7.

5.3.1 Theoretical Models of Giant Planet Fluxes

In order to use the measured contrast curves for each observed target star to determine which simulated planets could be detected, it is necessary to have a conversion from planet mass and age to NIR flux. As in Nielsen et al. (2008), we use the theoretical models of Burrows et al. (2003) and Baraffe et al. (2003) for the calculation of exoplanet flux, using the mass of each simulated planet and the age of the host target star, determining the flux density in the filter band (H or Ks) appropriate for the particular observation. In the cases of the GDPS (Lafrenière et al., 2007) and SDI (Biller et al., 2007) surveys, where the observation band was a specialized filter instead of the standard H bandpass, a correction factor is applied (see Section 5.3.2 for details). Though these two “hot start” models provide basically similar predictions, we perform our calculations with both, as the two models can predict significantly different NIR fluxes for exoplanets, depending

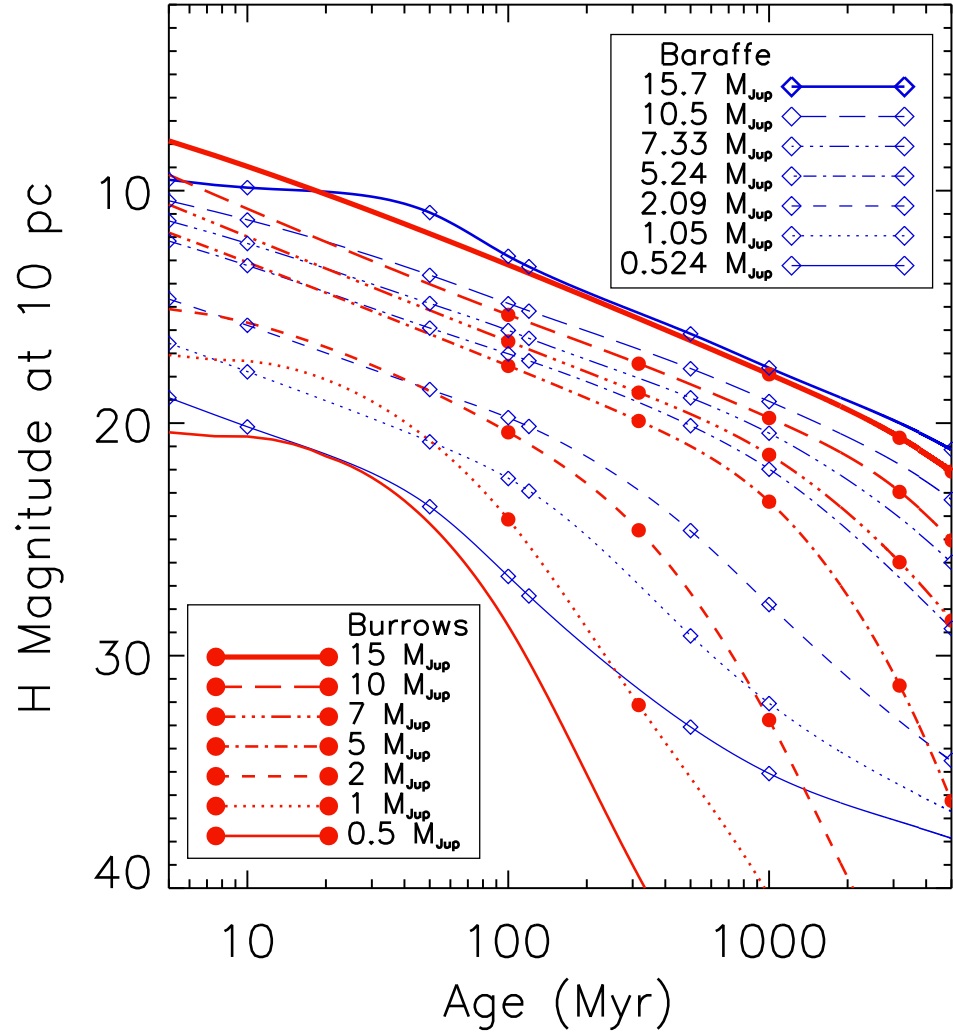


Figure 5.2 A plot of the age and H magnitude of planets, for different masses, as predicted by the Baraffe et al. (2003) and Burrows et al. (2003) models, represented by the thin blue lines and the thick red lines, respectively. The diamonds and circles are the H magnitudes given by the models themselves, while the lines show the interpolation and extrapolations beyond these points that we use when assigning H magnitudes to the simulated planets. The COND models of Baraffe et al. (2003) required very little extrapolation to fill the range of parameter space shown here, while far more extrapolation is required for the Burrows et al. (2003) models, especially at young ages and small masses.

on planet mass and stellar age, as shown in Fig. 5.2.

Since the publication of Nielsen et al. (2008), an additional set of theoretical models has been published by Fortney et al. (2008) for extrasolar planets for a range of masses and ages. The major difference between these new models and those from Burrows et al. (2003) and Baraffe et al. (2003) is that the Fortney et al. (2008) models are based heavily on the “core accretion” theory of planet formation (e.g. Hubickyj et al. (2005)), where giant planets are formed from an initial $\sim 10 M_{\oplus}$ core accreting gas from the protoplanetary disk. After the brief luminous accretion phase, these models predict consistently fainter NIR fluxes than the “hot start” models (until ~ 100 Myr to ~ 1 Gyr, when the models overlap nicely, see Fig. 1 of Fortney et al. (2008)), which do not base their initial conditions on planetary core accretion models. For more detail, consult Figure 8, and Tables 1 and 2, of Fortney et al. (2008).

As is the case with the Burrows et al. (2003) models, the Fortney et al. (2008) models do not cover the full range of planet parameters we consider here (masses between 0.5 and $15 M_{Jup}$, ages from 1 Myr to 10 Gyr), since Fortney et al. (2008) limit their calculations to planets with $T_{eff} > 400\text{K}$, leaving the consideration of cooler planets to future work. As a result, we extrapolate the models to masses below $1 M_{Jup}$ and above $10 M_{Jup}$, and at larger ages (the age a planet cools below 400 K depends on the mass of the planet, ~ 30 Myr for a $1 M_{Jup}$ planet, and ~ 1 Gyr for a $10 M_{Jup}$ planet). While not an ideal solution, as we are ignoring the complicated physical processes taking places in planets as we cross these boundaries in exchange for simple relationships between NIR fluxes and age and mass, we believe that this method provides a good overall picture of the fluxes of extrasolar planets as predicted by the Fortney et al. (2008) models. In Fig. 5.2, we plot the initial gridpoints of both the Baraffe et al. (2003) and Burrows et al. (2003)

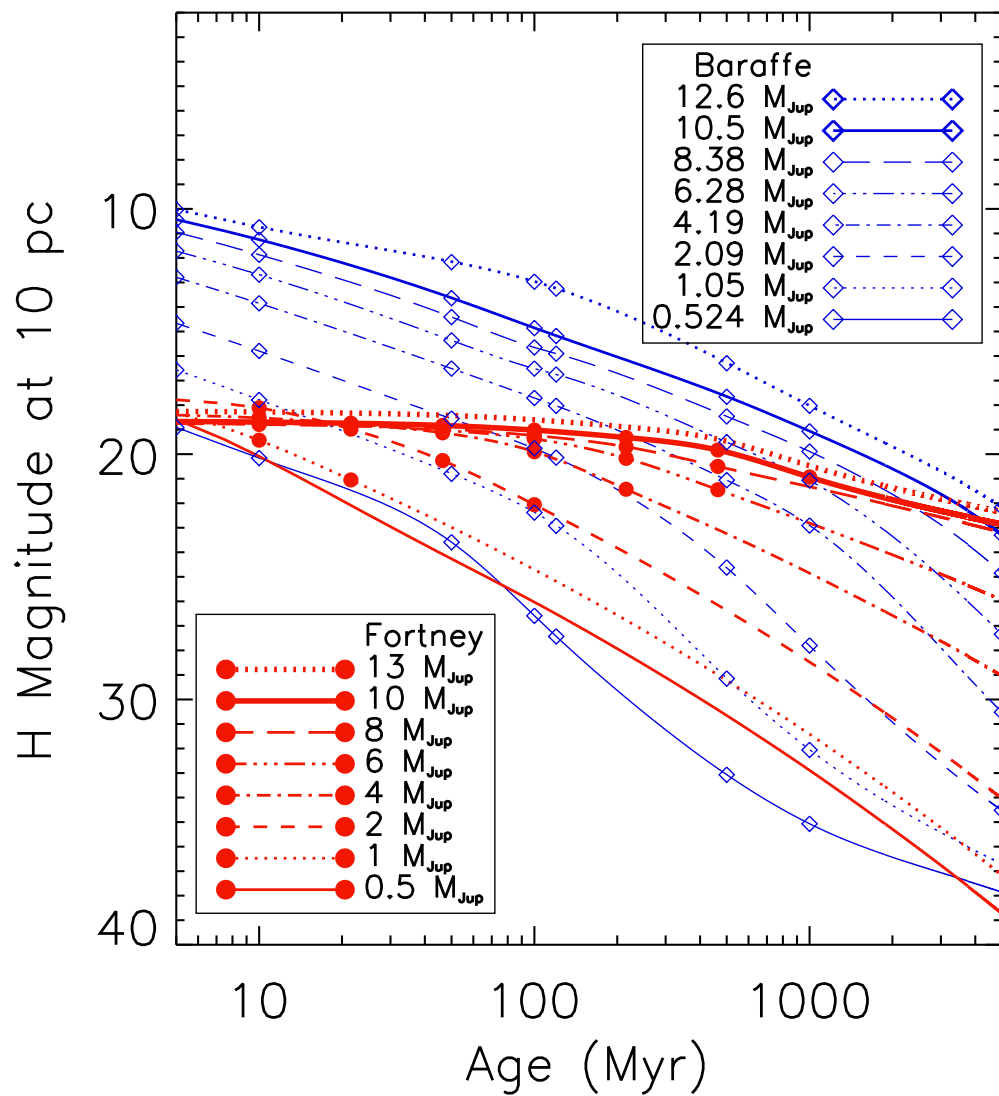


Figure 5.3 As with Fig. 5.2, a plot of the predicted fluxes of extrasolar planets of Baraffe et al. (2003), again represented by blue lines and open diamonds, this time plotted against the core accretion models of Fortney et al. (2008), the red lines with filled circles. In order to fill the parameter space of planet mass and stellar age we consider, it is necessary to extrapolate the Fortney et al. (2008) H magnitudes beyond the grid points of the models themselves, especially at larger ages and smaller masses.

models, as well as our extrapolations to the full range of parameter space. A similar plot comparing the predicted fluxes for the Baraffe et al. (2003) and Fortney et al. (2008) models is shown in Fig. 5.3. Our effort to map additional areas of model parameter space is worthwhile since this work is the first to apply these new core accretion models to the field of high contrast imaging surveys.

5.3.2 Narrowband to Broadband Colors

When we considered stars observed with the SDI method in Nielsen et al. (2008), we used a constant conversion from the broadband H magnitude predicted by the models to the measured contrast in the narrowband “off-methane” filter (SDI F1, 2% bandpass, centered at $1.575 \mu\text{m}$ (Close et al., 2005)). While this conversion factor was consistent with observed T6 objects (Biller et al., 2007), it would be expected to vary across a broad range of planet temperatures, corresponding to the large differences in ages and masses of the simulated planets. In this work, we used template spectra from the SpeX instrument of 132 low-mass objects, spanning spectral types from L0 to T8, to compute the difference between broadband H and narrowband filters as a function of effective temperature (M. Liu, private communication). Spectral types are converted to effective temperature by the polynomial fit of Golimowski et al. (2004), their Table 4. SpeX spectra were obtained from the online SpeX Prism Spectral Libraries (e.g. Cruz et al. (2004), Kirkpatrick et al. (2006), and Burgasser (2007)). Since the reliability of the models at reproducing the methane band when modeling planet atmospheres is still uncertain, we prefer this method to purely using the synthetic spectra from the models to make this color correction.

For GDPS target stars, we use this conversion for the NIRI CH4-short filter, to convert the model’s prediction of planetary H-band flux to this 6.5% bandpass filter, centered at $1.58 \mu\text{m}$. For SDI target stars, we follow the steps of the data

reduction used in computing contrast curves, computing planet fluxes for both the bluest “off-methane filter” (F1), and the “on methane filter” (F3) both with a 2% bandpass, centered at 1.575 and 1.625 μm , respectively. Just as is done for the survey images, the on-methane flux is subtracted from the off-methane flux, providing (for each value of effective temperature) the expected final flux in the subtracted image, as represented by the contrasts curves of Biller et al. (2007). For both the SDI and GDPS target stars, we use the appropriate effective temperatures predicted by the models to match these color corrections to simulated planets of each combination of age and mass.

To partially account for this effect in Nielsen et al. (2008), for SDI target stars, we had imposed an upper cut-off on planet mass, set by where the models predicted planet effective temperatures would rise above 1400 K for a given age. Above this temperature, the methane break would be so weak that subtracting the “on-methane” image from the “off-methane” image would simply remove all flux from the planet, as it is meant to do for the star. As a result, planets more massive than this limit were simply considered undetectable. With our more robust method that appropriately attenuates planet flux as a function of temperature, it is no longer necessary for us to impose this rather crude binary cut for SDI targets.

In principle, an SDI observation of a non-methanated companion should not suffer from self-subtraction of the companion signal, as the spatial scaled of these images in the three SDI filters are rescaled by wavelength before subtraction. This step aligns the speckles in the images (which scale as $\frac{\lambda}{D}$, where λ is the observation wavelength and D is the diameter of the telescope), but misaligns any physical objects (where separation from the primary star on the detector is not a function of wavelength). As such, following subtraction of images from two

different filters, a real companion should appear as a “dipole:” a positive and negative PSF, forming a radial line toward the primary star. The separation between the positive and negative parts of the dipole in the subtracted image would be given by $\Delta d \sim \frac{\Delta\lambda}{\lambda}d$, where Δd is the length of the dipole on the detector, $\Delta\lambda$ is the difference in wavelength between the two filters, and d is the separation on the detector between the primary star and the companion. The most extreme shift in filters for SDI observations is between the $1.575 \mu\text{m}$ and $1.625 \mu\text{m}$ filters, or 3%. Since the field of view for the NACO VLT SDI observations was only $2.5''$, the largest shift between positive and negative companions in the subtracted image would be 6.5 pixels. As the FWHM for these observations was typically 3.5 pixels, this dipole effect would easily be lost against the speckle background at large separations, and almost undetectable at small separations, where positive and negative companions would more closely overlap (Biller et al., 2007).

5.3.3 Completeness Plots

Using a similar method to Nielsen et al. (2008), we run Monte Carlo simulations of extrasolar planets at a grid of mass and semi-major axis points for each target star. For each star, then, we have what fraction of simulated planets could be detected as a function of planet mass and semi-major axis. These plots, for each of our 118 target stars, with the three sets of models we consider here, are available in the online version of Nielsen & Close (2010). In order to combine these results over all 118 target stars, we again make use of the concept of the “planet fraction,” or fraction of stars with a particular type of planet, defined such that

$$N(a, M) = \sum_{i=1}^{N_{obs}=118} f_p(a, M) P_i(a, M) \quad (5.1)$$

where $N(a, M)$ is the number of planets we would expect to detect, as a function of semi-major axis and planet mass, N_{obs} is the number of stars observed, and

$P_i(a, M)$ is the fraction of simulated planets, at a given combination of planet mass and semi-major axis, we could detect around the i th star in the sample. $f_p(a, M)$, then, is the fraction of stars that have a planet with a mass M and semi-major axis a . If every star had one Jupiter-mass planet at 5 AU, for example, then $f_p(5AU, 1M_{Jup}) = 1$, and the number of these Jupiter analogs we would expect to detect from the three surveys would simply be the sum of the detection efficiency for these planets around all target stars. That is, if we had 10 stars in our sample ($N_{obs} = 10$), and we had a 50% chance of detecting a Jupiter-like planet around each star ($P_i(5AU, 1M_{Jup}) = 0.5$), our expected number of detections of these planets would be 5.

In the case of not finding planets, as was the case for the three surveys of FGKM stars considered here, we can use the null result to set an upper limit on the planet fraction, f_p . If we assume that planet fraction is constant across all stars in our survey (we will reexamine this assumption in Section 5.3.5), we can remove f_p from the sum of Equation 5.1. Then, utilizing the Poisson distribution, where the probability of 0 detections given an expectation value of 3 (that is, $N(a, M) = 3$), is 5%, we can set the 95% confidence level upper limit on planet fraction with the equation

$$f_p(a, M) \leq \frac{3}{\sum_{i=1}^{N_{obs}} P_i(a, M)} \quad (5.2)$$

So, with the above example, where the expectation value is 5 for Jupiter-analogs over 10 target stars ($\sum_{i=1}^{N_{obs}=10} P_i(5AU, 1M_{Jup}) = 5$), not detecting any such planets would allow us to place a 95% confidence level upper limit of 60% on the fraction of stars with a Jupiter-twin ($f_p(a, M) < \frac{3}{5}$). Doing this over the entire grid of planet mass and semi-major axis allows us to plot what constraints can be placed on combinations of these planet parameters.

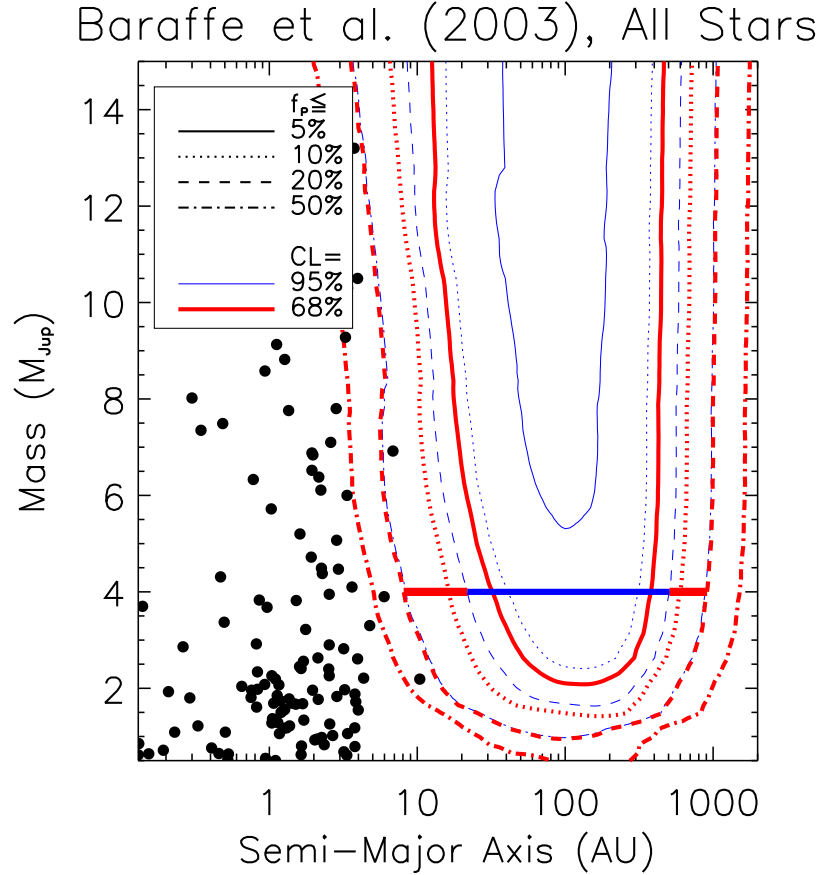


Figure 5.4 The upper limit on planet fraction (f_p , the fraction of stars with a planet of a given mass and semi-major axis, see Equation 5.1), at the 95% (blue, thin lines) and 68% (red, thick lines) confidence levels, using the theoretical models of Baraffe et al. (2003). With 95% confidence, we can say that less than 1 in 20 stars has a planet more massive than $8 M_{Jup}$ between 50 and 160 AU (constrained by the solid blue, thin curve). We plot a horizontal fiducial bar (again, with a thick red line and thin blue line) at $4 M_{Jup}$, intersecting the $f_p \leq 20\%$ contour at both 68% confidence (outer contour, thick red line) and 95% (inner contour, thin blue line). Hence, the horizontal line at the bottom right of the figure suggests no more than 1 in 5 stars would have a planet more massive than $4 M_{Jup}$ from 8.1 to 911 AU at the 68% confidence level, and between 22 and 507 AU at the 95% confidence level. Known radial velocity planets are shown as filled circles for comparison.

Burrows et al. (2003), All Stars

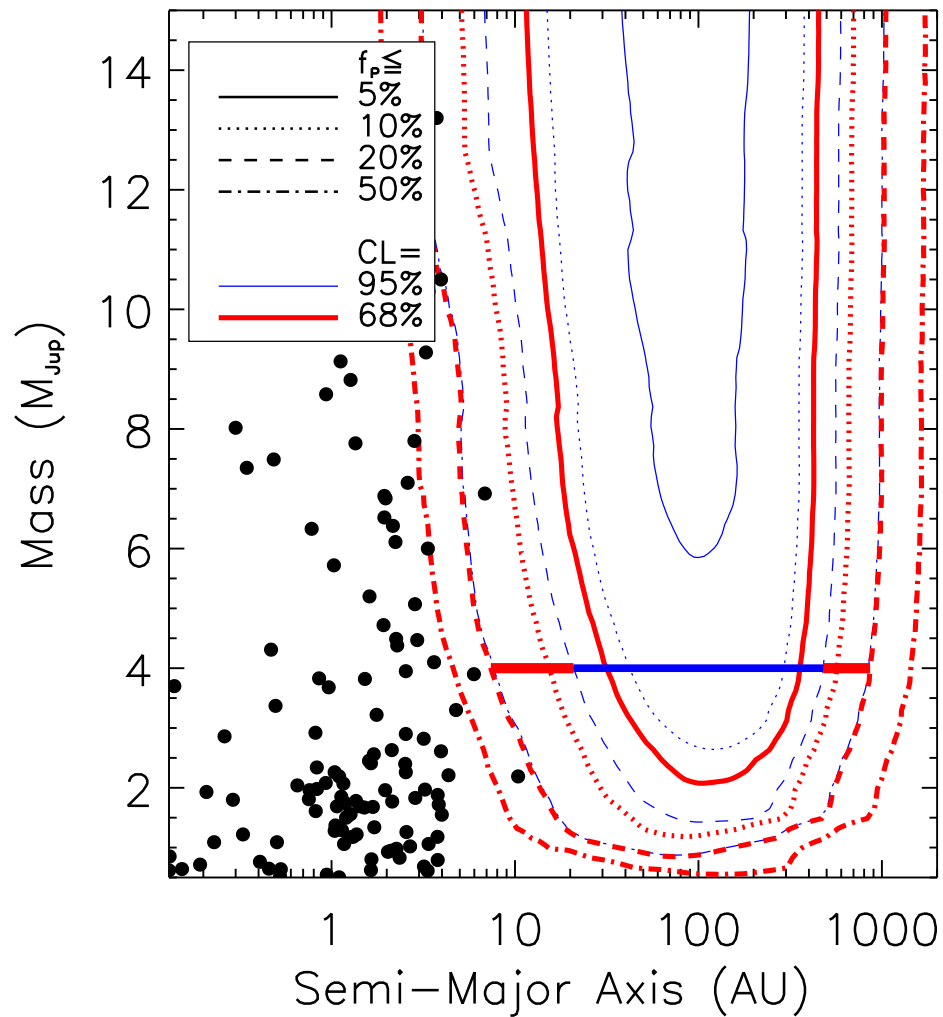


Figure 5.5 As with Fig. 5.4, the upper limit on planet fraction only now using the theoretical models of Burrows et al. (2003). The overall shape of the graph is quite similar, so with 95% confidence, we can place an upper limit on planet fraction of 5% for planets larger than $8 M_{Jup}$ with semi-major axis between 55 and 130 AU. As before, radial velocity planets are plotted as solid circles. The fiducial $f_p \leq 20\%$ limits for $4 M_{Jup}$ are between 7.4 and 863 AU at 68% confidence, and 21 to 479 for the 95% confidence level.

Fortney et al. (2008), All Stars

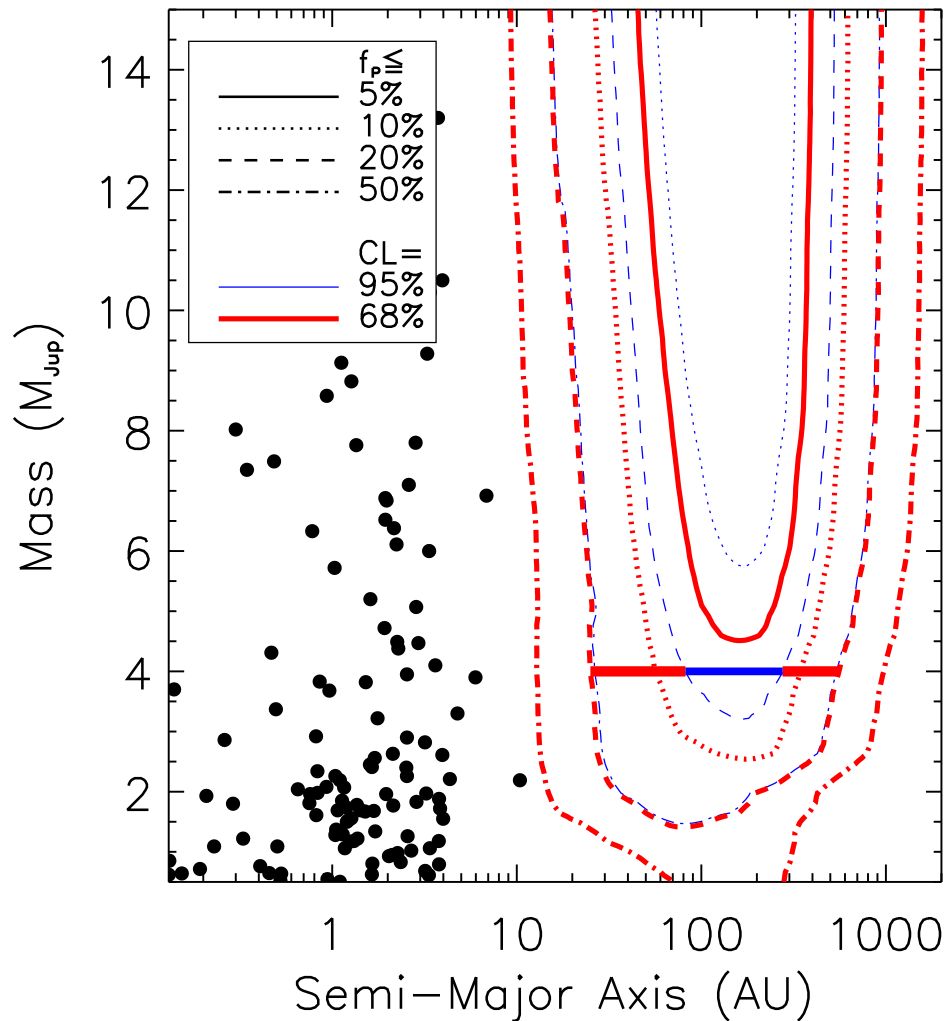


Figure 5.6 The same as Fig. 5.4 and Fig. 5.5, this time using the models of Fortney et al. (2008) to give the upper limit on planet fraction. Overall, the theoretical models of Fortney et al. (2008) are more pessimistic as to NIR fluxes of planets when compared to the hot-start models (Burrows et al., 2003; Baraffe et al., 2003). With these models, from 82 to 276 AU, less than 20% of stars can have a planet above $4 M_{Jup}$, at the 95% confidence level, and between 25 and 557 AU at 68% confidence.

Table 5.3. Summary of Results.

Target Stars	Mass Correction*	Confidence Level	Baraffe et al. (2003)	Burrows et al. (2003)	Fortney et al. (2008)
Completeness plots: semi-major axis range with $f_p < 20\%$ for $M > 4 M_{Jup}$					
All	None	68%	8.1 - 911 AU	7.4 - 863 AU	25 - 557 AU
All	None	95%	22 - 507 AU	21 - 479 AU	82 - 276 AU
M stars	None	68%	9.0 - 207 AU	8.3 - 213 AU	43 - 88 AU
M stars	None	95%	—	—	—
FGK stars	None	68%	25 - 856 AU	25 - 807 AU	59 - 497 AU
FGK stars	None	95%	38 - 469 AU	40 - 440 AU	—
All	$1 M_{\odot}$	68%	13 - 849 AU	13 - 805 AU	41 - 504 AU
All	$1 M_{\odot}$	95%	30 - 466 AU	30 - 440 AU	123 - 218 AU
All	$0.5 M_{\odot}$	68%	9.0 - 1070 AU	8.3 - 1016 AU	26 - 656 AU
All	$0.5 M_{\odot}$	95%	23 - 605 AU	22 - 573 AU	71 - 341 AU
Upper cut-off on power law distribution for semi-major axis with index -0.61					
All	None	68%	30 AU	28 AU	83 AU
All	None	95%	65 AU	56 AU	182 AU
All	Yes	68%	37 AU	36 AU	104 AU
All	Yes	95%	82 AU	82 AU	234 AU

* The “Mass Correction” column refers to whether or not the Johnson et al. (2007) result, that more massive stars are more likely to harbor giant planets, is used to weight the target stars by stellar mass. For the completeness plots, this correction is either not applied (None) or set to a specific stellar mass, to determine the upper limit on the frequency of giant planets around stars of that mass. For the limits on the upper cut-off on power law distributions, the correction is either applied (Yes) or not (None).

Fig. 5.4 gives the upper limit on planet fraction as a function of planet mass and orbital semi-major axis, using the models of Baraffe et al. (2003), with a similar plot using the theoretical models of Burrows et al. (2003) given in Fig. 5.5. We can place our strongest constraints on planets more massive than $\sim 4 M_{Jup}$ between 20 and 300 AU (fewer than 5% of stars can have such planets at 68% confidence); when stars of all spectral types are considered, the lower limit probed by direct imaging and the upper limit of the radial velocity method are still a factor of 5 apart. When we repeat the calculations using the models of Fortney et al. (2008), the decreased NIR flux predicted for giant planets reduces constraints that can be placed on extrasolar planets, with the “sweet spot” moving out to ~ 80 AU, as seen in Fig. 5.6.

While we continue to run calculations using all three sets of models, and re-

port the results here, for the sake of brevity we will henceforth only plot figures corresponding to the Baraffe et al. (2003) COND models. However, the figures appropriate to the Burrows et al. (2003) “hot-start” and Fortney et al. (2008) core accretion models are available in our supplement, available at this URL: <http://exoplanet.as.arizona.edu/~lclose/exoplanet2.html> The supplement also contains individual completeness plots for each of our 118 target stars, using each of the three models of planet fluxes. Additionally, we summarize basic results for all of our calculations in Table 5.3.

5.3.4 Testing Power Law Distributions for Extrasolar Planet Mass and Semi-Major Axis

These null results for extrasolar planets are also useful in setting constraints on the parameters of models for planet populations that assume power law distributions for the semi-major axis and mass distributions. Cumming et al. (2008) carefully examined the sensitivity of the Keck Planet Search, and determined that, over the range to which the radial velocity technique is sensitive (0.3 to 10 M_{Jup} , 2-2000 day orbital periods), planets follow a double power-law distribution with index -1.31 in mass and -0.61 in semi-major axis (-0.74 in orbital period). That is, $\frac{dN}{dM} \propto M^{-1.31}$ and $\frac{dN}{da} \propto a^{-0.61}$ (note that we define power law indices with respect to linear bins, $\frac{dN}{da}$, not the logarithmic bins of Cumming et al. (2008). Also, while Cumming et al. (2008) use α and β to refer to the power law indices for mass and period, respectively, we use α to refer to the power law index for semi-major axis).

Table 5.4. Binaries

Target	Sep (") ¹	Sep. (AU) ¹	Reference	Companion Type
Biller et al. (2007)				
HIP 9141	0.15	6.38	Biller et al. (2007)	mid-G
V577 Per A	7	230	Pounds et al. (1993)	M0
AB Dor	9 (Ba/Bb)	134 (Ba/Bb)	Close et al. (2005)	Binary M stars
AB Dor	0.15 (C)	2.24 (C)	Close et al. (2005)	Very low-mass M Star
HIP 30034	5.5	250	Chauvin et al. (2005)	Planet/Brown Dwarf
HD 48189 A	0.76 (B)	16.5	Fabricius & Makarov (2000)	K star
HD 48189 A	0.14	3.03	Biller et al. (2007)	K star
DX Leo	65	1200	Lowrance et al. (2005)	M5.5
EK Dra	SB	SB	Metchev & Hillenbrand (2004)	M2
HD 135363	0.26	7.65	Biller et al. (2007)	late K/early M
HD 155555 AB	SB (AB)	SB (AB)	Bennett et al. (1967)	G5 and K0 SB
HD 155555 AB	18 (C)	1060 (C)	Zuckerman et al. (2001a)	Target Star 155555 C, M4.5
HD 172555 A	71	2100	Simon & Drake (1993)	Target Star CD -64 1208, K7
HD 186704	13	380	Aitken & Doolittle (1932)	early M
GJ 799A	3.6	36	Wilson (1954)	Target Star GJ 799B, M4.5
HD 201091	16	55	Baize (1950)	K5
Eps Indi A	400	1500	McCaughrean et al. (2004)	Binary Brown Dwarf
HIP 112312	100	2400	Song et al. (2002)	M4.5
Masciadri et al. (2005)				
TWA 8A	13	270	Jayawardhana et al. (1999)	Target Star TWA 8B, M5
TWA 9A	9	576	Jayawardhana et al. (1999)	Target Star TWA 9B, M1
SAO 252852	15.7	260	Poveda et al. (1994)	HD 128898, Ap
V343 Nor	10	432	Song et al. (2003)	M4.5
BD-17 6128	2	100	Neuhäuser et al. (2002)	M2
Lafrenière et al. (2007)				
HD 14802	0.47	10	Lafrenière et al. (2007)	K6
HD 16765	4.14	89	Holden (1977)	~K
HD 17382	20.3	456	Lépine & Shara (2005)	M4.5
HD 19994	~5	~100	Hale (1994)	M3V
HD283750	124	2220	Holberg et al. (2002)	White Dwarf
HD 77407	1.7	50	Mugrauer et al. (2004)	~M
HD 93528	234	8200	Perryman et al. (1997)	HIP 52776, K4.5 ²
HD 96064	11.47	283 AU	Lippincott & MacDowall (1979)	NLTT 26194, M3
HD 102392	1.13	28	Lafrenière et al. (2007)	~M
HD 108767 B	23.7	639	Gould & Chanamé (2004)	A0IV
HD 130948	2.64	47	Potter et al. (2002)	Binary brown dwarfs
HD 139813	31.5	683	Stephenson (1960)	G0
HD 141272	17.8	350	Eisenbeiss et al. (2007)	M3
HD 160934	SB	SB	Hormuth et al. (2007)	early M, $a = 4.5$ AU
HD 160934	8.69	213	Lowrance et al. (2005)	~M
HD 166181	SB	SB	Nadal et al. (1974)	1.8 day orbit
HD 166181	0.102	3	Lafrenière et al. (2007)	~K
HD 167605	1.2	37	Arribas et al. (1998)	M4V
HD 206860	43.2	795	Luhman et al. (2007b)	T dwarf

Table 5.4—Continued

Target	Sep (″) ¹	Sep. (AU) ¹	Reference	Companion Type
HD 213845	6.09	139	Lafrenière et al. (2007)	late M
HD 220140	10.9	214	Lowrance et al. (2005)	mid M
HD 220140	963	19000	Makarov et al. (2007)	~M
HD 221503	339	4700	Gould & Chanamé (2004)	binary M stars
HIP 117410	1.84	50	Rossiter (1955)	early M

¹SB indicates a spectroscopic binary

²These stars have *Hipparcos* proper motion and parallax within errors, and similar values of calcium R'_{HK} (-4.424 and -4.451 for HD 93528 and HIP 52776, respectively).

Binarity is likely to disrupt planet formation, or at the very least change the underlying distribution of planets between binary stars hosting planets and single stars. Bonavita & Desidera (2007) have shown that the distribution of radial velocity planets for binary and single-star hosts is quite similar, and Holman & Wiegert (1999) suggest that planets are stable in binary systems with a planet semi-major axis $\lesssim 20\%$ of the binary separation. We take this into account for our consideration of power-law distributions of semi-major axis by excluding target stars with binaries within a factor of 5 of the planetary semi-major axis being considered. In Table 5.4, we give the results of a literature search for binaries among our target stars, including binary separation and binary type.

By adopting these power laws, and using the normalization of Fischer & Valenti (2005) to give the total fraction of stars with planets, we can then predict how many planets these three surveys should have detected for various power law fits. If a large number of planets is predicted, our null result can be used to strongly exclude that model. If we accept the power-law distribution for mass of Cumming et al. (2008) and the normalization of Fischer & Valenti (2005), the two remaining parameters are the semi-major axis power-law index α , and the semi-major axis upper cut-off (that is, what maximum semi-major axis the dis-

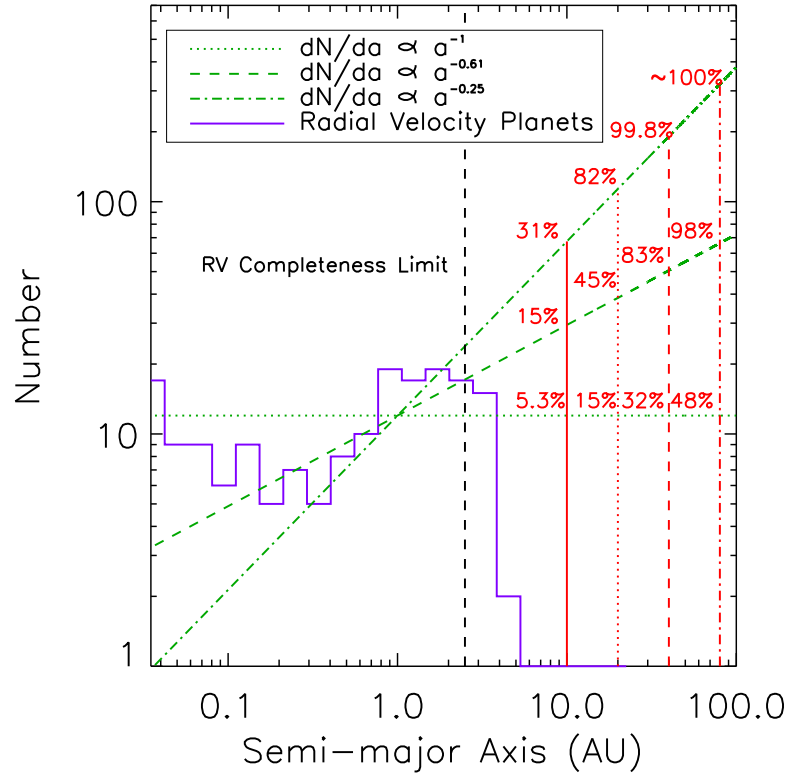


Figure 5.7 Twelve models for the semi-major axis distribution of extrasolar planets, using the planet luminosity models of Baraffe et al. (2003), with power law indices of $\alpha = -1$, -0.61 , and -0.25 , and upper cut-offs (the limit up to which there are planets, but beyond which planets no longer appear) of 10, 20, 40, and 80 AU. The solid purple line gives the histogram of known radial velocity planets, the horizontal and diagonal green lines give different values of the power law index, and the red vertical lines mark the upper cut-offs. The vertical black dashed line at 2.5 AU gives the approximate upper limit to which the radial velocity survey is complete to planets. The percentages at each intersection of power law and upper cut-off show the confidence with which that model ($\frac{dN}{da} \propto a^\alpha$ for $a \leq a_{cut-off}$, and $\frac{dN}{da} = 0$ for $a > a_{cut-off}$) can be rejected. For example, a planet population with $dN/da \sim a^{-1}$ and an outer cutoff of 10 AU is ruled out at 5.3% confidence. For the power law of index -0.61 (Cumming et al., 2008), at 95% confidence the upper cut-off must be less than 65 AU, which would fall between the dashed and dot-dashed vertical lines of this graph.

tribution continues to until planets are no longer present). We illustrate this in Fig. 5.7, where we depict various models of the semi-major axis distribution, and the confidence with which we can reject them, using the models of Baraffe et al. (2003). For 12 different combinations of semi-major axis power law index and upper cut-off we give the percentage we can reject each of these 12 models in this figure. For the model of Cumming et al. (2008), with $\frac{dN}{da} \propto a^{-0.61}$, and at 95% confidence, the upper cut-off must be less than 65 AU, and less than 30 AU with 68% confidence.

We again use the theoretical models for planet fluxes of Baraffe et al. (2003), and consider a broader range of power-law index α and upper cut-off in Fig. 5.8. As before, the results from the two hot start models (Burrows et al., 2003; Baraffe et al., 2003) are generally similar, as the upper cut-offs must be less than 28 and 56 AU (68% and 95% confidence) for the Burrows et al. (2003) models. The fainter predicted fluxes from the Fortney et al. (2008) models reduce the areas of parameter space that our null result can exclude: the 68% and 95% confidence level upper limits for upper cut-off become 83 and 182 AU, for a -0.61 power law index.

5.3.5 The Dependence on Stellar Mass of the Frequency of Extrasolar Giant Planets

In Sections 5.3.3 and 5.3.4, we assume the distribution and frequency of giant planets is constant across all the stars in our survey. Johnson et al. (2007) show this assumption to be incorrect by examining the frequency of giant planets around stars in three mass bins from radial velocity surveys, and showing that more massive stars are more likely to harbor giant planets (see their Fig. 6). As in Nielsen et al. (2008), we divide the target stars into two samples, one containing only M stars, and the other with FGK stars (Our sample contains a single A star, HD 172555 A, with spectral type A5, with all our stars F2 or earlier. We in-

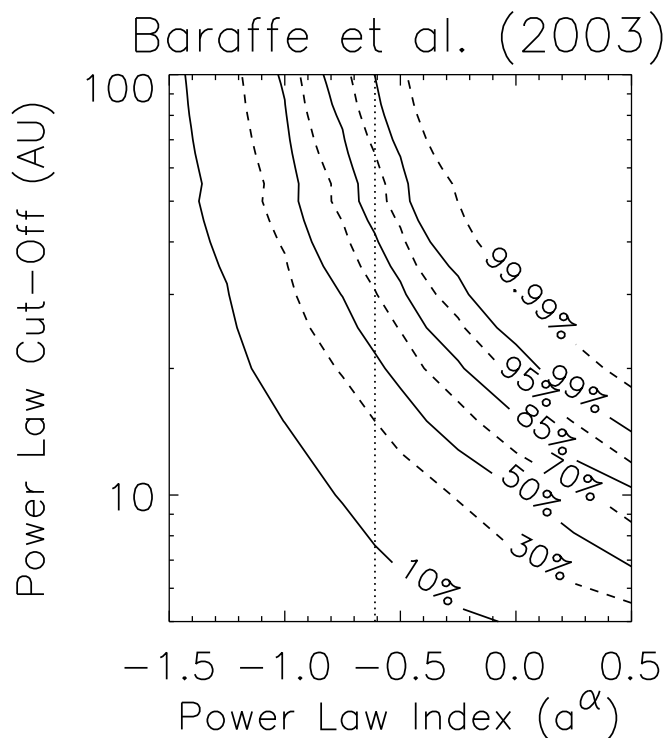


Figure 5.8 Contours showing the confidence with which we can exclude models of the semi-major axis distribution of extrasolar giant planets of the form $\frac{dN}{da} \propto a^\alpha$, with an upper cut-off beyond which there are no longer planets, using the models of Baraffe et al. (2003). The power law index of -0.61 as given by Cumming et al. (2008) is marked with a dotted line. The jags in the contours are due to binaries being removed as we move up in power law cut-off (binary target stars are pulled once the considered semi-major axis cut-off reaches one-fifth the binary separation). The pronounced jag between 50 and 55 AU corresponds to the binary M-dwarfs TWA 8A and TWA 8B (21 pc, 10 Myr) being removed from the sample, indicating the strong effect a few M stars have on our results. For the power law of index -0.61, the 68% and 95% confidence levels for rejection of this model are at 30 and 65 AU. Similar plots for the Burrows et al. (2003) and Fortney et al. (2008), for this and future plots, are available in the online version of Nielsen & Close (2010). The 68% and 95% confidence levels are 28 and 56 AU (Burrows et al., 2003) and 83 and 182 AU (Fortney et al., 2008).

clude this A star with the FGK stars; however, observations of this single star are not sufficient to make any meaningful statements about the population of planets around A stars). We then imagine a planet fraction (f_p) with one value for M stars, and another for stars of earlier spectral types.

In Fig. 5.9 we use the Baraffe et al. (2003) models to show the upper limit that can be placed on the planet fraction for M stars. Since only 18 of the 118 target stars are M stars, the smaller sample size greatly reduces the constraints that can be placed on planet fraction near the center of the contours, and the outer edge in semi-major axis. Interestingly, the small separation edge of the contours is virtually unchanged between Figs. 5.4 and 5.9, indicating that the power with which these surveys can speak to the populations of short-period giant planets is entirely due to the M stars in the surveys.

Fig. 5.10 uses the models of Baraffe et al. (2003) to give the upper limit on planet fraction for the FGK stars in the survey. The result for long-period planets and within the central contours is much the same as for stars of all spectral types (Fig. 5.4), but the contours at the smallest values of semi-major axis march outward without the M stars to provide high contrasts at small angular separations.

A more satisfying way to address the issue of stellar mass dependence is to weight the results by target star mass, so that all stars in the survey can be applied to the result simultaneously. To do this, we construct a linear fit to the metallicity-corrected histogram from Fig. 6 of Johnson et al. (2007), to give a correction to planet fraction as a function of stellar mass, as we show in Fig. 5.11. (Here we assume that the relation found by Johnson et al. (2007) for short-period planets (less than six years) applies to the entire range of semi-major axis. While this assumption is obviously untested, in the absence of better data we believe it is a good starting point.) In the case of setting upper limits on planet fraction, we

Baraffe et al. (2003), M Stars

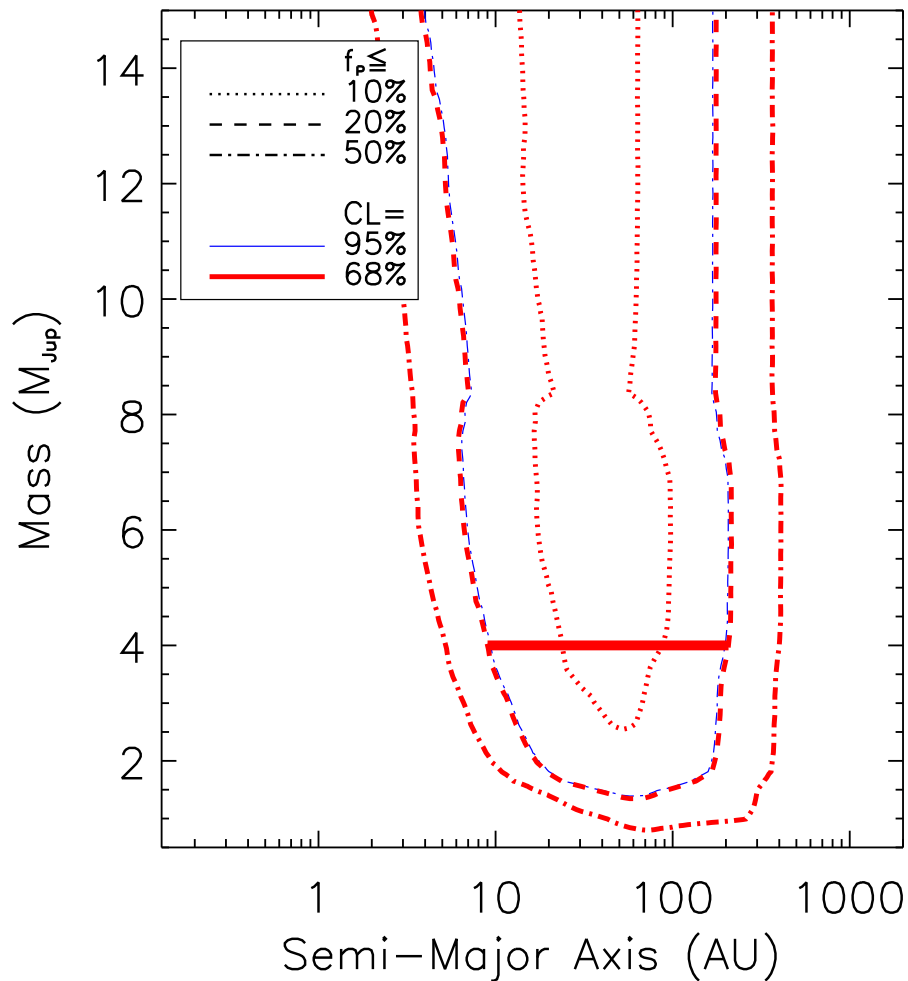


Figure 5.9 Contours giving the upper limit on planet fraction around all the stars of M spectral type in the three surveys, using the models of Baraffe et al. (2003). Comparing to Fig. 5.4, which considered stars of all spectral types, the behavior of the contours at small semi-major axis is roughly the same, while the outer edge and depth of the upper limit are limited by the reduced sample size (only 18 of the 118 target stars are M stars). For 68% confidence, fewer than 1 in 5 stars have a planet more massive than $4 M_{Jup}$ between 9.0 and 207 AU. For the models of Burrows et al. (2003) this range is 8.3 to 213 AU, and is 43 to 88 AU for the Fortney et al. (2008) models.

Baraffe et al. (2003), FGK Stars

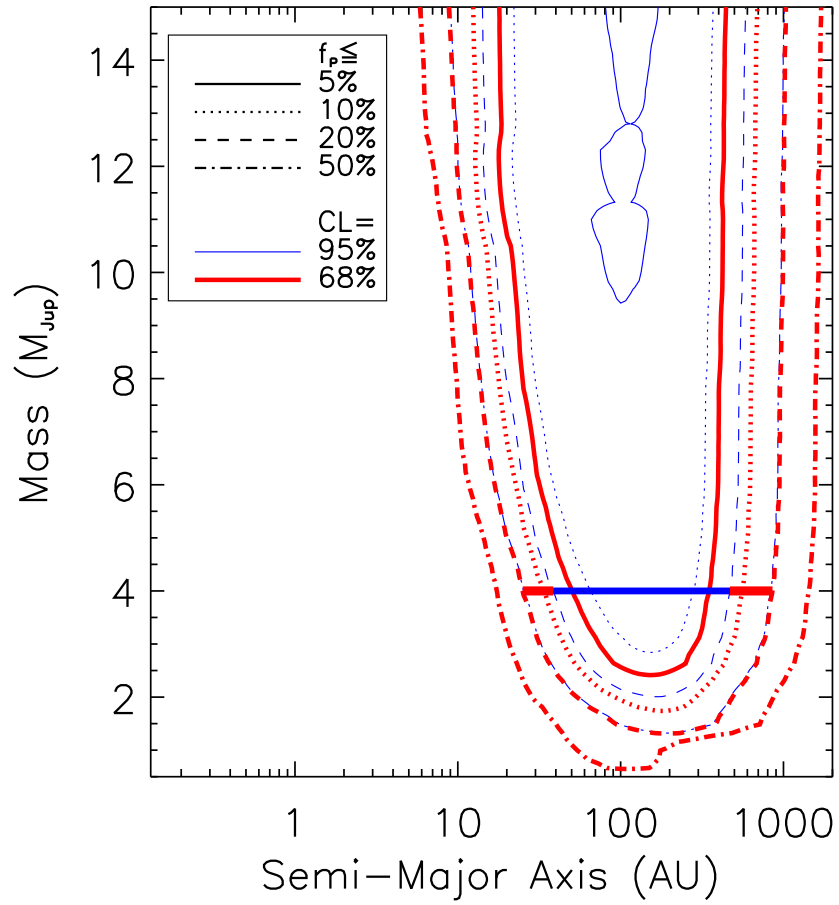


Figure 5.10 The upper limit on planet fraction, using only the FGK stars in our survey (as well as the single A star in the survey, HD 172555 A), using the models of Baraffe et al. (2003). The shapes of the contours and the behavior at large semi-major axes are roughly the same as in Fig. 5.4, when all stars were considered, but without the M stars and their favorable contrasts at small separations, the small-period planets are much less accessible. The 20% contours, at the 68% and 95% confidence levels, for planets more massive than $4 M_{Jup}$, are found between 25 and 856 AU and between 38 and 469 AU, respectively. For the Burrows et al. (2003) models, the 68% and 95% limit ranges are between 25 and 807 AU, and 40 and 440 AU; for the Fortney et al. (2008) models, the 95% confidence 20% contour never reaches $4 M_{Jup}$, but the 68% confidence range is from 59 to 497 AU.

Johnson et al. 2007 Mass Correction

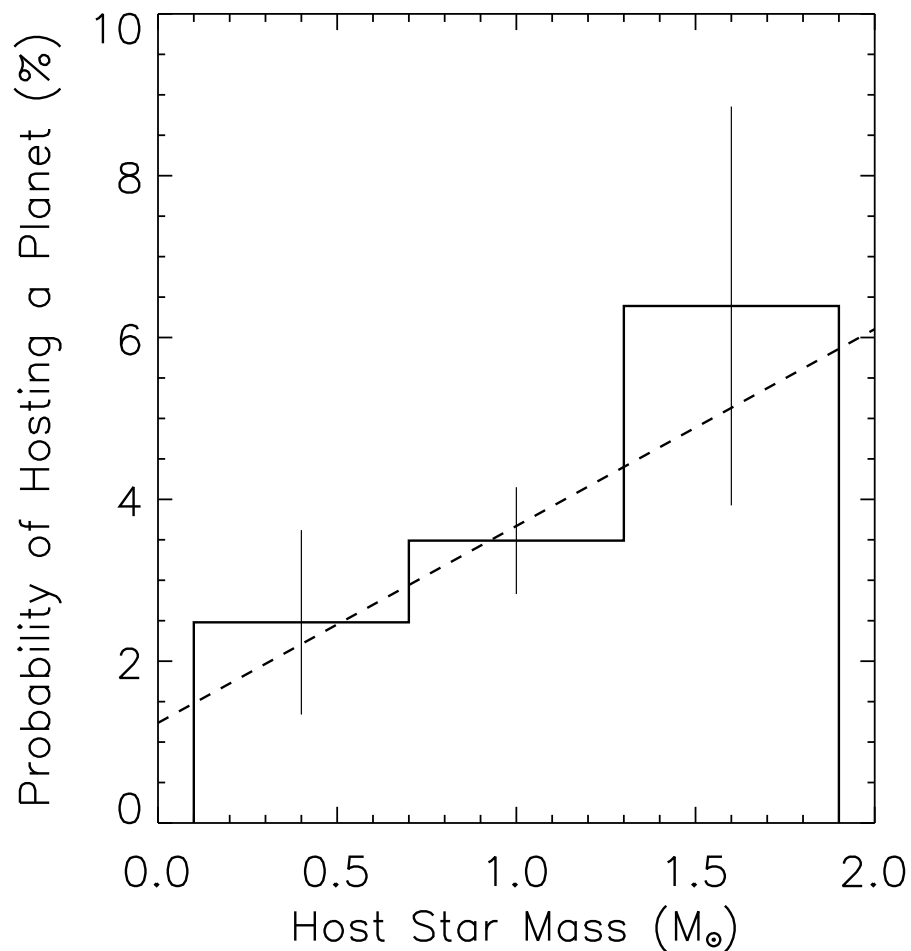


Figure 5.11 Our linear fit to the dependence of the likelihood a target star has of hosting a close-in, giant extrasolar planet as a function of stellar mass. The histogram shown is the metallicity-corrected histogram of Johnson et al. (2007) (their Fig. 6). As noted by Johnson et al. (2007), the probability for the high-mass bin is likely underestimated, so future work may show an even greater boost for the value of high-mass target stars. For the target stars considered in this work, 35 are in the low-mass bin, 78 are in the medium-mass bin, and 5 are in the bin for the highest masses.

now allow planet fraction to become a function of stellar mass (M_*) in addition to planet mass and semi-major axis (M_p and a). In that case we can specify planet fraction for the stellar mass of a solar mass ($f_{p,1.0}(a, M_p)$), and find the upper limit as with Equation 5.2, but now including an extra term for the mass correction:

$$f_{p,1.0}(a, M_p) \leq \frac{3}{\sum_{i=1}^{N_{obs}} P_i(a, M_p) mc_{1.0}(M_{*,i})} \quad (5.3)$$

where $mc_{1.0}(M_{*,i})$ is the mass correction as a function of the stellar mass of the i th star in the sum, normalized to $1.0 M_\odot$, and defined by $mc_{1.0}(M_*) = \frac{F_p(M_*)}{F_p(1.0M_\odot)}$, where F_p is the fraction of stars with a detected radial velocity planet as a function of stellar mass, using the linear fit to the Johnson et al. (2007) results. Again, going back to our earlier example, imagine that we have 10 stars, each with 50% completeness to Jupiter-like planets. If all 10 stars are 1 solar mass, then $mc_{1.0}(M_*) = \frac{F_p(1.0M_\odot)}{F_p(1.0M_\odot)} = 1$, and as before the upper limit on planet fraction (for the 95% confidence level, as given by the 3 in the numerator) is 60%. On the other hand, if only four of the ten target stars had masses of $1 M_\odot$, and the remaining six had masses of $2.5 M_\odot$, we must weight the results to account for the greater likelihood of stars of earlier spectral types to have planets. A $2.5 M_\odot$ star is twice as likely to have a planet as a solar mass star (see Fig. 5.11), so for the four stars of $1 M_\odot$, $mc_{1.0}(1.0M_\odot)$ remains 1, as before, while for the stars of $2.5 M_\odot$, this factor doubles, $mc_{1.0}(2.5M_\odot) = 2$. In this case, Equation 5.2 becomes $f_{p,1.0}(a, M_p) \leq \frac{3}{0.5+0.5+0.5+0.5+1+1+1+1+1+1} = 3/8 = 37.5\%$. Including A stars in this fictional example almost doubles the constraint we can place on the fraction of stars with a giant planet. Similarly, M stars will be weighted against to account for their decreased likelihood of having planets. As an aside, we note that while our sample is spread across spectral type (1 A star, 8 F, 33 G, 58 K, and 18 M stars), only 18 of our target stars are more massive than the sun. Despite the increased

probability of finding planets around higher mass target stars, these stars are intrinsically brighter, and so moving earlier in spectral type very quickly results in any potential planet photons being swamped by the glare of its host star (though the recent discoveries of planets around A stars, e.g. Marois et al. (2008), show that this difficulty can be overcome and produce exciting results).

In Fig. 5.12, we plot the upper limit on planet fraction for stars of $1 M_{\odot}$, using Equation 5.3. When comparing Figs. 5.9 and 5.10 with Fig. 5.4, we see that the contours at small values of semi-major axis are set mainly by the 18 M stars in our sample, while the behavior at large separations and the depth of the contours at intermediate values of semi-major axis are set by the 100 FGK stars in the sample. So it is then not too surprising that Fig. 5.12 is quite similar to Fig. 5.4, with the contours corresponding to the smallest upper limits on planet fraction shrinking slightly, and the contour at lower semi-major axis moving to the right in the figure, as M stars are now given less weight.

Alternatively, instead of normalizing to solar-type stars, we can instead consider what constraints are placed on stars of $0.5 M_{\odot}$ (about an M0 spectral type). The constraints should become more powerful, as we assume a global decrease in the planet fraction for massive planets around lower-mass stars. (Again, this applies strictly to massive planets, $>0.5 M_{Jup}$. The direct imaging surveys considered here are not sensitive to Neptune mass planets, which may be more common around M-stars: Endl et al. (2008) suggest that Hot Neptunes may be ~ 4 times more prevalent orbiting M-stars than Hot Jupiters around FGK stars) In fact, the only result of this change is to multiply a constant factor by the right-hand-side of Equation 5.3 corresponding to the ratio of the likelihood of finding a planet around a solar mass star to that of finding a planet around a star of $0.5 M_{\odot}$, or 1.5 in this case. We plot these limits on planet fraction for half solar mass stars

Baraffe, Mass Correction to $1.0 M_{\odot}$

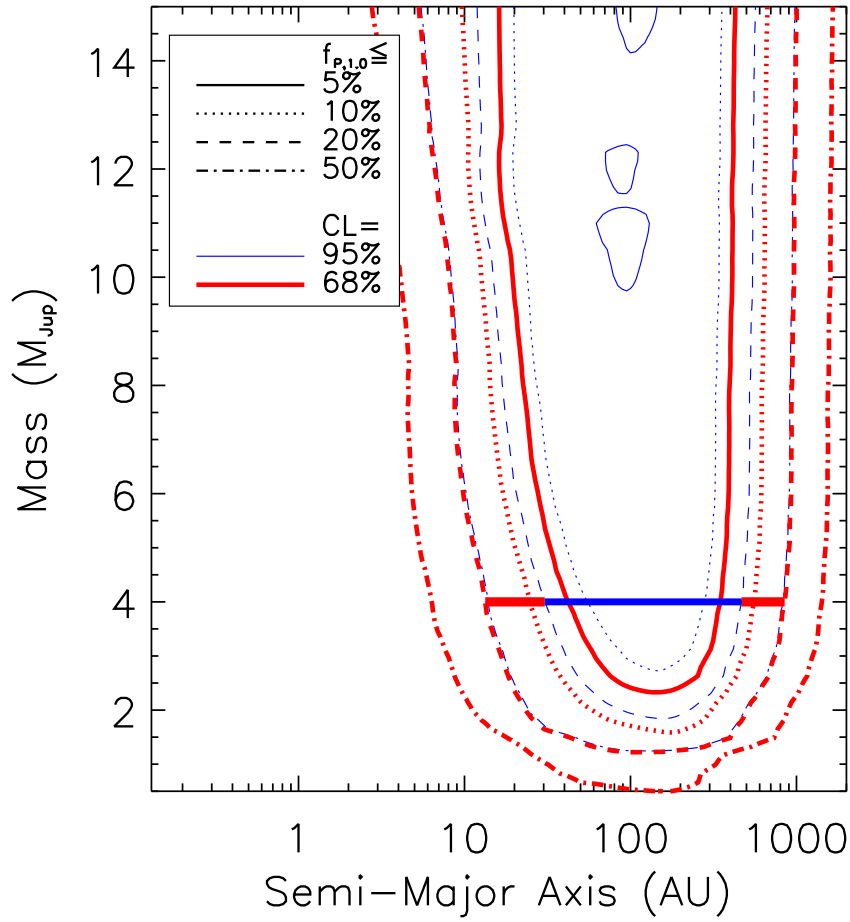


Figure 5.12 The upper limit on planet fraction for stars of $1 M_{\odot}$ ($f_{p,1.0}$), with constraints from target stars of higher and lower mass stars weighted according to a fit to the Johnson et al. (2007) dependence on stellar mass of the frequency of radial velocity planets, using the models of Baraffe et al. (2003). The plot is similar to that of Fig. 5.4, which weighted all stars equally, but the contours shrink slightly (mainly on the low separation side of the plot) as the M stars are now effectively given less weight. The 20% confidence level for planets more massive than $4 M_{Jup}$ are between 13 and 849 AU at 68% confidence, and between 30 and 466 AU for the 95% confidence level. For the Burrows et al. (2003) models, these ranges are 13 to 805 AU, and 30 to 440 AU, while for the models of Fortney et al. (2008) the limits are between 41 and 504 AU, and 123 and 218 AU.

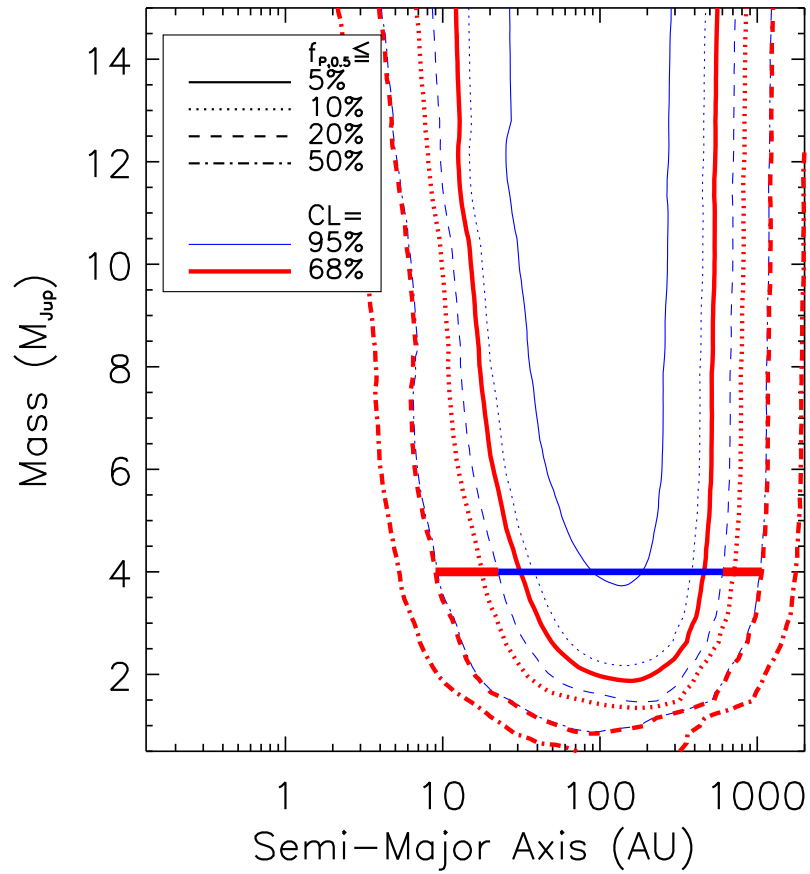
Baraffe, Mass Correction to $0.5 M_{\odot}$ 

Figure 5.13 The upper limit on planet fraction, this time normalizing to stars of a half solar mass ($f_{p,0.5}$), or about M_0 , using the models of Baraffe et al. (2003). The constraints become stronger, as expected, as our assumption going into this calculation is that lower mass stars are less likely to have planets overall. With this set of assumptions, the dearth of giant, large-separation planets around M stars is made quite clear. The possibility of lower mass, inner planets around M stars (and indeed, planets like those in our own solar system) remains, however. Fewer than 20% of M stars can have planets more massive than $4 M_{Jup}$ between 9.0 and 1070 AU at 68% confidence, and 23-605 AU at the 95% confidence level. These limits are 8.3 to 1016 AU and from 22 to 573 AU for the Burrows et al. (2003) models, as well as 26 to 656 AU and 71 to 341 AU for the Fortney et al. (2008).

in Fig. 5.13, with the models of Baraffe et al. (2003). As expected, the contours move outward, setting strong constraints on the frequency of giant planets in long-period orbits around M stars.

We also reconsider the implications of stellar mass on the constraints put on the power-law model for the semi-major axis distribution of extrasolar planets, as discussed in Section 5.3.4. Again, by using the linear fit to the results of Johnson et al. (2007), we boost the predicted number of planets for higher mass target stars, and suppress that number for lower mass stars. In Fig. 5.14 we show the same combination of three power law indices and four values of the upper cut-off as before, and the models of Baraffe et al. (2003), but now with the additional correction for the dependence of planet frequency on the stellar mass of each target star. The confidence level at which we can exclude each model drops compared to Fig. 5.7, as M stars are effectively given less weight. While the upper limit on planet fraction as a function of planet mass and semi-major axis is specific to a given stellar mass, Fig. 5.14 (and the next one, Fig. 5.15) need not be normalized to a specific spectral type. The Johnson et al. (2007) mass correction and the Fischer & Valenti (2005) planet fraction sets the absolute likelihood a given target star has a giant planet, which is used to calculate the predicted number of planets detected from our entire survey. Given our null result, this expectation value is used to set a confidence level with which the entire model (giant planet self-luminosity, giant planet fraction, dependence of planet fraction on stellar mass, and planet mass, semi-major axis, and orbital eccentricity distributions) can be rejected.

For the full range of power law index and upper cut-off, again with the Baraffe et al. (2003) models, we plot contours for the confidence level of rejection in Fig. 5.15. This figure is again generally similar to Fig. 5.8, but with the constraints

Johnson et al. 2007 Mass Correction

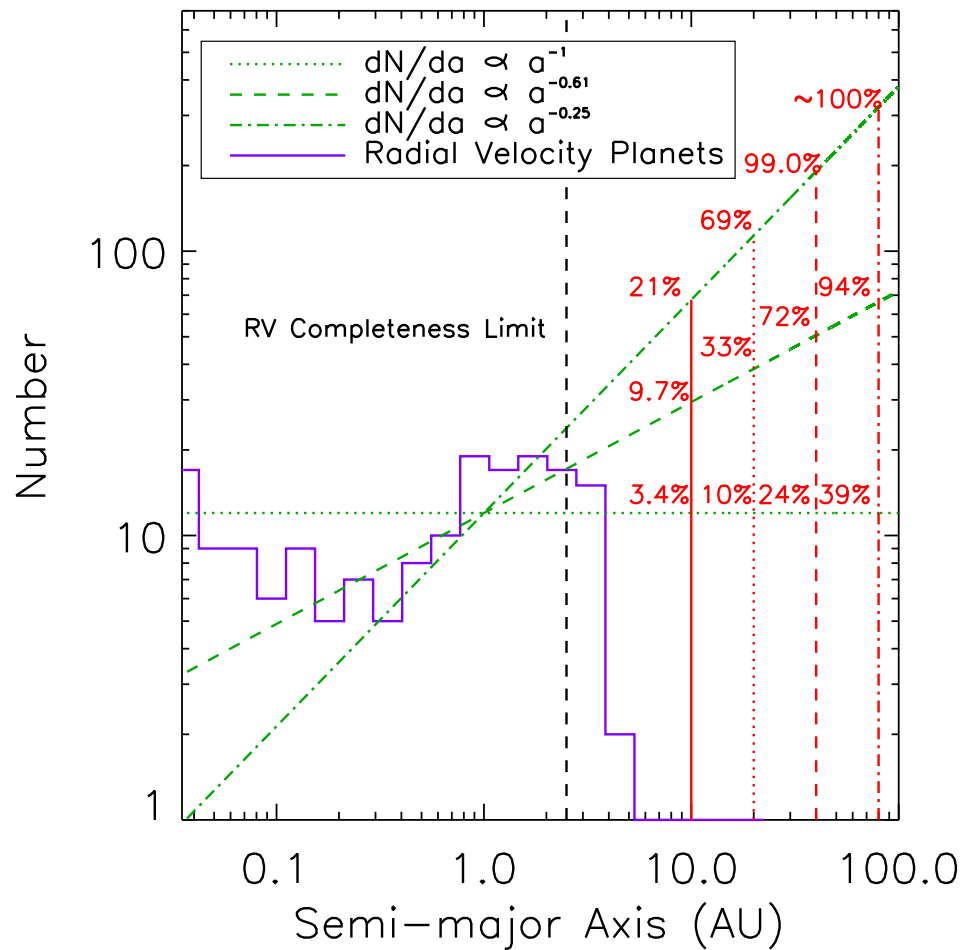


Figure 5.14 As with Fig. 5.7, power-law models for the semi-major axis distribution of extrasolar planets, and the confidence with which we can rule out these models, using the results of our survey and the models of Baraffe et al. (2003). This time, we utilize the results of Johnson et al. (2007) to appropriately give additional weight to high mass stars, which are more likely to harbor giant planets.

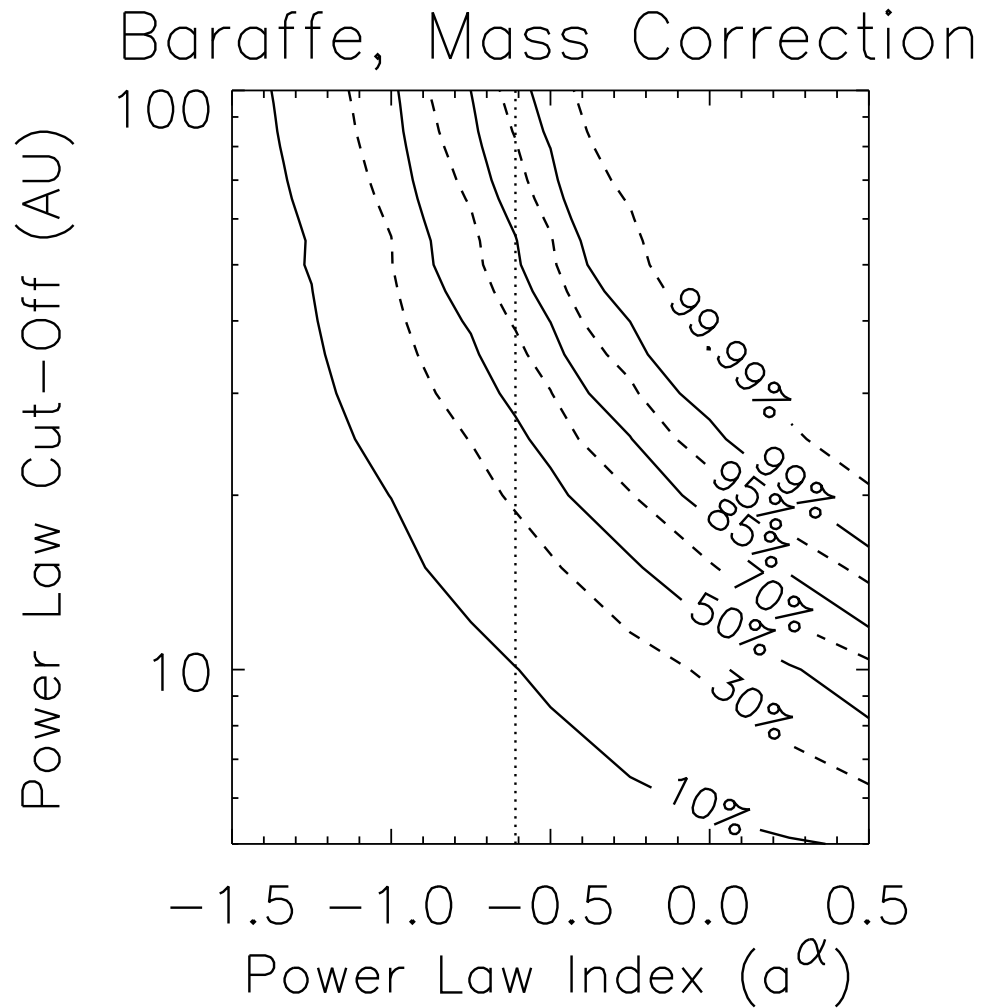


Figure 5.15 Contours showing the confidence with which we can exclude a model for the distribution of semi-major axis of extrasolar giant planets given by $\frac{dN}{da} \propto a^\alpha$ up to some upper cut-off. This figure shows the results for the models of Baraffe et al. (2003), with the stellar mass correction of Johnson et al. (2007) to account for the dependence of likelihood of finding giant planets upon the mass of the parent star. The upper cut-off for the Cumming et al. (2008) power law of index -0.61 (as marked by the dotted line) is 37 AU at the 68% confidence level, and 82 at 95% confidence. For the Burrows et al. (2003) models, the 68% and 95% confidence limits are at 36 and 82 AU, and at 104 and 234 AU for the Fortney et al. (2008) models.

slightly looser as M stars in the sample receive less weight. With the Johnson et al. (2007) mass correction, the 68% and 95% confidence level upper limits on the semi-major axis distribution cut-off are 37 and 82 AU for the Baraffe et al. (2003) models, respectively (without the mass correction, these were 30 and 65 AU). For the Fortney et al. (2008) models these move from 83 and 182 AU to 104 and 234 AU.

5.3.6 Ida & Lin (2004) Core Accretion Formation Models

As in Nielsen et al. (2008), we turn to the giant planet formation and dynamical evolution models of Ida & Lin (2004), which predict the final state of giant planets, mass and semi-major axis, following the core accretion scenario. We extract 200-300 planets from their Fig. 12, and use these masses and semi-major axes in our Monte Carlo simulations. We plot the predicted number of planets detected from these models in Fig. 5.16, with target stars divided by binarity. Even with our 118 target stars, without removing close binaries, not accounting for stellar mass (the Ida & Lin (2004) models were run with a $1 M_{\odot}$ primary star), and using the planet luminosities of the Baraffe et al. (2003) models, the Monte Carlo simulations show that for each of the three cases of Ida & Lin (2004), we would expect to detect about 1 planet for each. In Nielsen et al. (2008), we could only exclude the cases of Ida & Lin (2004) A, B, and C at 45%, 49%, and 50% confidence, respectively, with the expanded target star sample here these rejection levels only become 45%, 59%, and 63% (using the Burrows et al. (2003) models to be consistent with Nielsen et al. (2008)). When using the models of Baraffe et al. (2003), the limits for the sample of this Chapter are 38%, 58%, and 62%. The models of Ida & Lin (2004) predict very few giant planets in long-period orbits: fewer than 20% of the giant planets predicted by these models are beyond 10 AU, while our 68% confidence limit on the upper limit of the Cumming et al. (2008) power-law, 23 AU, gives

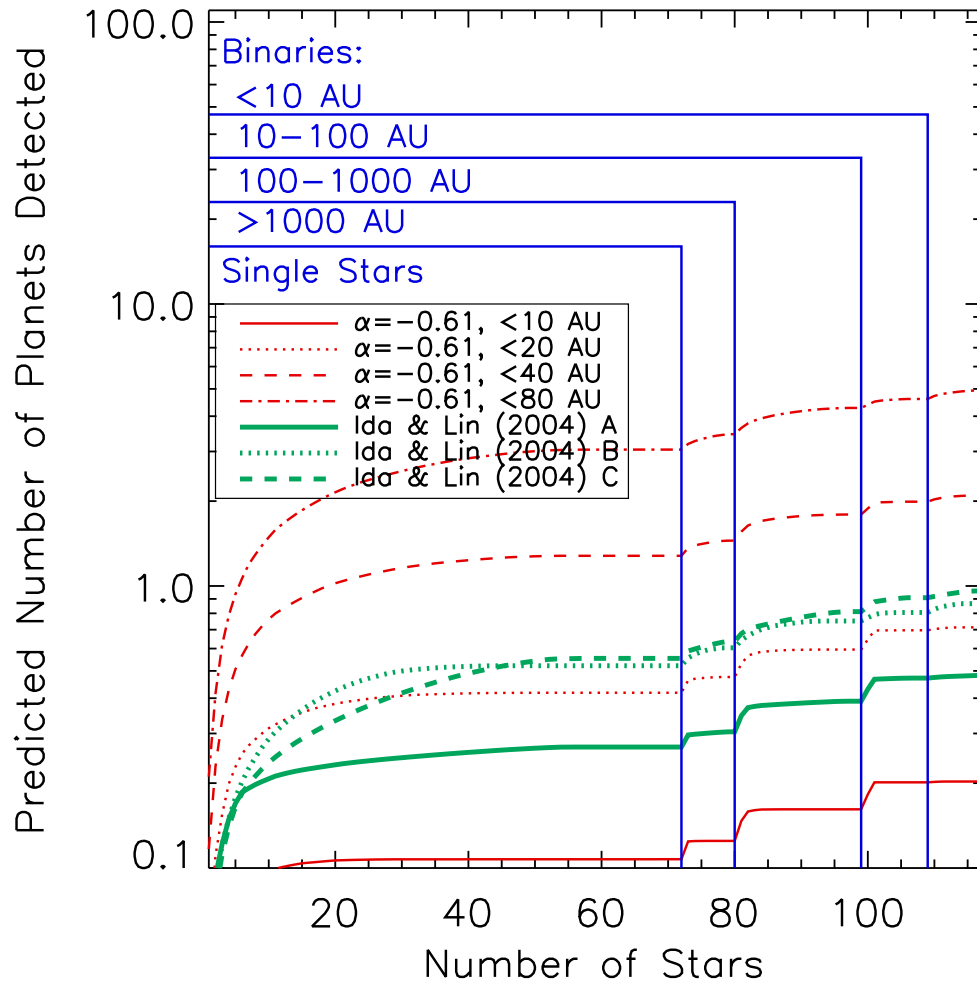


Figure 5.16 The number of planets we'd expect to detect, as a function of the number of stars in our survey. Target stars are divided into bins: one for single stars, and binaries divided by separation; within each bin the best targets are placed to the left of the graph, so they're "observed first" in this manner. Using the models of Baraffe et al. (2003), and not accounting for stellar mass effects or removing binaries, the core accretion models of Ida & Lin (2004) predict detecting between 0.5 and 1 planets with the combination of the Masciadri et al. (2005), Biller et al. (2007), and Lafrenière et al. (2007) surveys. The Ida & Lin (2004) models A, B, and C (green curves) can only be excluded with 38%, 58%, and 62% confidence, respectively.

30% of giant planets in orbits beyond 10 AU. However, our current limits can neither confirm nor rule out the Ida & Lin (2004) populations.

5.4 Discussion

Overall, the conclusions from this work are largely similar to those of Nielsen et al. (2008), that extrasolar giant planets are rare at large separations around Sun-like or less massive stars. Even for the models which predict the faintest planet NIR flux densities (Fortney et al., 2008), and weighting against the M stars (which provide the most favorable contrasts for finding planets), we find that at 95% confidence, fewer than 20% of solar-mass stars can have a planet more massive than $4 M_{Jup}$ in an orbit between 123 and 218 AU. Also, a power-law model for the semi-major axis distribution of giant planets following the results of Cumming et al. (2008) must have a cut-off of 104 AU at 68% confidence, and 234 AU at 95% confidence, again using the Fortney et al. (2008) models and the Johnson et al. (2007) mass correction.

It is worth noting that there are additional models of giant planet distributions beyond what we consider here. Cumming et al. (2008) found a good fit to distributions of close-in giant planets from radial velocity work using a single power-law for the distribution of semi-major axis. It is also possible, however, that while this is a good fit for giant planets within ~ 5 AU, it may not hold for planets at larger separations; perhaps a broken power law or some other distribution governs the population of giant planets in long period orbits. If all giant planets are formed beyond the snow line, perhaps the final distribution differs for planets that migrate inwards and those that remain beyond the snow line. Alternatively, there may be multiple methods of planet formation, such as the core accretion scenario and the disk instability model (e.g. Ida & Lin (2004) vs. Boss

(2007)), and the frequency with which each occurs is a function of distance from the star. Another possibility is that mass and semi-major axis are not independent distributions, which should become testable as the number of known exoplanets increases. Additionally, moving across spectral type may not only change the frequency of giant planets, but also their distributions of mass and semi-major axis. The analysis of Cumming et al. (2008) relied exclusively on solar-type (FGK) planet hosts, with the number of planets orbiting M stars being too small to draw any conclusions about a possible dependence of planet distributions on spectral type. These issues cannot be well addressed with further null results; they require a large number of detected planets at intermediate ($\sim 5\text{--}20$ AU) and large (>20 AU) separations to make statistically significant statements on long-period giant planet populations.

Since this Chapter was first prepared, the discovery of several planet candidates, via direct imaging, was announced; planets were detected around the three stars, all of A spectral type, HR 8799 (Marois et al., 2008), Fomalhaut (Kalas et al., 2008), and β Pic (Lagrange et al., 2009). These exciting discoveries are consistent with the predictions of Johnson et al. (2007), as even though planets within 100 AU (like the three found around HR 8799) should be easier to detect around lower-mass stars (where the self-luminosity of the star is smaller), similar planets have not been found around stars of solar mass or smaller. However, each one of these planetary systems is different from the other. Moreover, all are around more massive stars than were analyzed here. Since the full survey papers for each of these discoveries have not yet been published, it is difficult to incorporate these results into our analysis of Sun-like (and less massive) stars.

5.5 Conclusions

We have used Monte Carlo simulations to examine the null result from three direct imaging surveys (Masciadri et al., 2005; Biller et al., 2007; Lafrenière et al., 2007) to set constraints on the population of extrasolar giant planets. We use three commonly cited sets of planet models (Burrows et al., 2003; Baraffe et al., 2003; Fortney et al., 2008) in order to reach conclusions as broad as possible. Doubling the sample size, as expected, increased the strength of our null results. However, including better modeling for giant planets—using the stellar mass dependence of giant planet frequency of Johnson et al. (2007), and the core-accretion based luminosity models of Fortney et al. (2008)—have actually loosened the constraints reported in Nielsen et al. (2008). There is still some uncertainty, however, in which if any of these models of planet luminosity is correct; likely the truth may fall in between that of the optimistic “hot start” models and the somewhat pessimistic “core accretion” model.

With the COND models of Baraffe et al. (2003), a planet more massive than $4 M_{Jup}$ is found around 20% or less of FGKM stars in orbits between 8.1 and 911 AU, at 68% confidence. These limits become 7.4 to 863 AU for Burrows et al. (2003), and 25 to 557 AU for the models of Fortney et al. (2008). At 95% confidence, $4 M_{Jup}$ (and larger) planets are found around fewer than 20% of stars between 22 and 507 AU, 21 and 479 AU, and 82 and 276 AU for the models of Baraffe et al. (2003), Burrows et al. (2003), and Fortney et al. (2008), respectively.

Using the power law distribution of Cumming et al. (2008), with index -0.61, the upper cut-off for the distribution of giant planets is found at 30 and 65 AU, at the 68% and 95% confidence levels, respectively, using the models of Baraffe et al. (2003). With the models of Burrows et al. (2003) these limits become 28 and 56 AU, and with the Fortney et al. (2008) models they are 83 and 182 AU.

When we apply the Johnson et al. (2007) dependency of planet fraction on stellar mass, the M stars in our sample (where we achieve the greatest sensitivity to planets), are weighted down to account for their decreased likelihood of hosting a giant planet. As a result, the improved null results cited above retreat to levels similar to those cited in Nielsen et al. (2008) and Lafrenière et al. (2007). Given our results, fewer than 20% of solar-type stars have a $>4 M_{Jup}$ planet between 13 and 849 AU at 68% confidence with the Baraffe et al. (2003) models (also 13 and 805 AU for the models of Burrows et al. (2003), and 41 and 504 AU for the Fortney et al. (2008) models). At 95% confidence, for the models of Baraffe et al. (2003), Burrows et al. (2003), and Fortney et al. (2008), fewer than 20% of $1 M_{\odot}$ stars have $4 M_{Jup}$ planets between 30 and 466 AU, 30 and 440 AU, and 123 and 218 AU, respectively.

Applying the Johnson et al. (2007) results to the Cumming et al. (2008) model for semi-major axis distribution, giant planets cannot exist beyond 37 and 82 AU for the Baraffe et al. (2003) models at 68% and 95% confidence. The 68% and 95% confidence figures become 36 and 82 AU for the Baraffe et al. (2003) models and 104 and 234 AU for the models of Fortney et al. (2008). In general, the Johnson et al. (2007) dependence of planet fraction on stellar mass makes direct imaging planet searches more difficult, as the stars most likely to harbor giant planets are also the most luminous, giving extreme contrast ratios between star and planet that impede planet detection.

We note that while the constraints on giant planet populations from this and other work have, for the first time, reached the equivalent of extrasolar “Kuiper Belts,” there is still a gap (~ 5 - ~ 30 AU) between these results for FGKM stars and those of radial velocity surveys, which focus more on the inner solar system. Delving into this unprobed region from the direct imaging side can be achieved

two ways: increasing sensitivity to planets at small separations (achievable with dedicated planet finders using “extreme” adaptive optics, e.g. GPI (Graham et al., 2007) and VLT-SPHERE (Boccaletti et al., 2008)), or with large-scale surveys to increase the sample size of target stars, such as the 500 hour Near-Infrared Coronagraphic Imager (NICI) survey at Gemini South (Chun et al. 2008). Our technique can be applied to the results from any direct imaging survey for giant exoplanets, requiring only the target list and achieved contrast curves. By building up the statistics of null results, it will be possible to more directly focus direct imaging efforts on where planets are most likely to exist, and create a fuller picture of the distribution of extrasolar giant planets. Additionally, such an analysis helps to put the survey into context with respect to previous work, by determining what area of parameter space (in terms of both planetary and stellar parameters) the survey is probing, and so allows it to be compared directly to other surveys. There is also no limitation based on observation wavelength, even when target stars are observed by multiple surveys, since simulated planets are advanced in their orbits and compared to each contrast curve. As such, it will be interesting in future work to consider the results from L and M band surveys currently being conducted (e.g. Kasper et al. (2007)). Baraffe et al. (2003) and Burrows et al. (2003) predict planets with significantly lower contrasts to their parent stars at these longer wavelengths, and so the inclusion of results from such surveys could strengthen our null results, especially at large separations.

5.6 Online Figure Sets: Completeness Plots for Each Target Star

In the online version of Nielsen & Close (2010), we provide versions of Figures 5.8, 5.9, 5.10, 5.12, 5.13, and 5.15 for the planet flux models of Burrows et al. (2003) and Fortney et al. (2008), to complement the current versions of these plots

using the Baraffe et al. (2003) models. Additionally, we have produced online-only figure sets that give the completeness plots for each target star considered in this Chapter.

Each plot gives the completeness to planets from observations of a given target star by the three surveys considered in this article (Masciadri et al., 2005; Biller et al., 2007; Lafrenière et al., 2007), as a function of semi-major axis and planet mass. Stars that have been observed at multiple epochs by different surveys are handled by the method discussed in Section 5.3. Fig. 5.17 gives an example for the target star 2E 759, using the Baraffe et al. (2003) models of planet fluxes. This plot shows that for the Lafrenière et al. (2007) observation of this star, for planets whose orbital radius and mass place them within the inner contour, there was an 80% chance of detecting such a planet around this star, given the measured contrast curve for this observation. Fig. 5.18 and 5.19 give completeness plots for this same star, but with the planet flux models of Burrows et al. (2003) and Fortney et al. (2008), respectively. Similar plots for the remaining 117 target stars we consider here may be found in the online version of Nielsen & Close (2010)

5.7 Acknowledgments

We are grateful to the anonymous referee for providing many helpful comments that improved the quality of this Chapter. We thank Beth Biller for the publication and compilation of the SDI contrast curves, as well as a large amount of useful input in preparing these simulations. We also thank Elena Masciadri for providing published contrast curves, and the authors of Lafrenière et al. (2007) for the careful preparation and publication of their achieved contrasts and observational techniques. We thank Eric Mamajek for a great deal of assistance in determining the ages of our target stars, as well as Michael Liu for providing the

broadband-to-narrowband colors of low-mass objects. We thank Remi Soummer for the idea of presenting sensitivity to planets as a grid of mass and semi-major axis points, and we thank Daniel Apai for presenting the idea of constructing a grid of semi-major axis power law indices and cut-offs. We also thank Rainer Lenzen, Thomas Henning, and Wolfgang Brandner for their important work in the original data gathering, and helpful comments over the course of the project. This work makes use of data from the European Southern Observatory, under Program 70.C - 0777D, 70.C - 0777E, 71.C-0029A, 74.C-0548, 74.C-0549, and 76.C-0094. Observations reported here were obtained at the MMT Observatory, a joint facility of the University of Arizona and the Smithsonian Institution. Based on observations obtained at the Gemini Observatory, which is operated by the Association of Universities for Research in Astronomy, Inc., under a cooperative agreement with the NSF on behalf of the Gemini partnership: the National Science Foundation (United States), the Science and Technology Facilities Council (United Kingdom), the National Research Council (Canada), CONICYT (Chile), the Australian Research Council (Australia), Ministério da Ciência e Tecnologia (Brazil) and SECYT (Argentina) This Chapter makes use of data products from the Two Micron All-Sky Survey, which is a joint project of the University of Massachusetts and the Infrared Processing and Analysis Center/California Institute of Technology, funded by the National Aeronautics and Space Administration and the National Science Foundation. This research has made use of the SIMBAD database, operated at CDS, Strasburg, France. ELN is supported by a Michelson Fellowship, without which this work would not have been possible. LMC was supported by an NSF CAREER award and by NASA's Origin of Solar Systems program.

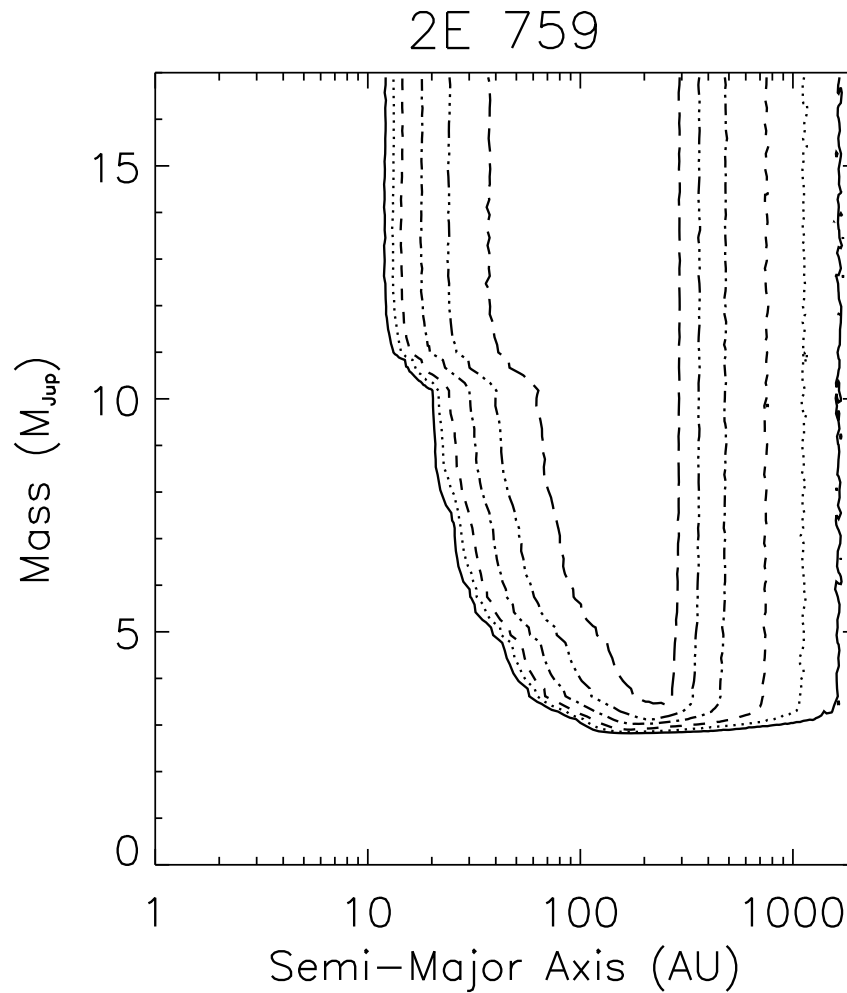


Figure 5.17 The completeness to planets for this target star, 2E 759, as a function of orbital semi-major axis and planet mass, based on all observations of this star from this work, using the models of Baraffe et al. (2003). A given contour is only plotted if observations of the star have reached that level of completeness; if no contours are plotted, then for no set of planet parameters are the observations 5% complete to planets. The contours plotted (from outside to inside) are 5% (solid line), 10% (dotted line), 20% (short dashed line), 40% (short dashed-dotted line), 60% (short dashed-dotted-dotted-dotted line), and 80% (long dashed line). Plots for the other 117 target stars are available in the online version of Nielsen & Close (2010).

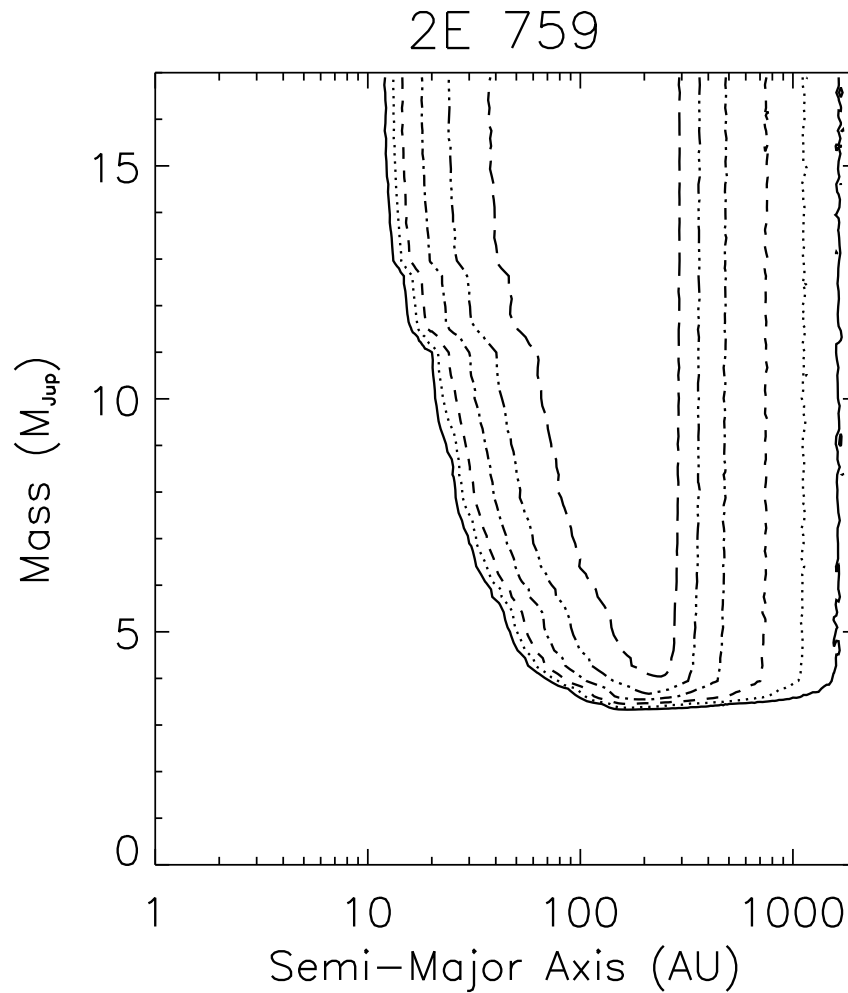


Figure 5.18 The completeness to planets for this target star, 2E 759, as a function of orbital semi-major axis and planet mass, based on all observations of this star from this work, using the models of Burrows et al. (2003). A given contour is only plotted if observations of the star have reached that level of completeness; if no contours are plotted, then for no set of planet parameters are the observations 5% complete to planets. The contours plotted (from outside to inside) are 5% (solid line), 10% (dotted line), 20% (short dashed line), 40% (short dashed-dotted line), 60% (short dashed-dotted-dotted-dotted line), and 80% (long dashed line). Plots for the other 117 target stars are available in the online version of Nielsen & Close (2010).

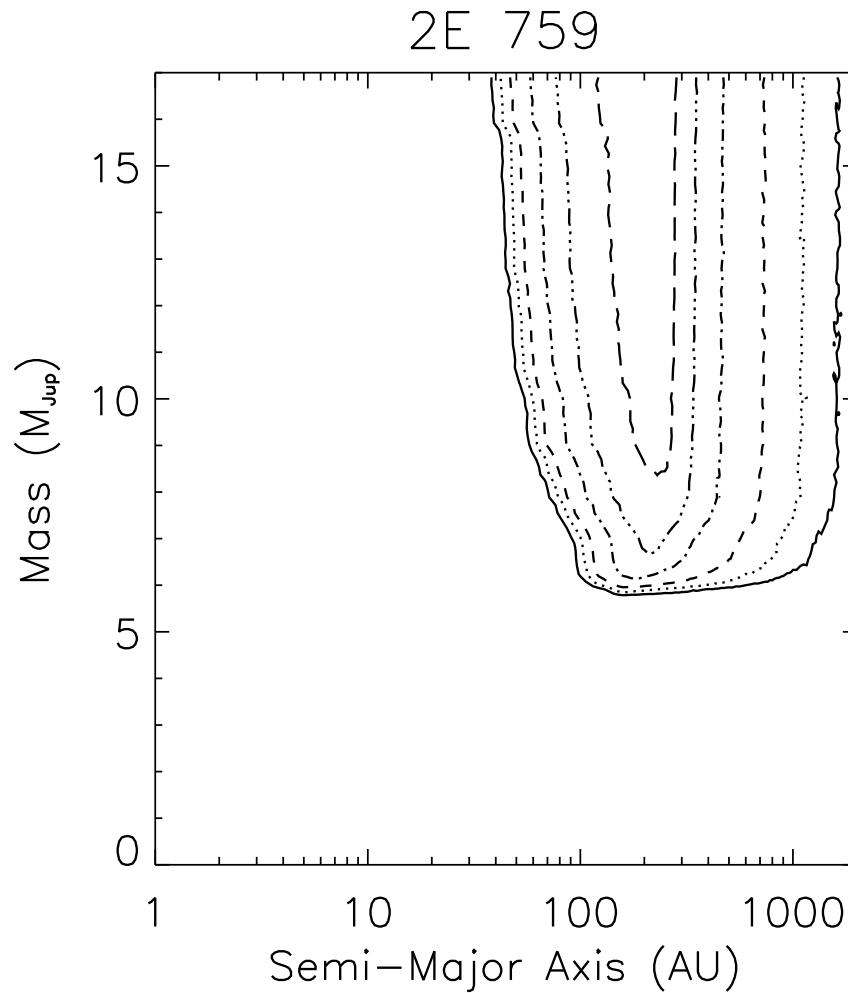


Figure 5.19 The completeness to planets for this target star, 2E 759, as a function of orbital semi-major axis and planet mass, based on all observations of this star from this work, using the models of Fortney et al. (2008). A given contour is only plotted if observations of the star have reached that level of completeness; if no contours are plotted, then for no set of planet parameters are the observations 5% complete to planets. The contours plotted (from outside to inside) are 5% (solid line), 10% (dotted line), 20% (short dashed line), 40% (short dashed-dotted line), 60% (short dashed-dotted-dotted-dotted line), and 80% (long dashed line). Plots for the other 117 target stars are available in the online version of Nielsen & Close (2010).

CHAPTER 6

CHOOSING THE TARGET LIST AND OBSERVING STRATEGY FOR THE
GEMINI NICI PLANET-FINDING CAMPAIGN

We describe the method by which we constructed the final Gemini NICI Planet-Finding Campaign target list. By combining numerous lists and catalogs, we construct an input list of 1352 nearby, young stars accessible from Gemini South. The results of Monte Carlo simulation show that the survey design and final target list are highly dependent on the assumptions and models that are input into the simulations. The final choice of target list is made to balance these competing directions, and to have a final result from the survey that addresses as many possibilities for planet populations and luminosity models as possible.

6.1 The Near Infrared Coronagraphic Imager (NICI)

The Near Infrared Coronagraphic Imager, or NICI, is a specialized instrument designed specifically for the purpose of directly imaging giant extrasolar planets. The instrument makes use of four techniques for achieving high contrast imaging at small separations: a high-order adaptive optics system, a Lyot coronagraph, a beam splitter with dual science cameras to perform Simultaneous Differential Imaging, and the ability to operate with the derotator off to utilize Angular Differential Imaging. The 85-element curvature wavefront sensor routinely returns $\sim 40\%$ Strehl in the H-band, for good observing conditions (better than median seeing for Gemini South, $\sim 0.5''$) and a bright ($V < 10$) guide star (as NICI uses a visible wavefront sensor, the V magnitude of the star is key). The partially transmissive coronagraphic mask greatly attenuates the starlight while allowing for photometric and astrometric measurements using the residual starlight that is

transmitted through the mask (Chun et al., 2008). A 50/50 beamsplitter sends light to two science cameras (Holmes and Watson), and in SDI mode the two beams are passed through medium band (4%) filters on either side of the $1.6\ \mu\text{m}$ methane bandhead. Fig. 6.1 shows NICI data with a simulated methane-rich companion placed in the data: the companion is heavily attenuated in the on-methane filter, while the residual stellar halo and speckles are identical between the two images. Finally, by allowing the image plane to rotate throughout the observation (ADI), speckles (especially at larger separations, where there's more sky rotation) are further reduced in amplitude. The final contrasts achieved by the NICI instrument are 15 magnitudes at $1''$ separation, deeper than any other instrument operating to date (Liu et al., 2010). Mounted at the 8.1m Gemini South telescope in Chile, the camera was commissioned in 2008, and is currently conducting science operations.

6.1.1 The Gemini NICI Planet-Finding Campaign

In order to make the optimal use of this instrument, Gemini has allocated 500 hours of guaranteed observing time to the Gemini NICI Planet-Finding Campaign. Led by PI Michael Liu, the Campaign seeks to answer fundamental questions about the nature and distribution of extrasolar planets by leveraging the superior capabilities of the instrument and the tremendous opportunity provided by the large amount of observing time. The Campaign time is allocated in “semi-classical” mode, with a block of time (typically ~ 1 week per month) assigned to the NICI Campaign, with Campaign observers monitoring the telescope observations in Chile via video link. When the seeing drops below $0.6''$, Campaign observations begin, thus saving the Campaign observing time for only the best seeing conditions. The Campaign has already discovered two previously unknown brown dwarf companions to target stars, and has published analyses of

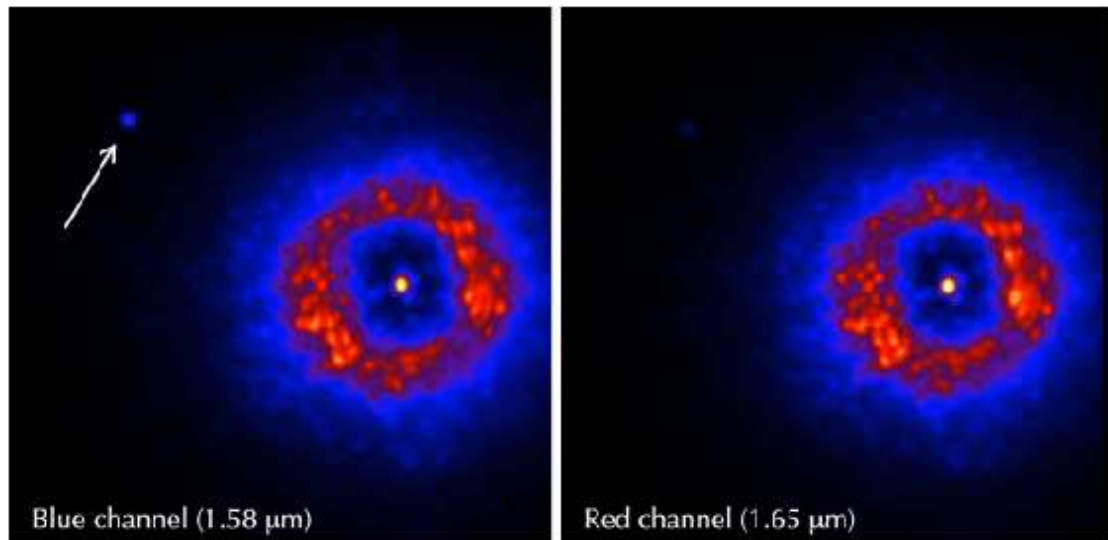


Figure 6.1 NICI data showing the SDI mode in action; the left image goes through the medium band “off-methane” filter, and so the artificial companion (upper left) is seen at normal brightness. The right image is the “on-methane” filter, which would attenuate a methane-rich object, as this artificial companion is assumed to be. Since the stellar halo and speckles are identical in the two filters, the two images may be subtracted from each other, leaving the companion’s signal behind. Figure from Liu et al. (2010).

these objects (Biller et al., 2010; Wahhaj et al., 2011).

6.2 Defining the Input Target List

With 500 hours of telescope time on a new instrument granted to the Campaign, our goal was to determine the most efficient way to utilize that time to answer the science questions of the Campaign. Our first step was to assemble an input target list broad enough to encompass as many nearby, young stars as possible. The final target list could then be drawn from this input list, based on our analysis of the individual stars. We used our planet population simulation code to determine the completeness of NICI to detecting planets around each of these stars, using a variety of assumptions about planet populations and observing strategies.

6.2.1 VLT Adaptive Optics H and Ks Band Imaging, SDI, GDPS Targets

There are 132 unique target stars observed at the VLT (with broadband H and Ks imaging (Masciadri et al., 2005)), at the MMT and VLT using Simultaneous Differential Imaging (Biller et al., 2007), and at Gemini North using Angular Differential Imaging (Lafrenière et al., 2007). These stars are all within ~ 50 pc, and either belong to established moving groups, or have ages determined by calcium H&K emission or lithium absorption. Since we have the individual contrast curves for each of these stars from the actual observations, the simulated planets are first run against those contrast curves before being compared to the NICI curve, so that only simulated planets that could be detected by NICI but were below the 5σ detection limit of all previous observations are considered detectable. (The simulated planets are advanced in their orbits from the times of the initial observations, e.g. ~ 2005 for VLT H and Ks band imaging, to an epoch of 2009.0 for a potential NICI observation. This is a relatively minor effect, as we're most sensitive to planets in very long period orbits). 95 of these stars have declinations

south of $+30^\circ$, and these are included in the list.

6.2.2 A Stars

A stars have been shown more likely to harbor close-in (periods less than 4 years) giant (greater than $2 M_{Jup}$) planets by Johnson et al. (2007), when compared to solar-type stars, though their greater intrinsic brightness makes detecting these planets challenging. To build up a sample of A stars, we've taken all stars in the Hipparcos catalog (Perryman et al., 1997) that are within 100 pc, have a spectral type of A or B, and luminosity class V or IV, and are below $+30^\circ$ in declination, yielding an additional 297 stars. Since there isn't a robust method to determine ages of these stars, we assume the stars have a uniform probability of being between 5 Myr and the main sequence lifetime of the star (depends on spectral type, going from 400 Myr for A0 to 1.8 Gyr for A9). we use "statistical ages" to determine the final probability of NICI detecting a planet around these stars, by simulating planets at ten ages (uniformly spaced in log space). Then, this curve (probability versus age) is interpolated into linear space, and the average probability is returned for each star.

6.2.3 Hipparcos R'_{HK} Stars

Calcium R'_{HK} is a good tracer of age for stars of spectral type $\sim F$ to $\sim K5$. We compiled stars from three large spectroscopic surveys of Calcium R'_{HK} emission (Gray et al., 2003b, 2006b; Wright et al., 2004), and used the age conversion of Mamajek & Hillenbrand (2008), keeping all stars younger than 1 Gyr, and cross-referenced with the Hipparcos catalog (Perryman et al., 1997), to limit this sample to stars within 50 pc and south of $+30^\circ$, giving 402 stars.

6.2.4 Additional Moving Group Stars

There are ~ 150 -200 stars in well-known young, nearby moving groups, not all of which were observed by the surveys described in 6.2.1. Using the membership lists of Zuckerman & Song (2004) and López-Santiago et al. (2006), removing binaries within $3''$ and stars north of $+30^\circ$, we add 183 stars to our target list. In general, these stars have more robust age determinations than stars from other samples, since the large number of stars per moving group (20-60) means that random noise in the age metrics can be averaged out and a more consistent age can be assigned to all members of the group.

6.2.5 Young Nearby M Stars

Neill Reid and collaborators have compiled a sample of young, nearby M stars based on activity and X-ray emission, with distances from photometric parallax. The ages of these stars are estimated to be less than 300 Myr (Allen & Reid, 2008). These were observed at Gemini with Altair, and the contrast curve of Daemgen et al. (2007) is applied for those objects observed at Gemini to exclude simulated planets that could have already been detected. As with the A stars, we allow a uniform distribution of ages, this time between 5 and 300 Myr. We again screen for binaries within $3''$ and stars above $+30$. In addition to these publicly available stars, we also use a private compilation of additional M stars based on additional work by these authors (Liu, 2008), for a total of 78 additional target stars.

6.2.6 Debris Disk Host Stars

Stars that are known to host debris disks may be more likely to harbor planets, and so we also include stars with known debris disks from Moór et al. (2006), Rhee et al. (2007), and Hillenbrand et al. (2008). Since the only criteria for inclusion in this catalog is the presence of a debris disk (as determined by imaging or

an infrared excess), these stars tend to be older on average than stars from other sources. There are 105 of these stars in the input target list. It is important to note that the presence of (bright) debris disks may lower our constraints to planets; we do not consider that effect quantitatively in our analysis here, though we caution that the final reduced data (and subsequent contrast curves) may be less sensitive than the estimates used in the simulations.

6.2.7 Additional Sources

We also include 104 stars from the Spitzer legacy program “The Formation and Evolution of Planetary Systems” (FEPS), as given by Carpenter et al. (2009). We add to this 81 stars from Su et al. (2006), a MIPS study of nearby A stars. And finally, we include 7 stars from the HST NICMOS survey conducted by Lowrance et al. (2005). We use stars that have declination below +30, and adopt the ages given by these individual papers. In total, the input target list consists of 1352 unique stars.

6.3 Simulation Parameters

With this input target list, we proceed to run Monte Carlo simulations on each target star, and determine the probability of detecting a planet around every star, given the simulations’ assumptions of planet populations and survey construction.

For all planet simulations, we assume a power-law distribution that matches observations of known radial velocity planets (Cumming et al., 2008): a power-law of index -0.61 that continues to some outer cut-off, beyond which planets are no longer found. Mass follows a power-law distribution of index -1.2, also from the Cumming et al. (2008) analysis. Orbital eccentricity is given by a fit to radial velocity planets, which are nicely modeled by simple linear fits, one for Hot

Jupiters (periods less than 21 days) and another for all other planets. Geometric distributions are used to model the viewing angles and orbital phases, and finally we solve for the separation between star and planet on the plane of the sky, which we convert to arcseconds given the distance to the star.

We compute the fluxes of the simulated planets given the age of the target star and the mass of the simulated planets, using the two classic models of giant planets, Burrows et al. (2003) and Baraffe et al. (2003), and the new core-accretion models from Fortney et al. (2008). To determine the probability a given target star has a planet, we use the Fischer & Valenti (2005) volume-limited sample, which gives $\sim 5\%$ of stars having a planet within 2.5 AU above $1.6 M_{Jup}$, which we then scale given the power-law distributions for mass and semi-major axis. Then, the sum of the probability of finding a giant planet for each target star, evaluated across all target stars, gives the predicted number of planets from the end of the survey.

We run the simulations with our current NICI contrast curve (Fig. 6.2), with three different parameters being toggled on and off. 1) We insert a population of GQ Lup-like objects (giant planets at large separations, Neuhäuser et al. (2005)), which consist of the same mass and eccentricity distributions, but with semi-major axis now a constant probability distribution between 60 and 500 AU, and a star having a 2% probability of hosting such a planet. 2) Switching between the 20% and median Gemini South seeing values, which set the Strehl as a function of guide star V magnitude. The strehl scales the contrast curve, as well as the faint limit for detecting a planet, regardless of separation. 3) Finally, we either allow all stars to have an equal likelihood of hosting planets, or use the Johnson et al. (2007) results to make a linear fit to the likelihood of harboring a giant planet as a function of stellar mass, and correct the expected number of detected planets

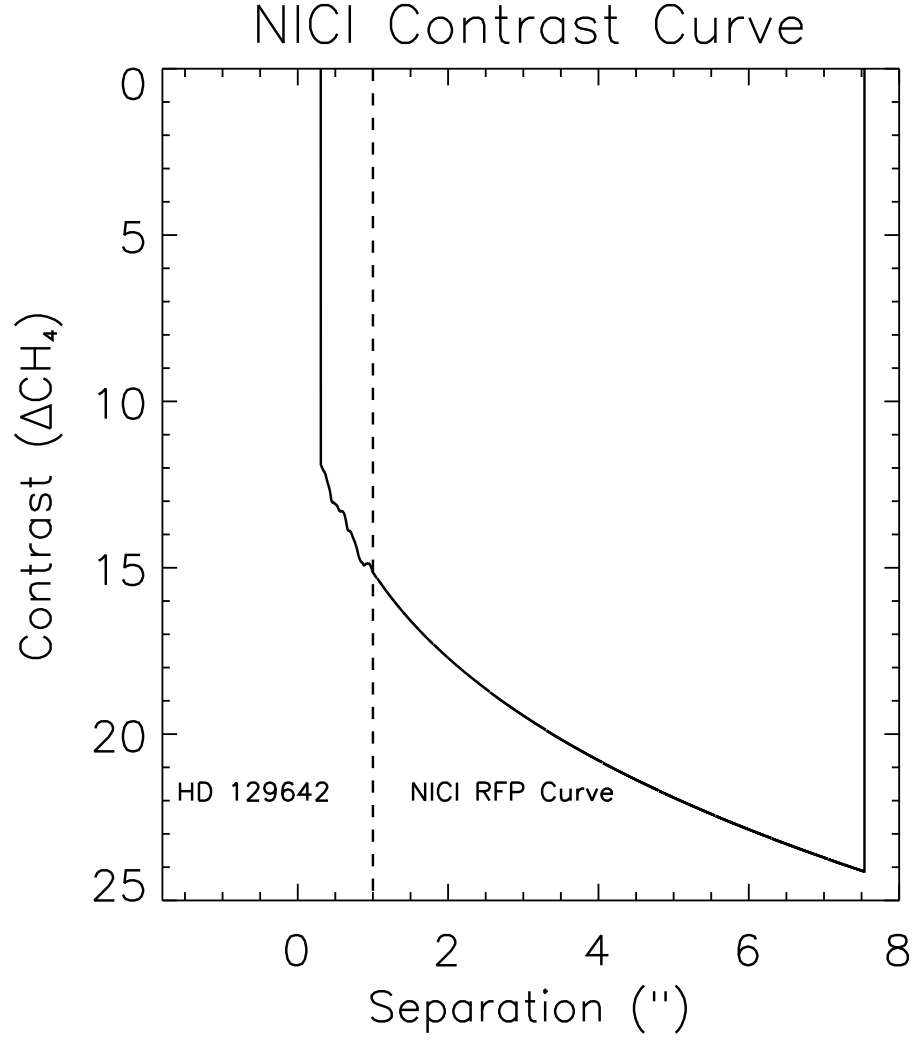


Figure 6.2 The contrast curve used to simulate the performance of NICI during the survey. Within an arcsecond, the curve is generated by Zahed Wahhaj in July 2008, for a single NICI target star observed during commissioning. Beyond 1", we use the NICI Request for Proposal (RFP) curve. We note that this is the contrast curve only, which can in theory reach arbitrarily faint planets, especially for faint target stars. For the simulations themselves, we use the more physical constraint that no planet fainter than $m_H=23$ can be detected from a NICI observation.

for this factor. This results in 8 sets of simulations, with the most optimistic being one with GQ Lup-like objects, 20% seeing, and no Johnson et al. (2007) scaling of planet fraction for stellar mass, and the worst having no GQ Lup-like objects, median seeing, and the Johnson et al. (2007) stellar mass scaling.

Finally, we do each of these simulations at four exposure times, 30 minutes, one hour, two hours, and four hours, scaling the contrast curve and minimum detectable planet flux by the square root of the exposure time.

6.4 Constructing a Survey

If we have 420 hours for the full NICI survey (the remaining 80 hours are reserved for follow-up of interesting objects), we need to find a good balance between the number of stars we want to observe and the exposure time for each target star. We're allowing 15 minutes of overhead per star for slewing and locking onto the star, as well as a 30% overhead on the total on-star integration time. Using these constraints, Fig. 6.3 gives the possible survey size as a function of integration time.

In Fig. 6.4, we give the range of expectation values for predicted number of planets across the eight sets of simulation parameters. Each pair of connected data-points go from the model which predicts the most detected planets (20th percentile seeing, a population of GQ Lup-like objects at large separations, and no scaling for the likelihood of having a giant planet with stellar mass), to the more pessimistic set (median seeing, no large-separation massive objects like GQ Lup, and weighting against M stars by scaling the planet fraction by stellar mass, as given by Johnson et al. (2007)). We denote four survey designs by the ID numbers 1, 2, 3, and 4, with exposure times of 30 minutes, 1 hour, 2 hours, and 4 hours, respectively, which allow for survey sizes of 556, 323, 175, and 92 stars. The

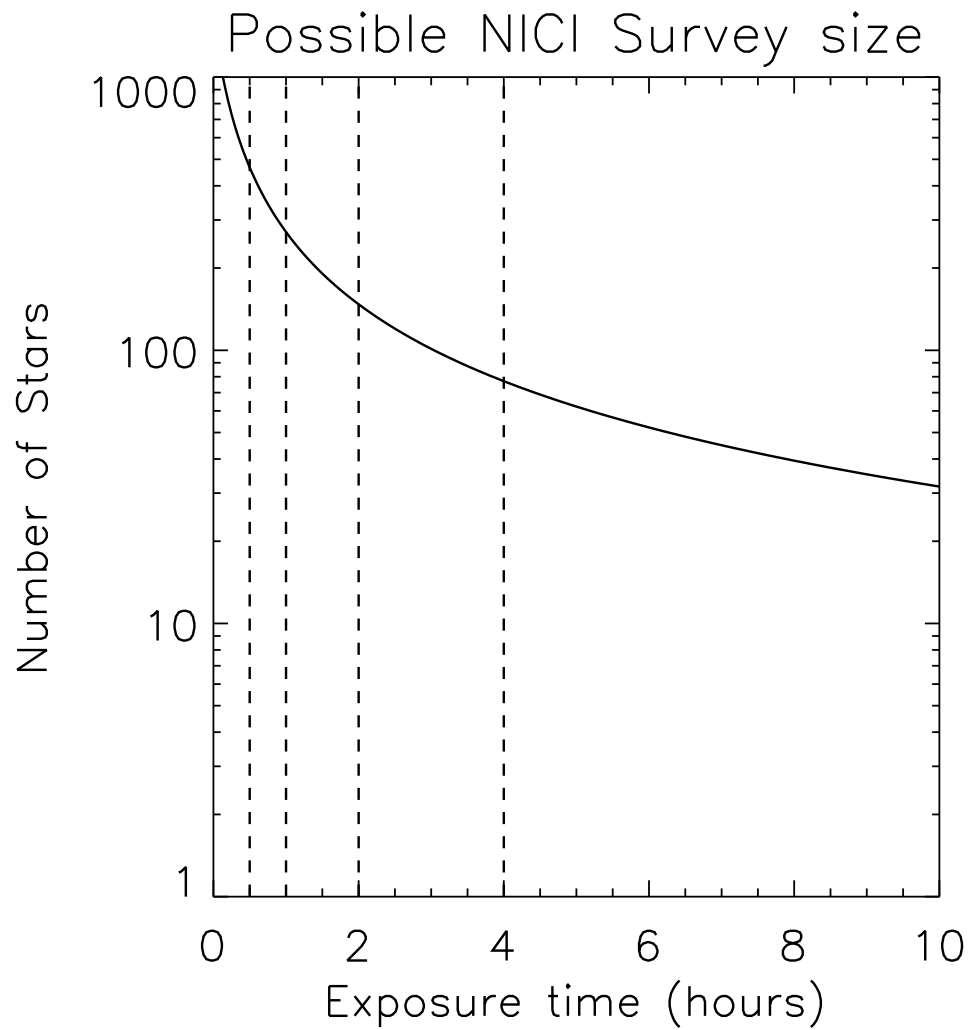


Figure 6.3 The number of stars we could include in our survey, assuming we have 420 hours of telescope time. The calculation assumes a 15 minute per star overhead, and a 30% overhead on the total integration time. Exposure times of 30 minutes, one hour, two hours, and four hours are marked.

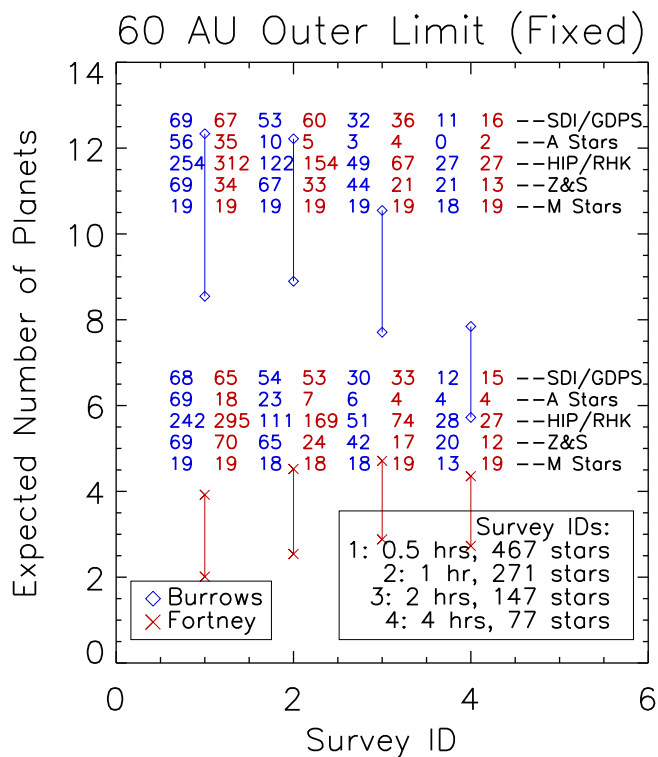


Figure 6.4 The predicted number of planets from our survey using two sets of models for planet fluxes (Burrows et al., 2003; Fortney et al., 2008), and with four basic survey designs: from a large survey with short integration times (467 stars at half an hour each) to a deep survey with much fewer stars (4 hours per star on 77 stars), and two other designs between the two extremes. The blue numbers (left) give, while using the Burrows et al. (2003) models, how many stars in each survey design come from the five target star sources, previously observed stars at the VLT, MMT, and Gemini North for SDI/GDPS, the A star sample, Hipparcos stars selected by calcium R'_{HK} emission, unobserved moving group stars (Z&S, denoting that most of these stars are from Zuckerman & Song (2004)), and the young, nearby M stars of Allen & Reid (2008). The red numbers (right) give the same target breakdown, only for the Fortney et al. (2008) models. The two connected data points at each survey type denote the most optimistic set of simulation parameters (20% seeing, GQ Lup-like objects, and no scaling for stellar mass), and the most pessimistic combination (median seeing, no GQ Lup-like objects, and using the Johnson et al. (2007) mass scaling). The top set of numbers correspond to the optimistic models (uppermost set of blue diamonds and red crosses), and the lower numbers are for the pessimistic case.

two sets of connected points correspond to the models of planet luminosities of Burrows et al. (2003) and Fortney et al. (2008), denoted by blue circles and red crosses, respectively.

For each survey design, the stars with the largest likelihood of planet detection are placed into the survey. The numbers in the center of the figure give what number of stars were drawn from each of the five sets of target stars. The top set of numbers is for the optimistic case, represented by the upper datapoints for both sets of luminosity models, and the bottom numbers for the pessimistic case. Frustratingly, the best survey design for the Burrows et al. (2003) models is #2, with 323 stars at 1 hour integration times, with the predicted yield of planets dropping significantly at larger exposure times and fewer targets. The Fortney et al. (2008) models, on the other hand, suggest the best survey design is to increase exposure time to two hours, and cut the number of stars by a half.

We note that this and subsequent plots were made when the input target list was only partially complete. As a result, these plots only show 467 stars, instead of having the full 1352 target stars that comprises the final input target list. However, since these were the plots used to determine the design of the NICI survey, we include them here.

6.4.1 Scaling the Upper Cut-Off with Spectral Type

Another likely model of planet populations would not only have M stars with fewer overall planets, but have M-star planets at closer star-planet separations. To account for this, we've also run a set of simulations with the semi-major axis cut-off scaled by the location of the snow line in the disk (this scales as the square root of the star's total luminosity), using 60 AU as the cut-off for solar-mass stars, and scaling it up or down based on spectral type of the target star. The GQ Lup-like objects in the optimistic cases are not scaled, and still reside between 60 and

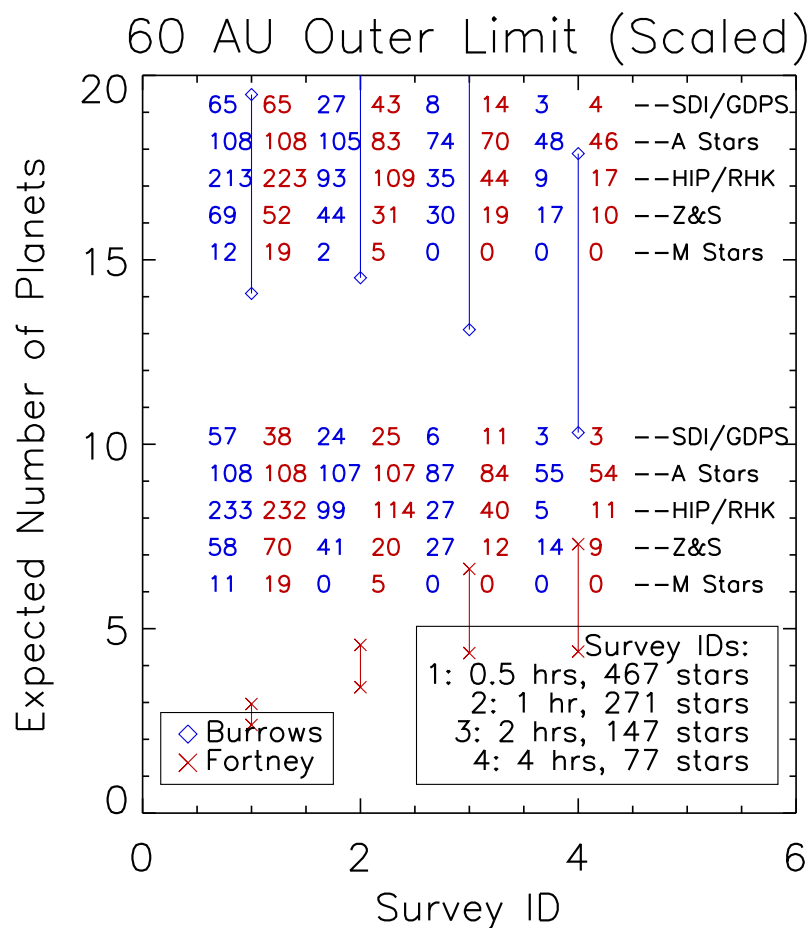


Figure 6.5 The same as Fig. 6.4, except with the outer semi-major axis limit is allowed to vary as a function of luminosity of the target star (to track the snow line). As we'd expect, M stars become less viable targets, while the A stars become very popular, accounting for most of the detectable simulated planets. The optimal survey design ranges from 1 to 4 hours, depending on the choice of models used for planet fluxes, and the input planet population models.

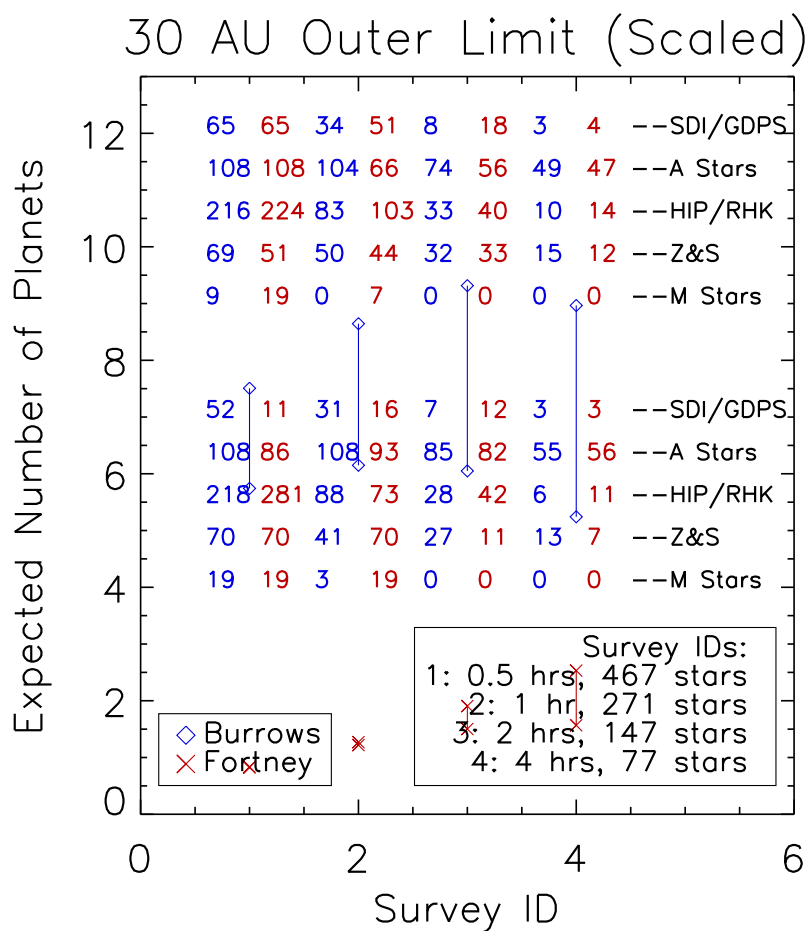


Figure 6.6 The same as Fig. 6.5, except with the outer semi-major axis limit now 30 AU.

500 AU for stars of all spectral types, in 2% of cases. Fig. 6.5 gives the results with this scaled outer semi-major axis limit. The “sweet spot” for both models in terms of survey design is about the same as it was with Fig. 6.4. This rewarding of A stars gives us many more predicted planets, mostly from the earlier spectral type target stars.

We must also consider the default of 60 AU for the outer cut-off: it is somewhat optimistic. When we consider the null result from the VLT H and Ks, SDI,

and GDPS surveys, using the stellar mass dependence of stellar mass from Johnson et al. (2007) (but with no GQ Lup-like objects, and no scaling of the outer cut-off of semi-major axis with stellar mass), we can exclude 60 AU or larger as the upper limit on semi-major axis at 92% confidence, for the models of Burrows et al. (2003). With the more pessimistic Fortney et al. (2008) models this limit drops to 68%, or about 1σ . In order to consider other possible descriptions of planet populations, we change this outer limit in to see what it does to our predictions. So we also consider these results for an outer limit of 50, 40, and 30 AU (excluded to 88%, 81%, and 70% confidence for the Burrows et al. (2003) models, and 55%, 40%, and 25% confidence for the models of Fortney et al. (2008)).

It is important to remember that these numbers are only for the case with a fixed outer limit, which is constant across all spectral types, which is not the model we're simulating here. The VLT broadband, SDI, and GDPS surveys combined contained only a single A star, so a model of planet populations that makes planet detection more likely would not be significantly constrained by previous null results.

We plot the results of the smallest outer cut-off, 30 AU, in Fig. 6.6. The main effect, as expected, is we expect to detect fewer planets overall (note the values of the Y-axis). As we move to smaller upper limits for semi-major axis, the Fortney et al. (2008) models maintain the same general shape, with the longest exposure times producing the most planets. This makes sense: given the faintness of these models, we need the longest exposure times to reach planets. The Burrows et al. (2003) models actually switch from advocating a 1 hour exposure time to 2 hours, but not by a large amount, and this changes whether we use the optimistic or pessimistic simulation parameters. Across the range of outer cut-off, the overall composition of the survey doesn't vary to a large extent.

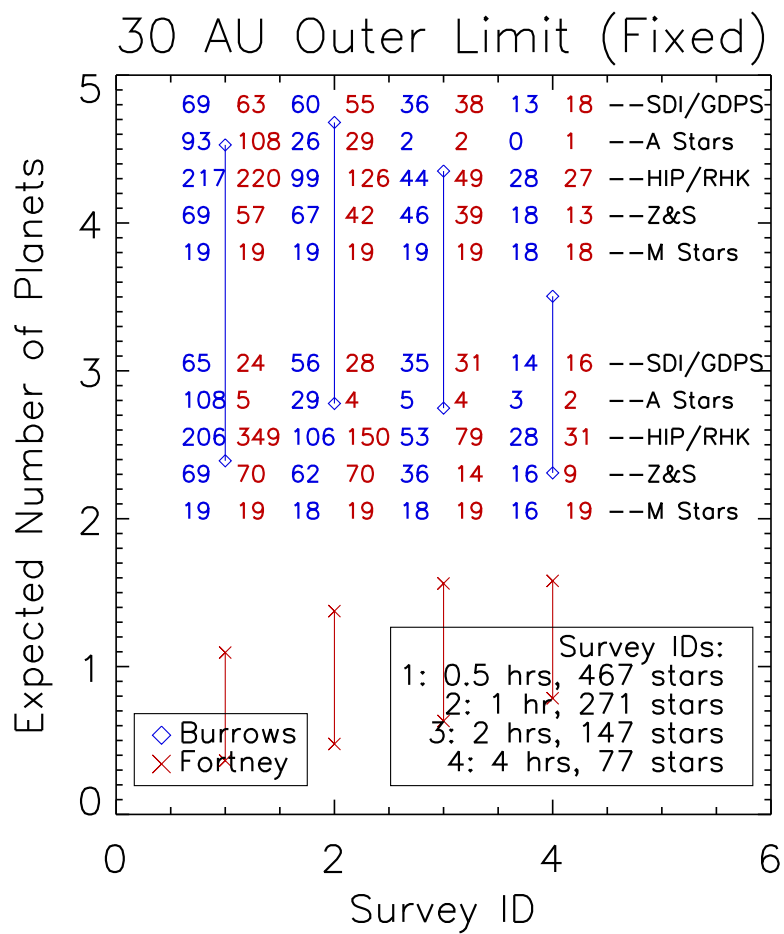


Figure 6.7 The same as Fig. 6.4, except with the outer semi-major axis limit now 30 AU.

In Fig. 6.7 we plot the same details on the survey as in Fig. 6.4, keeping the extent of the semi-major axis distribution fixed, but setting the outer edge at 30 AU. Again, moving to smaller outer limits on the semi-major axis distribution reduces the expected planet yield from the survey, and keeping the extent of the distribution fixed makes A stars less promising targets, while positively weighting M stars.

6.4.2 Parameters of the Target Stars

Next, we consider what types of stars make it into these different survey designs. For each of the hypothetical surveys of Fig. 6.5, we extract the target stars that make up those surveys, and plot their parameters in Fig 6.8 and Fig. 6.9. The surveys consist mainly of stars more massive than the sun, as expected from the fact that we scale the outer semi-major axis limit with stellar mass.

We reproduce these plots of target star parameters for the case of planets forming out 30 AU, regardless of the spectral type of the target star (fixed rather than scaled), in Fig. 6.10,6.11. A stars become less common in the surveys, as lower-mass stars can now have planets at much larger separations. These plots represent the major difficulty in designing the NICI Campaign: both the design of the basic survey parameters and the composition of the target list cannot be simultaneously optimized for all possible models of planet populations.

6.4.3 The Curve of Growth

In order to determine the relative worth of the different targets stars, we've also made plots that show how many planets we detect as we conduct the survey, showing which target stars are most likely to contain detectable planets, and which are less productive. In Fig. 6.12 and 6.13, we show two such curve-of-growth plots, giving the number of planets we'd expect to detect as a function of

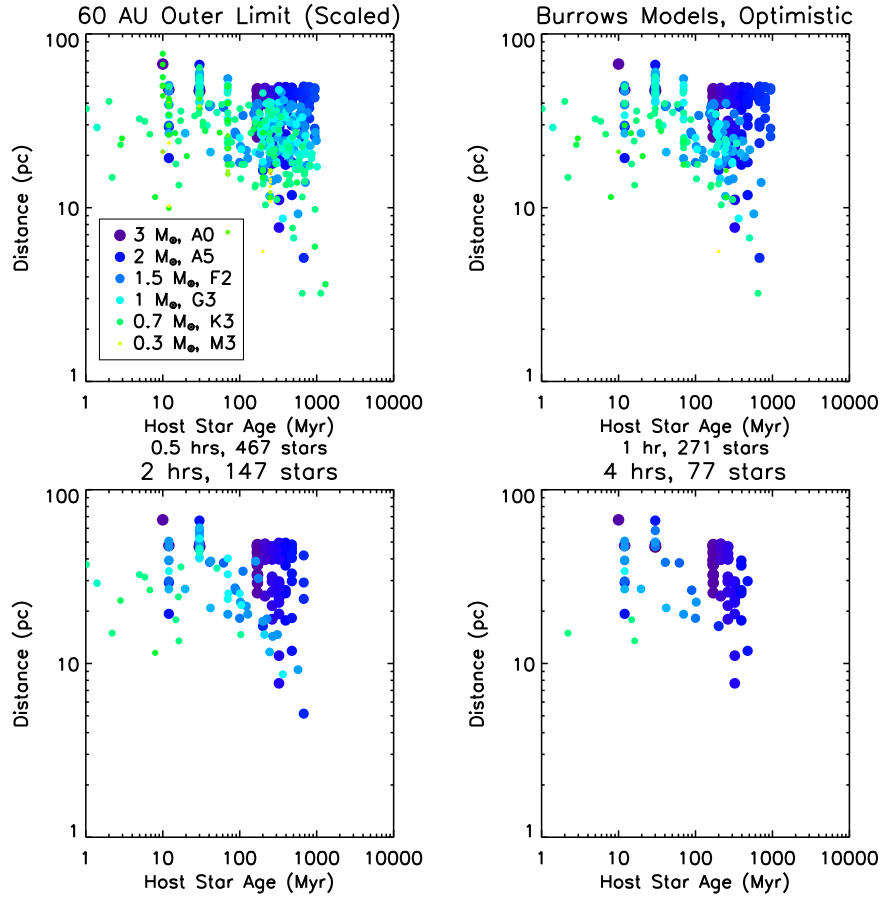


Figure 6.8 The target stars in the hypothetical surveys of Fig. 6.5, for the models of Burrows et al. (2003), using the optimistic planet parameters. The semi-major axis distribution continues out to 60 AU before being truncated, and this limit is scaled with the spectral type of the star. In all cases, stellar mass is estimated from the spectral type of the target star.

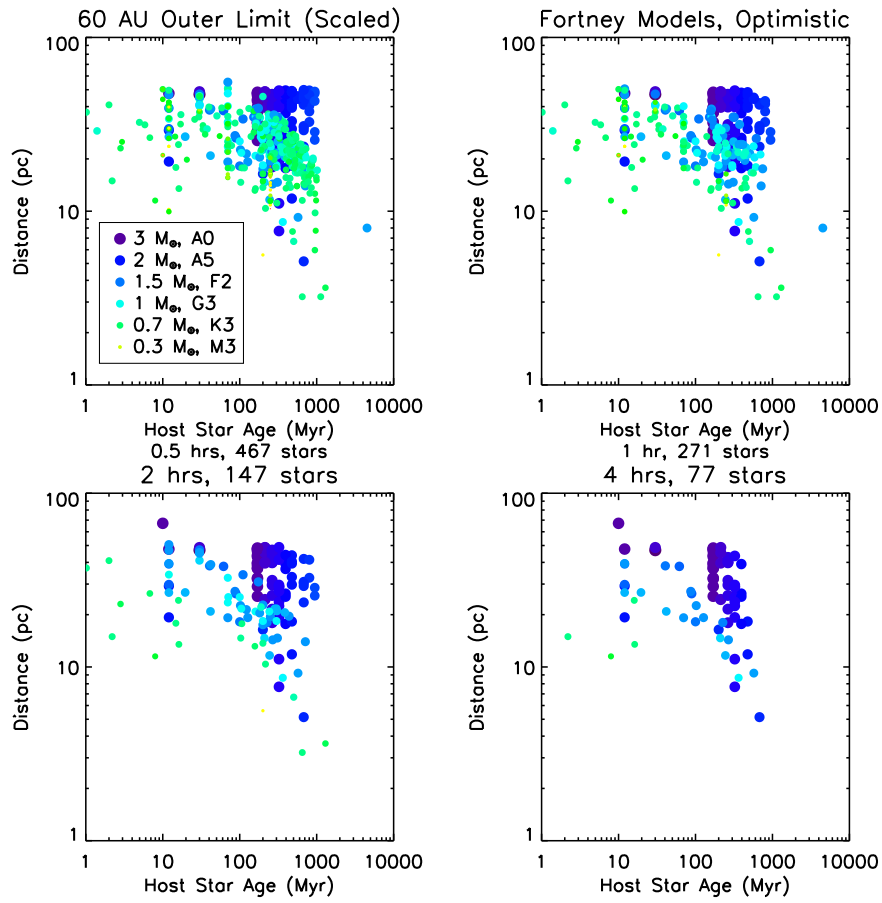


Figure 6.9 The same as Fig. 6.8, only with the optimistic parameters for the planet populations, and using the Fortney et al. (2008) models for planet brightness.

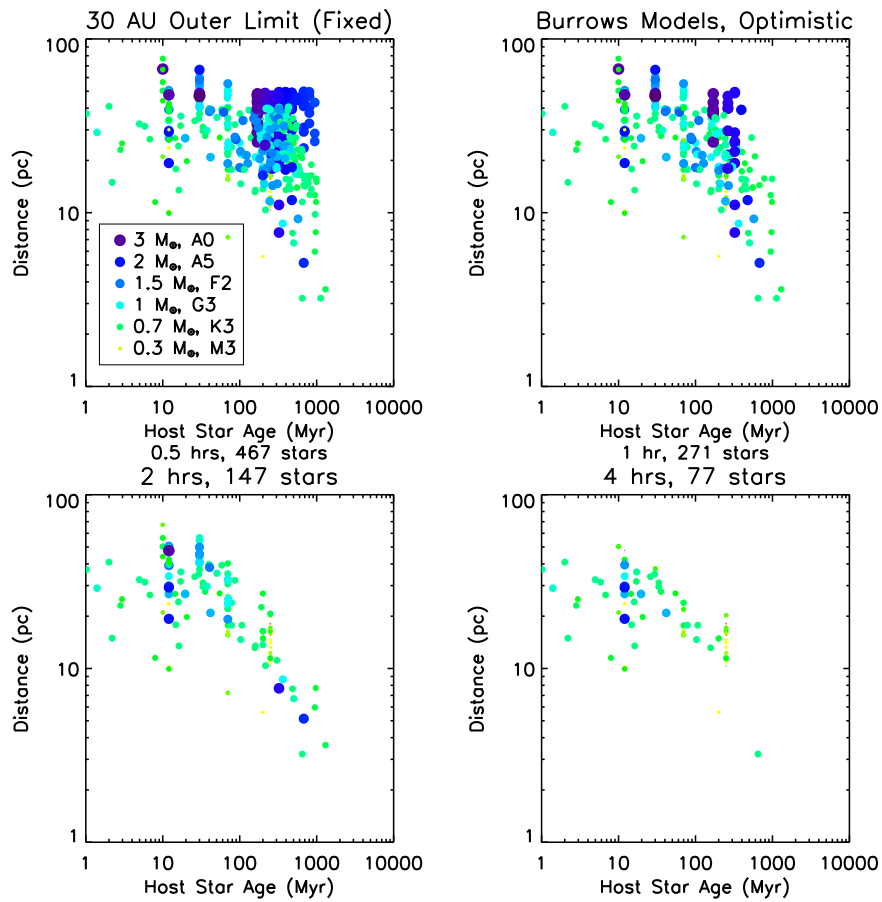


Figure 6.10 The target stars in the hypothetical surveys of Fig. 6.7, for the models of Burrows et al. (2003), using the optimistic planet parameters. The semi-major axis distribution continues out to 30 AU before being truncated, which is constant across all spectral types of target stars. In all cases, stellar mass is estimated from the spectral type of the target star.

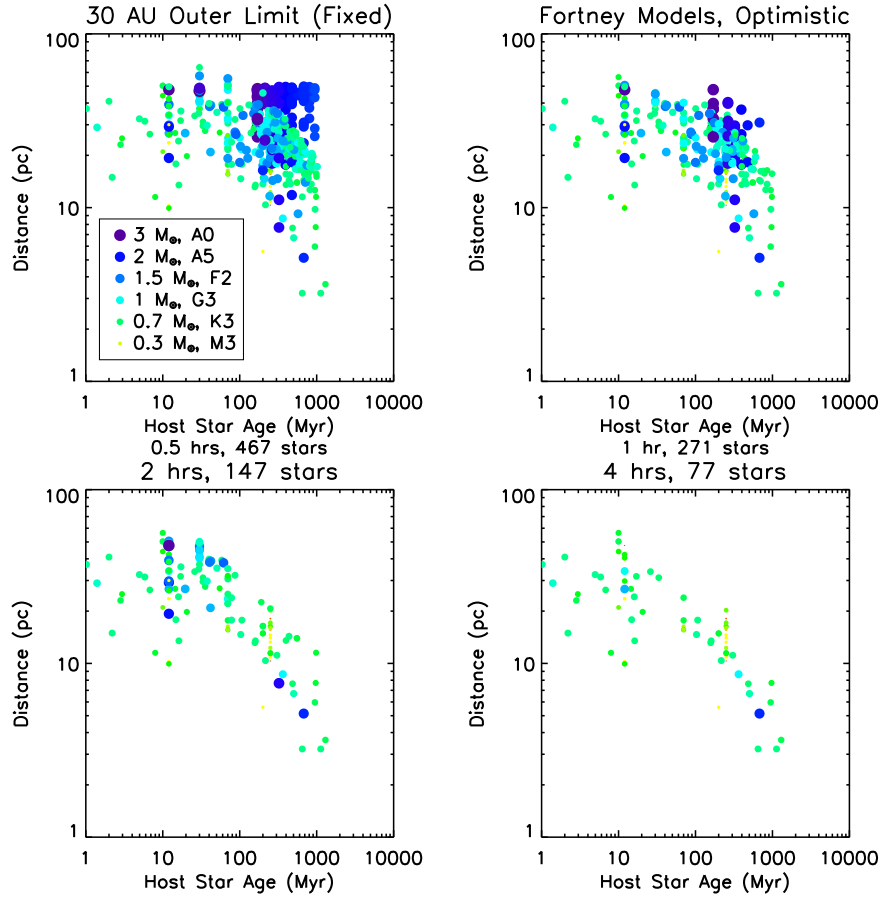


Figure 6.11 The same as Fig. 6.10, only with the optimistic parameters for the planet populations, and using the Fortney et al. (2008) models for planet brightness.

the number of stars in the survey. For the most part, we're adding a significant number of planets across the survey, except for the largest, most shallow survey. Which is unsurprising, as it would be unlikely there to be 500 equally good target stars for direct imaging planet searches.

For each set of four plots, the left two panels contain the pessimistic case of planet populations, the right two the optimistic case. The top two panels show the curves of growth for different exposure times, and the bottom two panels break up the 1 hour survey into the different input target list samples. Since each survey is limited to 420 hours of total telescope time, the smaller exposure time surveys encompass more stars than the deeper surveys. The Fortney models show a common characteristic, that there are a limited number of target stars where NICI can go deep enough to detect Fortney planets. So while planets are initially detected at a reassuring rate, the curve quickly levels off, so that adding additional target stars is not expected to yield additional planets.

This effect is even more stark in the 30 AU Fixed case (Fig. 6.13). With most planets close to their parent star (and so in a part of the contrast curve where it is more difficult to detect faint planets), there is a relatively small number of target stars that are predicted to make good targets with the Fortney models, especially at 1 hour integration times.

6.4.4 Implications for Spectral Type Composition of the Campaign Target List

We consider the properties of the target stars, and its influence on the probability of detecting planets, given different input models. In Fig. 6.14, we plot the mass of the target star as a function of its expected number of detected planets, for the 60 AU scaled planet populations and the optimistic case. Each star is plotted twice, once as the red point for the Fortney models, once as the blue point for the Burrows models. The most favorable stars are the highest mass stars, especially

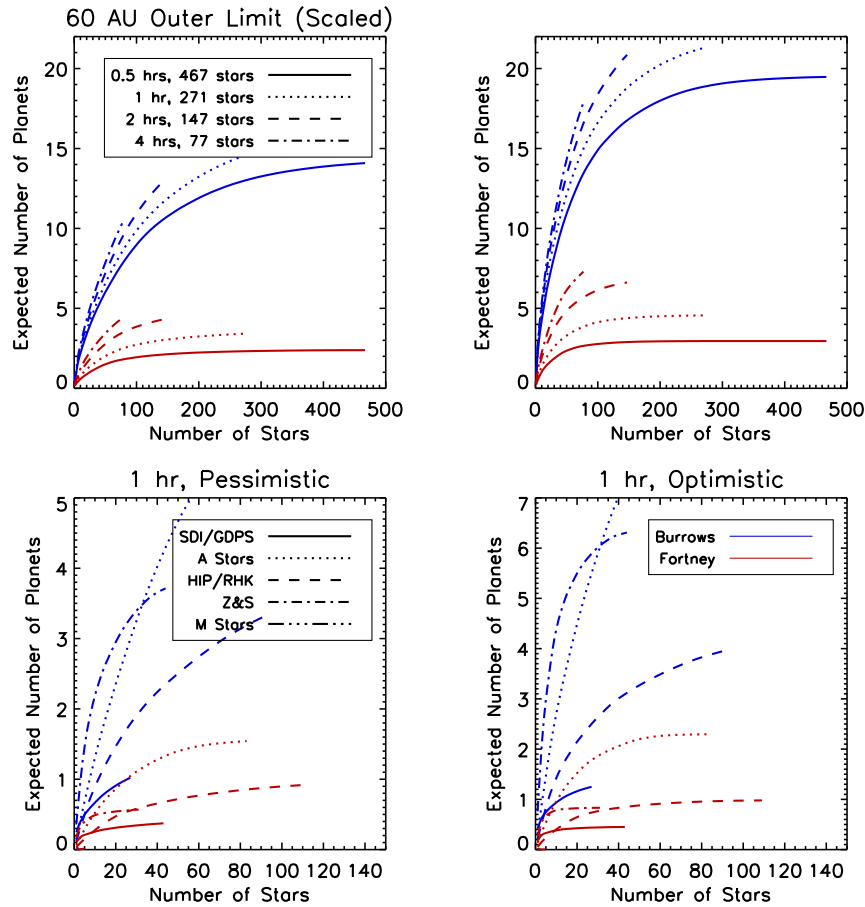


Figure 6.12 The expected planet yield as a function of survey size (at each point along the x-axis, if a survey is conducted of the best 30 stars, say, in the survey, the y-axis gives the expected number of planets). The two left-hand plots give the results for the pessimistic set of planet parameters, no GQ Lup objects, Johnson et al. (2007) mass scaling, and median seeing, and the optimistic case is given on the right. The top two plots contain stars from all sources for the four survey designs, and the bottom plots break up the sample by target source. In these plots, the outer limit of semi-major axis is at 60 AU for solar mass stars, and allowed to scale with spectral type.

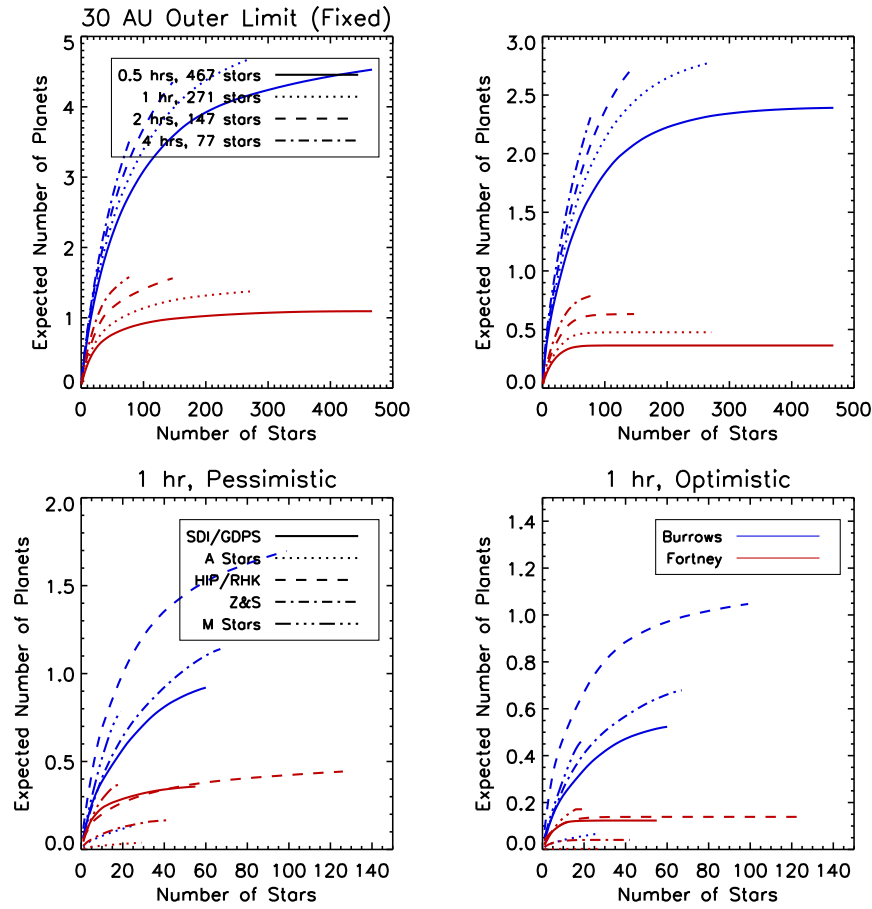


Figure 6.13 The same as Fig. 6.12, except with the outer limit on semi-major axis fixed at 30 AU for all stars.

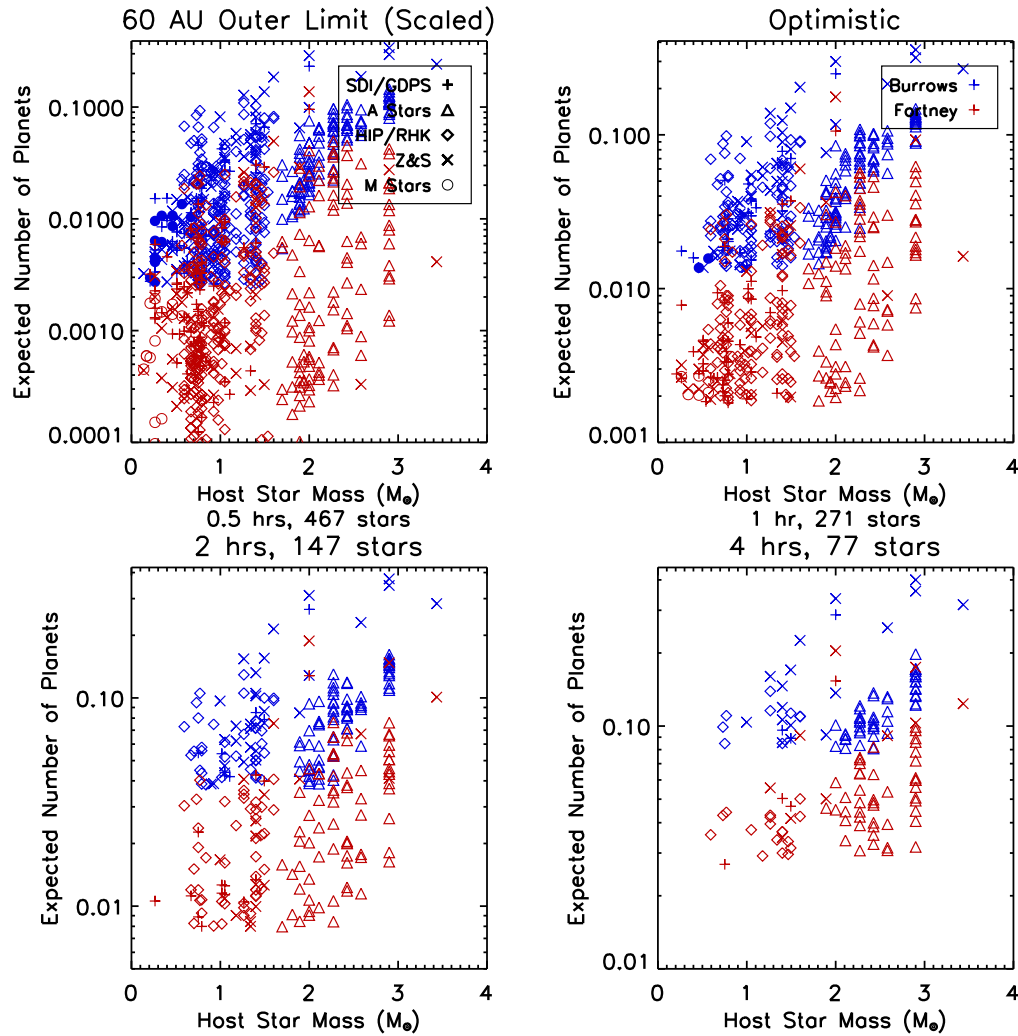


Figure 6.14 The probability of finding a planet around each target star in the four types of surveys, using the optimistic planet parameters and the scaled 60 AU upper limit on semi-major axis, as a function of the mass of the target star, as estimated from spectral type.

for the 1-hour exposure time plot. Some lower mass stars achieve high probabilities, but overall the best stars are the A stars ($M > 2 M_{\odot}$). The Fortney models show the same general trends, except the predicted planet yields are systematically lower than those for the Burrows models.

Figure 6.15 shows this spectral type distribution again, only now for the 30 AU Fixed case (though again for the optimistic model). The trend has almost exactly reversed, with the lowest mass stars now reaching the highest probabilities. Since planets extend out to 30 AU for stars of all spectral types, the high contrasts required for the A stars make them much less favorable targets. For longer exposure times, stars more massive than the sun have almost disappeared, making the preferred sample almost exclusively one of low-mass stars.

Making a similar plot for distance to the target star, as in Fig. 6.16, the results are as we would expect. The closest stars achieve the highest planet yields, as smaller-period planets become accessible to NICI. Looking at age, as in Fig. 6.17, again the youngest stars are the most favored. The spike at 150 Myr represents the young M-star sample (their probabilities are computed in a statistical manner, for ages between 0 and 300 Myr, but for plotting purposes they're shown at their average age of 150 Myr here). For this model of planet populations, the youngest, closest, lowest mass stars are favored for the NICI Campaign. However, as the model is altered to allow the outer radius to scale with spectral type, the recommendations for survey design and composition change dramatically.

6.4.5 Properties of the Detected Planets

Finally, we examine the parameters of the simulated planets we'd detect with NICI. In Fig. 6.18, we plot histograms of "detectable" simulated planets, broken up by target star source, with the area under each histogram showing the expected number of planets detected. These plots use the 60 AU scaled model, and

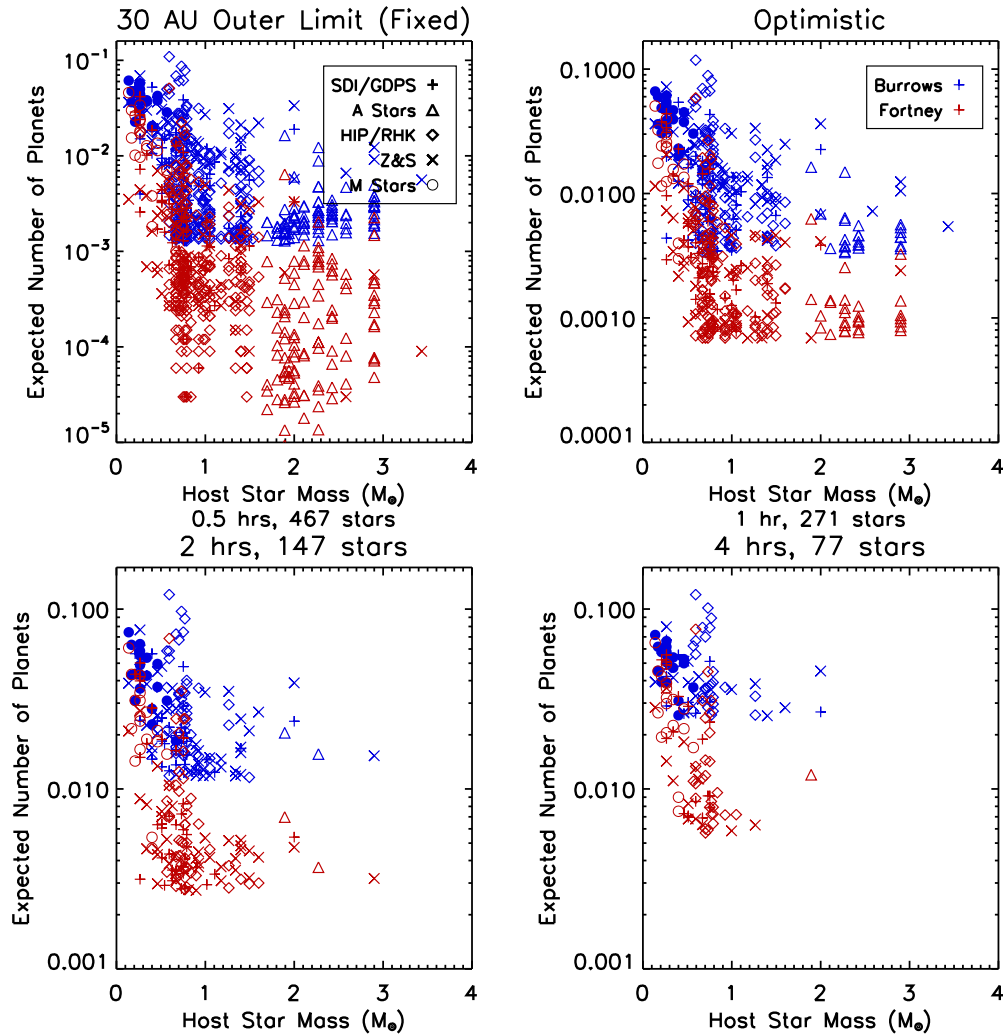


Figure 6.15 The probability of finding a planet around each target star in the four types of surveys, using the optimistic planet parameters and the fixed 30 AU upper limit on semi-major axis, as a function of the mass of the target star, as estimated from spectral type.

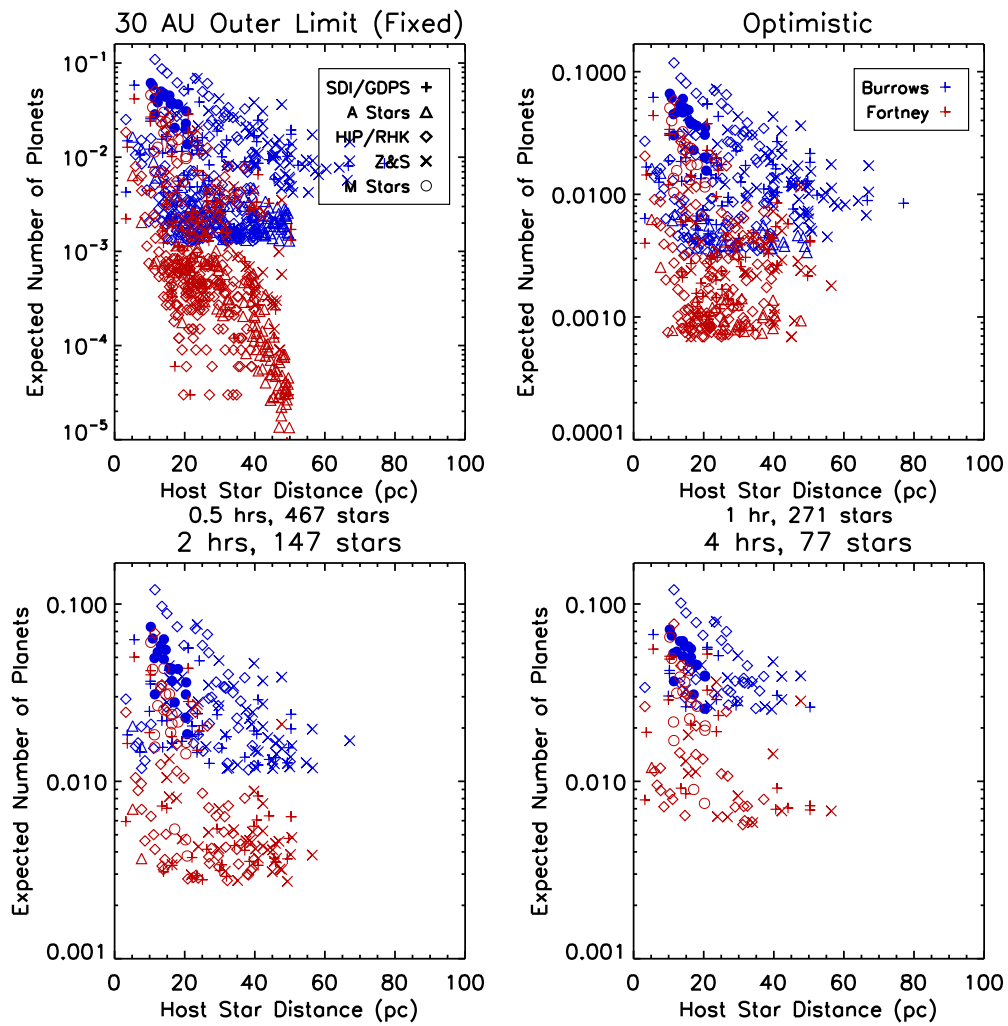


Figure 6.16 The probability of finding a planet around each target star in the four types of surveys, using the optimistic planet parameters and the fixed 30 AU upper limit on semi-major axis, as a function of the distance to the target star.

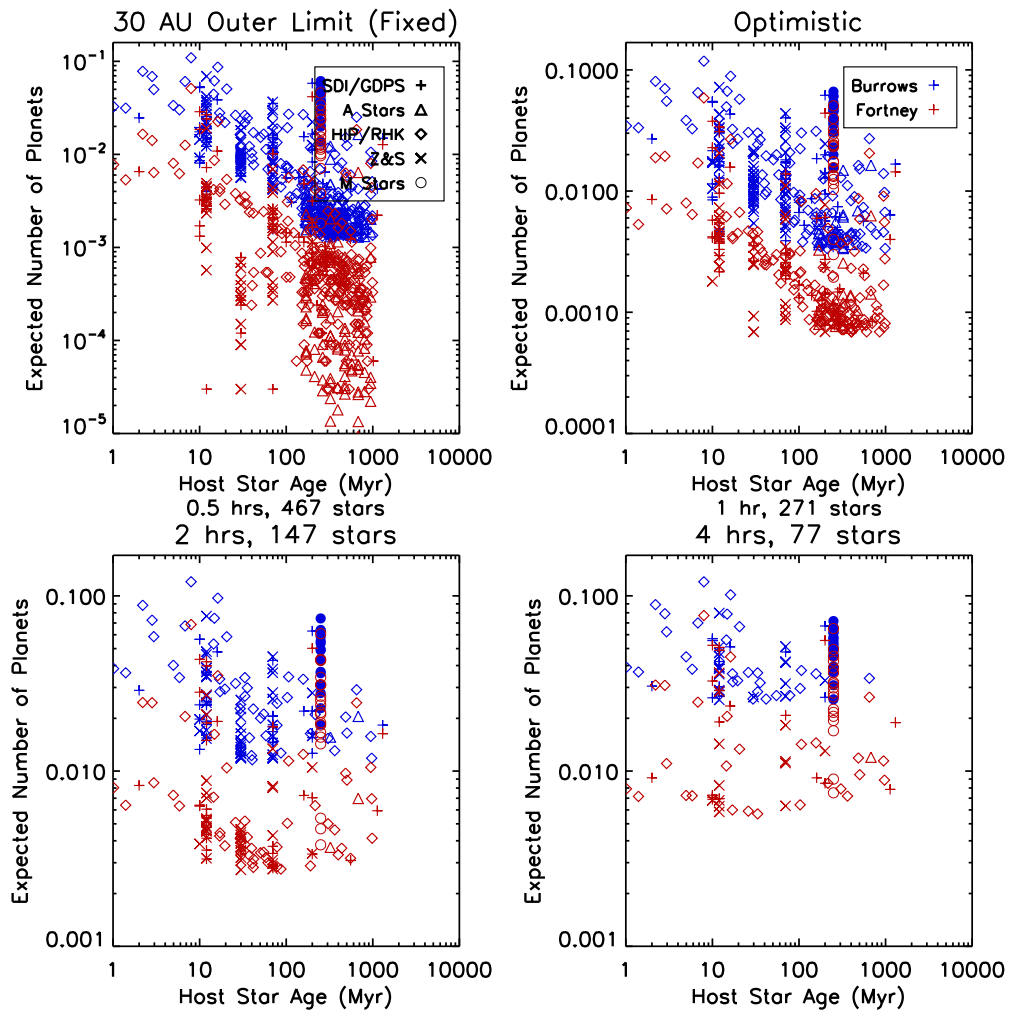


Figure 6.17 The probability of finding a planet around each target star in the four types of surveys, using the optimistic planet parameters and the fixed 30 AU upper limit on semi-major axis, as a function of the age of the target star.

the optimistic set of planet parameters. With the Burrows et al. (2003) models, most of the planets around M stars that we're seeing are within an arcsecond, and mostly between 5 and 20 AU. For A stars, most planets are well beyond an arcsecond, outside of 100 AU. The other three surveys (which contain ranges of spectral types) have planets spread across many separations. The bulk of the planets are 10-15 magnitudes fainter than the primary, and have an apparent H from 14 to 18.

For the Fortney et al. (2008) models, which predict systematically fainter planets, we find overall fewer planets, and in very different places (see Fig. 6.19). Most of the detectable planets (except for those around M stars) are outside of 2'', and closer to 100 AU (we're really depending on those GQ Lup objects). As expected, we need a more extreme ΔH (14-18) to reach planets, which are at apparent magnitudes of 18-20 for those that we do find.

In Fig. 6.20, we again plot the properties of the detectable planets, using the Burrows models, but now for the 30 AU Fixed case. The semi-major axis plot shows a clear bifurcation, with the inner planets following distributions consistent with radial velocity planets (<30 AU), and the other objects following the GQ Lup distribution (>60 AU). The most planets now come from the youngest target stars, especially from the Zuckerman & Song (2004) young moving group objects. The A stars, on the other hand, do the worst of the various input samples.

For the Fortney models, in Fig 6.21, the same general trends hold, only with a decrease in the overall expected number of planets detected. Finally, we plot all the detectable planets in term of the observable quantities, ΔH and separation, in Fig. 6.22 and 6.23. As we would expect, the detectable planets trace out the input contrast curve. For the Burrows models, the planets pile up at the inner edge of the NICI coronagraphic mask; with the 30 AU fixed cases, most

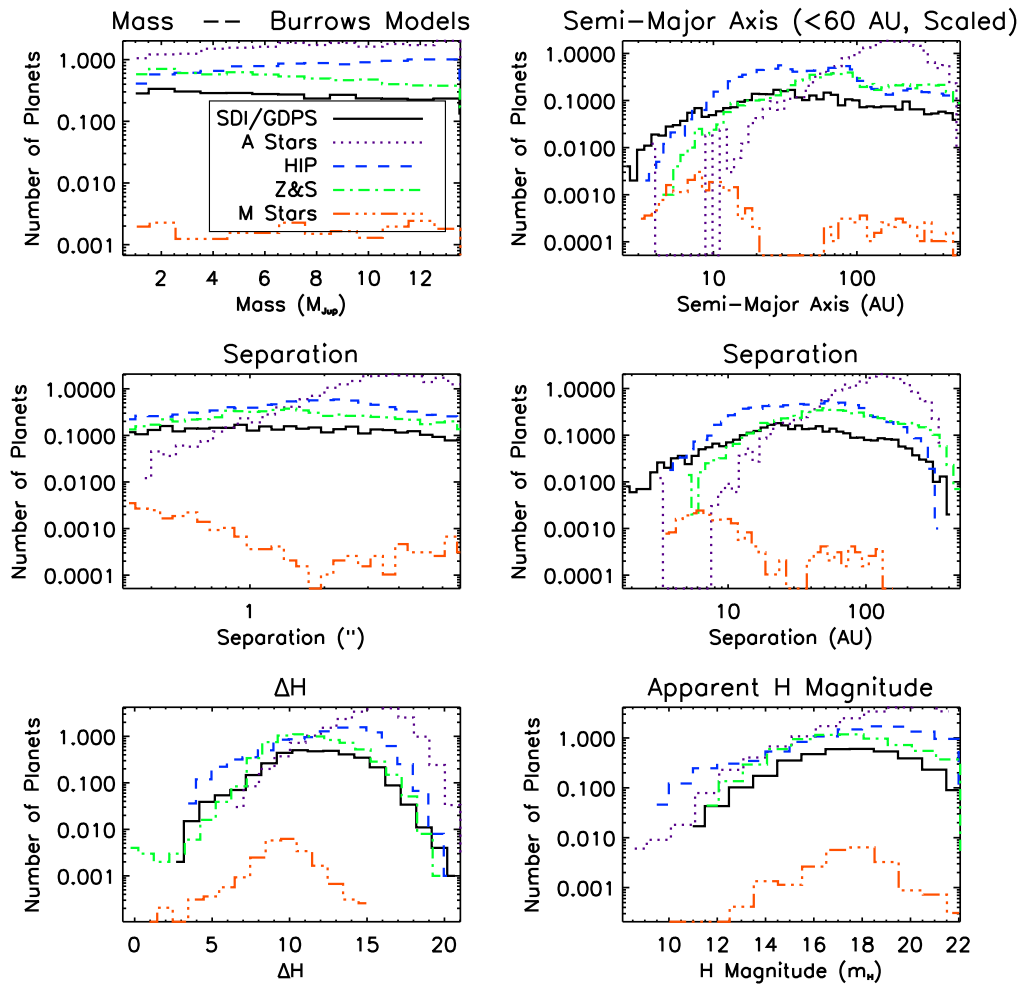


Figure 6.18 Histograms giving mass, semi-major axis, on-sky separation (both in arcseconds and AU), delta H magnitude, and apparent H magnitude for the simulated planets NICI could detect, using the models of Burrows et al. (2003). These planets are again from the optimistic scenario, with GQ Lup-like objects, 20th percentile seeing, and no scaling of the likelihood of finding a planet with stellar mass. The outer limit for semi-major axis, however, is scaled by stellar mass, with a value of 60 AU at a solar mass. The area under each histogram represents the number of planets we'd expect to detect from the given set of target stars.

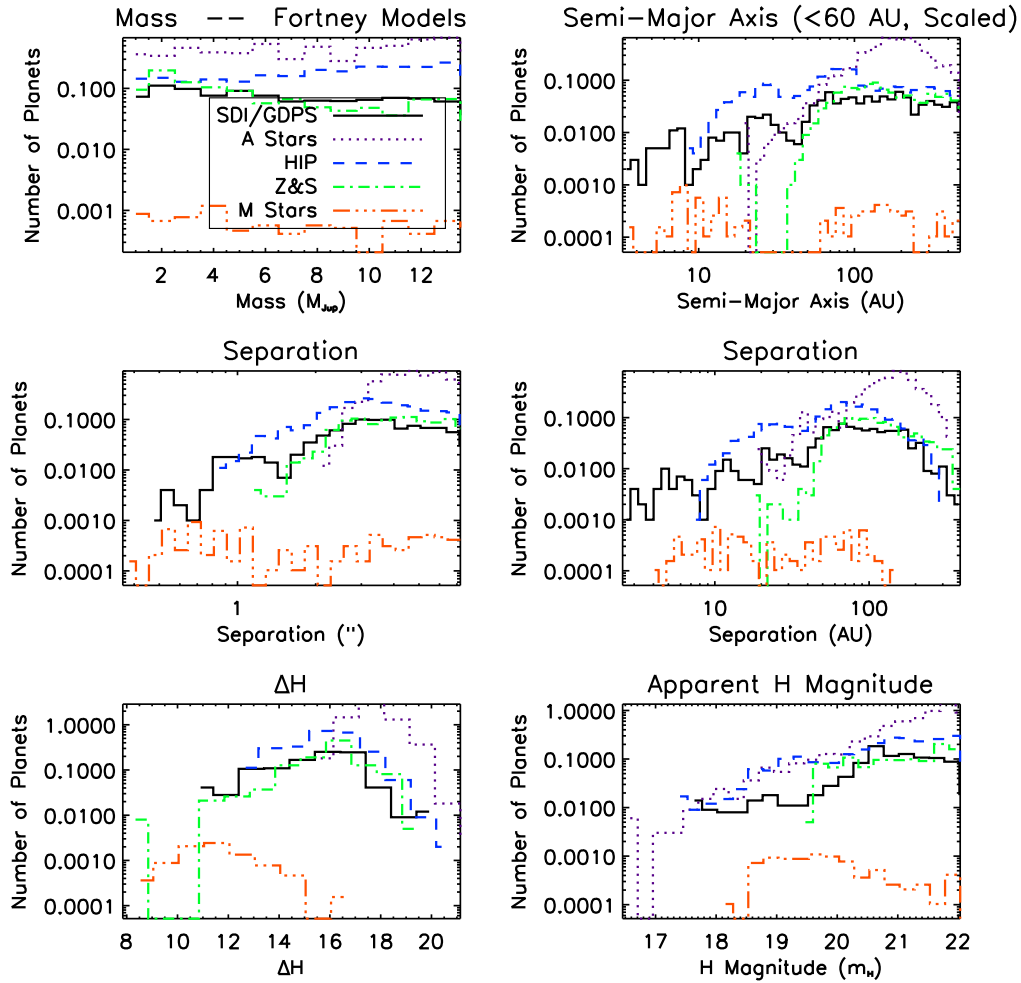


Figure 6.19 Histograms giving mass, semi-major axis, on-sky separation (both in arcseconds and AU), delta H magnitude, and apparent H magnitude for the simulated planets NICI could detect, using the models of Fortney et al. (2008). These planets are again from the optimistic scenario, with GQ Lup-like objects, 20th percentile seeing, and no scaling of the likelihood of finding a planet with stellar mass. The outer limit for semi-major axis, however, is scaled by stellar mass. The area under each histogram represents the number of planets we'd expect to detect from the given set of target stars.

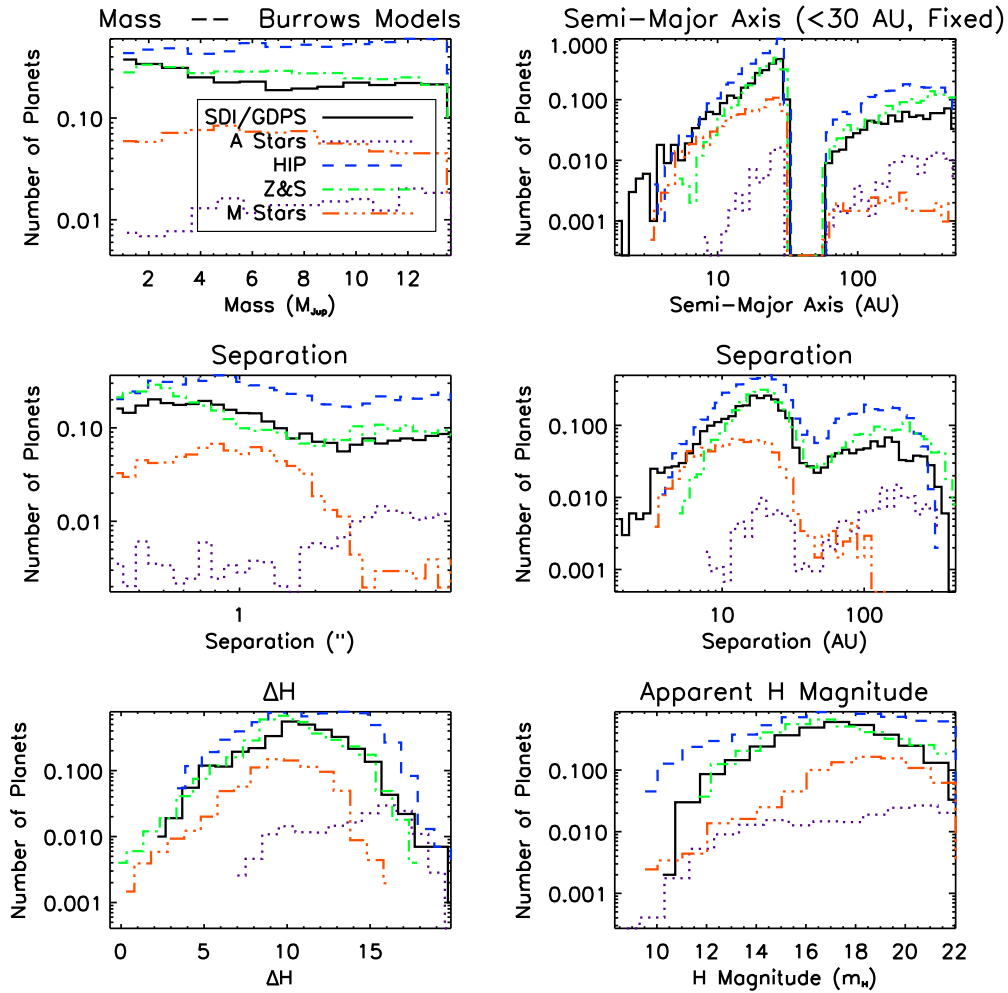


Figure 6.20 Histograms giving mass, semi-major axis, on-sky separation (both in arcseconds and AU), delta H magnitude, and apparent H magnitude for the simulated planets NICI could detect, using the models of Burrows et al. (2003). These planets are again from the optimistic scenario, with GQ Lup-like objects, 20th percentile seeing, and no scaling of the likelihood of finding a planet with stellar mass. The area under each histogram represents the number of planets we'd expect to detect from the given set of target stars.

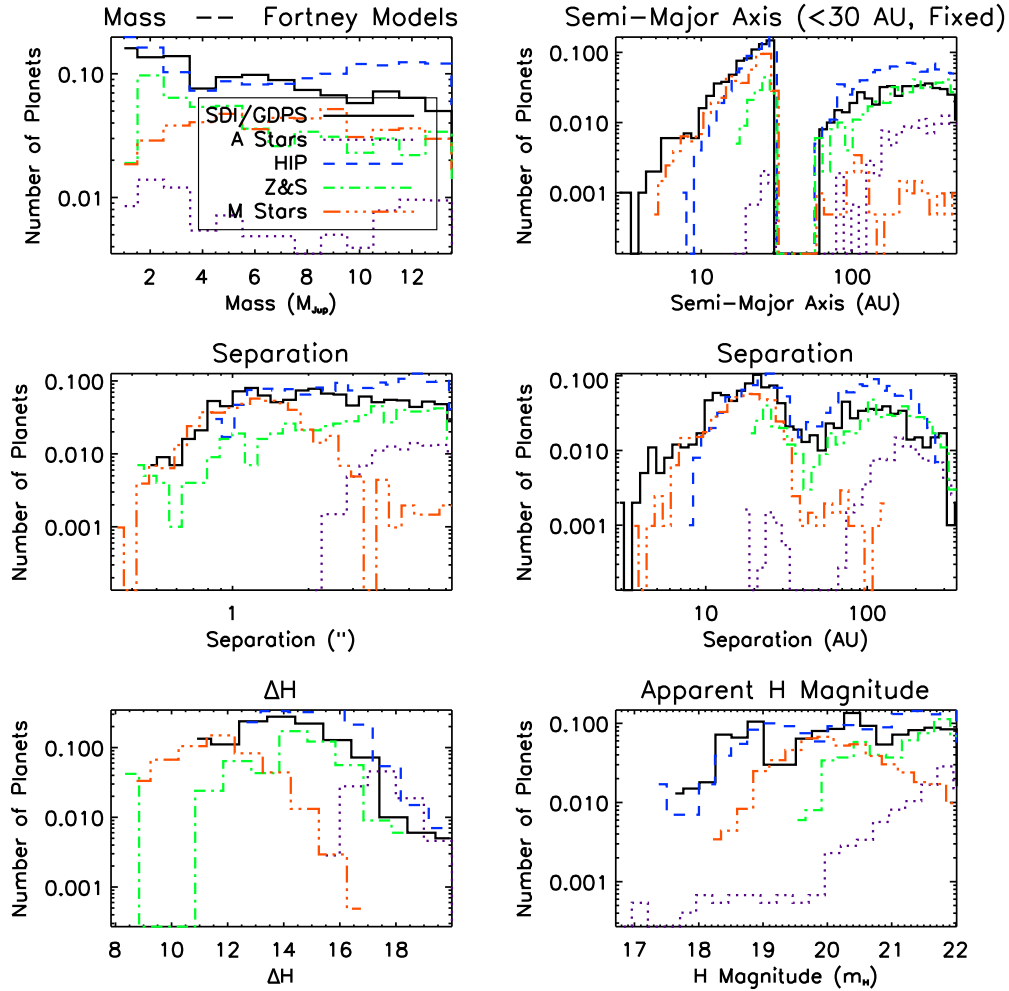


Figure 6.21 Histograms giving mass, semi-major axis, on-sky separation (both in arcseconds and AU), delta H magnitude, and apparent H magnitude for the simulated planets NICI could detect, using the models of Fortney et al. (2008). These planets are again from the optimistic scenario, with GQ Lup-like objects, 20th percentile seeing, and no scaling of the likelihood of finding a planet with stellar mass. The outer limit for semi-major is fixed at 30 AU. The area under each histogram represents the number of planets we'd expect to detect from the given set of target stars.

planets are close to their star, so most detections are at the inner working angle of the system. For Fortney planets, the key is the overall faintness of the planets, so most detectable planets are beyond $1''$, where the contrast curve becomes sensitive enough to reach Fortney planets.

6.5 Final Survey Design

The analyses we have considered so far lead to a disturbing bifurcation: a NICI Campaign conducted under the assumption that the 60 AU scaled model of planet populations is correct would draw from a target list composed mostly of early-type stars, while the 30 AU Fixed model suggests a Campaign observing mainly late-type stars. There's a secondary split, where the Burrows models favors short exposure times and a large number of target stars, while the Fortney models point to long exposure times, and observations of only the best stars. In a sense, it's becoming necessary to pick a distribution of extrasolar planet populations before conducting the survey that is meant to measure that very distribution. There is an additional observing mode consideration: SDI observations are able to effectively attenuate the speckle noise within $1''$, but at the cost of throughput (light is first reduced by 50% at the beamsplitter, then cut down by the 4% methane filter). Analysis of the contrasts achieved with NICI show that we are speckle noise limited within $1''$, and shot noise limited outside of $1''$. So Fig. 6.22 and 6.23 give different answers for this as well: the Fortney planets are detectable beyond $1''$, so SDI would hinder the detections, while Burrows planets are expected to be in the inner arcsecond, where they would greatly benefit from SDI.

For the final survey design, we choose a path of compromise between these competing interests. Each star is observed with a "hybrid" mode, 60 minutes of ADI (no beamsplitter, all the light passes through the broadband H filter and is

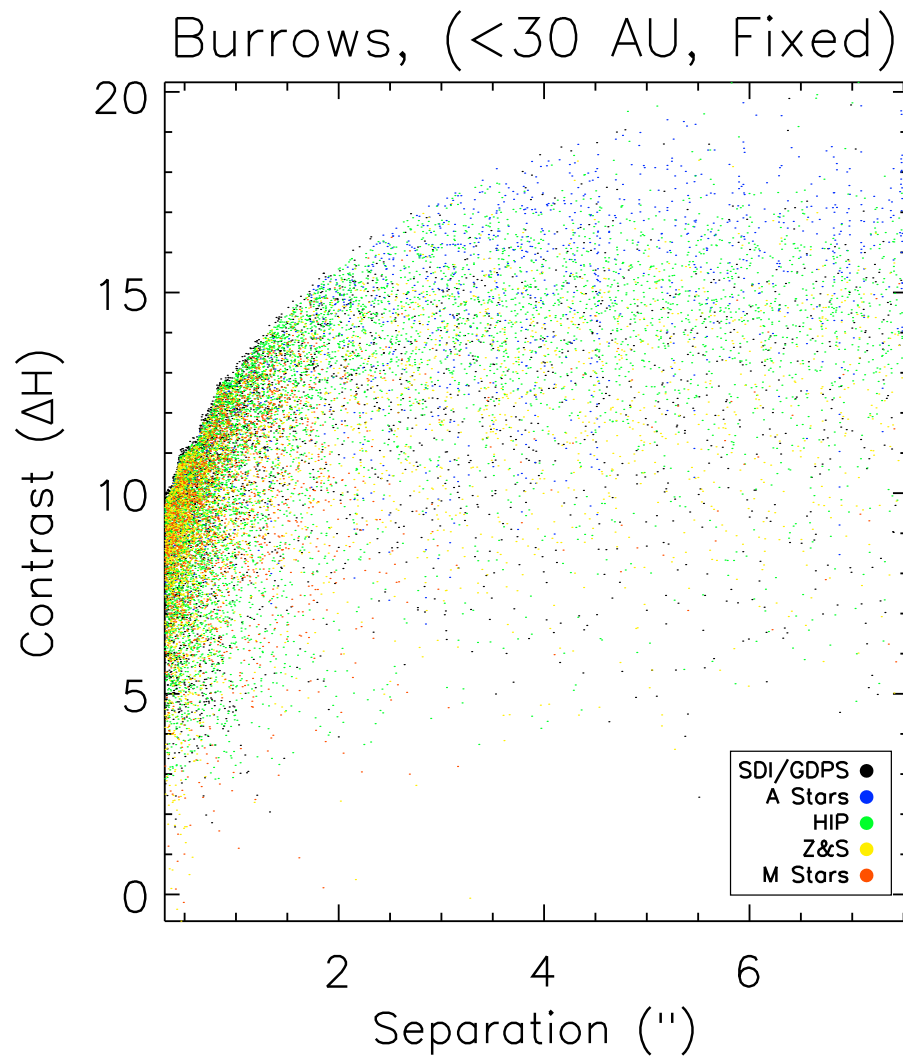


Figure 6.22 All detectable planets, the ones that were in the previous histograms, with contrast plotted against separation. As expected, they trace out the input contrast curve quite nicely. This plot uses the models of Burrows et al. (2003).

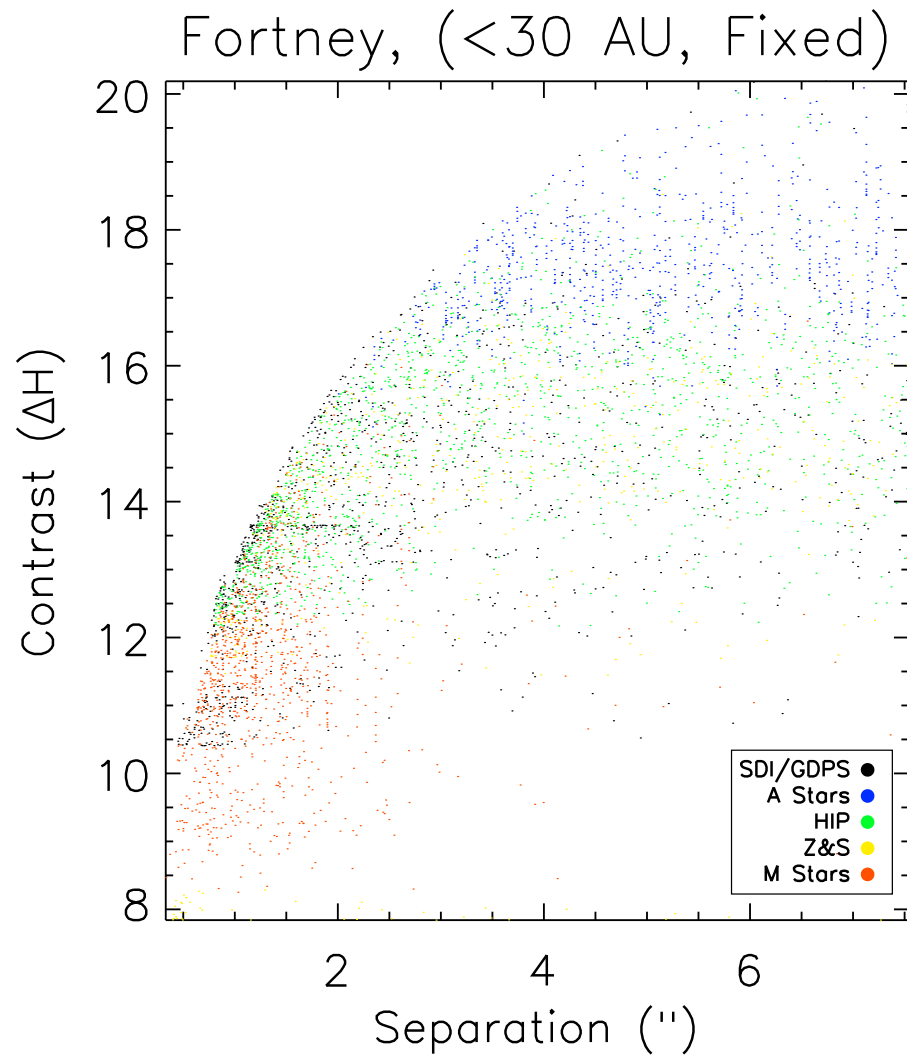


Figure 6.23 All detectable planets, the ones that were in the previous histograms, with contrast plotted against separation. This plot uses the models of Fortney et al. (2008).

observed with only one science camera), and 30 minutes of combined ADI and SDI. This exposure time also represents a halfway point between the deep survey preferred by the Fortney models, and the shallow survey for the Burrows models. Finally, we choose the highest-ranked target stars from both the 60 AU scaled and 30 AU Fixed lists. We also set up a quota system where we require a minimum number of stars in various mass bins (otherwise our survey would become half A stars and half M stars), to allow us to use the results to examine planet population data as a function of spectral type.

There are certainly compelling arguments against such a solution, namely the idea that we should commit to a model and place all our resources into testing that model. For example, we might simply begin by assuming the 30 AU Fixed Burrows model is the correct representation of reality, and draw our target stars so that we maximize the number of planets predicted by this model. Then, should we have a null result, we can reject this model with high statistical confidence, and embrace an alternate model. But this is not a compelling argument to me, since it assumes there are a limited number of planet population models (for example, the two we have considered here), and it is simply a matter of testing each of them in sequence. There are a number of free parameters in our power-law fits, and that's not even allowing for more complicated distributions of planet parameters beyond simple power laws.

A null result has limited ability to direct us to the proper model of reality, it can only rule out certain models. It is only by detecting planets in these surveys that we can make solid progress toward coming up with a unified distribution of exoplanet populations. A null result from the completed NICI Campaign will still be valuable, it would rule out the 60 AU scaled and 30 AU fixed models for the Burrows models of planet fluxes, and place strong constraints on the 60

AU scaled Fortney model. By balancing our priorities, we have chosen a final Campaign target list of 300 stars, which will allow us to place strong constraints on the population of extrasolar giant planets.

6.6 Current NICI Planet-Finding Campaign Status

As of May 2011, the NICI Planet-Finding Campaign is entering its final year. Over 200 stars have been imaged for at least one epoch, with first epoch observations, and second-epoch confirmations, being conducted on a regular basis. Two discovery papers have been published thus far, announcing brown dwarf companions to NICI target stars (Biller et al., 2010; Wahhaj et al., 2011). We have a number of candidates that, given their age and brightness, are consistent with planet-mass companions. Most of the similar objects analyzed to date with second-epoch astrometry have proven to be background stars, but we continue to sort through the list of candidates to determine which, if any, are physical co-moving companions (Liu et al., 2010).

The contrasts achieved have been consistent with predictions made before the start of the Campaign, and the instrument has performed well throughout the Campaign. A preliminary analysis of the stars without detected companions (a null result for this subset of the final NICI observing list) places constraints on extrasolar planet populations that are significantly stronger than presented in Nielsen & Close (2010). With or without detected planets from the NICI stars that remain to be observed (or re-observed for second epoch follow-up), the final results from the NICI Campaign will greatly shape our knowledge of exoplanet populations.

CHAPTER 7

CONCLUSIONS AND FUTURE DIRECTIONS

In this thesis, I have put forward my experience in designing direct imaging surveys, and using null results from existing surveys to place constraints on the populations of extrasolar planets. In this concluding section, I look ahead to future direct imaging surveys, with existing and future instruments, and what important scientific questions should be addressed by these new endeavors.

7.1 A Unified Distribution of Extrasolar Planet Populations

As radial velocity surveys became more efficient at finding planets over the last 16 years, we have learned a lot about the populations of extrasolar giant planets. The very existence of Hot Jupiters was a surprise, and as the number of planets continued to grow, more could be said about planet distributions. Some of the relations measured to date include the correlation between planet frequency and metallicity (Fischer & Valenti, 2005), power-law fits to orbital period and planet mass (Cumming et al., 2008), and a correlation between planet frequency and stellar host mass (Johnson et al., 2007). A robust quantitative description of planet parameters, and how their distribution depends on properties of the host stars, will be a strong constraint on theories of planet formation and evolution, and will shape our understanding of extrasolar planets.

In essence, the function that planet searches (using any method) are attempting to define is:

$$\frac{dN}{da \, dM_p \, de \, dM_* \, d\tau_* \, d[Fe/H]_*} \quad (7.1)$$

that is, the frequency of planets as a function of orbital semi-major axis, planet

mass, eccentricity, stellar mass, stellar age, and stellar metallicity. (In fact, it may be even more complicated than this, as binarity among planet host stars should have a strong effect on the formation and evolution of planets.) Such an expression would greatly inform planet formation theories, and the time dependence will set the constraints on models of how planetary systems evolve with time.

To define this function, it will be necessary to discover planets throughout this six-dimensional parameter space. Radial velocity and transit surveys have made extraordinary progress in finding planets at small separations (semi-major axis $\lesssim 5$ AU), and have been pushing down to smaller and smaller masses. The Kepler mission is likely to fill out much of this parameter space within 1 AU, for masses down to almost an Earth mass. Yet direct imaging serves an important role, as it will be the only planet search technique sensitive to planets at larger separations. It is also complementary to radial velocity techniques in terms of stellar age, in that RV surveys prefer older, less active stars for precise radial velocity measurements, while direct imaging campaigns are focused on the youngest stars, where the planets are the most self-luminous. It will be by combining the statistics from planet discoveries across every search technique that we can truly build a unified distribution of planet populations.

It is again important to note that while null results are a powerful tool for setting constraints on particular models of planet populations (as I have done in Chapters 4 and 5), null results alone will not allow us to determine which of many competing models of planet distributions best fits reality. In the case of the model that follows the RV-derived power law distributions of Cumming et al. (2008) with no correction for mass of the host star, for example, planets must be found only within 23 AU at 68% confidence. However, other limits can be found by scaling the planet frequency with host mass (the Johnson et al. (2007) correction),

or scaling the outer semi-major axis cut-off with host star mass (as in Chapter 6). And similarly for toggling between the Baraffe et al. (2003) models and Fortney et al. (2008) models. We can construct a model of planet populations with a given semi-major axis distribution, upper cut-off, mass distribution, planet frequency, and using the Baraffe et al. (2003) models, and determine that such a model, given the sensitivity of our survey, was expected to return 3 planets, for example. We can then conclude with 95% confidence that that model is incorrect. However, the model is a convolution of multiple assumptions, and the null result by itself does not guide us to which assumption (or assumptions) must be revised. Many different constraints can come from many different potential planet population models using null results, but actual planets are required to choose between the different models.

7.2 Other Model Possibilities

It is also worth noting that there are other possible models of planet populations beyond those that I have considered previously. As I have noted, multiple planet detections will be necessary to evaluate if these models conform with observed results. But when choosing observing strategies and target lists, it is prudent to consider as many plausible models as possible, in order to maximize the likelihood of success for the survey.

7.2.1 Correlated Distributions

In many cases, when determining a subset of the distribution of Eqn. 7.1, the assumption is typically that the distribution of each parameter is independent of all others, so that

$$\frac{dN}{da dM_p de dM_* d\tau_* d[Fe/H]_*} = f(a) g(M_p) h(e) i(M_*) j(\tau_*) k([Fe/H]_*) \quad (7.2)$$

For example, Cumming et al. (2008) assume that mass and orbital period are described by independent power laws. Similarly, Johnson et al. (2010) find an equation for planet frequency as a function of stellar host mass and metallicity, but the two are assumed independent. In fact, all of my own simulations assume that each parameter is drawn from an independent distribution. (with two minor exceptions: 1) I assume orbital eccentricity has two distributions, divided at an orbital period of 21 days. In practice, since no Hot Jupiter is detectable by direct imaging, my results depend entirely on the eccentricity distribution for outer planets. 2) For the Ida & Lin (2004) models, planets are drawn from outputs to their simulations, so mass and semi-major axis are correlated. However, these models do not figure strongly into my results, due to the low number of expected planets.)

In practice, however, it is reasonable to expect that many of these distributions are highly correlated. It's well-known that eccentricity of radial velocity planets follows two distributions, one for Hot Jupiters and another for longer-period planets, as I show in Fig. 4.2. While Johnson et al. (2007) have shown that the frequency of planets correlates strongly with stellar host mass, it would not be unexpected for other planet properties to also correlate with host mass. Perhaps the power law governing planet mass distribution also changes with spectral type, so lower-mass stars have lower-mass planets. As we assume in Chapter 6, it is also likely that the outer limit to which planets are found also scales with spectral type (as may the power law index for semi-major axis).

Determining these interdependencies is quite involved, as it requires a large enough number of detected planets across a many-dimensional parameter space

(and a full understanding of the completeness to each detected planet and to regions of non-detections) to determine the mathematical description of planet properties. Properties as a function of age will be most difficult, as evolution of a planetary system is likely most rapid in the first ~ 100 Myr after formation, and nearby stars younger than that age are limited, and quantized in groups of fixed ages, rather than in a well-sampled continuous distribution. In fact, it may be the case that parameterized (or partially parameterized) prescriptions for these variables may be all that's possible for the foreseeable future. Nevertheless, it is an effect that those studying planets should keep in mind, and we should continually check out data for correlations, as it is these correlations that are likely to tell us much about the physics behind the formation and evolution of planets.

7.2.2 Alternatives to Single Power Law Fits

In astronomy, it is unavoidable to attempt to fit most distributions with a power law, in no small part because power laws are typically the best description of most distributions. Distributions of planet mass and semi-major axis for RV planets are best fit by power law distributions, as shown by Cumming et al. (2008). Yet it is worth considering the possibility that more complicated distributions may do a better job describing some of the parameters of extrasolar planets. For example, while a smooth power law nicely fits giant planets at small separations, it's entirely possible that there are breaks in this distribution representing different types of planets and formation mechanisms. Neptune-mass planets likely form differently from Jupiter-mass planets, so a break in the mass distribution will likely become apparent as the number of detected Neptune-mass planets increase. If there are two formation mechanisms for giant planets operating at different orbital distances, the semi-major axis distribution is likely to show a break as well.

The only obvious way to measure such a break is to have adequate statistics of planet populations on both sides of the break; for the semi-major axis distribution, this will mean planets at larger separations than those being found by the radial velocity technique. While it is technically possible to set limits on a multiple component function with a null result (in addition to the known power law index for semi-major axis at small separations, we would also need the index at large separation, the location of the break, and the upper cut-off, one dimension more than the analysis that goes into Fig. 5.8), detected planets would provide much more solid constraints, in addition to showing whether this broken power law model is correct or not.

7.3 Upcoming Surveys with Dedicated High-Contrast Planet Finders

The NICI Planet-Finding Campaign represents a massive leap forward in direct imaging planet searches, with a more sensitive instrument, and an unprecedented 500 hours of observing time dedicated to the planet-finding mission. Yet within the next year, new instruments dedicated to imaging exoplanets will come online that achieve even higher contrasts, and are likely to push to even larger time commitments, opening up the field of exoplanet detection to an extraordinary extent.

GPI, the Gemini Planet Imager (Graham et al., 2007), and SPHERE, the Spectro-Polarimetric High-contrast Exoplanet Research instrument (Boccaletti et al., 2008), are both set to come online in 2012, and achieve contrasts between 10^6 and 10^7 within $1''$ of the target star. This increased sensitivity, especially right at the inner working angle of the instrument, will reach planets that have been hidden from previous surveys. Fig. 7.1 shows the expected contrast of the GPI instrument, as a function of separation and target star magnitude. For the brightest stars,

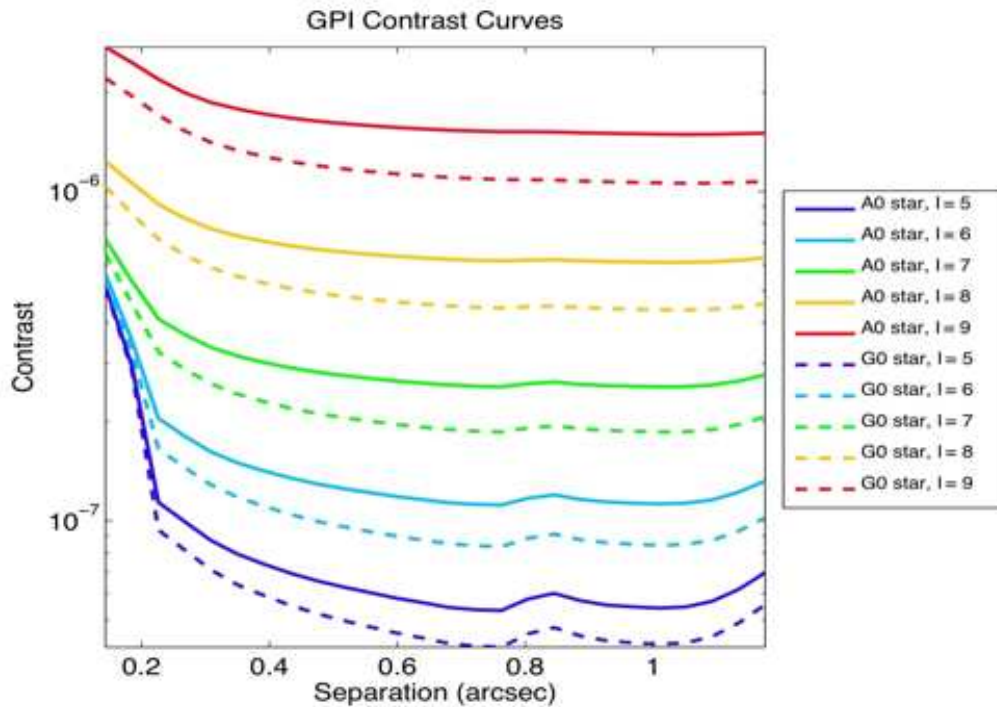


Figure 7.1 The predicted 5σ contrast from the Gemini Planet Imager (GPI). As a reminder, the NICI instrument is achieving contrast ratios of 15 magnitudes (10^{-6}) at $1''$ around the brightest stars. For the brighter target stars, GPI will reach planets up to and beyond a factor of 10 fainter, at separations down to 3 times smaller, than NICI's current performance. However, for all planets past $\approx 1.5''$ GPI has no sensitivity, nor is GPI any more sensitive than NICI for stars with $I \lesssim 8$ mag. Figure from Gemini GPI instrument page, <http://www.gemini.edu/node/11552>

GPI should reach contrasts up to a factor of 10 higher at $1''$, and up to a factor of 100 higher at $0.5''$, than NICI. With SPHERE promising similarly impressive contrasts, and both instruments likely to be available for a combined exposure time of several thousand hours over the first 2-3 years, for the purpose of directly imaging exoplanets, the number of directly imaged planets should increase dramatically by 2014. Other instruments already online and being completed, such as HiCIAO at Subaru, MagAO at the Magellan telescope, and the LBT Interferometer, will provide even further opportunities for planet discoveries and characterization (Hodapp et al., 2008; Close et al., 2010; Hinz, 2009).

This amazing opportunity will be coupled with the responsibility to make the most out of these incredible contrasts and time allocations. It will be essential to keep in mind previous null results (and detected planets) from less sensitive instruments when designing both the observing strategy and target list. Such an eye to the past not only informs a survey design that maximizes the number of expected planets, but also focuses the survey to probe areas of parameter space that have not been reachable with previous efforts.

Additionally, there is much to be gained from pushing both radial velocity and direct imaging to their limits, and image a radial velocity planet (or take radial velocity data on the host star of a directly imaged planet, as the case may be). As I have discussed in Chapter 2, there is great value in providing constraints to the masses given by models of extrasolar planet fluxes, and independent planet mass measurements will provide strong bounds to these models.

In the long term, extremely large telescopes such as the Giant Magellan Telescope (GMT) will push to fainter, closer-in planets than can currently be reached. I show an example of planet simulations (as described in Chapter 4.3) in Figures 7.2 and 7.3. Contrasts offered by these giant telescopes will push to planets at

lower masses closer to their stars, accessing areas of parameter space not previously probed.

7.4 Direct Detection of Extrasolar Planets from Space

Beyond GPI and SPHERE, the next frontier of directly imaging extrasolar planets will be dedicated planet-imaging spacecraft, specifically built to achieve higher contrasts and raw sensitivity than can be obtained from ground-based observations. In the medium-term, a mission such as EXCEDE (Greene et al., 2007), designed to study planets and disks with a high contrast visible light coronagraph, will enable the study of planets (in reflected light) at separations more commonly associated with the radial velocity technique. This overlap of techniques is key, as planets that can be detected by both radial velocity and imaging allow for the testing and calibration of models of planet atmospheres. Models of planet atmospheres will have to fit both the near infrared emission spectrum measured by instruments such as GPI and SPHERE, and the visible light reflection spectrum from a spacecraft like EXCEDE. Having to reproduce such a wide range of wavelengths will strongly constrain models, and deepen our physical understanding of the nature of these objects.

At the even longer term is TPF, the Terrestrial Planet Finder. Though the proposed instrument has many designs and configurations (and none are currently fully funded by NASA), it is likely that there will be, within a few decades, a spacecraft that meets the basic design requirements of TPF: to detect and characterize the atmosphere of an Earth analog orbiting a star within 10 pc. The potential here for the main science driver is both obvious and immense: to characterize Earth-like planets around nearby stars will be to truly place our own planet into context, and see if there are other planets that are suitable for animal life like

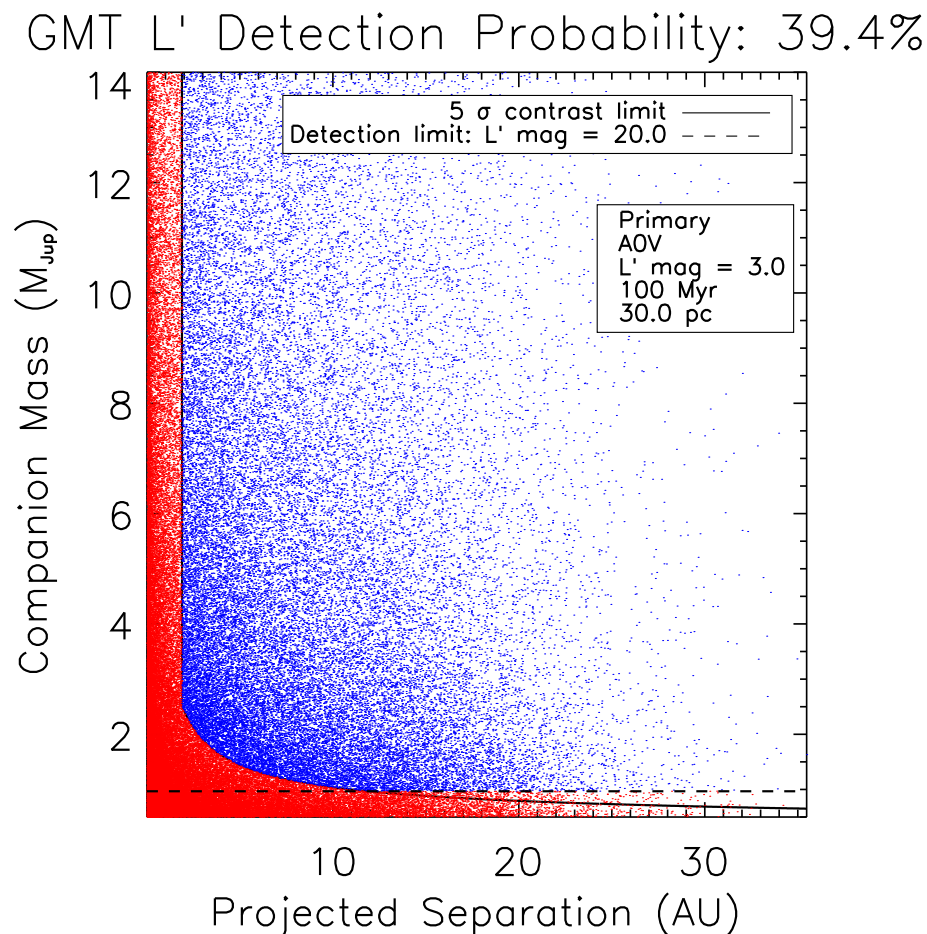


Figure 7.2 The predicted ability of the Giant Magellan Telescope to detect planets around a 100 Myr A star at 30 pc, observing in the L' band. In this case, almost 40% of the simulated planets could be detected, as the contrast curve easily reaches into the equivalent of the giant planet region of our own solar system (though at high planet masses). This simulation assumes a distribution of planets consistent with known radial velocity planets, that continues out to a maximum semi-major axis of 20 AU (consistent with current direct imaging null results), and uses the Baraffe et al. (2003) models of planet brightnesses. GMT 5 σ contrast provided by Philip Hinz.

GMT L' Detection Probability: 33.7%

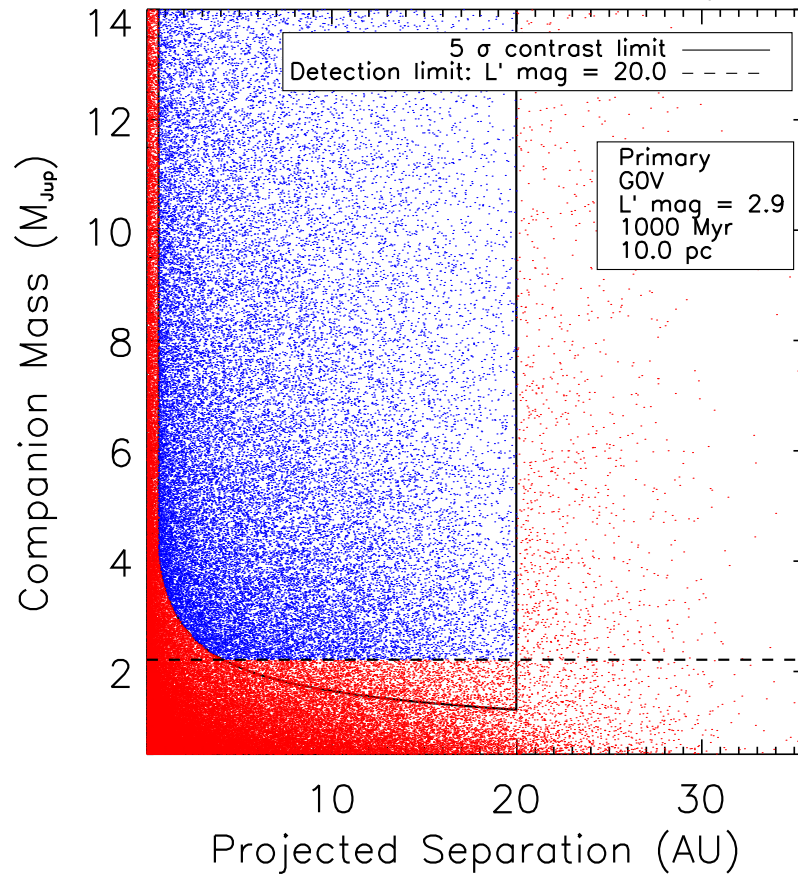


Figure 7.3 As in Figure 7.2, the simulated ability of the GMT to detect planets at L', this time for a solar-mass star slightly younger than our own Sun. A third of the simulated planets are detected, and again the separations of giant planets in our own solar system are probed, if only at the $2 M_{Jup}$ and above level. GMT contrast curve provided by Philip Hinz.

us. But such an instrument will not be able to help itself, while searching for the signal of Earth-analogs, to detect the “noise” of exo-Neptunes and Jupiters in intermediate orbits. Again, the hope will be that techniques overlap, that Jupiters and Neptunes (and the Earths!) around nearby stars are detected with both imaging and radial velocity, and so complete, consistent models can be refined to fully reproduce all observable quantities, including mass. This census of planets (over many decades in mass) will greatly inform the picture of planet populations, and from there our understanding of how planetary systems form and evolve. Terrestrial Planet Finder is designed (and named) to find Earth-like planets, but it will be an invaluable tool to discover and characterize extrasolar planetary systems, placing not just our own planet, but our own Solar System into context, as we shed light on the mechanisms by which these systems are born and change over time.

7.5 Final Thoughts

The field of directly imaging extrasolar planets looks bright indeed, with exciting prospects for the near, medium, and far term likely to revolutionize our understanding of extrasolar planets, their structure, their formation, and their evolution. One ongoing flaw in the field, however, has been the disparate nature of surveys and analyses conducted to date. It is natural for surveys to be conducted with a particular (sometimes narrow) science goal in mind, especially when observing time is at a premium. However, typically the results from these individual surveys are isolated limits set by that survey alone, with multiple surveys of similar depths placing similar constraints on populations of extrasolar planets. Much greater conclusions can be reached, however, by combining the results from these various survey into a larger analysis, with a greater sample of

target stars. Even duplicating target stars is of value, as single stars that have been observed at multiple epochs (allowing greater orbital coverage), and multiple wavelengths, can allow for greater completeness to planets than a single observation (Biller et al., 2010). More effort should be placed into combining the almost decade-long backlog of direct imaging surveys, both with and without null results, into a unified constraint on planet populations at large separations.

There is also the issue of overlap in surveys: young, nearby stars make the best targets for direct imaging surveys. This is well known, as is the fact that there are a limited number of young, nearby stars in the sky. Both SPHERE and GPI will have similar capabilities, will observe at similar wavelengths, and will observe at similar epochs (2012-2014). In a sense, this is natural in science, and has positive benefits: the fierce competition will lead to both sides streamlining their surveys, frontloading their best targets, and publishing results as quickly as possible. It will also place pressure on the data reduction and analysis, so that no detectable planets are missed, lest the competitors pick up an overlooked planet that one's own team could have discovered. Yet at the same time, there is a sense of waste, that should the two teams coordinate, a larger total target list could be constructed, and the statistical constraints placed on planet populations by the combination of the results from the two instruments could define the distributions of giant exoplanets to an unprecedented degree.

If one is to put the names of the stars in the Beta Pic moving group, for example, into the Gemini and VLT archives, one finds observations of these objects going back several years, often more than once per year, each with a proposal title that includes some variant of the phrase "search for giant planets." Some of these observations represent complimentary search techniques, some represent gains in contrast from previous attempts, but many are simple duplications of

other observations. Yet it is this strong competition that leads to quick publications, and frenetic activity to confirm, follow up, and analyze objects like Beta Pic b and the HR 8799 planets. I don't have a clear solution to this question, about which path is preferred from the point of view of getting the maximal science from extrasolar planet observations. But in a way, the question is likely to be answered for us, for the odds of forming the political alliance necessary for the two competing instrument teams to cooperate on target list selection is so vanishingly small, that outright competition is the only plausible possibility.

Nevertheless, I am hopeful that out of the fires of that competition will still rise a grand statistical sample from which we can gain a better understanding of the populations of giant extrasolar planets. And while the first 100 target stars on a direct imaging survey are quite obvious, it's the next few hundred where different assumptions and search priorities come into play. So while the Beta Pic, AB Dor, and Tuc/Hor moving groups will be on each target list, there should still be a large number of stars that are observed by only one instrument, increasing the total target sample. (In fact, this is another benefit of competition, that in order to out-perform the opposing team, each group will be highly motivated to be as clever and innovative as possible in their target selection.) And after each team publishes its survey analysis papers, possibly with not-quite overlapping conclusions on planet populations, these two results can be combined (and combined with previous results, as well), and we as a community can move toward a truly unified picture of extrasolar planet populations.

REFERENCES

- Abt, H. A. 1985, *ApJS*, 59, 95
- Aitken, R. G. & Doolittle, E. 1932, *New general catalogue of double stars within 120 of the North pole ...* ([Washington, D.C.] Carnegie institution of Washington, 1932.)
- Alcala, J. M., Krautter, J., Schmitt, J. H. M. M., Covino, E., Wichmann, R., & Mundt, R. 1995, *A&AS*, 114, 109
- Allen, P. R., Trilling, D. E., Koerner, D. W., & Reid, I. N. 2003, *ApJ*, 595, 1222
- Allen, P. R., & Reid, I. N. 2008, *AJ*, 135, 2024
- Ambruster, C. W., Brown, A., Fekel, F. C., Harper, G. M., Fabian, D., Wood, B., & Guinan, E. F. 1998, in *Astronomical Society of the Pacific Conference Series*, Vol. 154, *Cool Stars, Stellar Systems, and the Sun*, ed. R. A. Donahue & J. A. Bookbinder, 1205–+
- Appenzeller, I., Thiering, I., Zickgraf, F.-J., Krautter, J., Voges, W., Chavarria, C., Kneer, R., Mujica, R., Pakull, M., Rosso, C., Ruzicka, F., Serrano, A., & Ziegler, B. 1998, *ApJS*, 117, 319
- Arribas, S., Mediavilla, E., & Fuensalida, J. J. 1998, *ApJL*, 505, L43+
- Baize, P. 1950, *Journal des Observateurs*, 33, 1
- Baraffe, I., Chabrier, G., Barman, T. S., Allard, F., & Hauschildt, P. H. 2003, *A&A*, 402, 701
- Baraffe, I., Chabrier, G., Allard, F., & Hauschildt, P. H. 1998, *A&A*, 337, 403

- Benedict, G. F., McArthur, B. E., Gatewood, G., Nelan, E., Cochran, W. D., Hatzes, A., Endl, M., Wittenmyer, R., Baliunas, S. L., Walker, G. A. H., Yang, S., Kürster, M., Els, S., & Paulson, D. B. 2006, *AJ*, 132, 2206
- Bennett, N. W. W., Evans, D. S., & Laing, J. D. 1967, *MNRAS*, 137, 107
- Bidelman, W. P. 1951, *ApJ*, 113, 304
- . 1985, *ApJS*, 59, 197
- Biller, B. A., Kasper, M., Close, L. M., Brandner, W., & Kellner, S. 2006, *ApJL*, 641, L141
- Biller, B. A., Close, L. M., Masciadri, E., Nielsen, E., Lenzen, R., Brandner, W., McCarthy, D., Hartung, M., Kellner, S., Mamajek, E., Henning, T., Miller, D., Kenworthy, M., & Kulesa, C. 2007, *ApJS*, 173, 143
- Biller, B. A., Close, L., Lenzen, R., Brandner, W., McCarthy, D. W., Nielsen, E., & Hartung, M. 2004, *Proc. SPIE*, 5490, 389
- Biller, B. A., et al. 2010, *ApJL*, 720, L82
- Boccaletti, A., Carillet, M., Fusco, T., Mouillet, D., Langlois, M., Moutou, C., & Dohlen, K. 2008, *ArXiv e-prints*, 807
- Bonavita, M. & Desidera, S. 2007, *A&A*, 468, 721
- Bonfils, X., Forveille, T., Delfosse, X., Udry, S., Mayor, M., Perrier, C., Bouchy, F., Pepe, F., Queloz, D., & Bertaux, J.-L. 2005, *A&A*, 443, L15
- Borucki, W. J., et al. 2011, *arXiv:1102.0541*
- Boss, A. P. 2007, *ApJL*, 661, L73

- Bowyer, S., Lampton, M., Lewis, J., Wu, X., Jelinsky, P., & Malina, R. F. 1996, *ApJS*, 102, 129
- Brandeker, A., Jayawardhana, R., Ivanov, V. D., & Kurtev, R. 2006, *ApJL*, 653, L61
- Briggs, K. R., & Pye, J. P. 2004, *MNRAS*, 353, 673
- Brown, R. A. 2004, *ApJ*, 607, 1003
- Burgasser, A. J. 2007, *ApJ*, 659, 655
- Burrows, A., Sudarsky, D., & Lunine, J. I. 2003, *ApJ*, 596, 587
- Butler, R. P., Vogt, S. S., Marcy, G. W., Fischer, D. A., Wright, J. T., Henry, G. W., Laughlin, G., & Lissauer, J. J. 2004, *ApJ*, 617, 580
- Butler, R. P., Wright, J. T., Marcy, G. W., Fischer, D. A., Vogt, S. S., Tinney, C. G., Jones, H. R. A., Carter, B. D., Johnson, J. A., McCarthy, C., & Penny, A. J. 2006, *ApJ*, 646, 505
- Carpenter, J. M., et al. 2009, *ApJS*, 181, 197
- Chabrier, G., Baraffe, I., Allard, F., & Hauschildt, P. 2000, *ApJ*, 542, 464
- Chauvin, G., Lagrange, A.-M., Dumas, C., Zuckerman, B., Mouillet, D., Song, I., Beuzit, J.-L., & Lowrance, P. 2004, *A&A*, 425, L29
- Chauvin, G., Lagrange, A.-M., Zuckerman, B., Dumas, C., Mouillet, D., Song, I., Beuzit, J.-L., Lowrance, P., & Bessell, M. S. 2005, *A&A*, 438, L29
- Chauvin, G., et al. 2005, *A&A*, 430, 1027
- Chen, Y. Q., Nissen, P. E., Benoni, T., & Zhao, G. 2001, *A&A*, 371, 943
- Christian, D. J. & Mathioudakis, M. 2002, *AJ*, 123, 2796

- Chun, M., et al. 2008, *Proc. SPIE*, 7015,
- Close, L. M. & Males, J. R. 2009, *ArXiv e-prints*
- Close, L. M., Lenzen, R., Guirado, J. C., Nielsen, E. L., Mamajek, E. E., Brandner, W., Hartung, M., Lidman, C., & Biller, B. 2005, *Nature*, 433, 286
- Close, L. M., Nielsen, E. L., Guirado, J. C., Biller, B. A., Lenzen, R., Brandner, W., Hartung, M., & Lidman, C. 2006, *IAU Colloq. 200: Direct Imaging of Exoplanets: Science & Techniques*, 11
- Close, L. M., Zuckerman, B., Song, I., Barman, T., Marois, C., Rice, E. L., Siegler, N., Macintosh, B., Becklin, E. E., Campbell, R., Lyke, J. E., Conrad, A., & Le Mignant, D. 2007, *ApJ*, 660, 1492
- Close, L. M., Thatte, N., Nielsen, E. L., Abuter, R., Clarke, F., & Tecza, M. 2007a, *ArXiv Astrophysics e-prints*, astro-ph/0703564
- Close, L. 2010, *Nature*, 468, 1048
- Close, L. M., Gasho, V., Kopon, D., Males, J., Follette, K. B., Brutlag, K., Uomoto, A., & Hare, T. 2010, *Proc. SPIE*, 7736,
- Codona, J. L., & Angel, R. 2004, *ApJL*, 604, L117
- Codona, J.L., Angel, R., Close, L., Potter, D. 2005, private communication
- Cowley, A. P., Hiltner, W. A., & Witt, A. N. 1967, *AJ*, 72, 1334
- Cowley, A. P. 1976, *PASP*, 88, 95
- Cruz, K. L., Burgasser, A. J., Reid, I. N., & Liebert, J. 2004, *ApJL*, 604, L61

- Cumming, A., Butler, R. P., Marcy, G. W., Vogt, S. S., Wright, J. T., & Fischer, D. A. 2008, *PASP*, 120, 531
- Currie, T., et al. 2011, *ApJ*, 729, 128
- Cushing, M. C., Rayner, J. T., & Vacca, W. D. 2005, *ApJ*, 623, 1115
- Cutispoto, G., Pallavicini, R., Kuerster, M., & Rodono, M. 1995, *A&A*, 297, 764
- Cutri, R. M., Skrutskie, M. F., van Dyk, S., Beichman, C. A., Carpenter, J. M., Chester, T., Cambresy, L., Evans, T., Fowler, J., Gizis, J., Howard, E., Huchra, J., Jarrett, T., Kopan, E. L., Kirkpatrick, J. D., Light, R. M., Marsh, K. A., McCallon, H., Schneider, S., Stiening, R., Sykes, M., Weinberg, M., Wheaton, W. A., Wheelock, S., & Zacarias, N. 2003, 2MASS All Sky Catalog of point sources. (The IRSA 2MASS All-Sky Point Source Catalog, NASA/IPAC Infrared Science Archive. <http://irsa.ipac.caltech.edu/applications/Gator/>)
- Daemgen, S., Siegler, N., Reid, I. N., & Close, L. M. 2007, *ApJ*, 654, 558
- Eggen, O. J. 1962, *Royal Greenwich Observatory Bulletin*, 51, 79
- . 1964, *AJ*, 69, 570
- Eggen, O. J. 1996, *VizieR Online Data Catalog*, 5008, 0
- Eisenbeiss, T., Seifahrt, A., Mugrauer, M., Schmidt, T. O. B., Neuhäuser, R., & Roell, T. 2007, *Astronomische Nachrichten*, 328, 521
- Endl, M., Cochran, W. D., Wittenmyer, R. A., & Boss, A. P. 2008, *ApJ*, 673, 1165
- Evans, D. S. 1961, *Royal Greenwich Observatory Bulletin*, 48, 389
- Fabricius, C. & Makarov, V. V. 2000, *A&A*, 356, 141

- Fan, X., Strauss, M. A., Becker, R. H., White, R. L., Gunn, J. E., Knapp, G. R., Richards, G. T., Schneider, D. P., Brinkmann, J., & Fukugita, M. 2006, *AJ*, 132, 117
- Favata, F., Barbera, M., Micela, G., & Sciortino, S. 1993, *A&A*, 277, 428
- . 1995, *A&A*, 295, 147
- Favata, F., Micela, G., & Sciortino, S. 1997, *A&A*, 322, 131
- Fernández, D., Figueras, F., & Torra, J. 2008, *A&A*, 480, 735
- Festin, L. 1998, *MNRAS*, 298, L34
- Fischer, D. A. & Valenti, J. 2005, *ApJ*, 622, 1102
- Fleming, T. A., Gioia, I. M., & Maccacaro, T. 1989, *ApJ*, 340, 1011
- Fortney, J. J., Marley, M. S., Saumon, D., & Lodders, K. 2008, *ApJ*, 683, 1104
- Gaidos, E. J., Henry, G. W., & Henry, S. M. 2000, *AJ*, 120, 1006
- Gaudi, B. S., Albrow, M. D., An, J., Beaulieu, J.-P., Caldwell, J. A. R., DePoy, D. L., Dominik, M., Gould, A., Greenhill, J., Hill, K., Kane, S., Martin, R., Menzies, J., Naber, R. M., Pel, J.-W., Pogge, R. W., Pollard, K. R., Sackett, P. D., Sahu, K. C., Vermaak, P., Vreeswijk, P. M., Watson, R., & Williams, A. 2002, *ApJ*, 566, 463
- Gaudi, B. S. 2010, arXiv:1002.0332
- Gliese, W. & Jahreiss, H. 1991, NASA STI/Recon Technical Report A, 92, 33932
- Gliese, W. & Jahreiß, H. 1979, *A&AS*, 38, 423

- Golimowski, D. A., Leggett, S. K., Marley, M. S., Fan, X., Geballe, T. R., Knapp, G. R., Vrba, F. J., Henden, A. A., Luginbuhl, C. B., Guetter, H. H., Munn, J. A., Canzian, B., Zheng, W., Tsvetanov, Z. I., Chiu, K., Glazebrook, K., Hoversten, E. A., Schneider, D. P., & Brinkmann, J. 2004, *AJ*, 127, 3516
- Gorlova, N. I., Meyer, M. R., Rieke, G. H., & Liebert, J. 2003, *ApJ*, 593, 1074
- Gould, A. & Chanamé, J. 2004, *ApJS*, 150, 455
- Gould, A., Udalski, A., An, D., Bennett, D. P., Zhou, A.-Y., Dong, S., Rattenbury, N. J., Gaudi, B. S., Yock, P. C. M., Bond, I. A., Christie, G. W., Horne, K., Anderson, J., Stanek, K. Z., DePoy, D. L., Han, C., McCormick, J., Park, B.-G., Pogge, R. W., Poindexter, S. D., Soszyński, I., Szymański, M. K., Kubiak, M., Pietrzyński, G., Szewczyk, O., Wyrzykowski, Ł., Ulaczyk, K., Paczyński, B., Bramich, D. M., Snodgrass, C., Steele, I. A., Burgdorf, M. J., Bode, M. F., Botzler, C. S., Mao, S., & Swaving, S. C. 2006, *ApJL*, 644, L37
- Graham, J. R., Macintosh, B., Doyon, R., Gavel, D., Larkin, J., Levine, M., Oppenheimer, B., Palmer, D., Saddlemeyer, L., Sivaramakrishnan, A., Veran, J.-P., & Wallace, K. 2007, *ArXiv e-prints*, 704
- Graham, J.R., Macintosh, B., Ghez, A., Kalas, P., Lloyd, J., Makidon, R., Olivier, S., Patience, J., Perrin, M., Poyneer, L., Sevenson, S., Sheinis, A., Sivaramakrishnan, A., Troy, M., Wallace, J., Wilhelmsen, J. 2002, *AAS* 201, 2102
- . 2003b, *AJ*, 126, 2048
- . 2006b, *AJ*, 132, 161
- Greene, T. P., Schneider, G., Science, E., & Mission Team 2007, *Bulletin of the American Astronomical Society*, 38, #135.18

- Guirado, J. C., et al. 1997, *ApJ*, 490, 835
- Guirado, J. C., et al. 2006, *A&A*, 446, 733
- Hale, A. 1994, *AJ*, 107, 306
- Harlan, E. A. & Taylor, D. C. 1970a, *AJ*, 75, 507
- . 1970b, *AJ*, 75, 165
- Harlan, E. A. 1974, *AJ*, 79, 682
- Heard, J. F. 1956, *Publications of the David Dunlap Observatory*, 2, 107
- Helmer, L., Fabricius, C., Einicke, O. H., & Thoburn, C. 1983, *A&AS*, 53, 223
- Henry, T. J., Soderblom, D. R., Donahue, R. A., & Baliunas, S. L. 1996, *AJ*, 111, 439
- Herbig, G. H. & Spalding, Jr., J. F. 1955, *ApJ*, 121, 118
- Hillenbrand, L. A., & White, R. J. 2004, *ApJ*, 604, 741
- Hillenbrand, L. A., et al. 2008, *ApJ*, 677, 630
- Hinz, P. M. 2009, *American Institute of Physics Conference Series*, 1158, 313
- Hodapp, K. W., et al. 2008, *Proc. SPIE*, 7014,
- Holberg, J. B., Oswalt, T. D., & Sion, E. M. 2002, *ApJ*, 571, 512
- Holden, F. 1977, *PASP*, 89, 582
- Holman, M. J. & Wiegert, P. A. 1999, *AJ*, 117, 621
- Hormuth, F., Brandner, W., Hippler, S., Janson, M., & Henning, T. 2007, *A&A*, 463, 707

- Houk, N. & Cowley, A. P. 1975, Michigan Catalogue of two-dimensional spectral types for the HD star (Ann Arbor: University of Michigan, Departement of Astronomy, 1975)
- Houk, N. & Smith-Moore, M. 1988, in Michigan Spectral Survey, Ann Arbor, Dept. of Astronomy, Univ. Michigan (Vol. 4), (1988)
- Houk, N. 1978, Michigan catalogue of two-dimensional spectral types for the HD stars (Ann Arbor : Dept. of Astronomy, University of Michigan : distributed by University Microfilms International, 1978-)
- Houk, N. 1982, in Michigan Spectral Survey, Ann Arbor, Dep. Astron., Univ. Michigan, 3, (1982)
- Hubickyj, O., Bodenheimer, P., & Lissauer, J. J. 2005, *Icarus*, 179, 415
- Ida, S. & Lin, D. N. C. 2004, *ApJ*, 604, 388
- Israelian, G., Santos, N. C., Mayor, M., & Rebolo, R. 2004, *A&A*, 414, 601
- Itoh, Y., Hayashi, M., Tamura, M., Tsuji, T., Oasa, Y., Fukagawa, M., Hayashi, S. S., Naoi, T., Ishii, M., Mayama, S., Morino, J.-i., Yamashita, T., Pyo, T.-S., Nishikawa, T., Usuda, T., Murakawa, K., Suto, H., Oya, S., Takato, N., Ando, H., Miyama, S. M., Kobayashi, N., & Kaifu, N. 2005, *ApJ*, 620, 984
- Janson, M., Brandner, W., Henning, T., Lenzen, R., McArthur, B., Benedict, G. F., Reffert, S., Nielsen, E., Close, L., Biller, B., Kellner, S., Günther, E., Hatzes, A., Masciadri, E., Geissler, K., & Hartung, M. 2007, *AJ*, 133, 2442
- Jayawardhana, R., Hartmann, L., Fazio, G., Fisher, R. S., Telesco, C. M., & Piña, R. K. 1999, *ApJL*, 521, L129

- Johnson, J. A., Butler, R. P., Marcy, G. W., Fischer, D. A., Vogt, S. S., Wright, J. T., & Peek, K. M. G. 2007, *ArXiv e-prints*, 707
- Johnson, J. A., Aller, K. M., Howard, A. W., & Crepp, J. R. 2010, *PASP*, 122, 905
- Johns, M., Angel J. R. P., Schectman, S., Bernstein, R., Fabricant, D.G., McCarthy, P., Phillips, M. 2004, *SPIE* 5489, 441
- Jones, B. F., Fischer, D., Shetrone, M., & Soderblom, D. R. 1997, *AJ*, 114, 352
- Jones, B. F., Fischer, D., & Soderblom, D. R. 1999, *AJ*, 117, 330
- Kalas, P., Graham, J. R., Chiang, E., Fitzgerald, M. P., Clampin, M., Kite, E. S., Stapelfeldt, K., Marois, C., & Krist, J. 2008, *Science*, 322, 1345
- Kasper, M., Apai, D., Janson, M., & Brandner, W. 2007, *A&A*, 472, 321
- Kirkpatrick, J. D., Barman, T. S., Burgasser, A. J., McGovern, M. R., McLean, I. S., Tinney, C. G., & Lowrance, P. J. 2006, *ApJ*, 639, 1120
- Lachaume, R., Dominik, C., Lanz, T., & Habing, H. J. 1999, *A&A*, 348, 897
- Lafrenière, D., Doyon, R., Marois, C., Nadeau, D., Oppenheimer, B. R., Roche, P. F., Rigaut, F., Graham, J. R., Jayawardhana, R., Johnstone, D., Kalas, P. G., Macintosh, B., & Racine, R. 2007, *ApJ*, 670, 1367
- Lafrenière, D., Marois, C., Doyon, R., Nadeau, D., & Artigau, É. 2007, *ApJ*, 660, 770
- Lafrenière, D., Jayawardhana, R., & van Kerkwijk, M. H. 2010, *ApJ*, 719, 497
- Lagrange, A.-M., Gratadour, D., Chauvin, G., Fusco, T., Ehrenreich, D., Mouillet, D., Rousset, G., Rouan, D., Allard, F., Gendron, É., Charton, J., Mugnier, L., Rabou, P., Montri, J., & Lacombe, F. 2009, *A&A*, 493, L21

- Lambert, D. L. & Reddy, B. E. 2004, *MNRAS*, 349, 757
- Leaton, B. R. & Pagel, B. E. J. 1960, *MNRAS*, 120, 317
- Leggett, S. K., Allard, F., Berriman, G., Dahn, C. C., & Hauschildt, P. H. 1996, *ApJS*, 104, 117
- Lenzen, R., Close, L., Brandner, W., Biller, B., & Hartung, M. 2004, in *Ground-based Instrumentation for Astronomy*. Edited by Alan F. M. Moorwood and Iye Masanori. *Proceedings of the SPIE*, Volume 5492, pp. 970-977 (2004)., ed. A. F. M. Moorwood & M. Iye, 970–977
- Lenzen, R., et al. 2003, *Proc. SPIE*, 4841, 944
- Lineweaver, C.H., Grether, D. 2003, *ApJ* 598, 1350
- Lippincott, S. L. & MacDowall, R. J. 1979, *PASP*, 91, 471
- Liu, M. C. 2004, *Science*, 305, 1442
- Liu, M. C. 2008 private communication.
- Liu, M. C., et al. 2010, *Proc. SPIE*, 7736,
- Lowrance, P. J., Becklin, E. E., Schneider, G., Kirkpatrick, J. D., Weinberger, A. J., Zuckerman, B., Dumas, C., Beuzit, J.-L., Plait, P., Malumuth, E., Heap, S., Ter-rile, R. J., & Hines, D. C. 2005, *AJ*, 130, 1845
- Luhman, K. L., Wilson, J. C., Brandner, W., Skrutskie, M. F., Nelson, M. J., Smith, J. D., Peterson, D. E., Cushing, M. C., & Young, E. 2006, *ApJ*, 649, 894
- Luhman, K. L., Allers, K. N., Jaffe, D. T., Cushing, M. C., Williams, K. A., Slesnick, C. L., & Vacca, W. D. 2007, *ApJ*, 659, 1629

- Luhman, K. L., Patten, B. M., Marengo, M., Schuster, M. T., Hora, J. L., Ellis, R. G., Stauffer, J. R., Sonnett, S. M. and Winston, E., Gutermuth, R. A., Megeath, S. T., & Fazio, G. G. 2007b, *ApJ*, 654, 570
- Luhman, K. L., Stauffer, J. R., & Mamajek, E. E. 2005, *ApJL*, 628, L69
- Luhman, K. L., & Potter, D. 2006, *ApJ*, 638, 887
- Luhman, K. L. 1999, *ApJ*, 525, 466
- Lépine, S. & Shara, M. M. 2005, *AJ*, 129, 1483
- López-Santiago, J., Montes, D., Crespo-Chacón, I., & Fernández-Figueroa, M. J. 2006, *ApJ*, 643, 1160
- Maiolino, R., Rieke, G. H., & Rieke, M. J. 1996, *AJ*, 111, 537
- Makarov, V. V., Zacharias, N., Hennessy, G. S., Harris, H. C., & Monet, A. K. B. 2007, *ApJL*, 668, L155
- Malaroda, S. 1975, *AJ*, 80, 637
- Mallik, S. V., Parthasarathy, M., & Pati, A. K. 2003, *A&A*, 409, 251
- Mamajek, E. E. & Hillenbrand, L. A. 2008, *ArXiv e-prints*, 807
- Mamajek, E. E. 2007, private communication
- Marcy, G. W., Butler, R. P., Vogt, S. S., Fischer, D. A., Wright, J. T., Johnson, J. A., Tinney, C. G., Jones, H. R. A., Carter, B. D., Bailey, J., O'Toole, S. J., & Upadhyay, S. 2008, *Physica Scripta Volume T*, 130, 014001
- Marcy, G.W., Butler, R.P., Fischer, D.A., Laughlin, G., Vogt, S.S., Henry, G.W., Poubaix, D. 2002, *ApJ* 581, 1375

- Marley, M. S., Fortney, J. J., Hubickyj, O., Bodenheimer, P., & Lissauer, J. J. 2007, *ApJ*, 655, 541
- Marois, C., Lafrenière, D., Doyon, R., Macintosh, B., & Nadeau, D. 2006, *ApJ*, 641, 556
- Marois, C., Macintosh, B., Barman, T., Zuckerman, B., Song, I., Patience, J., Lafrenière, D., & Doyon, R. 2008, *Science*, 322, 1348
- Marois, C., Macintosh, B., Song, I., & Barman, T. 2005, *arXiv:astro-ph/0502382*
- Marois, C., Zuckerman, B., Konopacky, Q. M., Macintosh, B., & Barman, T. 2010, *Nature*, 468, 1080
- Martin, E. L., Rebolo, R., & Zapatero-Osorio, M. R. 1996, *ApJ*, 469, 706
- Martín, E. L., Brandner, W., Bouvier, J., Luhman, K. L., Stauffer, J., Basri, G., Zapatero Osorio, M. R., & Barrado y Navascués, D. 2000, *ApJ*, 543, 299
- Martin, E.L.: 2005 private communication.
- Masciadri, E., Mundt, R., Henning, T., Alvarez, C., & Barrado y Navascués, D. 2005, *ApJ*, 625, 1004
- Mathioudakis, M., Drake, J. J., Craig, N., Kilkenny, D., Doyle, J. G., Sirk, M. M., Dupuis, J., Fruscione, A., Christian, C. A., & Abbott, M. J. 1995, *A&A*, 302, 422
- Mayor, M., & Queloz, D. 1995, *Nature*, 378, 355
- Mayor, M. & Udry, S. 2008, *Physica Scripta Volume T*, 130, 014010
- McCaughrean, M. J., Close, L. M., Scholz, R.-D., Lenzen, R., Biller, B., Brandner, W., Hartung, M., & Lodieu, N. 2004, *A&A*, 413, 1029

- Metchev, S. A. & Hillenbrand, L. A. 2004, *ApJ*, 617, 1330
- Hoenig, S.F.: 2005 private communication.
- Mohanty, S., Jayawardhana, R., & Basri, G. 2004, *ApJ*, 609, 885
- Montes, D., López-Santiago, J., Gálvez, M. C., Fernández-Figueroa, M. J., De Castro, E., & Cornide, M. 2001, *MNRAS*, 328, 45
- Montes, D., López-Santiago, J., Fernández-Figueroa, M. J., & Gálvez, M. C. 2001a, *A&A*, 379, 976
- Mora, A., Merín, B., Solano, E., Montesinos, B., de Winter, D., Eiroa, C., Ferlet, R., Grady, C. A., Davies, J. K., Miranda, L. F., Oudmaijer, R. D., Palacios, J., Quirrenbach, A., Harris, A. W., Rauer, H., Cameron, A., Deeg, H. J., Garzón, F., Penny, A., Schneider, J., Tsapras, Y., & Wesselius, P. R. 2001, *A&A*, 378, 116
- Morgan, W. W. & Keenan, P. C. 1973, *ARA&A*, 11, 29
- Moór, A., Ábrahám, P., Derekas, A., Kiss, C., Kiss, L. L., Apai, D., Grady, C., & Henning, T. 2006, *ApJ*, 644, 525
- Mugrauer, M., Neuhauser, R., Guenther, E. W., Hatzes, A. P., Huéramo, N., Fernández, M., Ammler, M., Retzlaff, J., König, B., Charbonneau, D., Jayawardhana, R., & Brandner, W. 2004, *A&A*, 417, 1031
- NICI Planet Finding Campaign, Request for Proposals 2005
- Nadal, R., Pedoussaut, A., Ginestet, N., & Carquillat, J.-M. 1974, *A&A*, 37, 191
- Nesterov, V. V., Kuzmin, A. V., Ashimbaeva, N. T., Volchkov, A. A., Röser, S., & Bastian, U. 1995, *A&AS*, 110, 367

- Neuhauser, R. & Brandner, W. 1998, *A&A*, 330, L29
- Neuhäuser, R., Guenther, E., Mugrauer, M., Ott, T., & Eckart, A. 2002, *A&A*, 395, 877
- Neuhäuser, R., Guenther, E. W., Wuchterl, G., Mugrauer, M., Bedalov, A., & Hauschildt, P. H. 2005, *A&A*, 435, L13
- Nielsen, E. L., Close, L. M., Guirado, J. C., Biller, B. A., Lenzen, R., Brandner, W., Hartung, M., & Lidman, C. 2005, *Astronomische Nachrichten*, 326, 1033
- Nielsen, E. L., Close, L. M., & Biller, B. A. 2006, *IAU Colloq. 200: Direct Imaging of Exoplanets: Science & Techniques*, 111
- Nielsen, E. L., Close, L. M., Biller, B. A., Masciadri, E., & Lenzen, R. 2008, *ApJ*, 674, 466
- Nielsen, E. L., & Close, L. M. 2010, *ApJ*, 717, 878
- Noyes, R. W., Weiss, N. O., & Vaughan, A. H. 1984, *ApJ*, 287, 769
- Oswalt, T. D., Hintzen, P. M., & Luyten, W. J. 1988, *ApJS*, 66, 391
- Pallavicini, R., Pasquini, L., & Randich, S. 1992, *A&A*, 261, 245
- Pasquini, L., Liu, Q., & Pallavicini, R. 1994, *A&A*, 287, 191
- Patience, J., King, R. R., de Rosa, R. J., & Marois, C. 2010, *A&A*, 517, A76
- Perryman, M. A. C., Lindegren, L., Kovalevsky, J., Hoeg, E., Bastian, U., Bernacca, P. L., Crézé, M., Donati, F., Grenon, M., van Leeuwen, F., van der Marel, H., Mignard, F., Murray, C. A., Le Poole, R. S., Schrijver, H., Turon, C., Arenou, F., Froeschlé, M., & Petersen, C. S. 1997, *A&A*, 323, L49

- Perry, C. L. 1969, *AJ*, 74, 705
- Pinfield, D. J., Dobbie, P. D., Jameson, R. F., Steele, I. A., Jones, H. R. A., & Katsiyannis, A. C. 2003, *MNRAS*, 342, 1241
- Potter, D., Martín, E. L., Cushing, M. C., Baudoz, P., Brandner, W., Guyon, O., & Neuhauser, R. 2002, *ApJL*, 567, L133
- Pounds, K. A., Allan, D. J., Barber, C., Barstow, M. A., Bertram, D., Branduardi-Raymont, G., Brebner, G. E. C., Buckley, D., Bromage, G. E., Cole, R. E., Courtier, M., Cruise, A. M., Culhane, J. L., Denby, M., Donoghue, D. O., Dunford, E., Georgantopoulos, I., Goodall, C. V., Gondhalekar, P. M., Gourlay, J. A., Harris, A. W., Hassall, B. J. M., Hellier, C., Hodgkin, S., Jeffries, R. D., Kellett, B. J., Kent, B. J., Lieu, R., Lloyd, C., McGale, P., Mason, K. O., Matthews, L., Mittaz, J. P. D., Page, C. G., Pankiewicz, G. S., Pike, C. D., Ponman, T. J., Puchnarewicz, E. M., Pye, J. P., Quenby, J. J., Ricketts, M. J., Rosen, S. R., Sansom, A. E., Sembay, S., Sidher, S., Sims, M. R., Stewart, B. C., Sumner, T. J., Vallance, R. J., Watson, M. G., Warwick, R. S., Wells, A. A., Willingale, R., Willmore, A. P., Willoughby, G. A., & Wonnacott, D. 1993, *MNRAS*, 260, 77
- Poveda, A., Herrera, M. A., Allen, C., Cordero, G., & Lavalley, C. 1994, *Revista Mexicana de Astronomia y Astrofisica*, 28, 43
- Pye, J. P., McGale, P. A., Allan, D. J., Barber, C. R., Bertram, D., Denby, M., Page, C. G., Ricketts, M. J., Stewart, B. C., & West, R. G. 1995, *MNRAS*, 274, 1165
- Quintana, E. V., Lissauer, J. J., Chambers, J. E., & Duncan, M. J. 2002, *ApJ*, 576, 982
- Randich, S., Gratton, R., & Pallavicini, R. 1993, *A&A*, 273, 194

- Randich, S., Pallavicini, R., Meola, G., Stauffer, J. R., & Balachandran, S. C. 2001, *A&A*, 372, 862
- Raymond, S. N. 2006, *ApJL*, 643, L131
- Reid, I. N., Hawley, S. L., & Gizis, J. E. 1995, *AJ*, 110, 1838
- Reid, I. N., Kirkpatrick, J. D., Liebert, J., Gizis, J. E., Dahn, C. C., & Monet, D. G. 2002, *AJ*, 124, 519
- Reiners, A., Basri, G., & Mohanty, S. 2005, *ApJ*, 634, 1346
- Rhee, J. H., Song, I., Zuckerman, B., & McElwain, M. 2007, *ApJ*, 660, 1556
- Roeser, S. & Bastian, U. 1988, *A&AS*, 74, 449
- Rossiter, R. A. 1955, *Publications of Michigan Observatory*, 11, 1
- Rufener, F. & Bartholdi, P. 1982, *A&AS*, 48, 503
- Santos, N. C., Israelian, G., & Mayor, M. 2004, *A&A*, 415, 1153
- Sato, K. & Kuji, S. 1990, *A&AS*, 85, 1069
- Schild, R. E. 1973, *AJ*, 78, 37
- Schneider, G., & Silverstone, M. D. 2003, *Proc. SPIE*, 4860, 1
- Schwöpe, A., Hasinger, G., Lehmann, I., Schwarz, R., Brunner, H., Neizvestny, S., Ugryumov, A., Balega, Y., Trümper, J., & Voges, W. 2000, *Astronomische Nachrichten*, 321, 1
- Simon, T. & Drake, S. A. 1993, *AJ*, 106, 1660

- Skemer, A. J., Close, L. M., Sz\Hucs, L., Apai, D., Pascucci, I., & Biller, B. A. 2011, arXiv:1103.1880
- Soderblom, D. R., Jones, B. F., Balachandran, S., Stauffer, J. R., Duncan, D. K., Fedele, S. B., & Hudon, J. D. 1993a, AJ, 106, 1059
- Soderblom, D. R., Pilachowski, C. A., Fedele, S. B., & Jones, B. F. 1993b, AJ, 105, 2299
- Soderblom, D. R., King, J. R., & Henry, T. J. 1998, AJ, 116, 396
- Soderblom, D. R., King, J. R., Siess, L., Jones, B. F., & Fischer, D. 1999, AJ, 118, 1301
- Song, I., Bessell, M. S., & Zuckerman, B. 2002, ApJL, 581, L43
- Song, I., Zuckerman, B., & Bessell, M. S. 2003, ApJ, 599, 342
- Sozzetti, A., Udry, S., Zucker, S., Torres, G., Beuzit, J. L., Latham, D. W., Mayor, M., Mazeh, T., Naef, D., Perrier, C., Queloz, D., & Sivan, J.-P. 2006, A&A, 449, 417
- Stassun, K. G., Mathieu, R. D., & Valenti, J. A. 2007, ArXiv e-prints, 704
- Stephenson, C. B. 1960, AJ, 65, 60
- Stocke, J. T., Morris, S. L., Gioia, I. M., Maccacaro, T., Schild, R., Wolter, A., Fleming, T. A., & Henry, J. P. 1991, ApJS, 76, 813
- Strassmeier, K., Washuettl, A., Granzer, T., Scheck, M., & Weber, M. 2000, A&AS, 142, 275
- Su, K. Y. L., et al. 2006, ApJ, 653, 675

- Swain, M. R., Vasisht, G., & Tinetti, G. 2008, *Nature*, 452, 329
- Terndrup, D. M., Krishnamurthi, A., Pinsonneault, M. H., & Stauffer, J. R. 1999, *AJ*, 118, 1814
- Thatte, N., Abuter, R., Tecza, M., Nielsen, E. L., Clarke, F. J., & Close, L. M. 2007, *MNRAS*, 378, 1229
- Torres, C. A. O., da Silva, L., Quast, G. R., de la Reza, R., & Jilinski, E. 2000, *AJ*, 120, 1410
- Ungren, A. R. & Staron, R. T. 1970, *ApJS*, 19, 367
- Vysotsky, A. N., Janssen, E. M., Miller, W. J., & Walther, M. E. 1946, *ApJ*, 104, 234
- Wahhaj, Z., et al. 2011, *ApJ*, 729, 139
- Waite, I. A., Carter, B. D., Marsden, S. C., & Mengel, M. W. 2005, *Publications of the Astronomical Society of Australia*, 22, 29
- Webb, R. A., Zuckerman, B., Platais, I., Patience, J., White, R. J., Schwartz, M. J., & McCarthy, C. 1999, *ApJL*, 512, L63
- Wichmann, R., Schmitt, J. H. M. M., & Hubrig, S. 2003, *A&A*, 399, 983
- Wilson, Jr., R. H. 1954, *AJ*, 59, 132
- Wright, J. T., Marcy, G. W., Butler, R. P., & Vogt, S. S. 2004, *ApJS*, 152, 261
- Zapatero Osorio, M. R., Lane, B. F., Pavlenko, Y., Martín, E. L., Britton, M., & Kulkarni, S. R. 2004, *ApJ*, 615, 958
- Zboril, M., Byrne, P. B., & Rolleston, W. R. J. R. 1997, *MNRAS*, 284, 685
- Zuckerman, B. & Song, I. 2004, *ARA&A*, 42, 685

Zuckerman, B., Song, I., Bessell, M. S., & Webb, R. A. 2001a, *ApJL*, 562, L87

Zuckerman, B., Webb, R. A., Schwartz, M., & Becklin, E. E. 2001b, *ApJL*, 549, L233

Zuckerman, B., Song, I., & Bessell, M. S. 2004, *ApJL*, 613, L65